



HAL
open science

Propriétés photoélectriques de vitrocéramiques et cristaux de chalcogénures

Ilia Korolkov

► **To cite this version:**

Ilia Korolkov. Propriétés photoélectriques de vitrocéramiques et cristaux de chalcogénures. Matériaux. Université de Rennes, 2017. Français. NNT : 2017REN1S145 . tel-01822716

HAL Id: tel-01822716

<https://theses.hal.science/tel-01822716>

Submitted on 25 Jun 2018

HAL is a multi-disciplinary open access archive for the deposit and dissemination of scientific research documents, whether they are published or not. The documents may come from teaching and research institutions in France or abroad, or from public or private research centers.

L'archive ouverte pluridisciplinaire **HAL**, est destinée au dépôt et à la diffusion de documents scientifiques de niveau recherche, publiés ou non, émanant des établissements d'enseignement et de recherche français ou étrangers, des laboratoires publics ou privés.

Année 2017



THÈSE / UNIVERSITÉ DE RENNES 1
sous le sceau de l'Université Bretagne Loire

pour le grade de
DOCTEUR DE L'UNIVERSITÉ DE RENNES 1
Mention : Sciences de Matériaux
Matière, Molécules et Matériaux (3M)

présentée par

Ilia Korolkov

UMR-CNRS 6226
Institut des Sciences Chimiques de Rennes
Equipe Verres et Céramiques
UFR Sciences et Propriétés de la Matière

**Propriétés
photoélectriques de
vitrocéramiques et
cristaux de
chalcogénures**

**Thèse soutenue à Rennes
le 10 novembre 2017**

devant le jury composé de :

Hewak Dan

Professor - University of Southampton/ *rapporteur*

Barreau Nicolas

MCF-HDR - Université de Nantes/ *rapporteur*

Guillemet Sophie

DR CNRS - Université Paul Sabatier, Toulouse /
examineur

Lhermite Hervé

MCF - Université de Rennes 1 / *examineur*

Zhang Xiang-Hua

DR CNRS - Université de Rennes 1/ *co-directeur de
thèse*

Adam Jean-Luc

DR CNRS - Université de Rennes 1/ *directeur de
thèse*

Памяти моего учителя,
профессора Татьяны Викторовны Бочаровой

Pour renaître
De tes cendres
Il te faudra
Réapprendre
Aimer vivre, rester libre

Délaisser
Tes amertumes
Te frayer
Jusqu'à la lune
Un passage, il faut me croire

Mylène Farmer «Il n'y a pas d'ailleurs»

Acknowledgments

First of all, I would like to thank a lot my two supervisors, Professor Jean-Luc Adam and Professor Xiang-Hua Zhang who believed in me and invited to prepare this thesis in their group. I really learned a lot from them about how to work in science, how to push the boundaries and of course how to handle with fails (those I had a lot). Their kind and patient guidance was a great lesson for me about how to take care of nasty students like I am. It was an amazing time in a dream team full of new experiences scientific, linguistic and personal. Full of jokes of Professor Joahn Troles, I could barely understand, around a morning coffee, loud laugh of doctor Claudia Goncalvez (and her successor Enora Lavanant) and strict and thorough guidance of doctor Catherine Boussard-Pledel. I have never experienced such an atmosphere of warmness and trust in a big scientific group which is rather a family than just a research team.

During these 3 years I traveled a lot, carefully collecting all the tickets, which I have more than two hundreds now. Thanks to this PhD I was able to see different European countries, to talk to hundreds of people and better understand culture and mentality of Western Europe. I loved France and French language, which is definitely my second language now, freedom and cultural (culinary) diversity it proposes. I would like to specifically thank Jean-Luc and Zhang for this opportunity to see the world and to better understand myself.

I am grateful to doctor Michel Cathelinaud for the collaboration and fruitful conversations around physics and optics and doctor Jean-François Bergamini for AFM and Nespresso.

Also I would like express my sincere thanks to doctor Hervé Lhérmite for his help with solar devices characterization and for his participation in the committee. To Thierry and Thierry for their engineer and glassware guidance. My thanks to doctor Laurent Calvez who helped me a lot in the begging of my thesis and after with SEM. And doctor François Cheviré for his kindness and help with XRD refinement.

I want to remark my friends who supported me and helped me to integrate into a new and sometimes complicated world. My sincere thanks to doctor Claudia Goncalvez with whom we passed this PhD way together form the beginning to the end. Also, to doctor Solenn Cosic for her curly hairs and awesome parties we had. You are the most kind and supportive persons I have met in my life.

I am grateful to my men, Tomas Halencovic and Giuseppe Palma. You were always around to hang out but also to support me in the very dark moments of these three years. You two are amazing and I love you both, you would not believe how much!

I am grateful to doctoral alumni of glasses and ceramics group: Radwan Chahal, Emeline Baudet and Antoine Brehault (welcome back, by the way) who helped me a lot and taught me how to handle with solid state synthesis. And of course doctor Mathieu Hubert whose thesis inspired me for working with chalcogenides.

I want to thank netherland lord I van Kharaldin, who somehow did not forget about me and has been founding a time to support our distance relationships. Baltika 9 in padik is waiting for us when I return. And my twin-brother Andrey, for giving me a part of Illiandr atmosphere by skype. I am grateful to my wife Valentina (future doctor, I hope) with whom we had a lot of beautiful moments together. And the last but not least, my beloved Valeria. I met you probably in the most awful and distracting period of my life and you breathed a new hope and new passion in me, without you I could barely finish this work.

Of course my eternal thanks to my parents for their support moral and sometimes financial. Мам, пап, спасибо, я вас люблю.

I would like to remark a contribution of my former team of the Integral Electronics department in Saint-Petersbourg State Polytechnic University. Especially I would like to thank Professor N.T. Sudar and Professor V.M. Kapralova for deep knowledge of disordered semiconductors, which was vital for working with chalcogenides. To visiting professors D.V. Shamshur and V.A. Moshnikov for giving a broad outlook and real erudition in physics and molecular electronics. Also to Professor V.R. Meshkov for his patience and eager to give fundamental knowledge in mathematical physics, which was very useful for the comprehension of the conductivity mechanism in heavily doped crystals.

And finally, I am grateful to my teacher, professor T.V. Bocharova, who brought me in the world of condensed matter physics and gave me an opportunity to advance in science, to her this thesis is devoted.

Table of contents

Résumé détaillé en français.....	-i-
General introduction.....	1
Chapter I State-of-the art in the domain of solar energy harvesting	
1.Context of study.....	3
1.1.Energy consumption nowadays, part of renewable energy sources on the energy consumption diagram.....	3
1.2.Question of environnement pollution.....	5
1.3.Common problems of alternative energy sources.....	6
1.4. Survey on different types of solar energy harvesting systems.....	6
2.Physical principles of solar cell functioning.....	10
2.1.Charge generation on a p-n junction interface.....	10
2.2.Crystalline silicon based solar cells.....	11
2.3.Amorphous silicon based solar cells.....	17
2.4.Heterojunction based solar cells. Multi-junction architecture for solar cells.....	22
2.5.Dye sensitized solar cells. Grätzel cell.....	25
2.6.Perovskite architecture for solar cells.....	26
3.Chalcogenide materials in the domain of solar cells.....	29
3.1.Definition and general properties of chalcogenide materials.....	29
3.2.Crystalline chalcogenides application for solar energy harvesting.....	30
3.2.1.Binary systems.....	31
3.2.2.Ternary systems.....	33
3.2.3.Quaternary systems.....	35
3.3.Chalcogenide glass-ceramics for photovoltaic applications.....	36
3.3.1.Chalcogenide glasses and their application.....	37
3.3.2.Photovoltaic effect in glass-ceramics of pseudoternary GeSe ₂ -Sb ₂ Se ₃ -CuI system.....	40
4.Conclusion.....	45
5.References.....	46

Chapter II Investigations on charge photo generation and charge transfer mechanism in 40GeSe₂-40Sb₂Se₃-20CuI bulk glass-ceramics.

1. Establishing of iodine crucial role in charge photogeneration and transfer in 40GeSe ₂ -40Sb ₂ Se ₃ -20CuI glass-ceramics.	54
1.1. Effect of iodide introduction on the chalcogenide glass structure.....	54
1.2. Glass precursor preparation and characterization.....	55
1.2.1. Glass synthesis	55
1.2.2. Thermal properties	56
1.3. Controlled crystallization of glass.	59
1.3.1. Characterization by XRD.....	59
1.3.2. Observation by SEM.....	61
1.3.3. Surface potential measurement	62
1.3.4. Photoelectrochemical (PEC) measurements	65
2. Influence of Iodine doping on the electrical properties of Sb ₂ Se ₃	69
2.1. Influence on the structure and the electric conductivity.....	69
2.2. On the photoelectric properties.....	74
3. Fine tuning of the 40GeSe ₂ -40Sb ₂ Se ₃ -20CuI glass precursor	76
3.1. On fine tuning in this system.....	76
3.2. Glass precursor preparation and characterization.....	77
3.3. Preparation and characterization of glass-ceramics.....	79
3.4. Optimization of annealing procedure of Ge ₁₁ Sb ₂₂ Cu ₅ I ₅ Se _{58.8} glass-ceramic.	83
4. Influence of stoichiometric deviations on Sb ₂ Se ₃ electrical properties.....	86
5. Conclusion	96
6. References.....	97

Chapter III Improvement of photoelectric properties of glass-ceramics in pseudo-ternary system xGeSe₂-ySb₂Se₃-(1-x-y)CuI

1 Introduction.....	98
2 Influence of small additives of sulphur on electric properties of 40GeSe ₂ -40Sb ₂ Se ₃ -20CuI glass-ceramics.	101
2.1. On Fermi level tuning in Sb ₂ Se ₃	101
2.2. Synthesis peculiarities of sulphur containing glass precursor.....	103

2.3. Glass precursor characterization.....	105
2.4. Controllable crystallization of sulphur-containing precursors.	108
2.5. Electric properties of sulphur-containing glass-ceramics.....	111
3 Variety of cation substitutions in 40GeSe ₂ -40Sb ₂ Se ₃ -20CuI glass precursor.....	113
3.1. On the cation substitutions in glass-ceramics.....	113
3.2 Glass precursors preparation	114
3.3. Structural and electric properties of 40GeSe ₂ -40Sb _{2-x} Bi _x Se ₃ -20CuI.glass-ceramics	115
3.4. Structural and electric properties of 40GeSe ₂ -40Sb _{2-x} Sn _x Se ₃ -20CuI glass-ceramics.....	119
3.5. Structural and electric properties of xGeSe ₂ -(1-x) Sb ₂ Se ₃ -20CuI glass-ceramics	130
4. Study of xGeSe ₂ – y Sb ₂ Se ₃ – (1-x-y)Cu(Br,Cl) system	136
4.1 On the utilization of CuBr and CuCl.....	136
4.2 Glass precursor preparation.....	137
4.3 Glass precursor analysis. Controllable crystallization. Electric properties	139
5.Conclusion.....	145
6.References	146

Chapter IV Preparation of thin film solar cells via magnetron sputtering

1.Introduction.....	147
2.Preparation of targets for magnetron sputtering	149
2.1.Preparation of chalcogenide targets by melting-quenching process	149
2.1.1.Targets synthesis	149
2.1.2.Targets characterization	151
2.2.Preparation of targets by hot pressing	154
2.2.1.Targets preparation and characterization	154
3.Thin films preparation and characterization	156
3.1.Some fundamentals of magnetron sputtering.....	156
3.2.Preparation of bulk heterojunction within thin films based on 40GeSe ₂ -40Sb ₂ Se ₃ -20CuI composition.....	159
3.3.Preparation of thin films based on Cu ₃ SbSe ₄ composition	172
3.4.Fabrication of planar heterojunction with thin films of p-type [40GeSe ₂ -40Sb ₂ Se ₃ -20CuI].....	176
4.Conclusion	182
5.References.....	183
General conclusion and prospectives.....	185

Résumé détaillé en français

1. Introduction.

Ce travail est inspiré par le nombre des recherches sur les nouveaux matériaux pour les applications photovoltaïques. La réduction exponentielle du prix des composants des batteries solaires et la croissance de leur efficacité ont élargi le champ d'application des cellules solaires. Dans les derniers 35 ans, ces matériaux ont parcouru le chemin des prototypes à buts scientifiques, extrêmement chers, jusqu'au produit commercial disponible pour les entreprises et consommateurs privés.

Tandis que le silicium est toujours un matériau majeur pour la fabrication commerciale des batteries solaires (ayant plus de 90% du marché), son rendement de conversion présente une efficacité comprise entre 11% et 15% seulement. En même temps, les derniers résultats dans le domaine des batteries solaires à base de perovskite, font état de cellules avec 30% d'efficacité. Les cellules de Grätzel organiques-non organiques, bas-coût, qui utilisent des petites molécules organiques en tant de sensibilisateur, donnent une efficacité comparable à celle des modules à base de silicium. Les batteries solaires à base de nanoparticules de chalcogénures sont aussi des dispositifs d'intérêt grâce à leur flexibilité spectrale et à leur stabilité chimique. Récemment, des cellules sensibilisées par des nanoparticules de solution solide quaternaire de chalcogénures ont démontré 12% d'efficacité. Des batteries solaires à base de couches minces de CdTe avec une efficacité de conversion de 20% sont connues depuis longtemps.

Vu les tendances, il est de grande importance, d'effectuer des études sur de nouveaux matériaux photoélectriques, puisque les technologies existantes présentent plusieurs limites comme une efficacité trop faible, un prix élevé ou une durée de vie insatisfaisante.

Dans ce travail, l'étude sur les vitrocéramiques et cristaux de chalcogénures pour les applications photovoltaïques est présentée. Nous avons démontré la fabrication de verres et cristaux de nouvelles compositions, les études optiques, électriques ainsi que structurales des échantillons massifs. Nous avons également effectué la fabrication de cellules solaires à base de couches minces à partir des compositions étudiés. Dans le présent travail, nous éclaircirons un cycle qui va de l'élaboration des nouvelles compositions chimiques jusqu'à la fabrication d'une cellule solaire fonctionnelle.

Ce travail est apparu comme la suite d'une recherche sur les vitrocéramiques transparentes dans l'infrarouge, dont le but était d'améliorer les propriétés mécaniques de celles-ci. Il a été mis en lumière que les verres du system pseudo – ternaire « $\text{GeSe}_2 - \text{Sb}_2\text{Se}_3 - \text{CuI}$ » après la céramisation possède une absorption inhabituelle dans le moyen infrarouge, comme le montre la fig. 1. Tandis que, normalement, les céramiques présentent une absorption dans le proche infrarouge en raison de la diffusion Rayleigh, l'absorption dans la région 3-12 μm est associée à la présence des porteurs de charge libres.

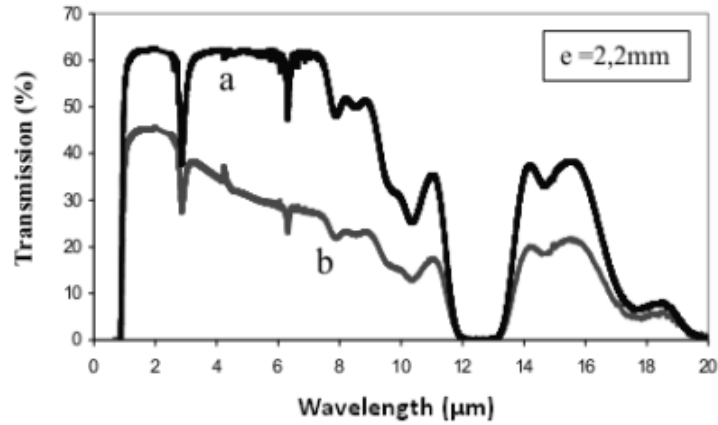


Figure 1 Courbe de transmission du verre (a) et de la vitrocéramique (b) de la même composition $60\text{GeSe}_2\text{-}30\text{Sb}_2\text{Se}_3\text{-}10\text{CuI}$

Par conséquent, le système « $\text{GeSe}_2 - \text{Sb}_2\text{Se}_3 - \text{CuI}$ » a été étudié pour ses propriétés optiques, structurales et électriques et particulièrement photoélectriques. Il a été trouvé que, pendant la céramisation, un réseau cristallin microstructuré se formait. La croissance simultanée des deux types des cristaux, Sb_2Se_3 et Cu_2GeSe_3 , favorise le recouvrement de Sb_2Se_3 qui ont la forme d'une baguette par des microcristaux de Cu_2GeSe_3 qui possèdent une conductivité élevée. Par ce moyen, les cristaux de Sb_2Se_3 , qui ne sont pas conducteurs, constituent une topologie continue recouverte par Cu_2GeSe_3 qui assure une conductivité dans l'échantillon massif. Le mélange intime de ces deux types des cristaux a été montré par Microscopie Electronique à Transmission Haute-Résolution (HRTEM). Cette coexistence a permis de suggérer la présence d'une jonction p-n entre Sb_2Se_3 de type n et Cu_2GeSe_3 de type p, où Sb_2Se_3 joue le rôle d'un absorbeur et Cu_2GeSe_3 celui de la phase qui assure la séparation des charges générées et les conduit vers les électrodes. Le mécanisme de la génération et du transfert de charge est montré dans la figure 2.

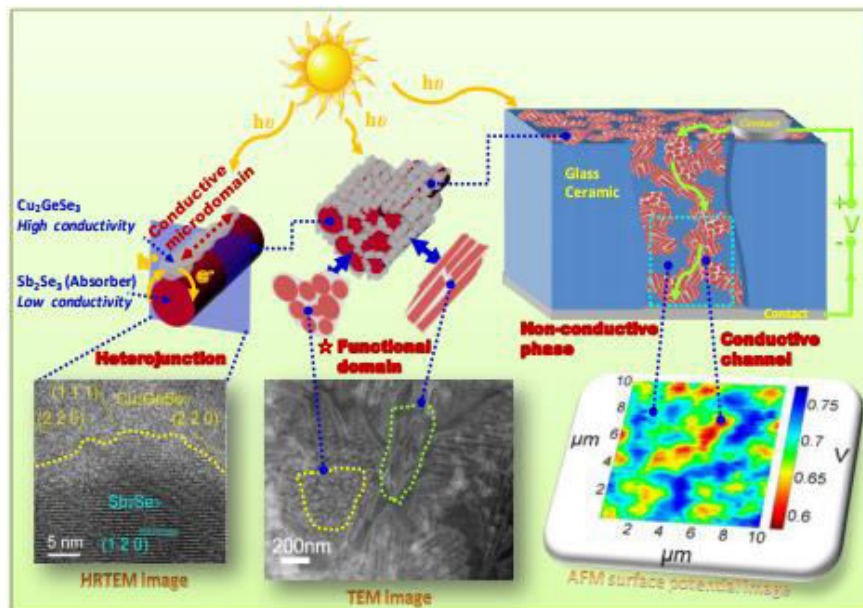


Figure 2 Mécanisme de la photo-génération, de la séparation et du transport des charges dans les vitrocéramiques du system “ $\text{GeSe}_2\text{-Sb}_2\text{Se}_3\text{-CuI}$ ”.

D'après l'expérience photo-électro-chimique (PEC), dont le schéma est montré dans la fig.3 (a), il est bien visible que deux types des cristaux existent dans la vitrocéramique: le type p avec une intense photoconductivité sous voltage négatif, et le type n avec une photoréponse prononcée sous potentiel positif. La meilleure composition $40\text{GeSe}_2\text{-}40\text{Sb}_2\text{Se}_3\text{-}20\text{CuI}$, dont la courbe PEC est montrée à la fig.3(b), atteint un photocourant de $74 \mu\text{A}/\text{cm}^2$ pour une tension appliquée de -0.6V et jusqu'à $100 \mu\text{A}/\text{cm}^2$ pour une tension de $+0.6\text{V}$.

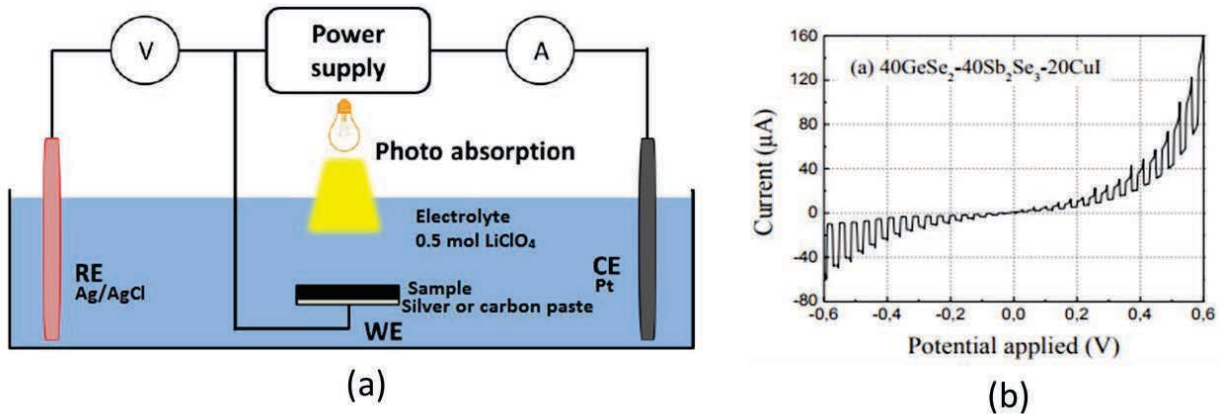


Figure 3 expérience photo-électro-chimique (PEC) à trois-électrodes (a), courbe PEC, qui démontre une forte photoconductivité des semi-conducteurs de type - p et de type - n dans la vitrocéramique $40\text{GeSe}_2\text{-}40\text{Sb}_2\text{Se}_3\text{-}20\text{CuI}$ (b).

2. Recherche sur le mécanisme de la photogénération de charges et du transfert de charges dans la vitrocéramique du système « $\text{GeSe}_2 - \text{Sb}_2\text{Se}_3 - \text{CuI}$ ».

Dans l'étude précédente, il a été démontré que l'iode se localise majoritairement dans la phase Sb_2Se_3 et, probablement, joue un rôle important dans les propriétés photoélectriques. A cet égard, nous avons réalisé une analyse de l'influence de l'iode sur la structure et sur le comportement photoélectrique de la vitrocéramique $40\text{GeSe}_2\text{-}40\text{Sb}_2\text{Se}_3\text{-}20\text{CuI}$.

L'analyse thermique a indiqué que la réduction de l'iode dans CuI_x n'influence pas beaucoup les températures de transition vitreuse et de cristallisation, ainsi que la stabilité des verres, tandis que l'augmentation de la quantité d'iode réduit les températures de cristallisation et de transition vitreuse substantiellement, comme il est montré dans la figure 4. Cela rend compte de la dépolymérisation du verre ou I prend la place de Se^{2-} dans la matrice vitreuse. Ayant la charge -1 au lieu de -2 pour Se^{2-} , I n'est pas capable de former plus qu'une liaison chimique et par conséquent termine la chaîne entraînant la dépolymérisation du verre.

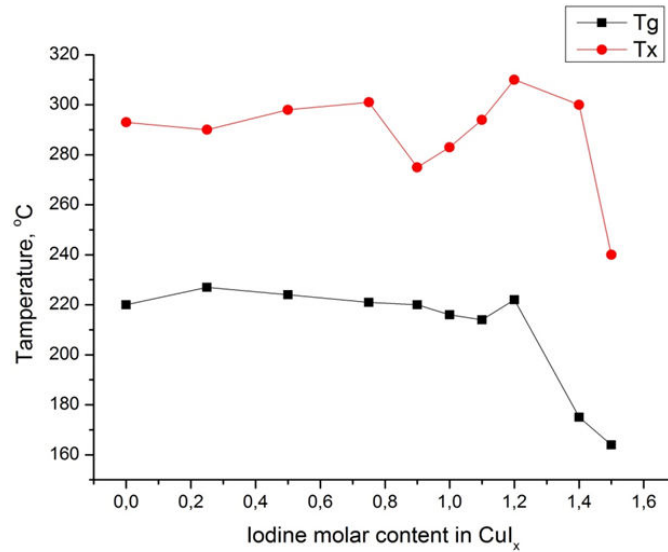


Figure 4 Températures de transition vitreuse et de cristallisation de la vitrocéramique $40GeSe_2-40Sb_2Se_3-20CuI_x$ en fonction de la quantité d'iode.

Après la céramisation, qui habituellement est effectuée pendant 1 heure sous la température de cristallisation (T_x) dans un four ventilé pour assurer une cristallisation homogène, les échantillons massifs ont été étudiés par diffractométrie de rayons X (DRX), dont les spectres sont montrés dans la fig. 5. Il a été constaté que l'augmentation de la quantité d'iode n'entraîne pas l'apparition de nouvelles phases ou de changement non-négligeable des phases existantes jusqu'au seuil de $CuI_{1.4}$ dans la vitrocéramique $40GeSe_2-40Sb_2Se_3-20CuI_{1.4}$. Au-delà, la quantité d'iode est suffisante pour engendrer une cristallisation importante d'une phase de $SbISe$ (fig.5 (a), lignes roses et vertes). C'est également la concentration de l'iode qui entraîne une sévère dépolymérisation du verre précurseur. En même temps, en diminuant la concentration de l'iode dans le composant CuI_x on n'observe pas de nouvelles phases ni de décalages importants de la position des signaux DRX existants (fig.5(b)). Cela signifie qu'aucun changement flagrant dans les constantes de maille de Sb_2Se_3 n'a lieu pour des concentrations d'iode ne dépassant pas le seuil noté ci-dessus.

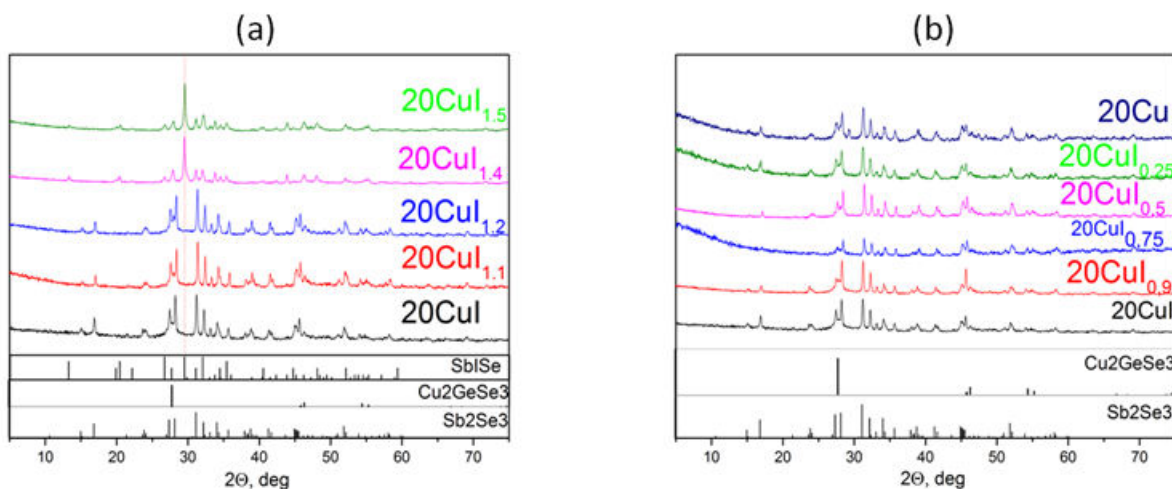


Figure 5 Spectres DRX des vitrocéramiques de composition $40GeSe_2-40Sb_2Se_3-20CuI_x$ avec variation de la quantité d'iode dans le précurseur vitreux.

On peut quand même constater certains changements topologiques pour les vitrocéramiques ayant une quantité réduite d'iode, dans la fig.6. La structure des baguettes de Sb_2Se_3 habituelle pour la vitrocéramique $40GeSe_2-40Sb_2Se_3-20CuI$ cède la place aux structures plus serrées, où les baguettes forment des feuilles de plus grand taille.

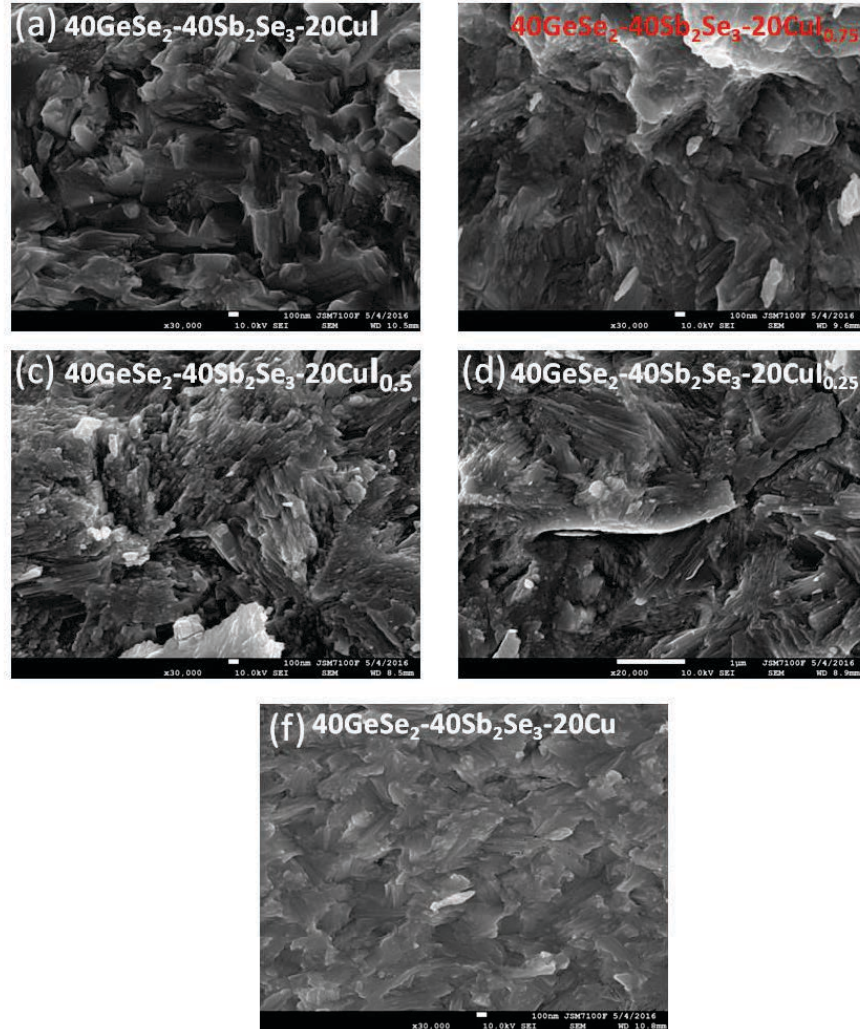


Figure 6 Image MEB des vitrocéramiques à base du verre $40GeSe_2-40Sb_2Se_3-20CuI_x$ avec une quantité d'iode réduite

Beaucoup plus importants sont les changements au niveau du potentiel de surface qui est montré dans la fig.7. La vitrocéramique $40GeSe_2-40Sb_2Se_3-20CuI$ possède plusieurs zones de potentiel différent (fig.7 (a)). Il est important que les zones de potentiel élevé (orange) soient liées entre elles à la surface ; elles ont une largeur de $1 \mu m$ environ. Avec la diminution de la quantité d'iode on constate que ces zones deviennent d'abord moins prononcées, comme c'est le cas pour $40GeSe_2-40Sb_2Se_3-20CuI_{0.75}$ (fig.7 (b)). Elles disparaissent pour les vitrocéramiques $40GeSe_2-40Sb_2Se_3-20CuI_{0.5}$ (fig.7(c)) et $40GeSe_2-40Sb_2Se_3-20CuI_{0.25}$ pour lesquelles on observe une surface avec un potentiel homogène (fig.7 (d)). On peut conclure que la distribution de l'iode, qui coexiste avec Sb_2Se_3 , n'est pas homogène et que ce dernier est capable de modifier le potentiel Kelvin de Sb_2Se_3 et, par conséquent, de modifier le niveau de Fermi de Sb_2Se_3 . Sb_2Se_3 enrichi avec de l'iode forme les « passages » d'un potentiel de surface élevé.

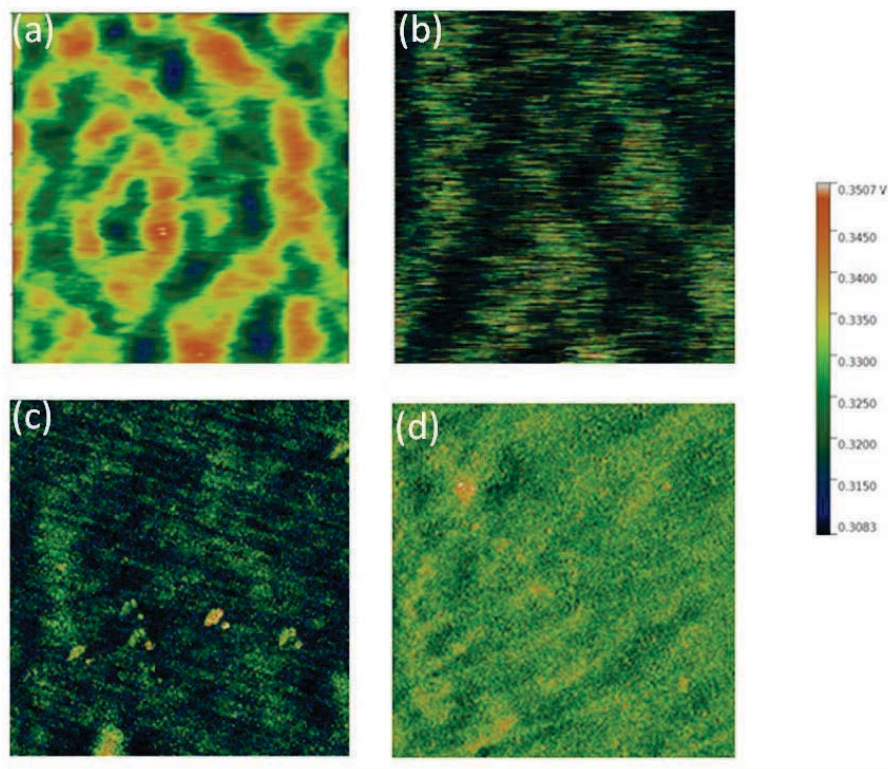


Figure 7 Image du potentiel de surface (Kelvin probe microscope) des vitrocéramiques avec des quantités d'iode différentes : (a) $40\text{GeSe}_2\text{-}40\text{Sb}_2\text{Se}_3\text{-}20\text{CuI}$, (b) $40\text{GeSe}_2\text{-}40\text{Sb}_2\text{Se}_3\text{-}20\text{CuI}_{0,75}$, (c) $40\text{GeSe}_2\text{-}40\text{Sb}_2\text{Se}_3\text{-}20\text{CuI}_{0,5}$, (d) $40\text{GeSe}_2\text{-}40\text{Sb}_2\text{Se}_3\text{-}20\text{CuI}_{0,25}$

Ces résultats sont en bon accord avec les mesures de conductivité de la vitrocéramique, qui dépend fortement de la concentration en iode (fig.8). La baisse de la quantité de l'iode dans un composant entraîne une diminution très importante de la conductivité. Pour la vitrocéramique $40\text{GeSe}_2\text{-}40\text{Sb}_2\text{Se}_3\text{-}20\text{Cu}$, où il n'y a pas d'iode, on constate une baisse de conductivité de 10^4 fois par rapport à la vitrocéramique $40\text{GeSe}_2\text{-}40\text{Sb}_2\text{Se}_3\text{-}20\text{CuI}$, qui, en effet, démontre la meilleure conductivité parmi toutes les vitrocéramiques préparées.

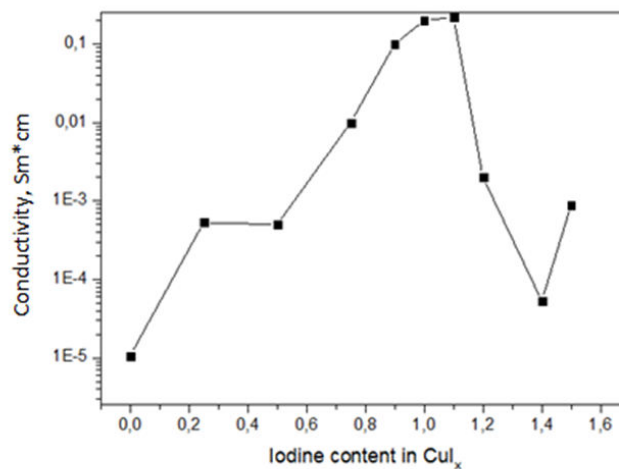


Figure 8 Conductivité des vitrocéramiques $40\text{GeSe}_2\text{-}40\text{Sb}_2\text{Se}_3\text{-}20\text{CuI}_x$ en fonction de la quantité d'iode.

Il est possible de conclure que l'augmentation de la quantité d'iode favorise la cristallisation d'une phase de SbISe qui est fortement résistive ($\sigma < 1 \mu\text{S}/\text{cm}$) et qui ne contribue pas à la conductivité ; elle peut aussi jouer un rôle négatif servant comme centre de diffusion des porteurs de charge.

En conclusion, il a été démontré que la présence d'iode dans la vitrocéramique est de grande importance. L'insertion de l'iode dans la phase de Sb_2Se_3 modifie ses propriétés électroniques sans modification visible de la structure cristalline ou changement important de la topologie. Puisque la structure colonnaire de Sb_2Se_3 est maintenue, les sites enrichis par l'iode sont capables de former les « passages » conducteurs bien visibles sur les images de « Kelvin probe microscope ». On a obtenu une corrélation claire entre la quantité d'iode et la conductivité. Il est possible de conclure que Sb_2Se_3 dopé avec l'iode est responsable de la conductivité de la vitrocéramique, et pas Cu_2GeSe_3 . En même temps, une concentration optimale de l'iode existe (i.e. CuI , $\text{CuI}_{1.1}$), une présence excessive entraînant la formation d'une phase secondaire de SbISe qui empêche la formation de la phase conductrice et implique la baisse de la conductivité au total.

3. Les propriétés photoélectriques des cristaux de chalcogénures à base de Sb_2Se_3 .

3.1. Les cristaux Sb_2Se_3 dopé par de l'iode

Pour vérifier l'hypothèse de l'influence de l'iode sur la conductivité de la vitrocéramique $40\text{GeSe}_2\text{-}40\text{Sb}_2\text{Se}_3\text{-}20\text{CuI}$, nous avons extrait la phase Sb_2Se_3 et étudié ses propriétés structurales et photoélectriques. Les résultats obtenus pour les vitrocéramiques dont la quantité d'iode est réduite ont relevé qu'en l'absence de Sb_2Se_3 suffisamment dopé avec de l'iode, Cu_2GeSe_3 n'assurait pas la conductivité dans le volume de l'échantillon. On pouvait supposer que Cu_2GeSe_3 non seulement ne contribue pas substantiellement à la conductivité de la vitrocéramique mais aussi peut être considéré comme une phase parasite qui sert comme centre de diffusion des porteurs de charge supplémentaires. Le rôle d'une phase vitreuse résiduelle dans la vitrocéramique était aussi soupçonnable.

Nous avons préparé une série de cristaux à base de Sb_2Se_3 avec une quantité d'iode variant de 3 mol.% à 20 mol.% par rapport à la quantité de Se initial. Leurs signaux DRX sont présentés dans la fig. 9. La phase secondaire de SbISe apparaît pour les échantillons avec 8% d'iode et plus, et devient très prononcée pour 15% et 20% d'iode. De plus, il est intéressant de noter l'absence de modification structurale de la phase majoritaire Sb_2Se_3 même pour la quantité d'iode élevée. On peut conclure que l'insertion de l'iode ne joue pas significativement sur les constantes de maille de Sb_2Se_3 qui est capable de maintenir sa structure cristalline en présence d'une grande quantité de dopant.

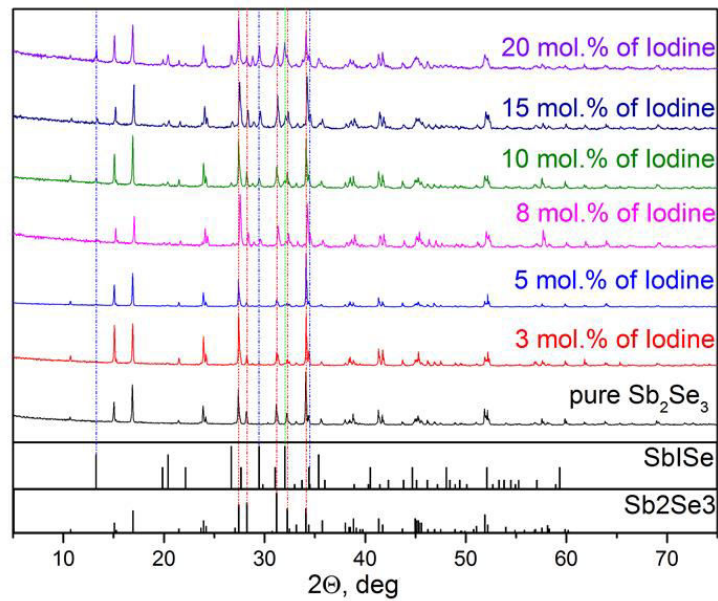


Figure 9 Spectres DRX des cristaux à base de Sb_2Se_3 avec différentes quantités d'iode.

Comme attendu, les cristaux Sb_2Se_3 dopés démontrent une forte inhomogénéité au niveau de la composition. Dans la fig.10, on observe plusieurs zones topologiquement différentes. La zone constituée de baguettes séparées contient plus d'iode (point 1 et point 2) par rapport aux zones avec une structure plus serrées qui rappellent un bâton allongé (point 3). Cela peut aussi expliquer l'inhomogénéité dans la vitrocéramique ainsi que la transformation des baguettes en feuilles pour les échantillons massifs ayant une quantité d'iode réduite.

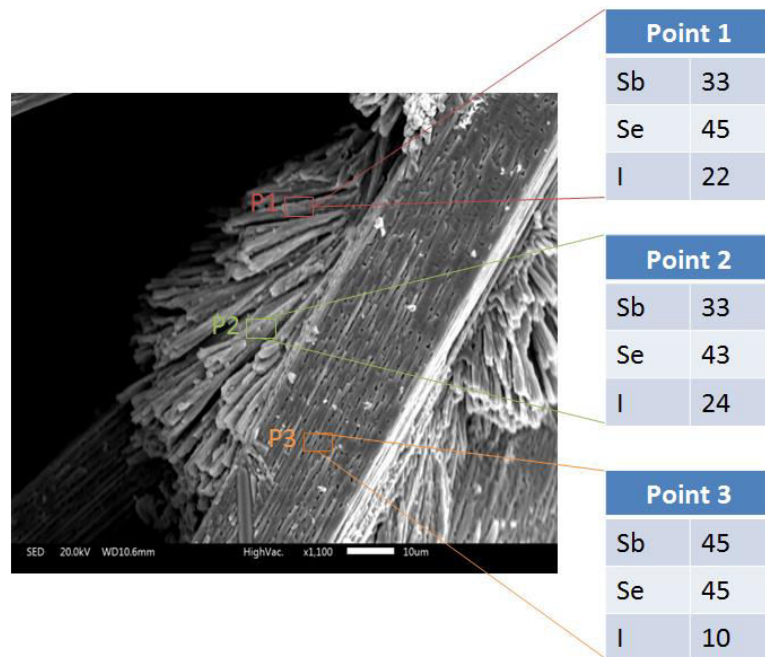


Figure 10 Image MEB et analyse chimique (EDS) de Sb_2Se_3 dopé 20 % mol. en iode.

Nous avons trouvé que 3 % mol. d'iode introduit dans Sb_2Se_3 réduit la résistivité d'un facteur 10^6 . On a réussi à améliorer la résistivité jusqu'à $46 \text{ Ohm}\cdot\text{cm}$ pour l'échantillon avec 15 % mol. d'iode (fig.11 (a)). Au-delà, une légère croissance de la résistivité est observée. La photoconductivité est observée pour tous les cristaux activés par l'iode. L'intensité de courant, en général, suit la tendance de la conductivité. La densité de courant maximale est de $650 \mu\text{A}/\text{cm}^2$ sous un potentiel de $+0.6\text{V}$ pour Sb_2Se_3 dopé 20 % mol. en iode (fig.11 (b)), ce qui est 6.5 fois plus élevé par rapport à la meilleure vitrocéramique obtenue $40\text{GeSe}_2\text{-}40\text{Sb}_2\text{Se}_3\text{-}20\text{CuI}$. D'autre part, le photocourant obtenu sous potentiel négatif atteint son maximum pour Sb_2Se_3 dopé 20 % mol. de l'iode.

Tous les cristaux, qu'ils soient dopés ou non-dopés, sont de type N d'après la mesure optique du type de conductivité, à l'aide d'un testeur p-n Semilab.

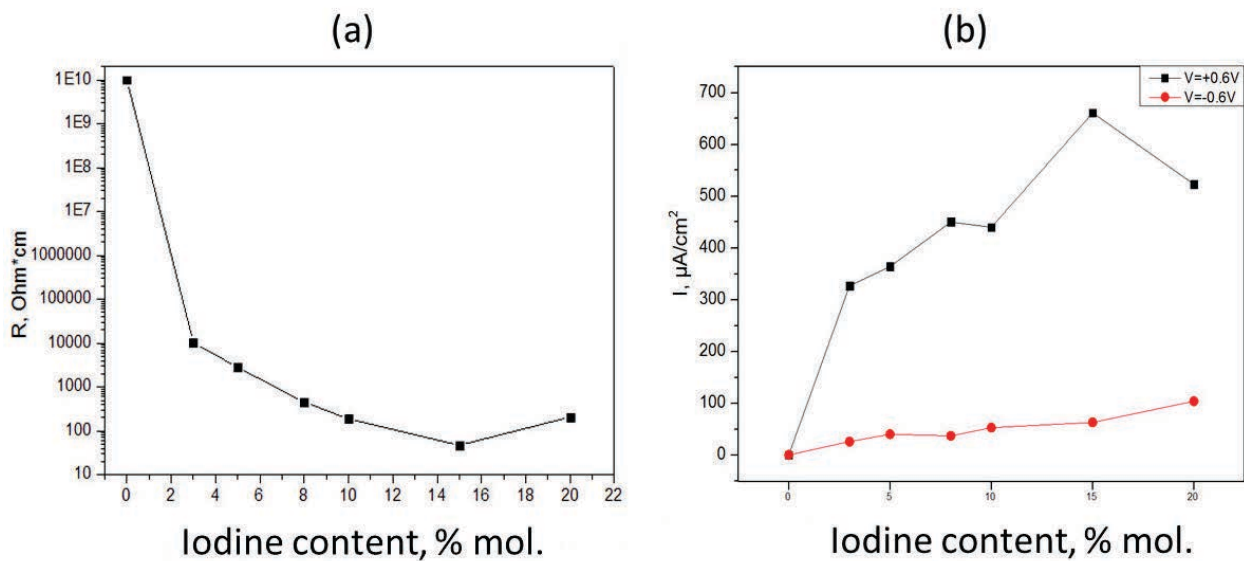


Figure 11 Dépendance de la résistivité (a), et de la densité de photocourant enregistrée par PEC en fonction de la concentration d'iode

Vu que la conductivité peut être représentée par la formule :

$$\sigma = \frac{ne^2}{meSN_s v_{th}}, \text{ où}$$

n – concentration des porteurs de charge, e – charge élémentaire, m_e masse effective des porteurs de charge, S – section de diffusion, N_s – nombre des points de diffusion par unité de volume, v_{th} – vitesse thermique,

nous pouvons conclure que la croissance de conductivité observée est due à l'augmentation de concentration de charge n . Ce qui est compréhensible si on suppose que l'iode prend la place du sélénium dans la structure cristalline de Sb_2Se_3 . Ayant des rayons atomiques similaires : $r(\text{Se}^{2-}) = 184 \text{ pm}$ et $r(\text{I}) = 220 \text{ pm}$, l'insertion de l'iode dans la maille est possible sans sévère distorsion de celle-ci. D'autre part, l'iode ne peut partager qu'un électron et par conséquent termine la chaîne, en même temps l'un des électrons de l'atome de Sb devient non-compensé, comme il est montré dans la figure 12. Par conséquent, la concentration de porteurs de charge

est plus élevée dans le cas de Sb_2Se_3 dopé et leur concentration augmente avec la concentration d'iode. une substitution de ce type explique aussi le type N marqué de la conductivité dans les cristaux de Sb_2Se_3 dopé.

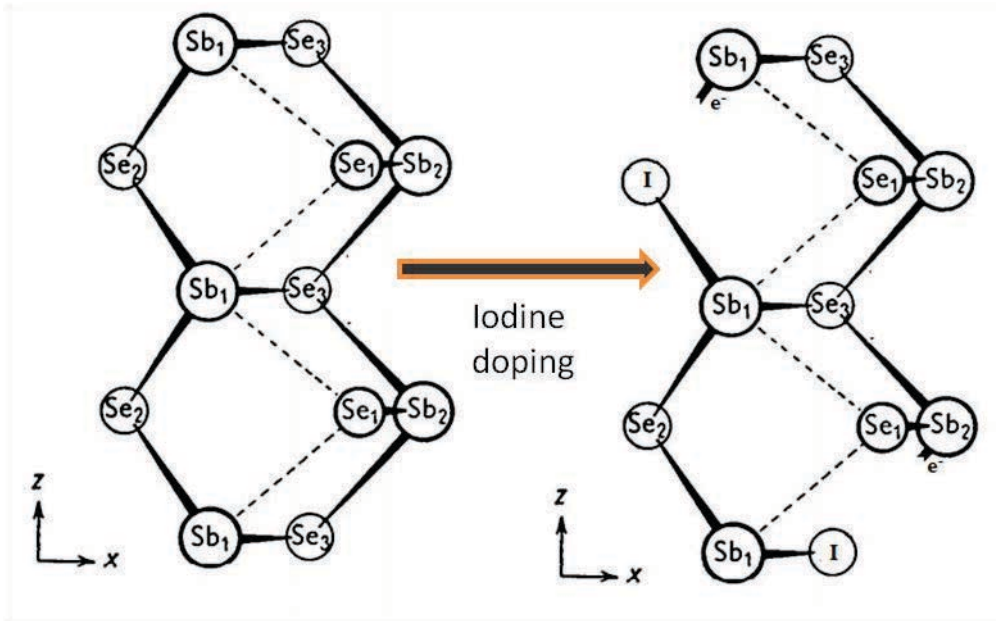


Figure 12 Modification structurale de Sb_2Se_3 après dopage par de l'iode.

Cependant, il y a une contre-force qui affecte la conductivité : c'est la taille et le nombre des cristaux de phase secondaire, qui jouent sur les paramètres S (section de diffusion) et N_s (nombre des points de diffusion par unité de volume). Probablement, pour Sb_2Se_3 avec plus de 15 % mol. d'iode, le contenu élevé de la phase $SbISe$ devient un facteur non-favorable pour la conductivité. Cette phase peut servir comme centre de diffusion des porteurs de charge très important, l'influence duquel ne peut pas être compensée par l'augmentation de la concentration des porteurs de charge libre n .

3.2. Les cristaux Sb_2Se_3 non-stoichiométriques

Après avoir constaté une forte inhomogénéité dans les échantillons massifs de Sb_2Se_3 dopés par de l'iode, nous avons fait des essais avec Sb_2Se_3 non-stoichiométrique pour élucider le rôle de l'inhomogénéité dans les propriétés photoélectriques de Sb_2Se_3 et son influence dans la vitrocéramique.

Dans les deux cas, excès et déficit de Se par rapport à la composition stœchiométrique, on observe que Sb_2Se_3 est capable de maintenir sa structure cristalline dans la vaste limite des compositions. En même temps, la présence d'une phase secondaire dans les deux cas est évidente. Pour les cristaux pauvres en Se, on constate la présence de Sb métallique tandis que pour les cristaux riches en Se ; on trouve la phase de Se pur, comme il est montré dans la fig. 13. Malgré tout, Sb_2Se_3 est une phase majoritaire même dans les cas de forte déviation de la stœchiométrie. Les courbes DRX ne relèvent pas de décalages

importants pour les pics de Sb_2Se_3 ; cependant, on observe un changement de l'intensité relative des pics, signe d'une variation dans le taux d'occupation des sites cristallins.

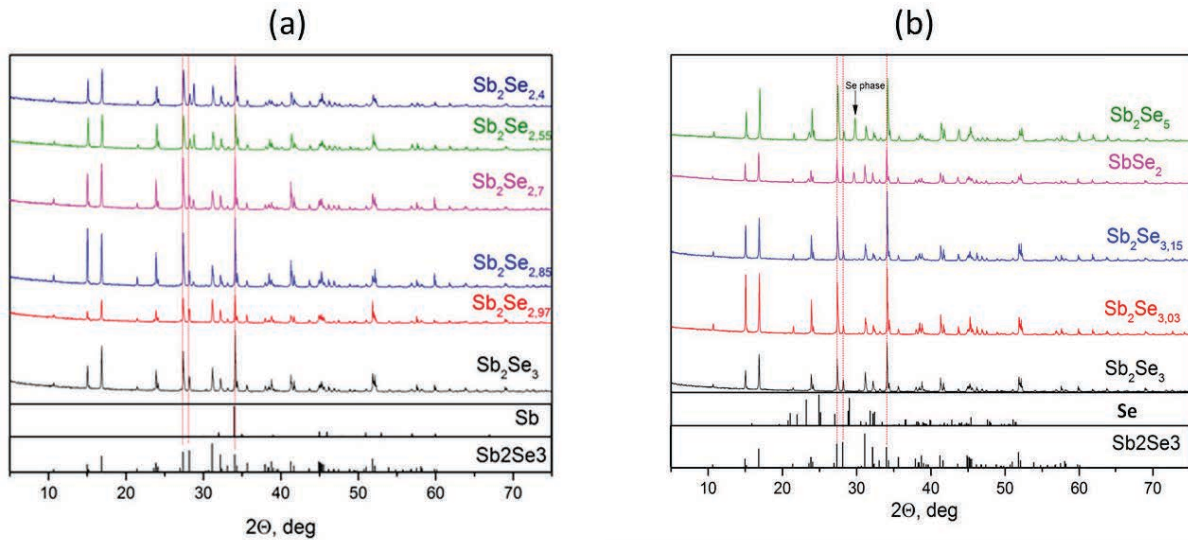


Figure 13 Spectres DRX des cristaux en présence d'un déficit (a) ou d'un excès (b) de Se

Les inhomogénéités sont clairement mises en évidence par imagerie MEB et analyse chimique EDS de $\text{Sb}_2\text{Se}_{2.7}$, comme le montre la fig.14, On constate une déviation de la composition dans le même zone topologique (point 3, point 4), tandis que les endroits topologiquement différents possèdent une composition similaire (point 2, point 4). Prenant en compte la variation dans l'intensité relative des pics DRX, on peut conclure que l'occupation atomique est aléatoire, en même temps la structure cristalline de Sb_2Se_3 , ainsi que les constantes de maille sont maintenues. On ne trouve pas d'agrégats importants de Sb métallique sur l'image MEB.

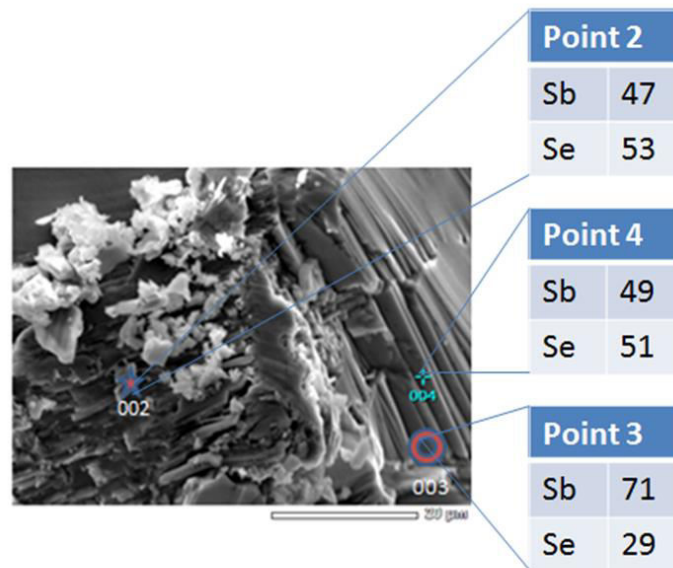


Figure 14 Image MEB et analyse chimique EDS de $\text{Sb}_2\text{Se}_{2.7}$.

L'inhomogénéité produite par une déviation de la composition stœchiométrique joue beaucoup sur la conductivité des cristaux, comme il est démontré dans la fig.15 (a). Il suffit de retirer 3% de Se pour baisser la résistivité d'un facteur 10^5 . On continue d'abaisser la résistivité en retirant du Se, pour atteindre $14 \text{ Ohm}\cdot\text{cm}^2$ pour $\text{Sb}_2\text{Se}_{2.4}$. En même temps, on ne voit pas de comportement métallique dans l'expérience PEC où le photocourant augmente proportionnellement avec le taux de Se retiré (fig.15 (b)). Celui-ci atteint son maximum de $380 \mu\text{A}/\text{cm}^2$ sous le potentiel positif de $+0.6\text{V}$ et $95\mu\text{A}$ sous -0.6V . Tous les cristaux avec déficit de Se sont du type N d'après l'expérience optique.

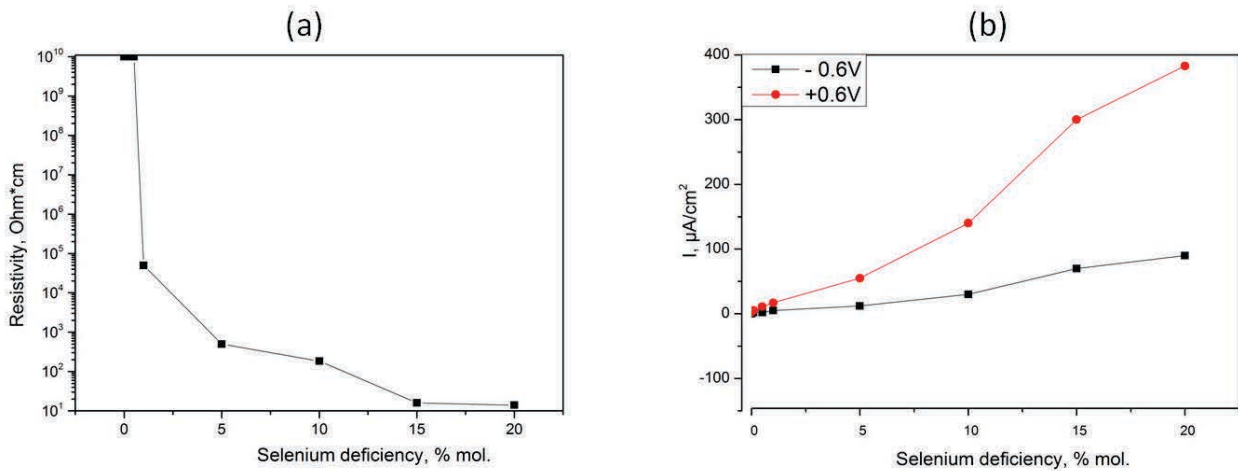


Figure 15 Dépendance de la conductivité (a) et de la densité de photocourant (b) des cristaux Sb_2Se_3 avec déficit de Se.

Les cristaux en excès de Se démontrent le même comportement structural d'après les mesures DRX. D'autre part, on trouve facilement les sites de précipitation de Se métallique même pour les échantillons avec 3% d'excès de Se. En même temps, dans le cas de l'excès de Se, la structure maintient la proportion stœchiométrique beaucoup mieux, l'excès de Se précipitant, comme il est montré à la fig.16.

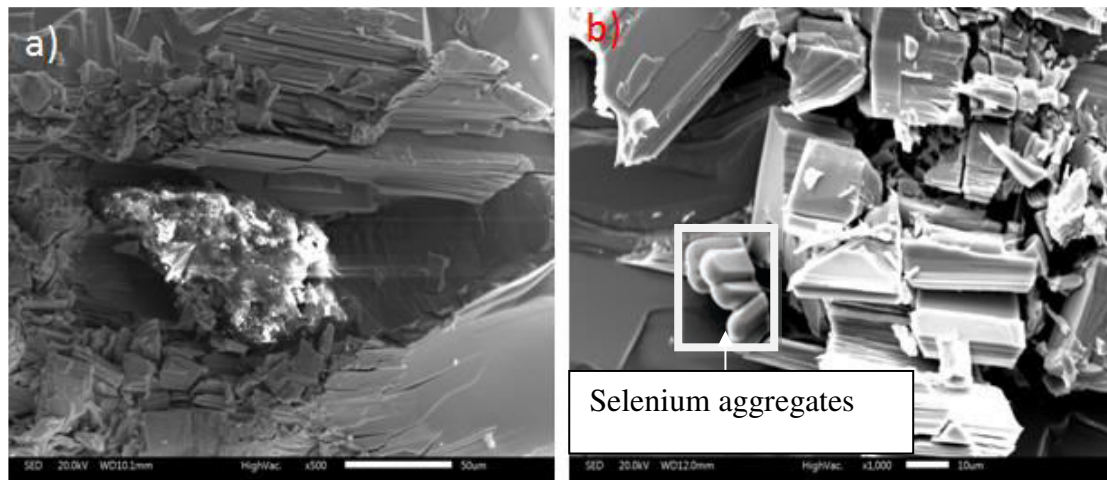


Figure 16 Image MEB de $\text{Sb}_2\text{Se}_{3,03}$

Nous avons trouvé que l'excès de Se conduit à une conductivité du type P, avec une résistivité relativement élevée égale à $45 \cdot 10^6 \text{ Ohm} \cdot \text{cm}$ pour Sb_2Se_5 . Cet composant est d'un intérêt particulier vu son comportement en commutation (fig.17) : il subit un saut de courant sous le potentiel de $+0.4\text{V}$ qui désigne une transition dans l'état de haute conductivité (High Conductive State - HCS). Cette transition est complètement réversible sous le potentiel $+0.1\text{V}$, quand le composant revient dans l'état de basse conductivité (Low Conductive State - LCS). On observe le même effet sous le potentiel négatif -0.6V (HCS) et -0.2V (LCS). L'effet de changement de l'état de conductivité est réversible et se maintient pendant au moins 50 cycles dans l'électrolyte LiClO_4 . On observe également une faible photoconductivité sous potentiel négatif, ce qui est attendu pour les photoconducteurs du type P.

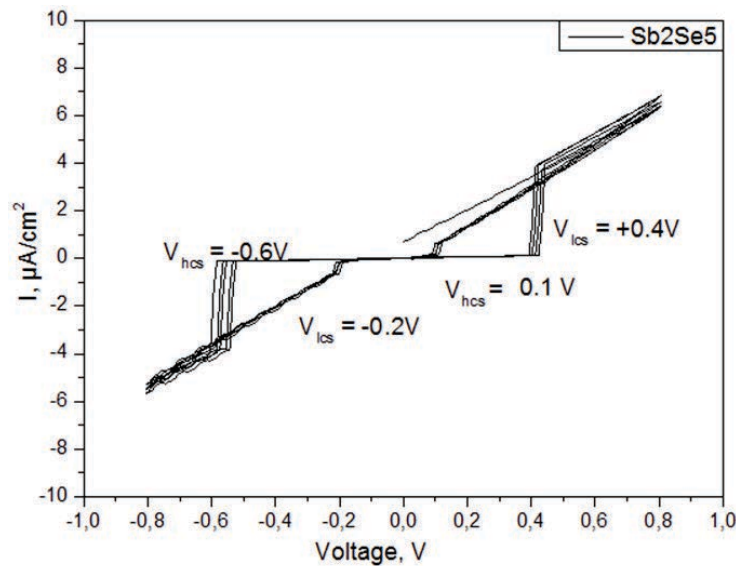


Figure 17 Courbe PEC de Sb_2Se_5 , plusieurs balayages.

Pour conclure, nous avons trouvé une forte inhomogénéité dans les cristaux Sb_2Se_3 déficitaires en Se. Ces cristaux sont des semi-conducteurs de type N avec une résistivité qui diminue proportionnellement au taux de Se retiré. On trouve une photoconductivité assez importante dans les cristaux déficitaires en Se de plus de 10 % mol. La résistivité minimale et le photocourant le plus élevé ont été trouvées pour $\text{Sb}_2\text{Se}_{2.4}$. L'excès de Se conduit à des cristaux de type P avec une conductivité et une photoréponse relativement faibles. En même temps, on peut faire varier le type de conductivité en modifiant le contenu de Se dans Sb_2Se_3 . L'observation d'une photoréponse sous potentiel négatif pour Sb_2Se_3 déficitaire en Se est possible grâce à l'inhomogénéité et à la présence des zones enrichies en Se, même dans le cas d'un déficit de celui-ci.

Dans la fig.18, la modification structurale possible est montrée. Nous supposons qu'il n'y a pas de fortes modifications des constants de maille et de la cellule unitaire, vu l'absence de décalage des pics DRX. En même temps, le déficit de Se peut entraîner la formation de lacunes au lieu de Se^{2-} . L'absence de Se^{2-} libère les électrons des atomes voisins Sb^{3+} , qui participaient à la liaison chimique. En l'absence de Se^{2-} , Sb joue le rôle d'un donneur d'électrons, qui explique la conductivité de type N ainsi que la baisse flagrante de la résistivité. Dans le cas de l'excès de Se, les ions Se^{2-} s'approchent de Sb^{3+} et attirent

partiellement la densité électronique de son côté en créant les espaces de la charge positive non compensée, i.e. un trou.

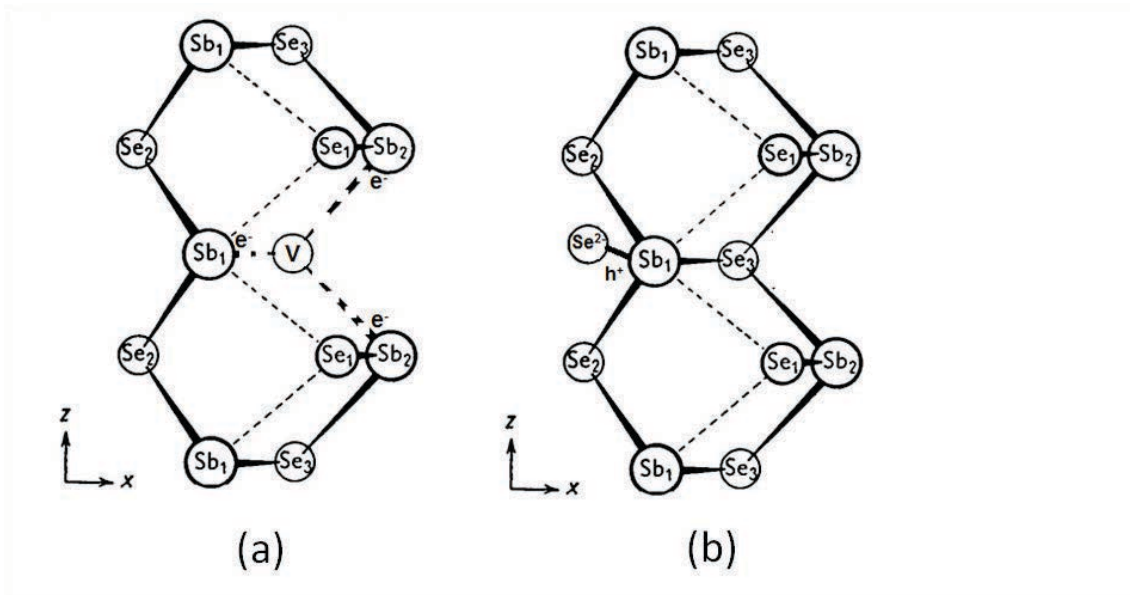


Figure 18 Modification structurale de Sb_2Se_3 en cas de déficit de Se (a) et d'excès de Se (b)

4. L'effet de la substitution du cation Sb par Sn dans la vitrocéramique du système « $GeSe_2-Sb_2Se_3-CuI$ »

La substitution d'un cation a été faite dans un verre précurseur pour modifier le niveau de Fermi du semi-conducteur Sb_2Se_3 pendant la céramisation. La substitution de Sb par Sn conduit à un résultat intéressant.

Ainsi, on a trouvé qu'il était possible d'obtenir un verre contenant jusqu'à 25 % mol. Sn, par rapport à la quantité de Sb initial, comme il est montré dans la fig.19. On peut noter que le précurseur avec 25 % mol. de Sn présente une dispersion marquée du type Rayleigh (ligne bleu) dans le proche infrarouge, signe de la présence d'une phase déjà cristallisée. Les composants contenant plus de 25 % mol. de Sn ne sont pas transparents vu leur forte cristallisation et la présence de cristaux de taille importante qui entraînent la diffusion de la lumière dans le moyen infrarouge.

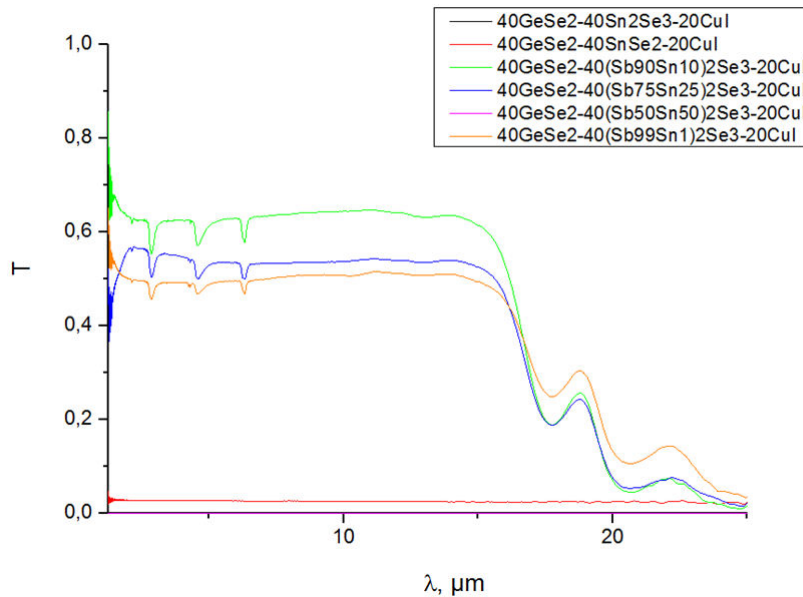
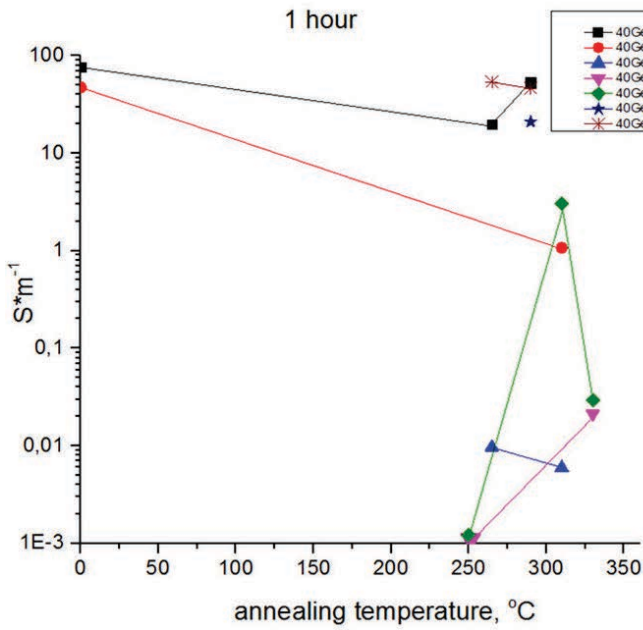


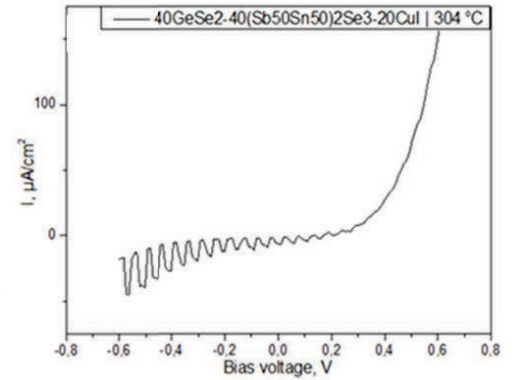
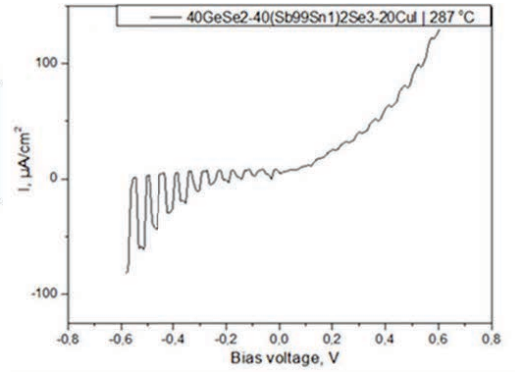
Figure 19 Spectre de transmission des verres précurseurs avec substitution de Sb par Sn, partielle et complète.

Tous les précurseurs avec substitution partielle étaient non-conducteurs et ont subi un recuit pendant une heure sous la température de cristallisation. Si le spectre DSC montre plusieurs pics de cristallisation, le précurseur a été recuit sous plusieurs températures différentes pour assurer la cristallisation d'une phase conductrice. Les conductivités des vitrocéramiques obtenues sont présentées à la fig.20 (a). Nous notons que la conductivité de la vitrocéramique $40\text{GeSe}_2\text{-}40\text{Sn}_2\text{Se}_3\text{-}20\text{CuI}$ n'évolue pas pendant le recuit additionnel tandis que la conductivité de $40\text{GeSe}_2\text{-}40\text{SnSe}_2\text{-}20\text{CuI}$ diminue après le recuit. Les valeurs de conductivité sont quand même comparables avec celle de la vitrocéramique de référence $40\text{GeSe}_2\text{-}40\text{Sb}_2\text{Se}_3\text{-}20\text{CuI}$ égale à 50-100 S/m. Nous notons aussi la conductivité assez élevée de la vitrocéramique contenant 50 % mol. de Sn, qui est égale à 5 S/m. D'autre part, il est évident que l'introduction de Sn dans des quantités allant de 1 % mol. à 50 % mol. affecte négativement la conductivité de la vitrocéramique massive, avec un minimum de conductivité atteint pour la vitrocéramique contenant 10 % mol. de Sn.

Les spectres PEC de la vitrocéramique dopée Sn sont quand même d'intérêt. Les vitrocéramiques avec 1% mol. (fig.20 (b) haut) et 50 % mol.(fig.20(b) bas) possèdent une conductivité suffisamment élevée pour enregistrer le signal du photocourant. Si on compare les figures 3b et 20b haut, on peut constater que la présence de Sn change le type de conductivité de la vitrocéramique. Ceci est confirmé également avec la mesure optique. Les vitrocéramiques dopées Sn sont toutes du type P ; leur courbe PEC montre l'effet de saturation sous potentiel négatif, avec une contribution du photocourant caractéristique d'un semi-conducteur de type P.



(a)



(b)

Figure 20 Conductivité de la vitrocéramique avec substitution de Sb par Sn après recuit (a), courbes PEC des vitrocéramiques $40\text{GeSe}_2 - 40(\text{Sb}_{99}\text{Sn}_1)_2\text{Se}_3-20\text{CuI}$ (en haut) et $40\text{GeSe}_2 - 40(\text{Sb}_{50}\text{Sn}_{50})_2\text{Se}_3-20\text{CuI}$ (en bas) (b).

Comme on le sait, les cristaux de Sb_2Se_3 sont responsables de la conductivité ; dans ce cas, il y a une concurrence entre une phase de Sb_2Se_3 dopée Sn et la phase cristalline SnSe_2 . Apparemment, si les deux existent, cela affecte défavorablement la microstructure du verre, ce qui entraîne un affaiblissement de la conductivité. Cependant, si l'une des phases est majoritaire et est capable de former son propre réseau conducteur, la conductivité augmente. En même temps, on conclut que le dopage de Sb_2Se_3 par Sn, conduit à un semi-conducteur de type P par le mécanisme dessiné à la fig. 21.

En conclusion, Sb_2Se_3 est un matériau très flexible au niveau de la conductivité, de la structure électronique, et du type des porteurs de charge majeurs. Même à faible dopage la substitution par Sn joue sur son comportement électronique. Cette flexibilité et ses propriétés photo-électriques en font un composé très prospectif pour l'élaboration de cellules solaires, photoconducteurs etc.

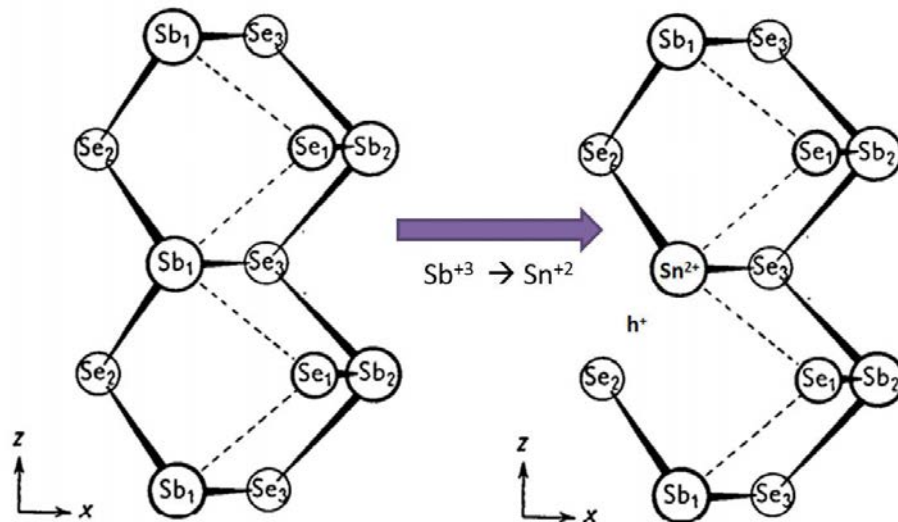


Figure 21 Mécanisme d'apparition de la conductivité de type P après le dopage des cristaux de Sb₂Se₃ par Sn.

5. Fabrication d'une cellule solaire à base de couches minces des vitrocéramiques et cristaux de chalcogénures

Des couches minces ont été préparées par pulvérisation cathodique de cibles de chalcogénures fabriquées à partir de produits de haute pureté.

Nous avons commencé notre étude sur les couches minces en fabricant une couche de composition identique à la vitrocéramique « 40GeSe₂-40Sb₂Se₃-20CuI ». Puisque la vitrocéramique possédait les deux phases, de type P et de type N, on aspirait à reproduire sa structure en configuration couche mince. Nous avons supposé qu'il serait possible d'avoir une couche amorphe dans laquelle on pourrait former une hétérojonction au sein de la couche grâce à une cristallisation contrôlée. Celle-ci est obtenue à l'aide d'un four de recuit installé dans la chambre de pulvérisation..

Les premiers essais ont démontré qu'il était possible d'obtenir une couche conductrice de « 40GeSe₂-40Sb₂Se₃-20CuI » à condition que celle-ci soit déposée sur une très fine sous-couche de CuI ($e = 3$ nm). L'image MEB de cette couche est présentée dans la fig. 22. Comme on peut le constater, la couche pré-déposée de CuI se distribue sur le substrat en forme d'îles sphériques non liées l'une à l'autre, ce qui est confirmé par l'absence de conductivité électrique de cette couche. En même temps, sur l'image MEB de la couche « 40GeSe₂-40Sb₂Se₃-20CuI » on voit clairement la présence d'entités sphériques enrichies par Cu et I, d'après l'analyse chimique.

Avec cette configuration, on a réussi à obtenir un résistivité de la couche égale à 10^2 Ohm*cm.

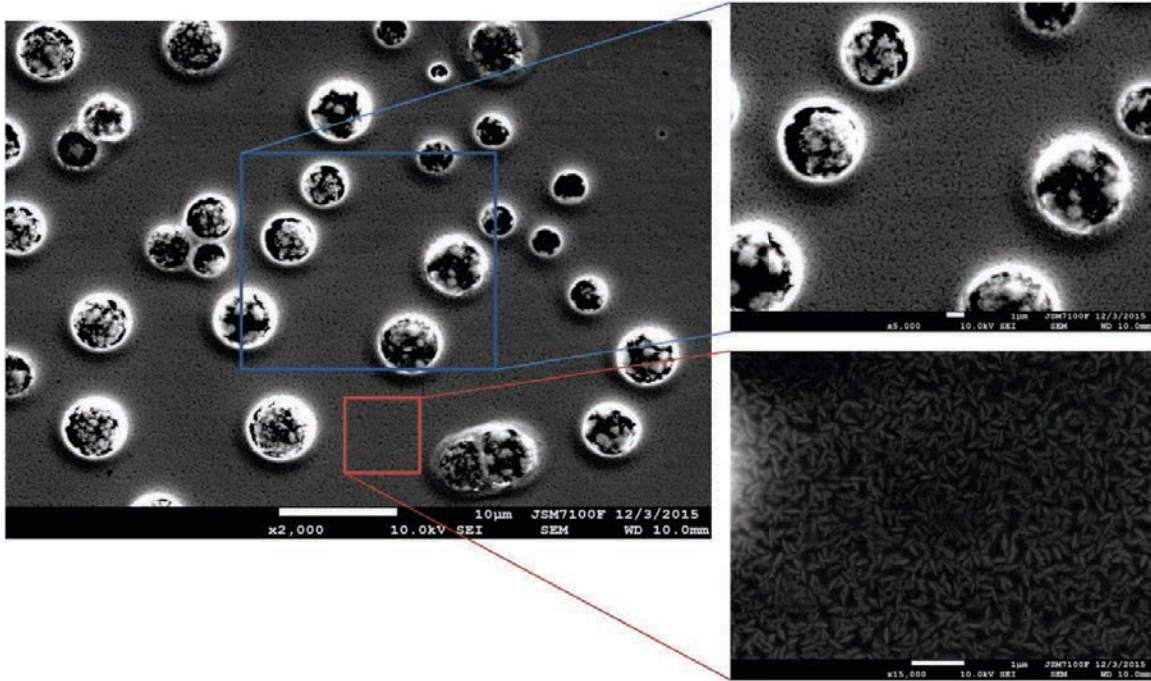


Figure 22 Image MEB de la couche de $40\text{GeSe}_2\text{-}40\text{Sb}_2\text{Se}_3\text{-}20\text{CuI}$ avec une sous-couche de CuI

L'analyse PEC, montrée dans la fig.23(a), confirme que la seule phase conductrice obtenue dans la couche est de type P. On observe un photocourant assez important ($700 \mu\text{A}/\text{cm}^2$) sous un potentiel négatif de -0.6V , tandis que sous potentiel positif, on ne remarque que l'interaction entre l'électrolyte et le semi-conducteur, caractéristique pour un semi-conducteur du type P. La cellule fabriquée à partir de ce composant ne montre qu'un comportement ohmique avec l'effet de photoconductivité. On ne remarque aucun effet photovoltaïque (fig. 23(b)).

L'absence de photoréponse a été attribuée à la faible quantité d'iode, lequel s'est perdu pendant le dépôt du fait de sa volatilité. En l'absence d'iode, Sb_2Se_3 ne peut pas être suffisamment dopé pour former les cristaux conducteurs de type N. Pour résoudre ce problème, une cible contenant un excès d'iode (IDEX) a été fabriquée. Cette couche présente bien les deux phases, type P et type N, dans l'expérience PEC (fig.24 (a)). Pourtant, l'effet photovoltaïque n'a pas été observé. Cela signifie que les deux phases coexistent dans une couche sans former d'hétérojonction dans le volume de celle-ci

Pour former une hétérojonction planaire, nous avons pris une couche IDEX et une couche de Sb_2Se_3 dopé iode (10 % mol.), qui est du type N, comme montré dans l'étude des cristaux massifs. Il a été mis en évidence par une mesure PEC, que ce composant possédait également 2 types des cristaux, avec une réponse de semi-conducteur de type N plus prononcée (par rapport à la couche IDEX seule), comme il est montré à la fig.24 (b).

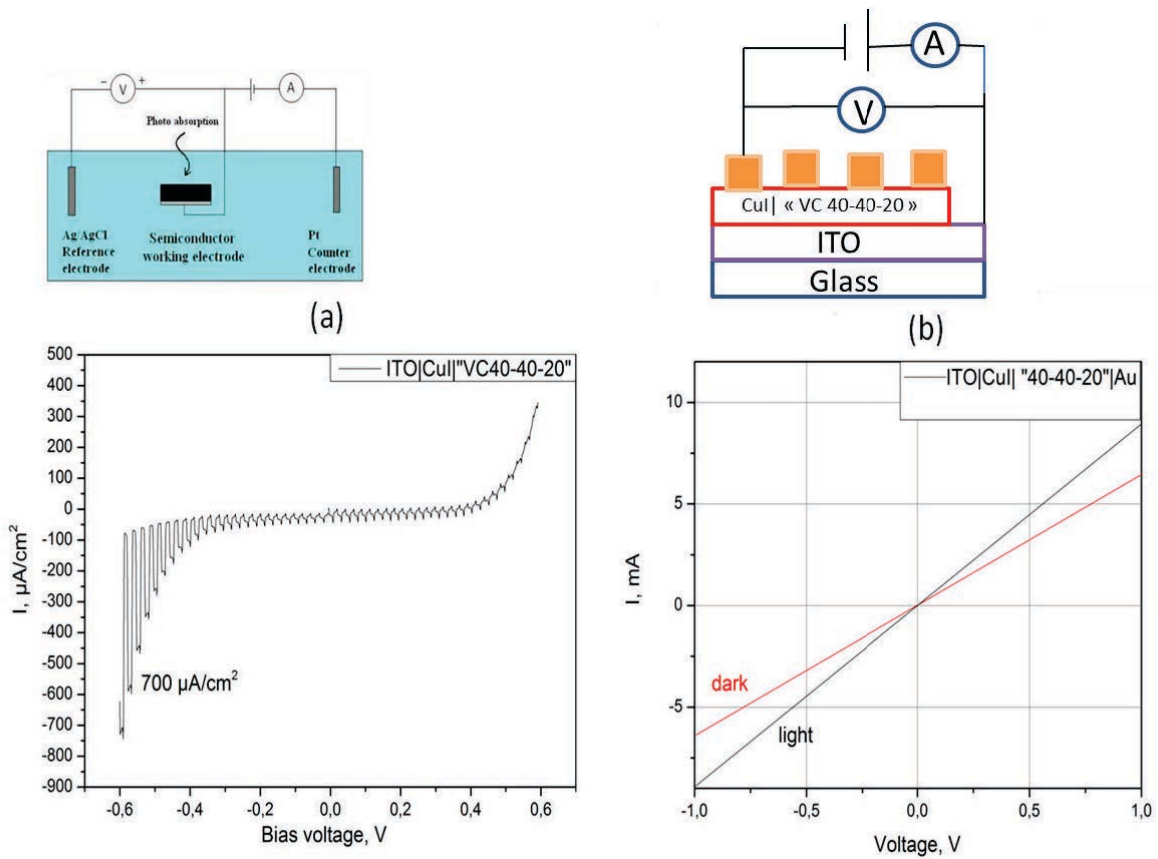


Figure 23 Courbe PEC de la couche de $40\text{GeSe}_2\text{-}40\text{Sb}_2\text{Se}_3\text{-}20\text{CuI}$ avec une sous-couche de CuI (a), étude d'une cellule solaire à base de cette couche (b)

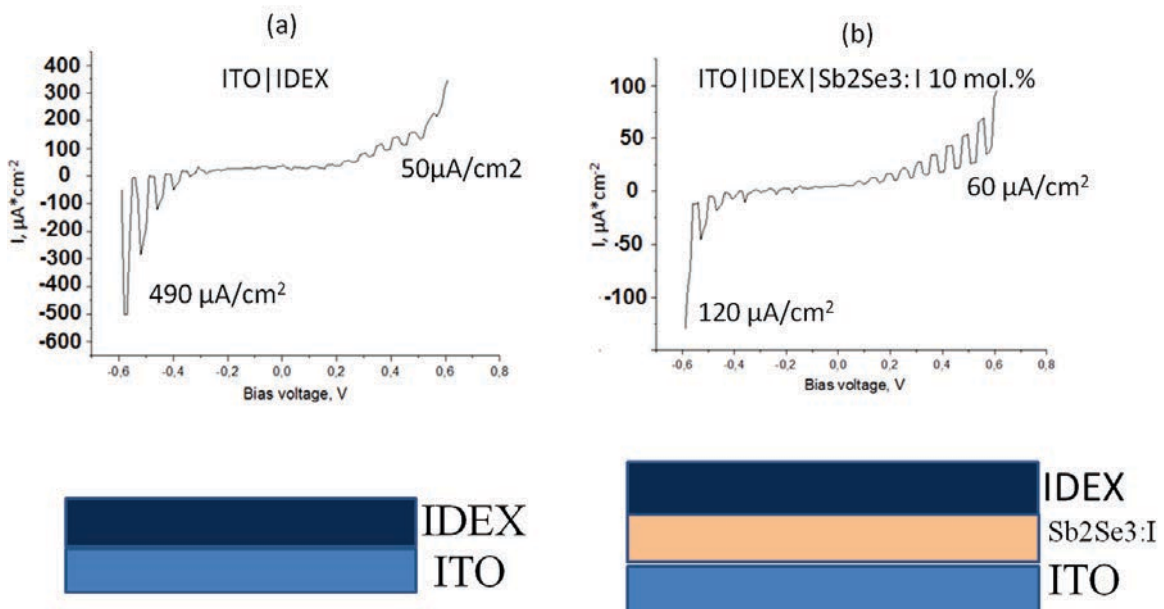


Figure 24 Courbes PEC de la couche IDEX (a) et du composant planaire des couches Sb₂Se₃ dopées iode et IDEX.

Une cellule solaire préparée à partir de ce composant planaire montre un effet photovoltaïque avec au maximum $J_{sc} = 10 \text{ mA/cm}^2$ et $V_{oc} = 255 \text{ mV}$, ce qui donne une efficacité de conversion de 2%.

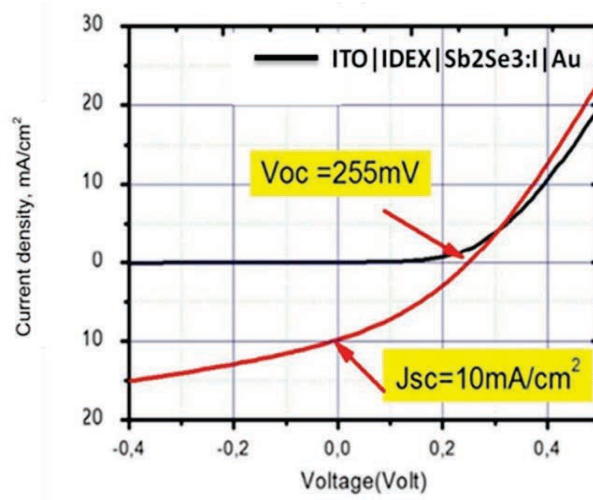


Figure 25 I-V Densité de courant de la cellule solaire à base des couches Sb_2Se_3 dopé iode et IDEX.

6. Conclusion

Nous avons développé et étudié un vaste nombre de compositions pour la fabrication de matériaux photo-électriques.

On a établi le rôle de l'iode dans le processus de génération de photo-charges, ainsi que les origines de la conductivité de la vitrocéramique massive. La performance photo-électrique est améliorée par rapport aux résultats antérieurs. On a montré que la phase de Sb_2Se_3 présente dans la vitrocéramique est très adaptable en termes de conductivité et de type des porteurs de charge majeurs lesquels peuvent être modifiés par simple dopage ou déviation de la stœchiométrie.

De cette manière, on a réussi à obtenir un photocourant de $650 \mu\text{A/cm}^2$ pour Sb_2Se_3 dopé à 15 % mol. en l'iode. Egalement, une simple variation dans la quantité de Se dans Sb_2Se_3 peut améliorer la conductivité d'un facteur 10^8 , permettant d'obtenir un photocourant de $380 \mu\text{A/cm}^2$ pour $\text{Sb}_2\text{Se}_{2,4}$, cristaux du type N. Les cristaux Sb_2Se_3 dopés Sn ainsi que les composants présentant un excès de Se montrent une conductivité du type P.

A partir des matériaux massifs, on a fabriqué des couches minces photoconductrices avec des phases du type P et du type N coexistant dans la même couche. La cellule solaire élaborée à partir des couches Sb_2Se_3 dopées iode et IDEX possède un effet photovoltaïque avec $J_{sc} = 10 \text{ mA/cm}^2$ et $V_{oc} = 255 \text{ mV}$ au maximum.

General introduction

In the year of 2016 humankind consumed over 14 000 MToe of energy. And more than 90% of it was extracted from non-renewable sources, i.e. oil, gas and coal. Being extremely polluting for the environment and unreliable from economic and political points of view, non-renewable sources can barely stand against the demands of tomorrow.

It is predicted that by the year of 2052 about 30 % of total energy consumption would be provided by renewable energy sources: wind, water and solar energy. This is not just a whim of rich and successful civilization but a prerequisite for its evolution in future. Especially, if we are speaking about highly populated regions with growing industrial economy like China or India. While the fact of global warming is disputed by a number of scientists it is difficult to deny unhealthy and highly polluted environment in industrial cities not only in developing countries but also in northern Europe and U.S.

On one hand “green energy” could improve the quality of life making the atmosphere less polluted. At the same time it is capable of giving real energy independence to the small companies and private consumers. Furthermore, alternative sources open a vast field of new applications, which could never exist without it. Indeed we can barely imagine space exploration without efficient solar energy harvesting techniques and breakthroughs in energy storage technologies.

This work is our contribution to the growing domain of solar cells. While crystalline silicon is still the most commercially successful material for solar panels, it is important to investigate new materials and new approaches for solar light harvesting. Material science nowadays is waiting for insight to overpass existing efficiency limits of light-to-electricity conversion.

Presented thesis was prepared in a scope of the study on chalcogenide glass-ceramics for photovoltaic applications performed by “Glass and ceramics” team of the department of Chemistry in university of Rennes 1.

Thesis consists of four chapters. In first chapter we gave a review on state-of-the-art in the domain of renewable energy sources. Basics of semiconductors physics needed for general comprehension of presented results are given in detail. We made a summary on solar cells techniques and materials commercially utilized and studied in laboratories nowadays. Chemical and physical peculiarities of chalcogenide materials are briefly given. Overview of previous work on chalcogenide glass-ceramics with photoelectric properties is given as well in the end of first chapter.

Second chapter is devoted to the elucidation of conductivity mechanism in glass-ceramics $40\text{GeSe}_2\text{-}40\text{Sb}_2\text{Se}_3\text{-}20\text{CuI}$. We investigated the influence of iodine on photoconductivity of glass-ceramics and Sb_2Se_3 crystals. We also carried out the study on the influence of stoichiometric deviations on electric properties of above-mentioned glass ceramics and Sb_2Se_3 crystals.

In third chapter studies on different modifications of $40\text{GeSe}_2\text{-}40\text{Sb}_2\text{Se}_3\text{-}20\text{CuI}$ glass-ceramic chemical composition are presented. We showed a strong influence of cation and anion substitutions on electric behavior of glass-ceramics.

Fourth chapter is devoted to the preparation of thin films based on studied bulk (glass-ceramics and crystals) compositions. We prepared and characterized a vast number of thin films with promising photoelectric properties. Planar p-n junction solar devices were fabricated and studied as well.

Chapter I

State-of-the art in the domain of solar energy harvesting

Table of contents

1.Context of study.....	3
1.1.Energy consumption nowadays, part of renewable energy sources on the energy consumption diagram.....	3
1.2.Question of environnement pollution	5
1.3.Common problems of alternative energy sources.....	6
1.4. Survey on different types of solar energy harvesting systems.....	6
2.Physical principles of solar cell functioning.	10
2.1.Charge generation on a p-n junction interface.....	10
2.2.Crystalline silicon based solar cells	11
2.3.Amorphous silicon based solar cells.....	17
2.4.Heterojunction based solar cells. Multi-junction architecture for solar cells.	22
2.5.Dye sensitized solar cells. Grätzel cell.....	25
2.6.Perovskite architecture for solar cells	26
3.Chalcogenide materials in the domain of solar cells.....	29
3.1.Definition and general properties of chalcogenide materials.....	29
3.2.Crystalline chalcogenides application for solar energy harvesting.....	30
3.2.1.Binary systems	31
3.2.2.Ternary systems	33
3.2.3.Quaternary systems.....	35
3.3.Chalcogenide glass-ceramics for photovoltaic applications	36
3.3.1.Chalcogenide glasses and their application	37
3.3.2.Photovoltaic effect in glass-ceramics of pseudoternary $\text{GeSe}_2\text{-Sb}_2\text{Se}_3\text{-CuI}$ system	40
4.Conclusion	45
5.References.....	46

1. Context of study

1.1. Energy consumption nowadays, part of renewable energy sources on the energy consumption diagram

Speaking about energy consumption, we usually utilize two major units: ton of oil equivalent (TOE)¹ and British thermal unit (BTU)². TOE is the amount of energy released by burning one tone of crude oil. Conversion to more common units is proposed by International Energy Agency³.

$$1 \text{ TOE} = 11.63 \text{ megawatt-hour (MWh)}$$

$$1 \text{ TOE} = 41.868 \text{ gigajoules (GJ)}$$

BTU is the unit which defines the amount of energy needed for increasing the temperature of one pound of water by one degree Fahrenheit.

$$1 \text{ BTU} = 0.293071 \text{ Wh}$$

$$1 \text{ BTU} = 1.054 \text{ to } 1.060 \text{ kJ}$$

Looking at fig. 1-1 it is easy to mention that major part of energy sources are attributed to fossil fuels, which can be considered neither ecological nor highly efficient. Nuclear energy sources are also known for producing hardly recycled wastes and nuclear pollution risks. Ecologically acceptable renewable sources such as hydroelectricity, wind and solar energy occupy less than 10 percent of the whole energy consumption pie.

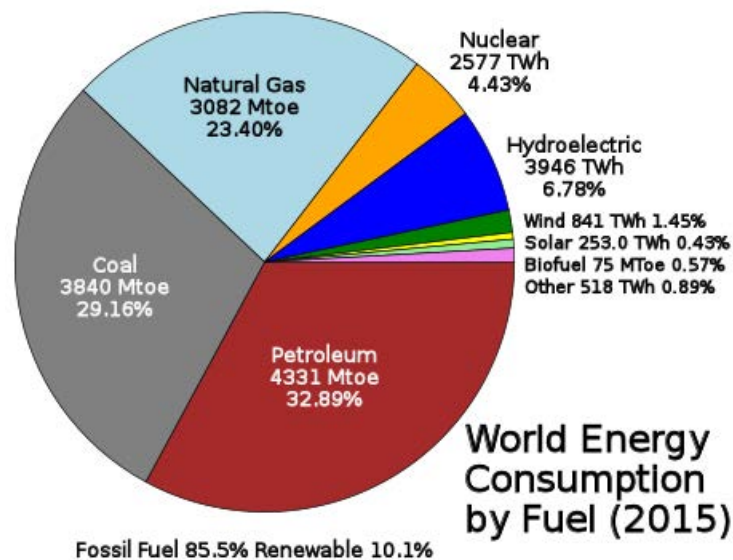


Figure 1-1 Energy consumption diagram (by source)⁴

Distribution of energy consumption per person by countries is shown in fig. 1-2. We can notice that the highest consumption rate concerns Nordic countries together with countries with highly-developed industry. It is expected that these countries are also responsible for high level of waste emission such as greenhouse gases, nuclear wastes etc.

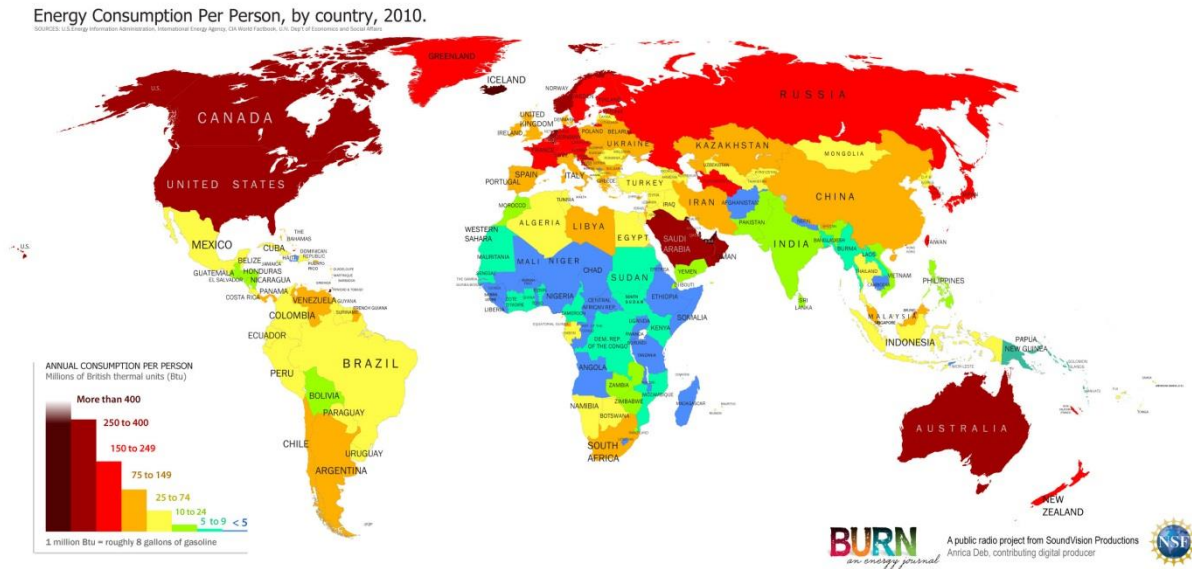


Figure 1-2 Energy consumption rate (by country)⁵

However, due to development of energy saving technologies, optimization of energy consumption and elaboration of renewable energy sources, it is expected that overall energy consumption will decrease and the amount of Oil and Gas in consumption diagram would severely shrink as it is shown in fig. 1-3. Authors are still debating on the increase of renewable source part^{6,7}. While Chefurka et al. are expecting negligible growth of renewed energy contribution and in particular very fable growth of solar energy consumption⁶, Randers expects more than 10 times growth of renewable source part by the year 2052⁷.

Authors also arguing around total consumption rate, however both researchers confirm its certain decrease due to expected breakthrough in energy saving technologies.

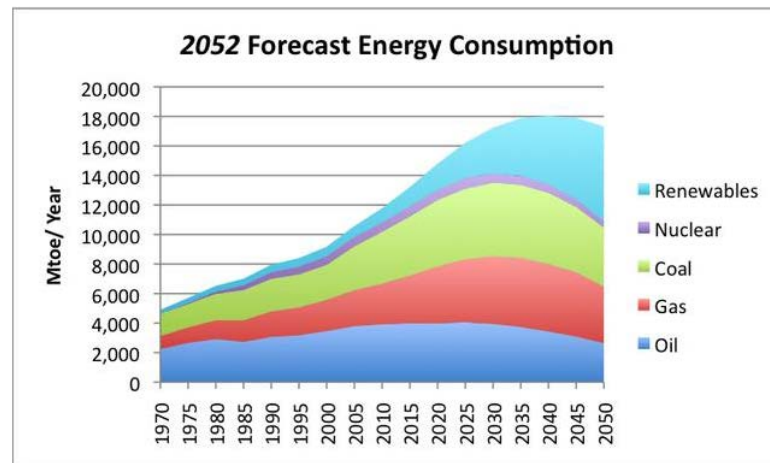


Figure 1-3 Energy consumption forecast⁶

Thus, we can conclude that scientific and technological efforts are needed to decrease fossil fuel consumption rate and substitute it with renewable sources. Development of energy saving and consuming optimization are also prerequisites to make these predictions come true.

1.2. Question of environment pollution

Emission of CO₂ is widely known for being responsible for greenhouse effect appearance and overall increase of temperature on Earth. In fig. 1-4, we observe that more than 50% of CO₂ emission comes from China, USA, Russia and India. At the same time more than 40% of CO₂ is produced by power plants and more than 20% by transport infrastructure⁸.

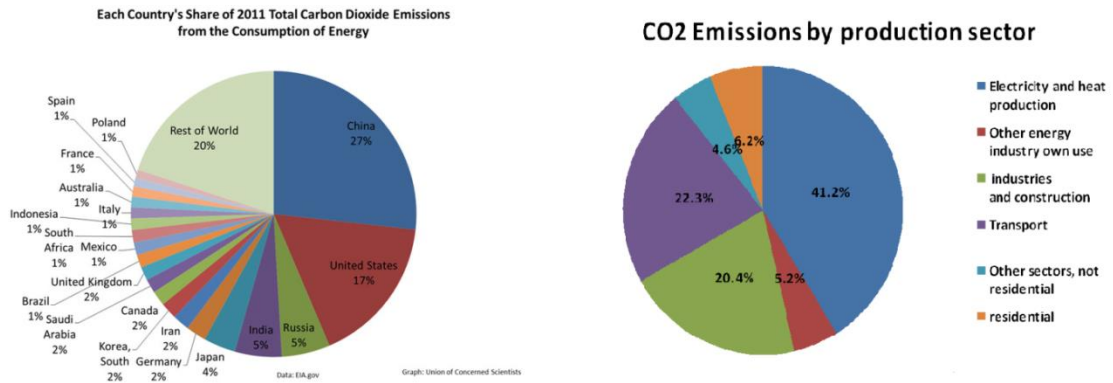


Figure 1-4 Total CO₂ emission by country (left) and distribution of emissions by production (right)⁷

In fig. 1-5 we observe a clear correlation between energy consumption (fig. 1-2), CO₂ emission rate and warming contribution by country⁹. The level of CO₂ pollution is directly related to the energy consumption which in its turn connected with population and level of production within the country. The dominance of fossil fuel in the chain of civil and industry energy production leads to inevitable increase of the environment pollution.

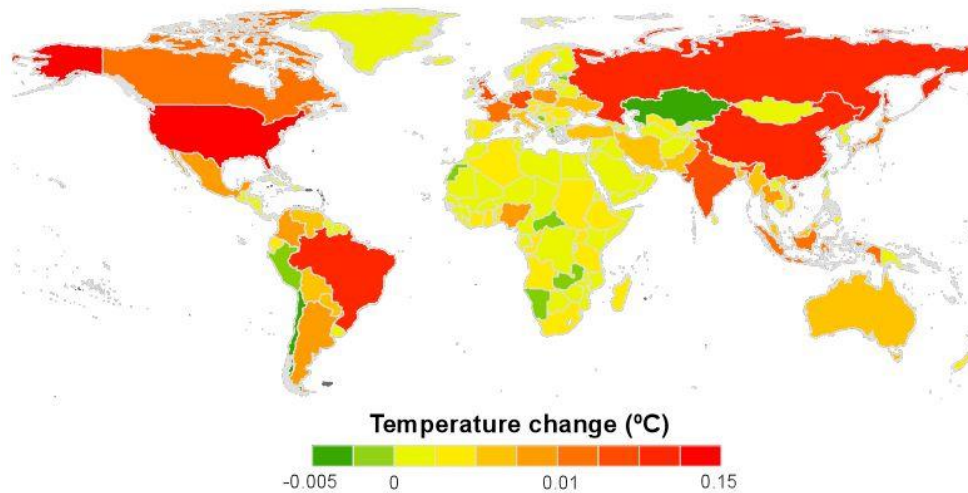


Figure 1-5 Warming contribution by country in a framework of global warming⁸

Turning to renewable sources of energy for electricity production and developing eco-friendly transportations, which use electricity instead of fuel, could decrease the total CO₂ emission by more than 60% with respect to existing rate⁸.

1.3. Common problems of alternative energy sources

Despite obvious technological and environmental advantages of renewable energy sources, we should mention certain of their deficiencies.

The most elaborated sphere of alternative energy is hydroelectricity. However hydroelectric power plants construction leads to significant submersion of soil causing ecosystem damaging including human and wild animals displacing, climate changes⁹ and loss of land^{10,11}. Essential changes in river flow could affect amount of electricity produced by a dam. At the same time water reservoirs of a power plant are known for making severe amount of methane¹². Geothermal sources used for electricity production via water evaporation bring a mixture of gasses influencing greenhouse effect, acid rain and radiation, particularly CO₂, H₂S, CH₄, NH₃, Rn¹³. Some toxic elements could be contained in geothermal source hot water, especially mercury, arsenic, boron, antimony etc.¹⁴

For hydrogen fuel it takes a lot of energy for its production via electrolysis and steam-methane reforming^{15,16}. Besides steam-methane method leads to emission of greenhouse gases such as CO and CO₂¹⁷. Biofuels, including ethanol fuel, are a good way for utilizing bio-wastes, but they cannot be considered as eco-friendly source of energy because of CO, CO₂, NO_x and volatile organic compounds emissions at levels above those of coal and natural gas^{18,19}.

Wind power is probably the less harmful for environment through the whole list of existing alternative sources. Its CO₂ (indirect) emission is estimated as 11-12 gCO₂eq/kWh which is 100 times lower compare to coal based power plant²⁰. It takes much less surface compared to solar cell stations and has no harmful ejections of chemical substances. The only issue for ecology is the use of rare earth neodymium for permanent magnet in power plants²¹. However, electricity production of such power plants is not continuous and depends on the meteorological circumstances.

1.4 . Survey on different types of solar energy harvesting systems

The sun is an incomparably enormous source of energy. Yearly, it brings to earth nearly 3 850 000 EJ, which is absorbed by Earth's surface and atmosphere²². With world energy consumption in the year 2010 of 539 EJ²³, 0.02% of solar flux turned to electric energy could completely cover humanity needs in energy. Attempts to convert solar energy to electricity are understandable since its ecological advantages and possibility to obtain energy independence for private and commercial needs. Recently it was reported that potential of solar energy conversion each year, taking into account such factors as insolation, atmosphere reflection and absorption as long as available land surface, equals to 1575 (min.) – 49837 (max.) EJ²⁴.

Known and utilizable techniques of solar energy harvesting nowadays are photovoltaics, concentrated solar power, solar thermal collectors and converting pumps and fans, which does not turn solar energy to electricity but uses heating and convection effects.

High-temperature collectors consist of reflecting mirrors and lenses in order to concentrate solar thermal energy on small pipes with water which is heated up to 300 °C (20 bar pressure). Created vapors are transferred to turbine-generator mechanism which produces electricity. Principle schema of this kind of power plants is depicted in fig. 1- 6. These kinds of collectors are the first existing solar energy harvesting mechanisms known since 1878 when it was presented by Augustin Muchot at Paris Universal Exhibition exist nowadays, for instance Ivanpah Solar Power Facility produces 377 MW per year, which

is, for example, enough to cover 10% of electricity consumption in France²⁵. Principle advantage of solar thermal power station is capability to store thermal energy which can be added to ensure 24 hour functioning period. With existing technologies thermal energy storing is much cheaper than those for electric energy, combining with vapor accumulation²⁶, it makes high-temperature collectors more advantageous for non-stop electricity production compare to photovoltaic cells. However it should be mentioned that these type of power plants demand high intensity of illumination. Thus, it is not possible to utilize it in regions with low average insolation like northern Europe or northern America.

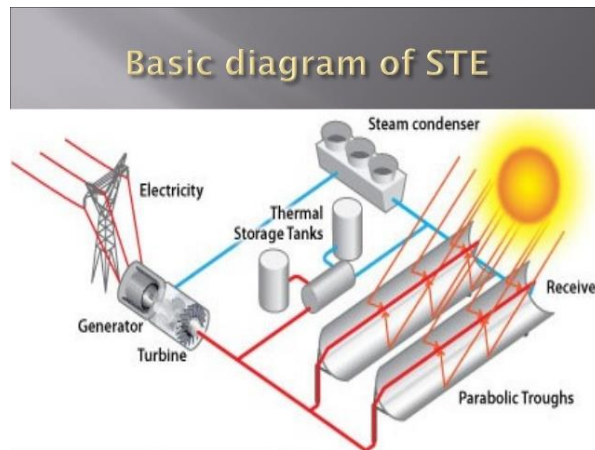


Figure 1-6 Principal schema of high-temperature collector, STE stays for Solar Thermal Energy²⁷

Concentrated solar power approach is very similar to above described high-temperature collectors. Having the same physical approach, it uses a system of lenses that focuses thermal energy onto a small area²⁸ (fig. 1-7). Focused thermal energy can be used for water heating or for thermal accumulation via molten salt technology²⁹. Today, it is a rapidly growing type of power plants, increasing by a factor of 10 its representation on the market within the last 10 years³⁰.



Figure 1-7 Concentrated solar power station³¹

Solar energy is also used to provide heating and ventilation in commercial building, which spend up to 30% of energy for these purposes yearly³². Mostly these systems consist of solar absorbing panels, which are capable to absorb and store thermal energy. It is connected to air conditioning system allowing cool air to circulate towards the thermal panel to be heated there and brought back inside the building (fig. 1-8). This simple improvement of natural ventilation based on convection allows significant increase of

air-condition capabilities especially when combined with the system of vents, which allows controlling air stream and makes possible to use wind as a part of air convection system³³.

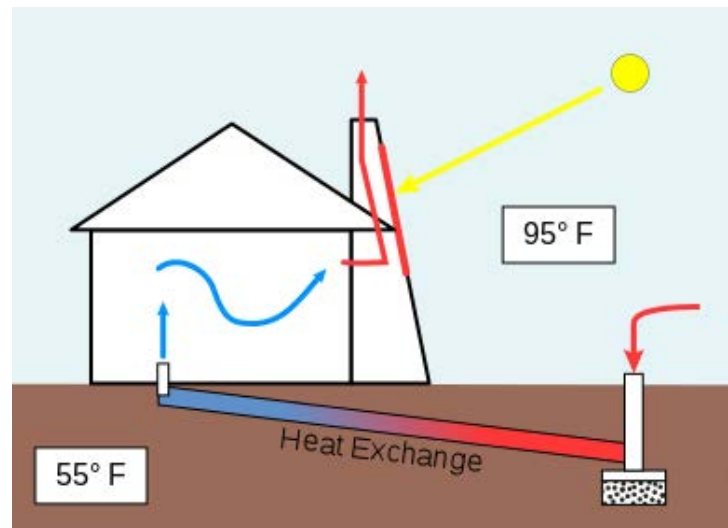


Figure 1-8 Heating exchange mechanism for solar-induced air condition system³⁴

Photovoltaic conversion of solar energy in electricity, which is the most utilized harvesting principle, is the object of this study. Photovoltaic cell uses semiconducting properties of materials which makes possible excitation of charge carriers via light illumination of photovoltaic cell surface and its transport towards electrodes³⁵. Most photovoltaic solar cells are made of mono crystalline silicon³⁶ (fig. 1-9 (a)) due to its well-appropriate electronic properties (direct band absorption) and low price. In fig. 1-9 (c), one can observe the decrease of solar cell price in the last decades as a reverse square function. At the same time, because of the price reduction and adjustment of silicon solar cells properties we observe an exponential increase in cumulative solar energy capacity³⁷ (fig. 1-9 (d)). An outstanding importance of solar cells is explained by its influence on the energy market³⁸. It makes the energy sources much more decentralized, increases concurrence and in consequence, may reduce energy price. It often leads to the energy independence of private housekeeping and small manufactures. Recently, only-electrical vehicles presented by Tesla could be recharged on special power stations fully supplied by solar cell power plants (fig. 1-9 (b))³⁹. Fast reduction of price per cell allows developing standalone systems such as traffic signs, public charging stations, automatic bicycle relays etc. Nowadays it is more and more usual to see solar panels on the roof of private houses. Taking in account the average north-European insolation of 900 kWh/m² and the cost of solar cell installation of 1700 euro/kW, it will give 100% return of investments in 7 years for an electricity price of 0.25 euro/kWh⁴⁰. Concerning unstable prices for coal, gas and naphtha and geopolitical influence on its accessibility it makes solar energy more and more attractive.

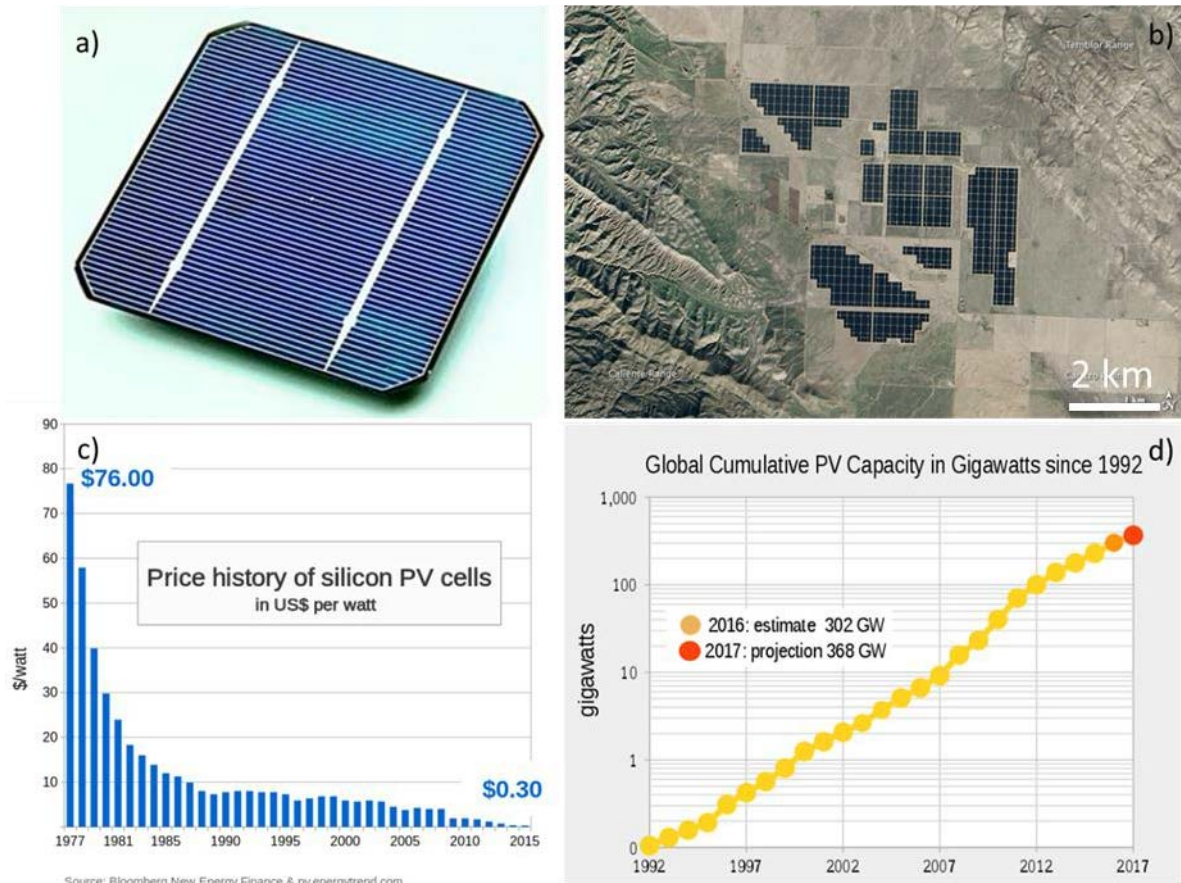


Figure 1-9 Image of silicon solar cell (a), Topaz solar power plant (b) , Price of silicone PV cell (c), global capacity of photovoltaic solar power plants (d)⁴¹

Despite all the advantages related to solar energy, there are a lot of deficiencies connected with this type of power production. Here we will underline only major of them:

- 1) Cost. Despite the reduction of the cost for solar cells fabrication one kW of energy made with solar cell is still more expensive than one kW produced from coal
- 2) Low efficiency of solar panels. Most of silicon based solar cells have their efficiency between 11 and 15%. Front end solar cells science is struggling for 20%. It leads to the problem of the scale: to produce enough power, solar panels should be larger.
- 3) Solar panel does not work at night which makes it necessary to install electrical capacitors which would maintain power supply during the night
- 4) A number of hazardous chemicals is used for producing solar cells, namely rare earths, cadmium, antimony
- 5) Solar panel has a negative energy balance which means that it takes more energy to fabricate one panel than it is capable to produce⁴²

To summarize, alternative energy sources based on solar energy conversion have reached a significant success so far. However each method of solar energy harvesting still demonstrates certain deficiencies. It is either low efficiency in Northern regions for Solar Thermal Energy stations, or limited application area for thermal convection systems. Despite an exponential growth of solar cells capacity and reduction of their price it is still have to be improved in terms of light conversion efficiency and price. For these purposes new prospective materials have to be investigated.

2. Physical principles of solar cell functioning.

2.1. Charge generation on a p-n junction interface.

For photovoltaic conversion two obvious steps are taking place: light absorption accompanied by light induced charge carrier excitation, and charge transfer of excited carrier towards metallic electrodes. Thus in the case of the most primitive solar cell we should provide thick p-type absorbing area with suitable energy gap E_g which would allow light induced excitation of charge carrier as it is shown in fig. 1-10. And thin n-type layer where built-in electric field drives excited carrier to the electrode. Mostly expanded nowadays, c-Si solar cells are based on this structure, which explains its relatively high thickness of 100 – 150 μm ⁴³

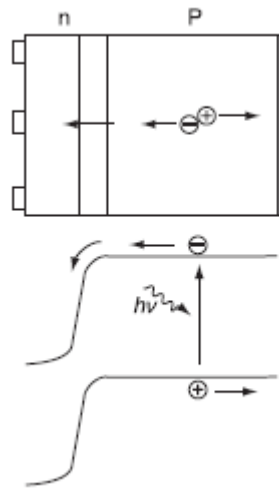


Figure 1-10 Simple p-n junction, typical for crystalline silicone (c-Si) solar cell⁴⁴

Another commonly utilized configuration for solar cells is so called hetero-face structure (fig. 1-11 (a)) where GaAlAs layer is a wide gap transparent semiconductor which prevents diffusion of excited electrons from GaAs layer towards the surface with further recombination. On the other hand, due to its wide gap GaAlAs does not absorb light significantly, thus total amount of photons can be absorbed in GaAs active layer. The typical structure of amorphous silicon (a-Si) solar cells is depicted in fig. 1-11 (b). It is known as “p-i-n” structure, which stands for heavily doped thin layers of silicon for p and n – type respectively separated with intrinsic semiconductor layer. Absorption and charge generation in this case occurs within the intrinsic layer, built-in electric field promotes charge separation towards doped regions where charges are collected and brought to electrodes. Example of chalcogenide based solar cell is given in fig. 1-11 (c). It consists of an active layer of CuInGaSe_2 where major generation of charge carriers occurs separated from the electrodes with wide gap layer which creates sort of potential barrier for charge carriers.

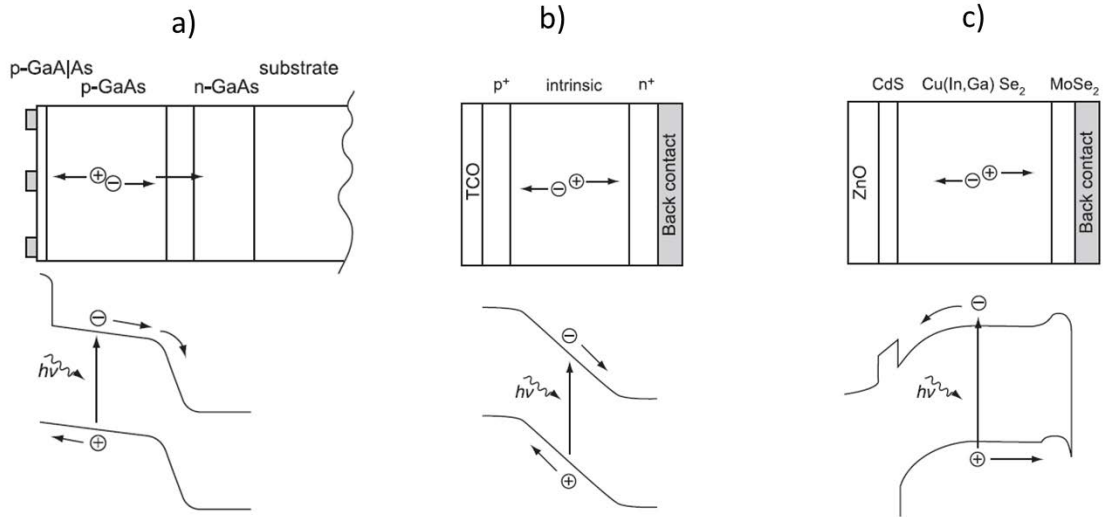


Figure 1-11 Common alternative configurations of p-n junctions for solar cells: a) heterostructure with GaAlAs passivation layer for electron barrier, b) p-i-n type structure with charge generation in intrinsic neutral layer, typical for amorphous silicon (a-Si) solar cell c) typical chalcogenide based solar cell with transparent large-gap window (CdS)⁴⁵

We can underline that these different techniques applied for solar cells preparation lead to significant differences in thickness; for instance c-Si -based cell can be up to 500 μm in thickness, while GaAs-based are only 1-2 μm thick. Absorption coefficients and absorption spectra profiles along with charge carriers lifetime play also a significant role.

Further, we will discuss in details each approach and give examples of commercialized materials.

2.2. Crystalline silicon based solar cells

Crystalline silicon (c-Si) cell is very convenient for the explanation of photovoltaic harvesting principles. As it is known, Si atom has 14 electrons, 4 of which are localized on the outer orbital and participate in chemical bonding (fig. 1-12 (a)). In a perfect c-Si crystalline cell each Si atom shares one valence electron with 4 neighbors, thus considering the body-centered cubic system for Si lattice one could represent a 5-atom basic unit of c-Si crystal cell (fig. 1-12 (b)). By the infinite translation of this basic unit we can obtain an infinite C-Si crystalline bulk (fig. 1-12 (c)).

Being an intrinsic semiconductor c-Si is capable of electric conductivity by means of free-charge carriers which can be excited upon illumination when a photon of sufficient energy strikes an electron (fig. 1-12 (c)). When an electron leaves an atomic shell it creates a hole, which represents positively charged “absence” of the electron. A flux of negatively charged free electrons and positively charged holes give rise to photogenerated electricity.

This primitive approach allows understanding of physical process which stays for charge excitation from valence to conductive band depicted in fig. 1-10

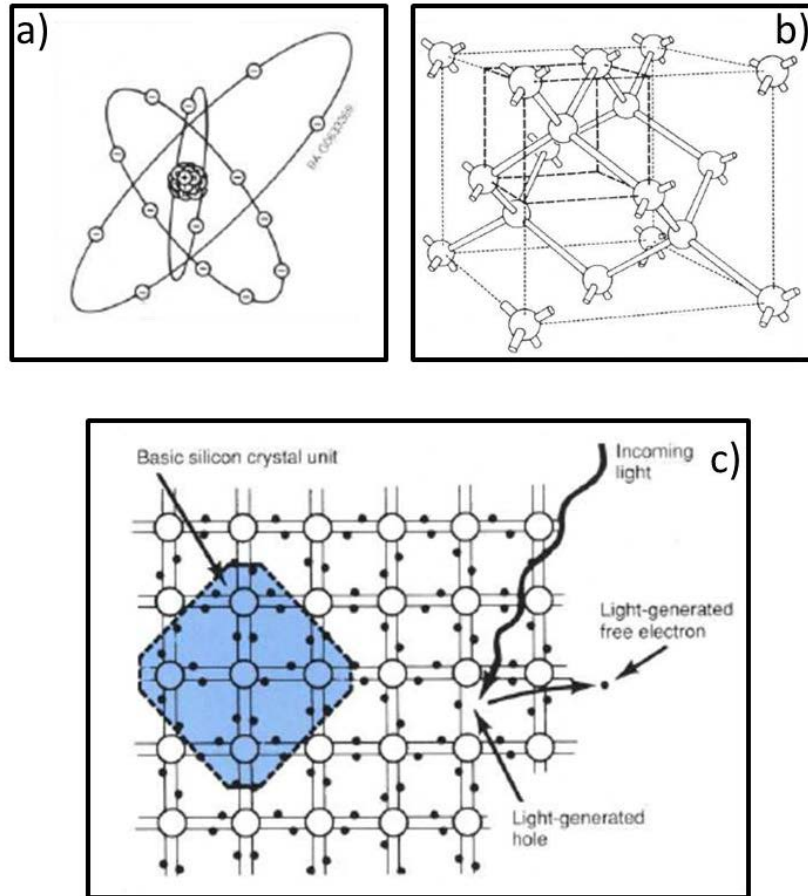


Figure 1-12 Simplified image of a) Si atom b) Si unit cell c) c-Si continuous bulk⁴⁶

However, without significant built-in electric field efficient charge separation and its transfer towards electrodes would be impossible. For this purpose we need to establish a contact between semiconductors with different electric properties (different Fermi levels). Created electric field will drive positive and negative charges in opposite directions thus preventing recombination.

Upon the introduction of phosphorus (fig. 1-13 (a)) one can obtain an unbounded electron since P has 5 valent electrons. In reverse for boron atom which has only 3 electrons to form a chemical bond, thus the absence of mutual electron with its Si atom neighbor creates a hole. After such doping we can obtain n-type spatial area where electrons are major charge carriers and p-type spatial area where electrons are minor charge carriers and holes are referred to majority carriers (fig. 1-13 (b)). Before contact, p-type and n-type zones are electrically neutral, which means the equality between positive protons and negative electrons, the excessive energy of free-charge carriers makes them “non-bonded” with the atoms and allows their percolation through crystal lattice.

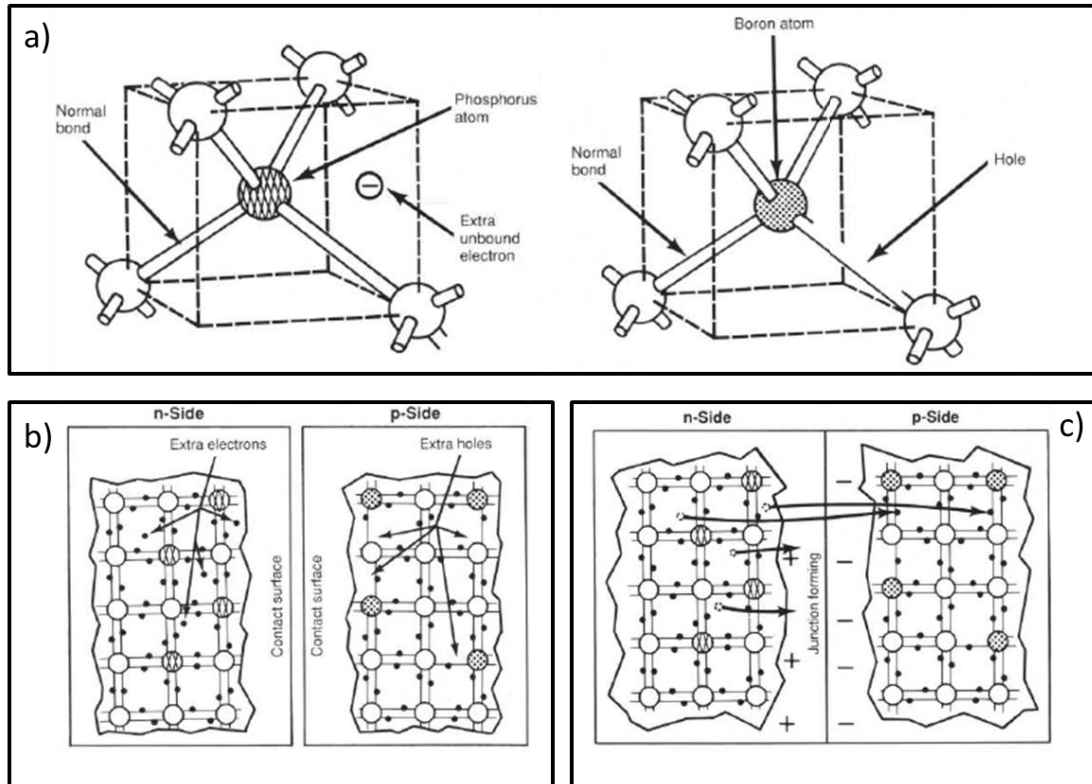


Figure 1- 13 Modification of c-Si electronic properties by means of doping with B or P (a) basic unit undergoes modification with appearance of free electron or hole, (b) doped c-Si n-type and p-type spatial areas before contact (c) formation of a p-n junction⁴⁵

When p-type and n-type zones are in contact (fig. 1-13 (c)), the electric field driven by charge carrier concentration gradient makes electrons from n-type zone penetrate into p-type material and holes from p-type zone to flow into n-type zone. While inside the bulk there is still a majority for electrons and holes in n-type and p-type zones respectively, in the vicinity of a p-n junction significant difference in charge carrier concentration occurs. As the diffusion of charge carriers continues the excessive positive charge accumulates on the n-type side and excessive negative charge on a p-type side of the interface, as it is shown in fig. 1-14. In turn, this creates an electric field on the p-n junction interface, which prevents further diffusion of charge carriers, according to Coulomb's law. On the other hand, spatial charges created at p-n junction interface do not allow holes (electrons) to penetrate deep inside n-type zone (p-type zone). Therefore, electrons and holes recombine with each other in a vicinity of p-n junction interface creating a depletion zone where the concentration of charge carriers is low (fig. 1-14). However ionized atoms create a strong electric field V_C in the junction area. This field does not expand in the bulk and thus does not influence the charge carriers behavior deep inside p-type and n-type zones. The depletion region and spatial area of ionized atoms grow until the moment where fluxes of minority and majority charge carriers through p-n junction are in equilibrium. At this moment, the p-n junction is characterized by the equilibrium contact potential difference, V_0 .

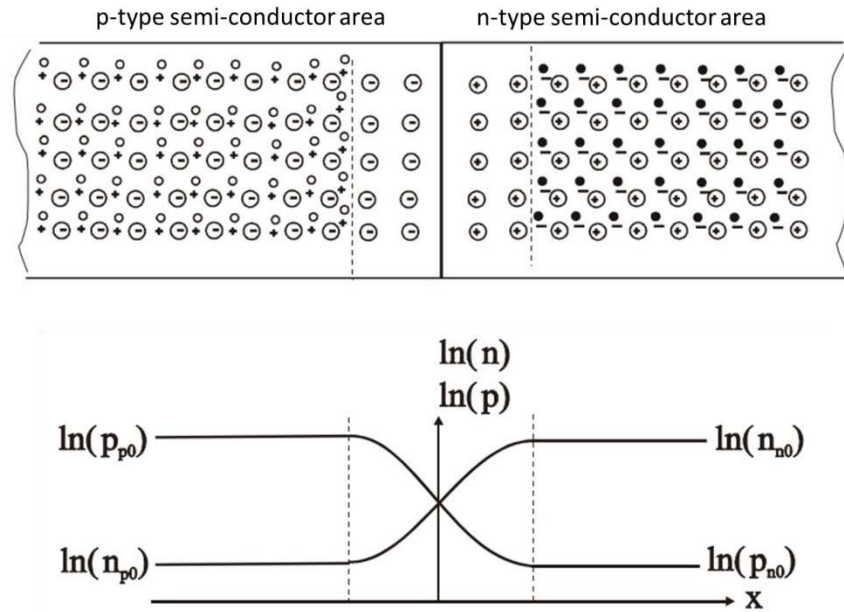


Figure 1-14 Concentration of charge carriers in the bulk and in vicinity of a p-n junction⁴⁶

Because of this additional electric field, one should consider not only electron (hole) potential energy in periodic crystalline structure but also a potential energy contributed by electric field. The energy diagram of dynamic equilibrium of p-n junction (fig. 1-15 (a)) shows that an electron in the bottom of p-type conduction zone has energy higher than the one in n-type conduction zone by a factor equal to ϕ_0 , where $\phi_0 = qV_0$. Energy levels have a shift proportional to the difference of electrochemical potentials between p-type and n-type zone and can be expressed by $\phi_0 = \mu_n - \mu_p$. Thus, at equilibrium, the difference of charge carrier potential energy is fully characterized by the nature of semiconductor.

When we apply an external voltage, as it is shown in fig. 1-15 (b), major charge carriers in depth on n-type and p-type zones are attracted to the electrodes. This entails the extension of depletion region because of the ionization of atoms. Increased electric field is characterized by applied voltage V and can be depicted as increase of p-n junction barrier ϕ_0 on qV , therefore $\phi_b = qV_0 + qV$. As one can conclude the flux of major charge carriers via p-n junction in this regime is almost impossible since they have to overcome the potential barrier produced by increased spatial charge. At the same time minor charge carriers do not have any barrier in this regime and obtain high kinetic energy (field driven) in case of their transition through a p-n junction interface.

In reverse if we apply “+” to p-type area and “-” to n-type (fig. 1-15 (c)) major charge carriers from the depth of n-type (p-type) regions will be repulsed from the electrodes and driven to the p-n junction interface. Ionized atoms will be populated with electrons (holes) on n-type (p-type) side in vicinity of interface and, therefore, the electric field produced by ionized atoms will decrease proportionally to applied voltage V , resulting in the reduction of barrier $\phi_b = qV_0 - qV$. In this regime the flux of major charge carriers through p-n junction is higher than one of minor charge carriers because of the external field driven reduction of potential barrier.

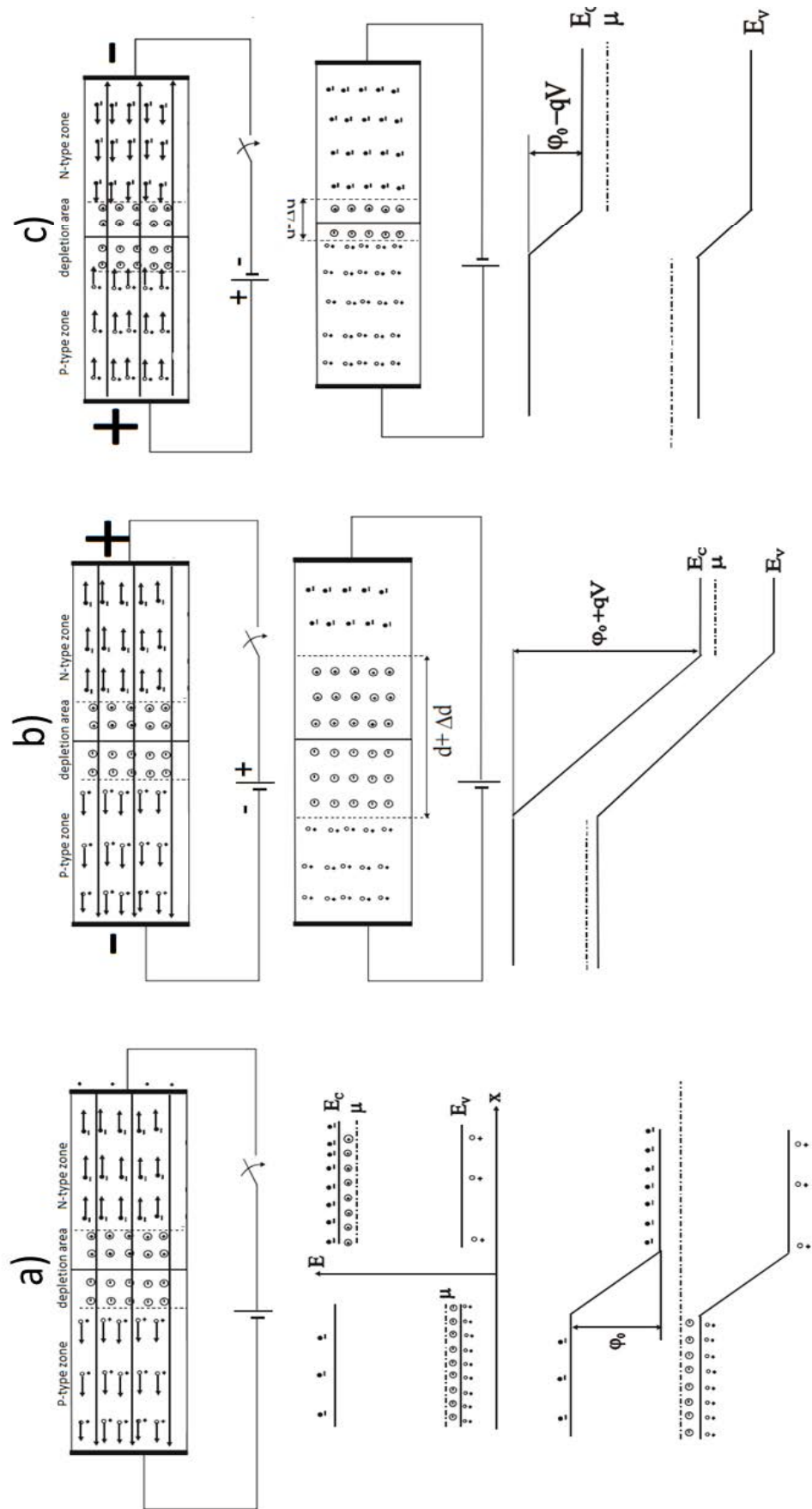


Figure 1-15 p-n junction interface with a depletion region immediately after contact (a), case of increased depletion region caused by external electric field (b), case of depletion region shrinking caused by external electric field⁴⁷

Considering this, we can explain I-V curve of p-n junction depicted in fig. 1-16. When we apply negative bias to p-type zone, the extension of depletion region and increase of potential barrier ϕ_b makes impossible the percolation of major charge carriers through p-n junction. At the same time, minor charge carriers do not have any barrier and accelerate because of the external field. When a minor charge carrier passes through the p-n junction, it becomes a major charge carrier and contributes immediately to the circuit current, thus after a certain threshold current I does not depend on voltage V , obtaining a saturation current value, I_s . When we apply positive voltage to the p-type zone, this entails shrinking of depletion region and reduction of potential barrier ϕ_b which increases the flux of major charge carriers. If one applies external voltage $V = \phi_0$, the p-n junction disappears which results in unimpeded flux of charge carriers in both directions.

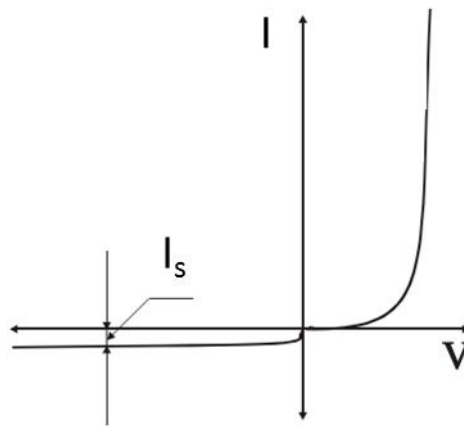


Figure 1-16 I-V curve of a p-n junction⁴⁷

Taking into account the basic concept of p-n junction functioning we can conclude that, for solar devices, light-induced generation of **electron-hole pair** in the vicinity of interface is very important, since **minor** charge carriers can be transferred through p-n junction (charge separation) and obtain kinetic energy equal to ϕ_b upon this transition.

Fig. 1-17 represents new electrons created in p-type zone and new holes created in n-type zone, which are transferred via p-n junction by built-in electric field (charge separation) During this transfer, charge carriers gain kinetic energy and contribute to the circuit current (charge transfer). Without this electric field-driven separation electron-hole pair would quickly recombine in the lattice.

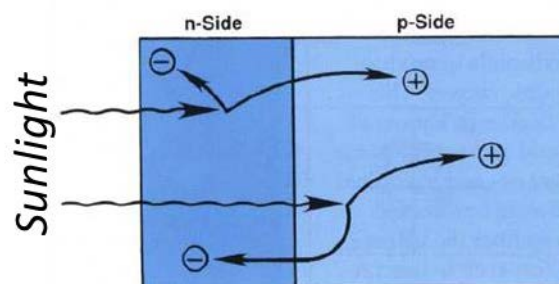


Figure 1-17 Electron-hole pair light-induced generation, charge separation, transition of minor charge carrier through the interface⁴⁶.

For the light-induced charge generation, the most important parameter is the energy gap, E_g , which describes the energy needed to excite the electron from valence band to conductive band as it is depicted in fig. 1-10. For c-Si, this value is equal to 1.1 eV.

Mostly-used nowadays c-Si solar cell that works according to the above-described model is depicted in fig. 1-18. It consists of a planar p-n junction and collecting electrodes. Electrons and holes being separated and transferred through p-n junction are collected on electrodes and brought to the electric circuit where they recombine, allowing repetition of this process. In the absence of external circuit, charge carriers are cumulated on the electrodes until the p-n junction reaches dynamic equilibrium, which occurs at open circuit voltage V_{oc} .

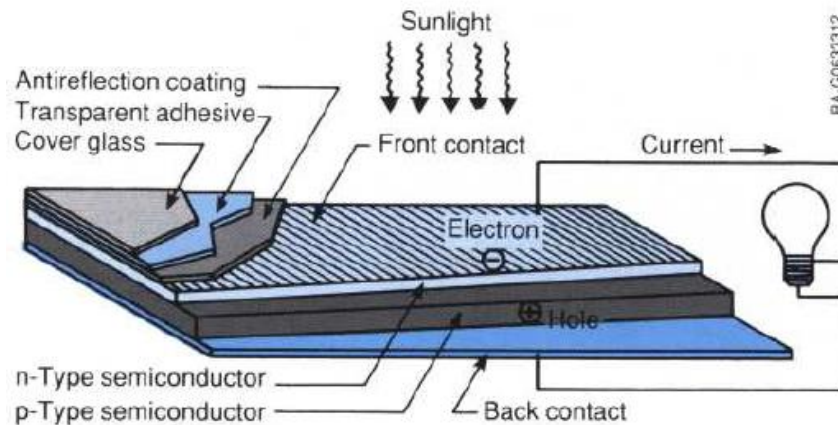


Figure 1-18 Schematic image of c-Si solar cell cross section⁴⁶.

One could notice that p-type layer is thicker than n-type. It refers to the minority charge carrier mobility and lifetime. It is known that electrons (minor charge carrier in p-type layer) possess higher mobility and longer lifetime, thus electron-hole pair generated in thicker p-type layer has higher possibility to reach p-n junction interface where it can be separated and transferred to the electrodes^{47,48}.

Cover glass and antireflecting coating are used to protect active materials from chemical and mechanical degradation and maximize the amount of solar energy brought to the absorber.

2.3. Amorphous silicon based solar cells

Mostly common amorphous silicon (a-Si)-based solar cells are made using p-i-n diode architecture, heterojunction structure and Schottky barrier device⁴⁹.

In turn, there are several types of p-i-n architecture used for a-Si solar cells. The most common structure fabricated on glass substrate is depicted in fig. 1-19(a). It is usually made with thin SiO_2 layer on soda-lime-silicate glass with a layer of TiO_2 of about 600-nm thickness. The thin p-layer of 10 nm is made of boron-doped a-Si, the n-layer of 20-30 nm thickness is phosphorus-doped a-Si and the i-layer is an intrinsic non-doped or slightly doped (<1 ppm) a-Si layer of 250-500 nm thickness^{50,51}. For heavily doped configuration (fig. 1-19 (b)), c-Si is usually utilized to form p⁺ and n⁺ zones in the same manner as for simple p-n junction solar cells, the two layers being divided by intrinsic a-Si layer. Stacked configuration (fig. 1-19(c)) is a tandem of two classic p-i-n cells where the thickness of both a-Si intrinsic

layers is adjusted in the way that the currents from both cells are similar and, since they are configured in series, then the voltages add⁵².

Usual conversion efficiency for these solar cells is 12-14 %^{53,54}. There is however a significant problem with solar energy harvesting since a-Si has a band gap of 1.7eV and most of infrared radiation does not contribute to the charge photogeneration.

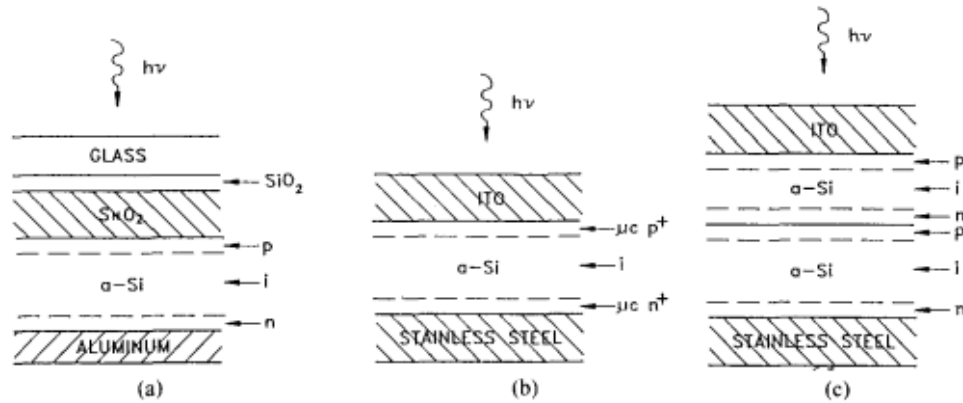


Figure 1-19 Typical variations of p-i-n solar cell architecture: (a) classic structure (b) configuration with heavily doped p+ and n+ zones, (c) stacked system of several p-i-n layers⁵³

In principal these cells consist of two junctions: “p-i” and “n-i” depicted in fig. 1-20. Since holes (electrons) concentration in p-type (n-type) layer is much higher than those in the intrinsic (i) layer, diffusion of holes (electrons) into intrinsic layer occurs. Upon recombination, depletion region of ionized atoms is formed. However, the gradient of charge carrier concentration between p (n) layer and i layer is much smoother than the one between p and n – layers for simple p-n junction cell. This is because of the equilibrium concentration of charge carriers in the intrinsic semiconductor. Thus, the potential difference between p (n) and i - layer in this case is lower compared to p-n junction. In consequence, the depletion region is localized mostly in the intrinsic layer. When light-induced electron-hole pair occurs in the intrinsic layer, charge carriers are immediately involved in electric field created by spatial charges in the vicinity of “p-i” and “n-i” junctions and, therefore, holes are brought in p-layer and electrons in n-layer.

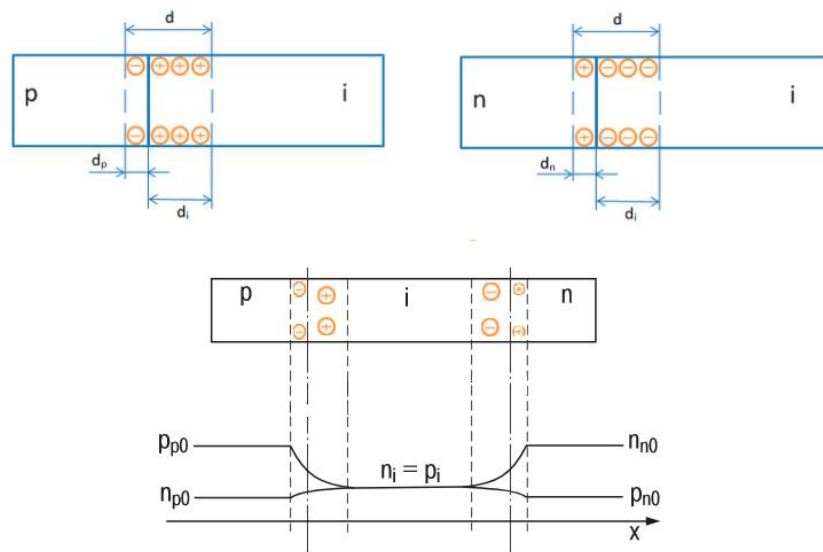


Figure 1-20 p-i-n diode schematic representation

The doping concentration of p and n – layers allows a fine tuning of the electrochemical potential and charge carrier concentration profile. It results in depletion region width change, which in its turn affects the kinetic energy gained by photogenerated charge carriers upon the transition through “p-i” or “n-i” junction.

A heterojunction cell is commonly made by depositing a-Si on antimony-doped tin oxide or indium-tin-oxide, as depicted in fig. 1-21. In phosphorous doped a-Si layer a slight diffusion of P into the intrinsic layer occurs during deposition making it n-type. Thus n-n⁺ heterojunctions are formed. P-n⁺ heterojunctions can be made by boron doping of a-Si intrinsic layer or by depositing undoped a-Si on p-type GaAs followed by the phosphorization of intrinsic a-Si layer. However, these devices show lower photocurrent and open circuit voltage since doping of amorphous silicon entails creation of trap-type defects that reduce the charge carriers lifetime.

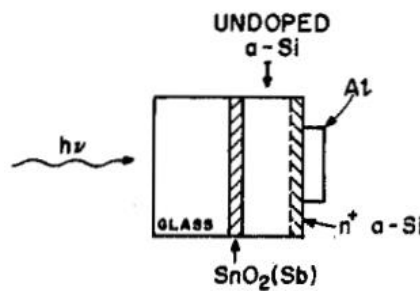


Figure 1-21 a-Si heterojunction solar cell⁴⁹

a-Si solar cells with Schottky barrier are normally made of a P-doped a-Si layer on the top of steel substrate, with relatively thick a-Si intrinsic layer (up to 1µm) and metallic contacts on top of it⁵⁵ (fig. 1-22). Transparent antireflecting coating such as ZrO₂ is usually utilized. a-Si solar cells with Schottky barrier are known for high collection efficiencies at short wavelengths in case of front illumination. Back illumination is much less efficient which is understandable since holes generated on the “n⁺-i” interface have difficulties to cross a thick a-Si layer towards the electrode.

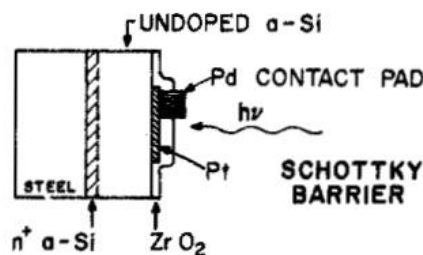


Figure 1-22 a-Si with Schottky barrier solar cell⁵⁶

The Schottky barrier is a type of metal-semiconductor junction (MSJ), sometimes called the surface barrier diode. Since harvesting of charge carriers is provided by metallic (ohmic) electrodes it is very important to discuss physical principles of MSJ functioning.

We will consider two common ways to obtain MSJ interface: metal wire connected to the semiconductor to form a point contact (so called cat’s whisker) and deposited metal contact on top of the active layer depicted in fig. 1-23 (a) and (b), respectively.

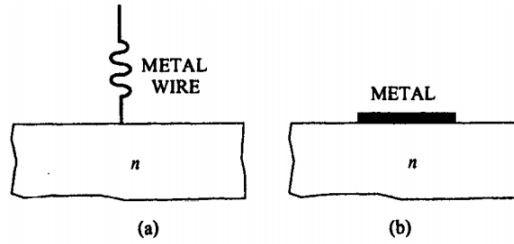


Figure 1-23 Schottky barrier (MSJ) established by point contact (a) and metal electrode deposition (b)⁵⁶

As it is clear from fig. 1-24, the Schottky barrier $q\phi_B$ depends on the chemical nature of the metals and semiconductors to be used. For n-type SC $q\phi_{Bn}$ is defined as the difference between metal and SC electron affinity. Since, for the metal, electron affinity χ and work function ϕ_m are the same, it is usually represented as

$$\phi_{Bn} = \phi_m - \chi_{sc}, (1.1)$$

where χ_{sc} is the electron affinity of the semiconductor.

While for p-type, it is equal to the difference between E_g and $q\phi_{Bn}$

$$\phi_{Bp} = E_g - \phi_{Bn}, (1.2)$$

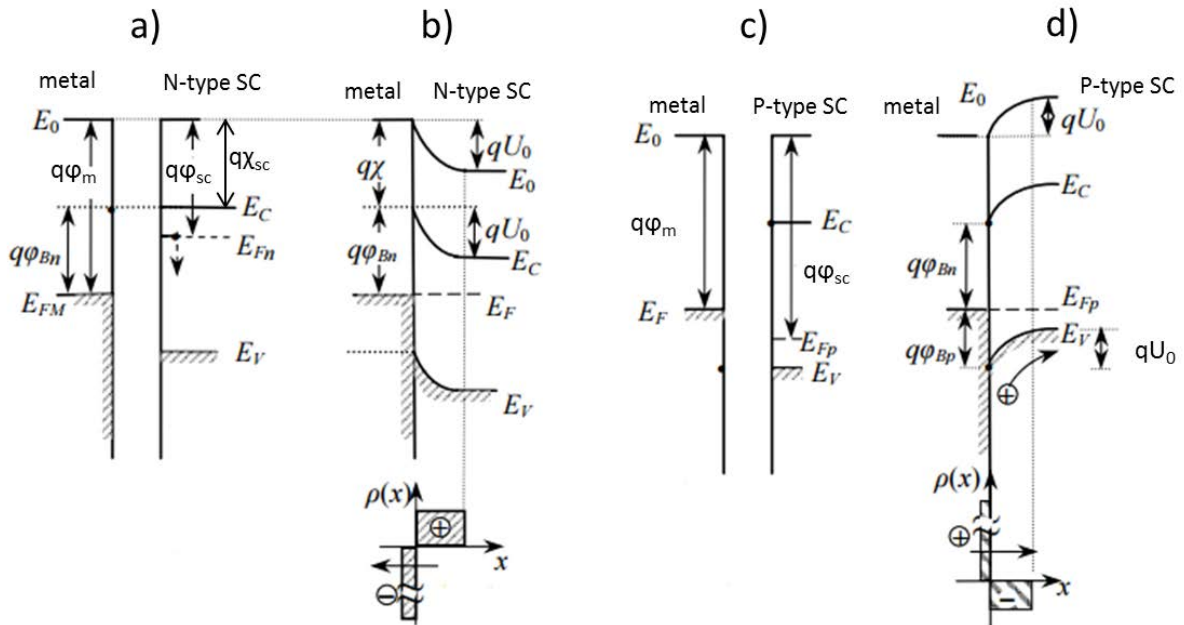


Figure 1-24 Establishment of Schottky barrier (MSJ) before contact with n-type SC (a), metal - n-type SC junction (b), before contact with p-type SC (c), metal - p-type semiconductor junction (d)^{57,58}

When the metal and semiconductor are in contact, a dynamic equilibrium is established after a certain time. Similarly to p-n junction, n-type semiconductor gives the excess of electrons to the metal, forming a depletion region which consists of positively charged ionized atoms. Thus, two barriers are formed: Schottky barrier ϕ_b which prevents electron diffusion in the semiconductor, and potential barrier eV_{bi} , which impedes electron injection from the semiconductor to the metal. By applying external voltage, one can modify eV_{bi} encouraging electron flux from semiconductor to metal, or inhibiting it. Since Schottky barrier is determined by the nature of materials, it is not affected by the applied bias, and, in

consequence, the current flux from metal to semiconductor does not depend on the voltage. Considering this, we can obtain I-V curve for Schottky barrier, as depicted in fig. 1-25

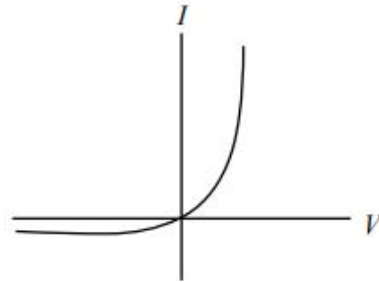


Figure 1- 25 I-V curve of Schottky barrier diode

The same is fair for MSJ between p-type semiconductor and metal, considering the polarity of applied bias.

Along with Schottky barrier type of MSJ, ohmic contact exists. As one could note in fig. 1-24 a prerequisite for the establishment of Schottky barrier establishing is that the work function of metal ϕ_m is higher than the work function of n-type semiconductor ϕ_{sc}^n (and vice-versa for p-type : $\phi_m < \phi_{sc}^p$). This “positive” difference results in the formation of an energy barrier at the interface of MSJ. In the opposite case, when $\phi_m < \phi_s^n$ ($\phi_m > \phi_s^p$), the barrier between metal and semiconductor is absent in dynamic equilibrium (fig. 1-26). Then, the flux of charge carriers from semiconductor to metal is not impeded, neither the current from metal to semiconductor via tunneling. Opposite to Schottky contact, where depletion takes places, we observe layers enriched with major charge carriers for ohmic contact.

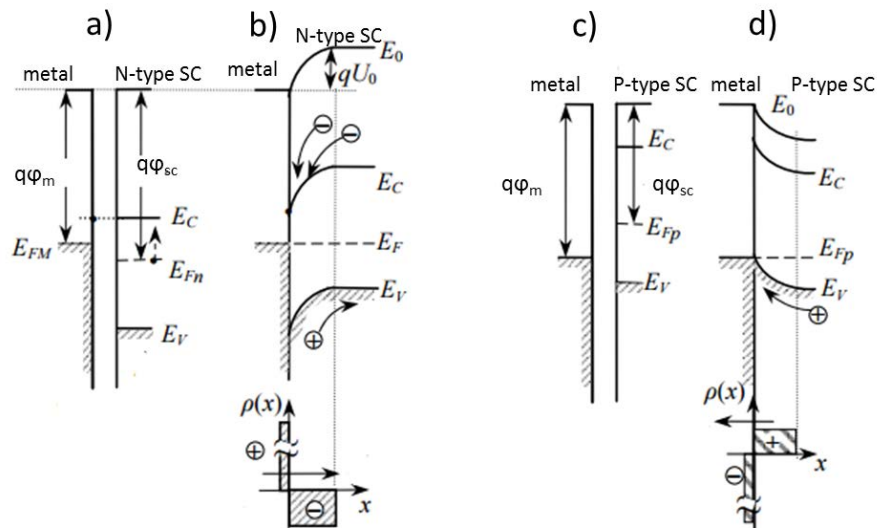


Figure 1-26 Establishment of Ohmic barrier (MSJ) before contact with n-type SC (a), metal - n-type SC junction (b), before contact with p-type SC (c), metal - p-type semiconductor junction (d)⁵⁹

Since the depletion region is not formed, there is no force that prevents unhindered charge carriers flux, thus I(V) function is linear and is represented by a straight line as in the case of simple resistor⁵⁹. (fig. 1-27)

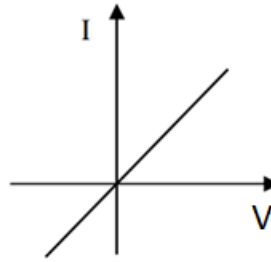


Figure 1-27 I-V curve of Ohmic type of contact

Therefore, it is extremely important to match the work functions of semiconductor and metallic electrodes to establish the needed type of MSJ.

2.4. Heterojunction based solar cells. Multi-junction architecture for solar cells.

Heterojunctions are electrical junctions of two semiconductors with two different E_g . They can be divided in two groups : isotypic ($n^+ - n$, $p^+ - p$) and anisotypic ($n^+ - p$, $p^+ - n$). From some point of view, MSJ can be considered as a particular case of heterojunction. Widely utilized heterojunctions are Si-Ge, Ge – GaAs, GaAs – GaP⁵⁹.

The main difference between homojunctions (fig. 1-15 (a)) and heterojunctions, is the potential barrier for electrons and holes. As shown in fig. 1-28, the barrier prevents injection of major charge carriers from narrow band gap to wide band gap semiconductor. Thus, heterojunction is characterized by the flux of only one type of charge carriers. For instance, in n-Ge – p-Si heterojunction, the flux of holes is negligible ($I_p/I_n = e^{-16}$), while for the symmetric homojunction this ratio is $I_p/I_n = 1$ ⁶⁰.

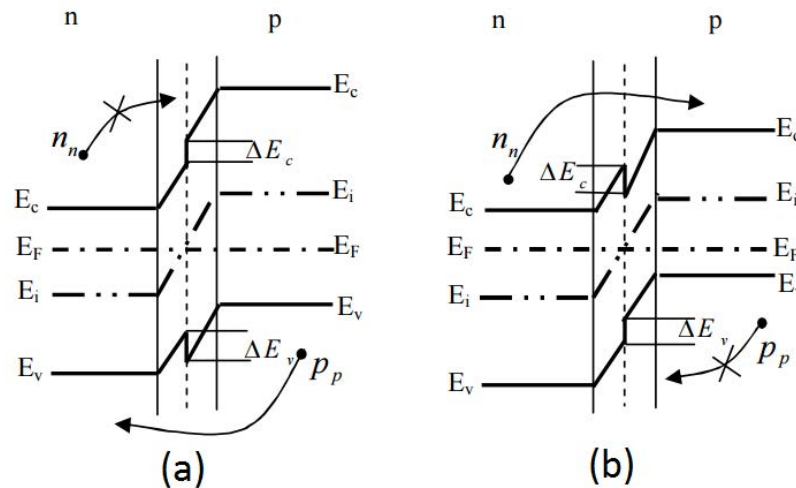


Figure 1-28 Heterojunction of wide band gap p-type semiconductor and narrow band gap n-type semiconductor (a), and vice-versa (b)⁶²

Silicon-based heterojunction solar cells made of a-Si:H / c-Si layers were brought by Fuhs et al. ⁶¹. Further modification brought it to a modern concept of heterojunction based solar cells with thin intrinsic layer of wide gap semiconductor (HIT)^{62,63}. From the schema of thin solar cell and band diagram in fig. 1-29, we can conclude that light-generated charge carriers driven by the built-in electric field are brought to the heterojunction interface where they are “jammed” between wider band gap layers: intrinsic layer (a-Si:H) and active layer (a-Si:H(p^+) for holes, a-Si:H(n^+) for electrons). The intrinsic layer plays the role of a membrane or of a dam for charge carriers where they can be accumulated to a certain extent. By this

confinement, it is possible to obtain higher open circuit voltage, since charge carriers do not pass this barrier too fast. However, the transition is fast enough to avoid recombination. Using this architecture an efficiency of 23.7% was reported recently by Kinoshita et al.⁶⁴

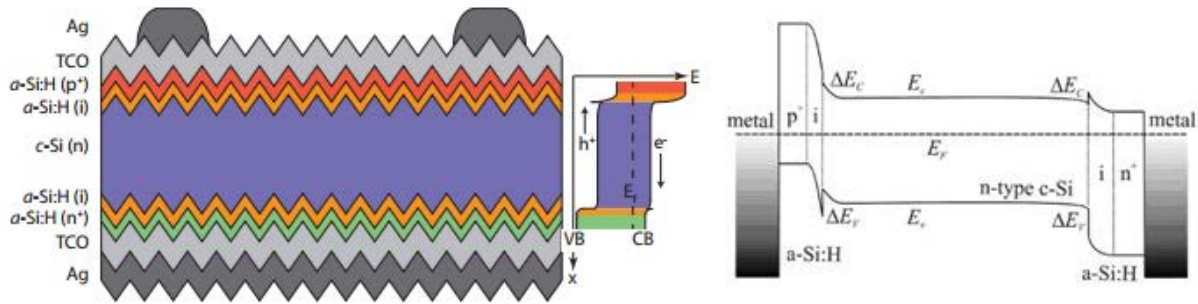


Figure 1- 29 Heterojunction silicon solar cell with thin intrinsic layer (HIT) and its band diagram^{65,66}

As an alternative to highly-doped silicon layers, transition metal oxides such as MoO_3 , V_2O_5 , WO_3 , known to be wide-gap materials with electronic donor states, are also utilized^{67,68}

Other materials are also studied for this architecture. For instance, solar cells based on $n\text{-Al}_x\text{Ga}_{1-x}\text{O}/p\text{-Cu}_2\text{O}$ heterojunction with 6 % efficiency are reported⁶⁹, as well as widely-studied chalcogenide based heterojunction, $n\text{-CdS}/p\text{-CuInSe}_2$, which has a very suitable band gap for solar energy harvesting, along with its direct band type that reduces the requirement of extended lifetime for minority charge carriers⁷⁰.

Multi-junction solar cells (MJSC) combine several heterojunctions (homojunctions) with different E_g for more efficient light harvesting. In some cases, it applies some approaches of “heterojunction with intrinsic thin layer” (HIT) structure. Usually made of III-V materials, multi-junction solar cells can reach efficiencies up to 24.7%⁷¹, that cannot be obtained for single-junction devices limited to 17.1%⁷²

In MJSC, active layers (subcells) are ranged in the order of E_g reduction, thus the whole range of spectra can be involved in the photo generation of charge carriers (fig. 1-30 (a)). As it can be seen in fig. 1-30(b), in the case of serial connection of several subcells, photocurrent degradation occurs due to non-ohmic type of junction between subcells. Rectifying the type of junction creates high resistance at the border between subcells, with undesirable accumulation of charge carriers in the potential wells formed at the border between wide gap and narrow band semiconductors. In other words, the device is facing parasitic diode on the interface between two subcells with inversed charge carrier flux.

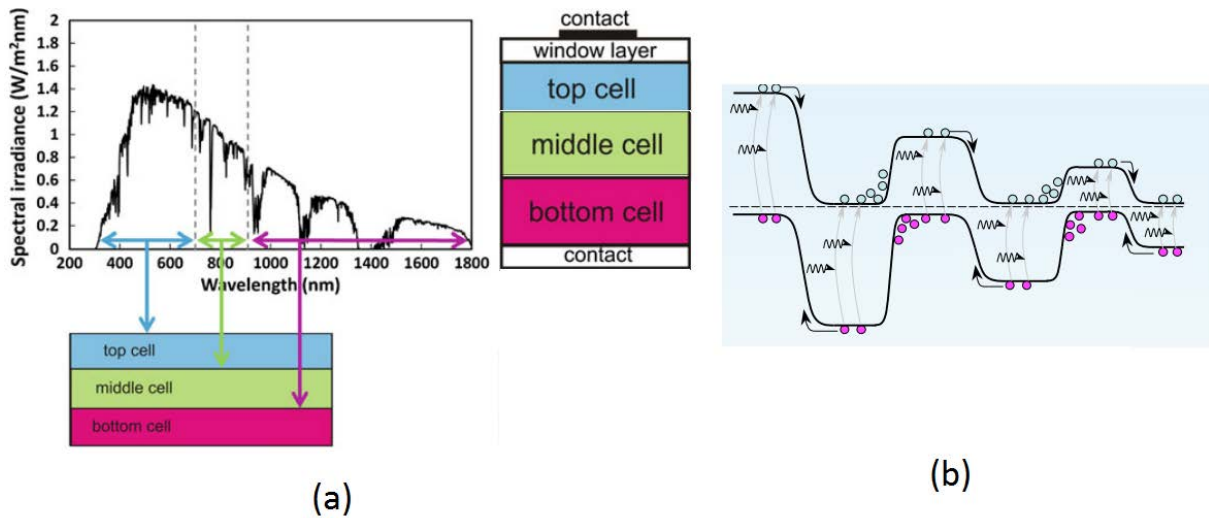


Figure 1- 30 Multi-junction solar cell, serial connection (a), its band diagram (b). Compilation ^{73,74}

To avoid these undesired effects, a sequence of active layers is separated by “window” layers. It allows reduction of surface recombination and scattering losses of charge carriers⁷⁵. Tunnel junctions are fabricated to provide low-resistance connection between the subcells. For instance we can consider the “InGaP – InGaAs – Ge” MJSC depicted in fig. 1-31(a). The role of tunnel junction is played by the wide-band-gap heavily-doped junction of “n-InGaP/p-AlGaP” semiconductors. As it was mentioned before, heavy doping of semiconductors leads to reduction of the depletion region due to high concentration of charge carriers. Thus, in the absence of strong electric field caused by ionized atoms, charge carriers can easily tunnel through the p-n junction of “n-InGaP/p-AlGaP” diode. After tunneling, they are dropped to the conductive (or valence) band of the next-lying semiconductor, where they are the minor charge carriers, which can be driven by the electric field to the p-n junction interface, and so on towards the collecting electrodes (fig. 1-31(b)).

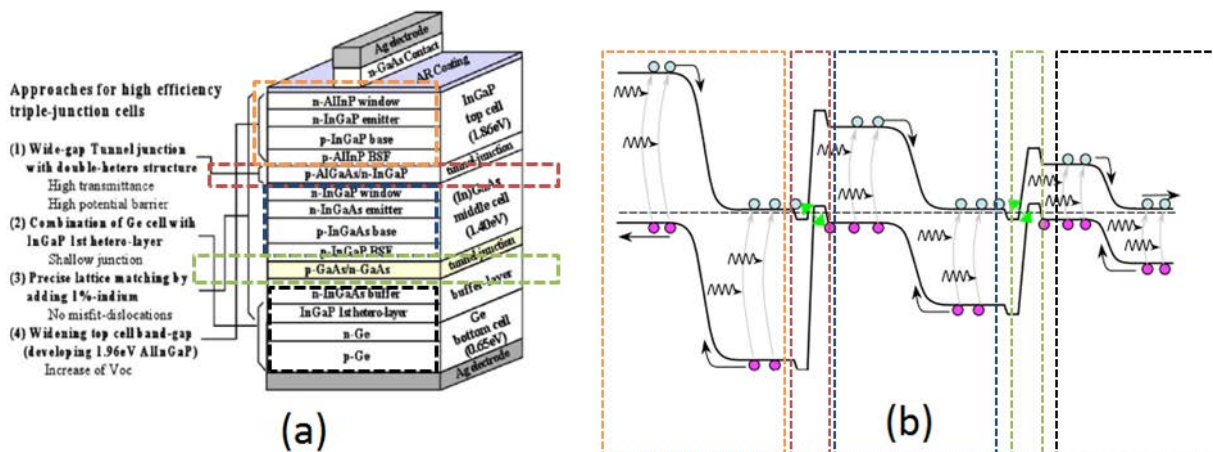


Figure 1- 31 Multi-junction solar cell schema with tunnel junctions (a), its band-diagram (b). Compilation ^{76,78}

MJSC approach to 40% efficiency of solar conversion^{77,78}, which is outstanding. However, the difficulties for its production along with high cost still limit its application on the market.

2.5. Dye sensitized solar cells. Grätzel cell.

In the previous sections, we were analyzing the physical behavior of solid-state junctions based on inorganic materials. Besides, devices containing organic molecules are also of great interest due to reduced requirements for chemical purity and to relatively low cost. Physical processes associated with charge generation in molecular organic solar cells, polymer solar cells and especially dye-sensitized photoelectrochemical solar cells (DSC) are quite different from those revised above and, therefore, causes a significant scientific interest. Researches concerning DSC raised after Grätzel et al. report on first DSC solar cell in 1991, which was based on electrochemical solution with dye-sensitizer molecules anchored to porous TiO₂ thin film^{79,80}.

Compared to previously regarded solid body junctions, where semiconductor interface is used for both charge generation and transport, dye sensitized solar cells utilize a sensitizer for electron-hole pair generation associated with sensitizer wide-gap semiconductor that is capable of collecting excited charge carrier from it^{81,82}. Thus, the processes for charge generation and transfer are separated between the sensitizer and the wide-band-gap semiconductor. Electronic properties of dye sensitizer allow harvesting broader-band solar energy compared to solid body junctions⁸³.

DSC, schematically represented in fig. 1-32, is made of conducting glass photoelectrode on which a thin film of porous TiO₂ (or ZnO / Nb₂O₅^{84,85}) is deposited. This film consists of nanometer-sized granules sintered together to provide electric conductivity. A nanolayer of dye-sensitizer molecules is then attached on top of the porous oxide. The rest of the space is filled with electrolyte such as iodide-triiodide couple⁸⁷.

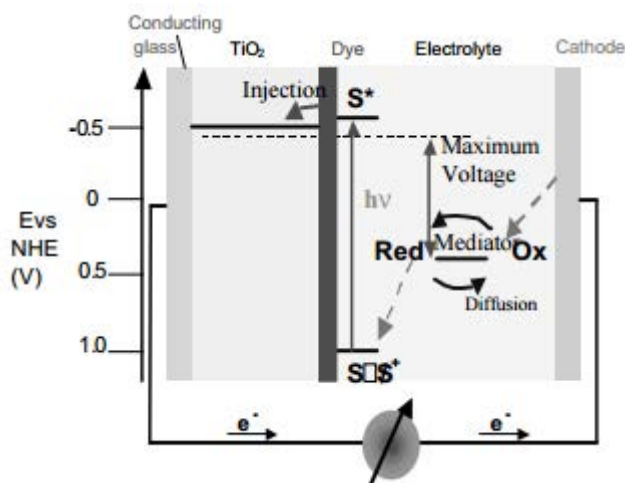
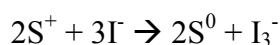
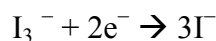


Figure 1-32 Principle schema of dye-sensitized solar cell⁸²

Electric process which takes place in DSC is presented in fig. 1-33. In the heart of the cell is the excitation of dye-sensitizer by incident light with electron-hole pair generation (1). Then, due to the difference in electron affinity between dye and porous semiconductor, electrons migrate from dye excited level to the conductive band of mesoporous TiO₂ film(2). Electrons are transferred to the collector electrode through TiO₂ (3). Regeneration of the dye to its neutral state occurs due to electron transfer from the electrolyte (4). Being oxidized, the dye is reduced by electron donor I⁻:



And, further, triiodide complex diffuses to the cathode where it is reduced back to its inner state:



The main ways of energy loss are spontaneous relaxation of excited state in dye-sensitizer (5), dye reduction with transferred electron (6) and triiodide reduction by the transferred electron in TiO₂ conductive band (7). Mechanism (7) recombination remits because of spatial separation of excited electron from oxidized iodine molecules by the barrier of dye sensitizer, which is non-conductive in the ground state⁸⁸.

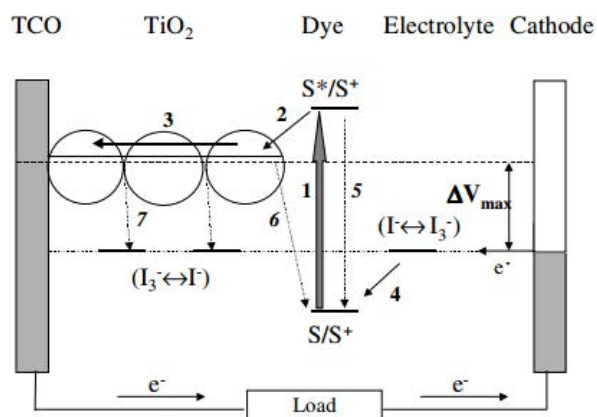


Figure 1- 33 Photoelectric RedOx process in dye-sensitized solar cell⁸⁶

The main advantage of this approach for solar energy harvesting is the high tunability of absorbed light wavelength. While TiO₂ is transparent up to 400 nm, widely-known ruthenium-based dye sensitizer presents an absorption cutoff that can be tuned from 800 to 1000 nm, as a function of ligand^{87,87}. That opens a vast field for the study of novel sensitizer molecules and its pairing with different transparent semiconductors. Along with Ru, different metallic complexes are known to be used as dye sensitizers, for instance Os, Re, Fe, Pt, and Cu – based complexes. More detailed list of metal-ligand structures can be found elsewhere⁸⁶.

2.6. Perovskite architecture for solar cells

The term perovskite is used to determine a crystal with structural formula ABX₃, where X = Cl, Br, I, O, with cation A is in the center of cubo-octahedral cage surrounded by 12 neighbor anions B⁸⁸ (fig. 1-34 (a)). Named after Russian mineralogist L.A. Perovskiy it was originally used to describe CaTiO₃ mineral and further to all the crystalline structures of above mentioned stoichiometry and crystal cell. Organic-inorganic lead- and tin-based perovskites CH₃NH₃(Pb, Sn)I₃, schematically presented in fig. 1-34 (b), have received a great interest recently due to their unique electronic properties providing outstanding efficiency for solar energy harvesting^{89,90,91,92}.

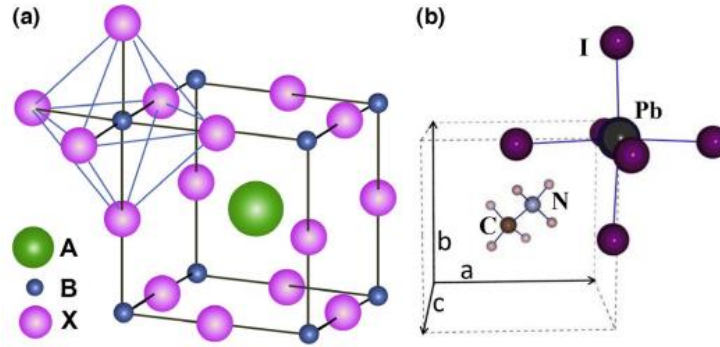


Figure 1- 34 Perovskite ABX_3 unit cell (a), cubic cell of $CH_3NH_3PbI_3$ perovskite⁹³

It was found out that upon the increase of dimensionality, halide perovskites show semiconductor-to-metal transition⁹⁴ and band gap shrinking upon 2D to 3D increase of dimensionality. Narrow band gap is beneficial for solar cells since it allows harvesting a wider spectrum of irradiation. First 3D $CH_3NH_3PbI_3$ perovskites were used as dye-sensitizers in 2009 with efficiency of 3.1%⁹⁵

There are several common structures for perovskite solar cells⁸⁸:

- 1) Dye-sensitized perovskite solar cell
- 2) Meso-superstructure
- 3) Planar p-n junction

For the first type, schematically presented in fig. 1-35 (a,b), the molecule of dye-sensitizer is simply replaced by perovskite (3) to form dots on a surface of porous TiO_2 (2), which is placed on a F-doped SnO_2 transparent glass-electrode (1). In this structure photoinduced electrons are gathered by TiO_2 wide band gap semiconductor (2), while holes are transported by hole-transport-material (HTM) (3) toward the counter electrode usually made of gold (4). Band gap and electron affinity of perovskite dots are aligned in the way that facilitates charge transfer of excited electrons into the conductive band of TiO_2 , and hole injection to HTM, as shown in fig. 1-35 (c). For this type of cells, efficiency up to 10% can be achieved^{96,97,98}.

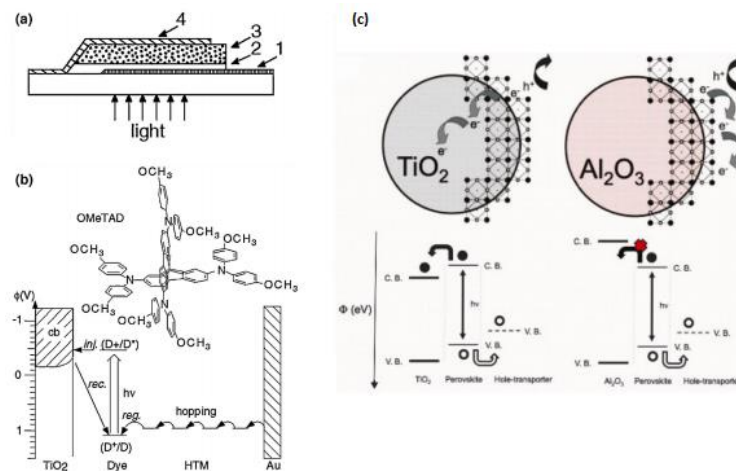


Figure 1-35 Perovskite based dye-sensitized solar cell, (a) device structure (b) sensitizing mechanism (c) charge transfer mechanism. Compilation^{98,93}

Another way to prepare perovskite solar cells is to replace conductive TiO_2 with scaffold of insulating Al_2O_3 , as shown in fig. 1-36(a). In this case, the thin coating of Al_2O_3 granules should be continuous in order to provide charge transfer toward electrodes. As an HTM medium, Spiro-OmeTAD is usually utilized. Electron injection does not occur into Al_2O_3 , which is used for spatial separation of perovskite layers from each other. In this case, the conductivity of perovskite is enough to bring charge carriers towards the electrode⁹⁹. Such media as Spiro-OMeTAD can be effectively adjusted for holes transport by means of variety of dopants¹⁰⁰. For large scale applications, small organic molecules with metallic ligands can substitute for Spiro-OMeTAD^{101,102}. An alternative meso-superstructure concept is to use yttrium-doped TiO_2 porous layer filled with perovskite. The so-called pillared structure is presented in fig. 1-36 (b). In addition, a thin coverage layer of perovskite is formed on top of the mesoporous material to assure effective charge separation in the vicinity of grain boundaries. The alignment of materials band is very important (fig. 1-36 (c)). For this purpose, doping of both transparent oxide and HTM can be performed. Thus, light-excited electrons are favored to drift towards $\text{Y}:\text{TiO}_2$, and, at the same time there is a potential barrier form Spiro-OMeTAD site. It is necessary that separated charges are transferred from each other as quickly as possible in order to reduce recombination losses. Thus HTM should possess high conductivity and adjusted “metal – semiconductor” interface. In this case, an Au electrode is installed to provide rectifying type of junction and higher V_{oc} .

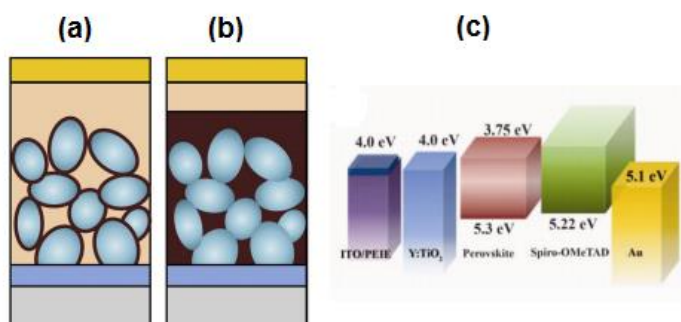


Figure 1-36 Meso-superstructure perovskite solar cell (a) perovskite thin film on scaffold Al_2O_3 , (b) perovskite infiltrated nanocomposite, (c) example of meso-superstructure flat bands alignment^{88,100}

Hole transport within the bulk perovskite makes it possible to fabricate planar heterojunction (fig. 1-37(a)) between TiO_2 and $\text{CH}_3\text{NH}_3\text{PbI}_3$ perovskite as long as their gap and electron affinity energies are aligned as it is shown in fig. 1-37 (b). The depletion zone which appears due to uneven distribution of charge carriers creates a strong electric field driving holes directly to the electrode and attracting electrons to the TiO_2 conductive band. The first cells with this architecture exhibited an efficiency of more than 5 %, which can be increased up to 8% by using a thinner nanoparticle TiO_2 film instead of the 100-nm thick TiO_2 layer^{103,104}.

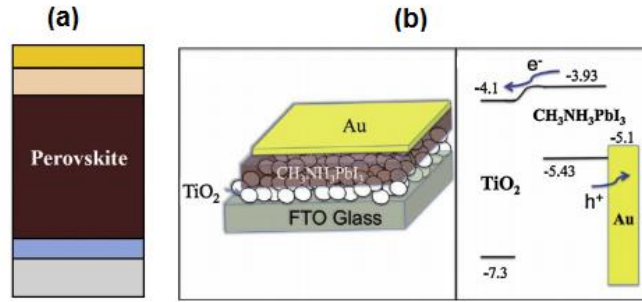


Figure 1-37 Planar p-n junction perovskite device (a) - schematic representation (b) - device sketch and charge transfer mechanism^{109,110}

In summary, due to its high flexibility in terms of absorption spectra, band gap, electron affinity, variety of architectures, and promising conversion efficiency (up to 30% recently¹⁰⁵) perovskite solar cells are one of the most attractive and widely studied materials nowadays in the domain of solar energy harvesting.

3. Chalcogenide materials in the domain of solar cells

3.1. Definition and general properties of chalcogenide materials

Chalcogens are the elements of group 16 in the periodic table, i.e. sulphur (S), selenium (Se) and tellurium (Te). Oxygen (O), which is settled in the same group, is very different by its chemical properties, thus not considered as a chalcogene. Certain authors treat polonium (Po) as a chalcogen element¹⁰⁶ but due to its particular radioactive properties and very limited applications we will not consider it further.

Despite the fact that the term “chalcogen” appeared only in 1930¹⁰⁷, chalcogenides are known for centuries. For instance sulphides were widely used for cosmetics, paintings and medicine in ancient Greece¹⁰⁸. Sulphide minerals such as antimonite (Sb_2Se_3), argentite (Ag_2S), galena (PbS), cinnabar (HgS), Pyrite (FeS_2), würtzite (ZnS) have been known for a long period of time, as along with Se- and Te-based minerals such as katulskite (PdTe), empresite (AgTe) or claustalite (PbSe), würtzit / sphalerite (CdSe)¹⁰⁸. Above mentioned minerals being source of chalcogens are earth abundant and easy to find in the earth’s crust, which makes this materials very attractive economically¹⁰⁹.

Far before the development of well-known chalcogenide glasses (ChGS) by Goirunova and Kolomiets in 1955, a number of experiments involving chalcogenide minerals were made. In 1865 Stefan found out a thermoelectric effect in PbS crystals. Schottky barrier contact (also known as rectifying contact) between metal and PbS semiconductor discovered by F. Braun in 1874 for the development of early-stage radio detectors. More applications for chalcogenide crystals were brought during world war II, when it was investigated for photoresistors that brought a major breakthrough in the domain of infrared sensing¹¹⁰.

Since that time crystalline chalcogenides showed themselves in vast field of applications. Sulphur based compounds are used in photodetectors for infrared sensing, photoconductors in Peltier elements. Selenides are widely used for solar energy, as electric rectifiers, photographic exposure – meters,

xerography and medicine. Tellurides are known for data storage devices, microprocessors manufacturing¹¹¹.

Chalcogens are capable of forming stable usually stoichiometric compounds, with all the groups of elements in the periodic table except noble gasses following classic valence trends, for instance Sb_2Se_3 , SiSe_2 , PbS etc. Most of chalcogenides are characterized by directional covalent bonding. Chalcogens show also a positive oxidation state when bonded with halides, nitrides and oxides, like SCl_2 , which are also considered as chalcogenides.

Particularly interesting in the context of solar cells materials, transition metal chalcogenides (TMC) like ZnCh , CdCh , MoCh_2 , etc., exist in various stoichiometries, which makes them highly tunable in terms of optical and electric properties due to the modification of band gap and energy transfer mechanism. Most conventional stoichiometries 1:1 and 1:2 TMC show highly covalent behavior constitutional of their zinc-blend and würtzit structure¹³²

Widely studied types of crystalline chalcogenides are nanocrystals and quantum dots of IV-VI semiconductors. For instance, due to extremely narrow band gap PbSe and PbS (0,28 – 0,41 eV) provide strong electron-phonon confinement and short lifetime for interband states; the small effective mass of charge carriers provide larger Bohr radius for excitons and allows stronger spontaneous emission^{112,113}. For these purposes, quantum dots are of particular interest since they allow saving all the positive properties of crystalline PbCh with exclusion of negative surface state effects. Due to increased Bohr radii and reduced surface-to-volume ratio, chalcogenide quantum dots have a great operational advantage compared to III-V semiconducting quantum dots in terms of photon confinement and intensity of electronic transition¹¹⁴. Due to low phonon energy, usual for chalcogenides, they demonstrate weak electron-phonon coupling and, thus, their band-gaps weakly depend on temperature^{115,116,117}.

3.2. Crystalline chalcogenides application for solar energy harvesting

In general, we can divide all the semiconductors into two types: direct bandgap and indirect bandgap. Since the gap is the minimal energy difference between the valence band (VB) and conductive band (CB), it is extremely important to match minima and maxima at the same values of momentum. For example, for GaAs (fig. 1-38(a)). This exigence is satisfied for momentum Γ . When the minimum and maximum occur at different momenta, additional energy is needed to transfer the electron from CB to VB, since a momentum transition is also needed, which is the case of c-Si (fig. 1-38(b)). These two cases are known as one-photon and two-photon s absorption. According to the law of total momentum conservation, indirect bandgap semiconductors demand two particles with energies ω and Ω for electron excitation instead of one particle with energy ω for direct band.

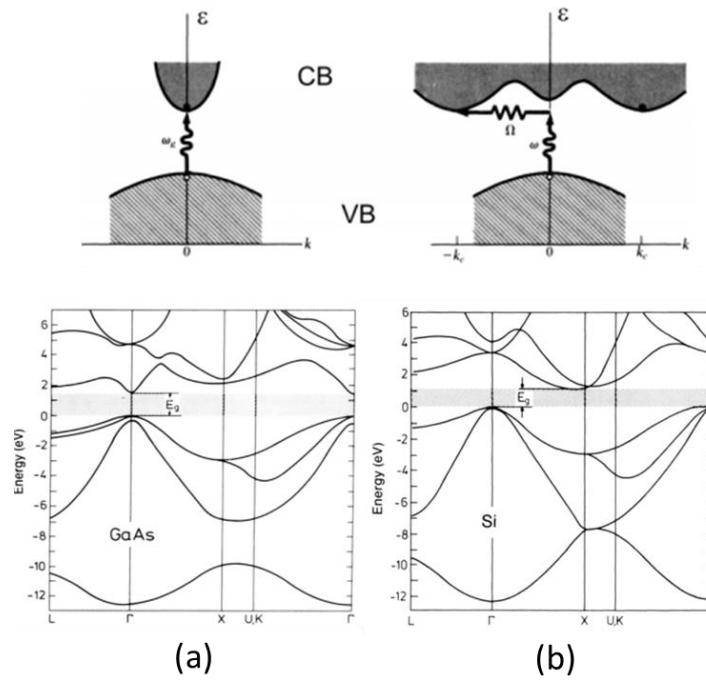


Figure 1-38 Direct (a) and indirect (b) bandgap semiconductors with momentum distribution sketches¹¹⁸

It is clear that indirect bandgap semiconductors are not as efficient for light absorption as direct bandgap, which makes chalcogenides much more suitable for solar energy harvesting compared to silica. c-Si absorber layers should be much thicker for effective absorption and, in consequence, it should provide larger lifetime for generated charge carriers to make them contribute to the light-induced current flow. Thus, for c-Si absorbers the absence of intrinsic defects is crucial and quality demands are much higher. At the same time, most of chalcogenides are direct band semiconductors, which provides them with high absorption coefficient and allows reducing of thickness and, therefore, increases the operation speed of the device. Also, it reduces the requirements for its quality in terms of crystallographic defects.

In addition, chalcogenides are highly tunable due to Se – S substitutions. This is favorable for the design of heterojunctions and multi-junction cells and also for optimizing the dye-sensitizer gap. For example, band gap of $\text{CuIn}_x\text{Ga}_{1-x}(\text{Se},\text{S})$ can be tuned within a wide range of energies from 1.5 eV to 1 eV^{119,120,121}.

In conclusion, chalcogenides are very attractive for the use in solar cells, which motivates a large number of studies in the past decades. Here, we will mention the most important of them.

3.2.1. Binary systems

$\text{A}^{\text{II}}\text{-B}^{\text{VI}}$ semiconductors are of particular interest due to the variety of their electronic and optical properties. They usually crystallize in zinc-blend configuration and show broad distribution of lattice constants and band gap energy, as shown in fig. 1-39. Among them, CdTe is the most suitable for light absorption due to its narrow band gap of 1 eV - 1.5 eV and high absorption coefficient of 10^5 cm^{-1} below 800 nm¹¹¹.

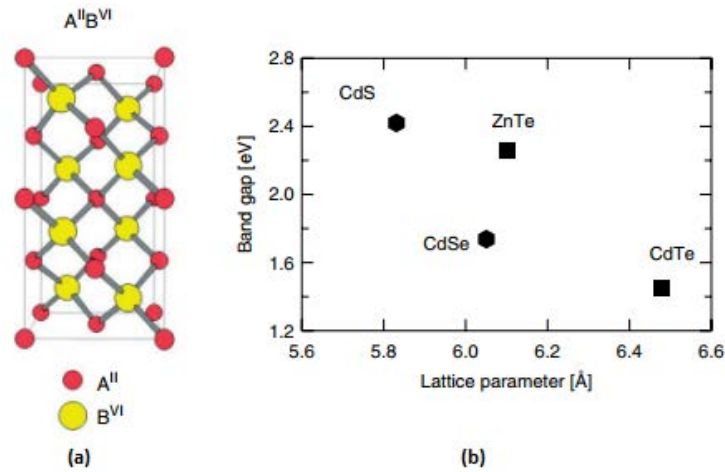


Figure 1-39 Zinc-blend crystalline structure (a), band width and lattice parameter distribution for $A^{II}-B^{VI}$ materials (b)¹²².

Being highly stoichiometric this material demonstrates p-type conductivity and has been used as an absorber layer in combination with n-type CdS, firstly in 1972, showing a 6% conversion efficiency¹²³. It is one of the most efficient single-junction solar cell: usually made as a planar p-n junction of thick p-type absorber CdTe (~10 μ m) and thin layer of n-type CdS (~100 nm) on top of transparent conductive oxide with gold electrodes as a bottom-electrode, as shown in fig. 1-40, it achieves nowadays 21% efficiency¹²⁴.

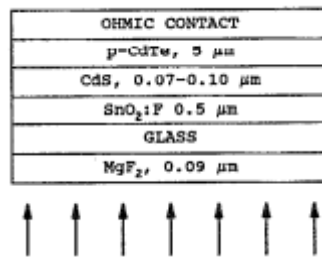


Figure 1-40 Typical planar p-n junction of p-CdTe/n-CdS solar cell¹²⁵

Fabrication of this type of junctions is often connected with high temperature treatment, resulting in atomic diffusion at the interface with creation of $CdSe_xS_{1-x}$ solid solution, which shifts the electrical junction away from metallic contact and improves the electrical characteristics of the device

$A^{II}-B^{VI}$ are also suitable for $A^{III}-B^V$ pairing. For instance, p-InP/n-CdS heterojunction, made in similar way, demonstrated a high efficiency, over 70%, for 550-910 nm light with total solar power conversion of 12.5%, which makes this junction promising for stacked heterojunction devices¹²⁶.

Recently $A^{II}-B^{VI}$ compounds were utilized for colloidal quantum dots preparation¹²⁷. In fig. 1-41, a concept of Se to Sulphur substitution is shown. Due to its higher electronegativity, sulphur contributes to the extension of the band gap, which allows tuning of the gap in wide range of energies, by preparing different layers of quantum dots tuned for specific emission spectra. Aligned band facilitates energy transfer from deeper active layers towards TiO_2 . Being used as dye sensitizers, they provide high efficiency (12 %) for light harvesting, being paired with transparent conductive oxide¹²⁸

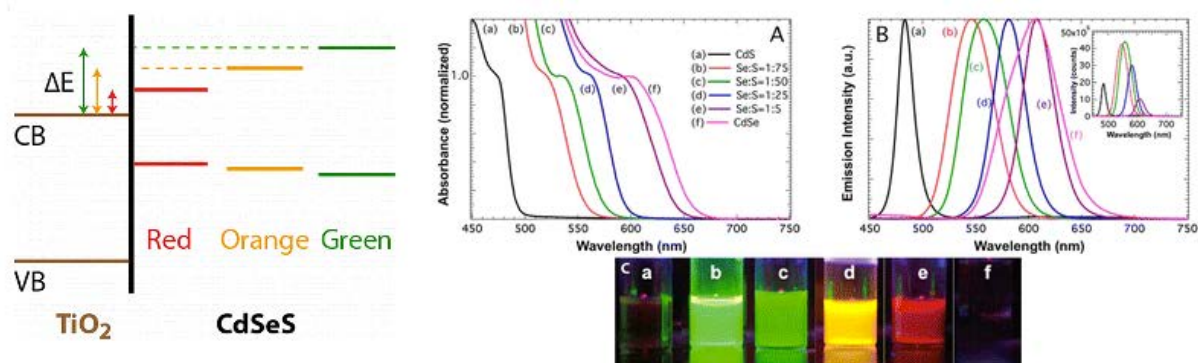


Figure 1-41 CdSe_xS_{1-x} colloidal quantum dots used as dye-sensitizer. Band alignment and absorption spectra with clear trend to blue shift upon Se content increase¹³⁸

The same idea was applied to Pb_xCd_{1-x}S quantum dots, where cation substitution was performed in order to extend the light absorption range (fig. 1-42). This cell achieves efficiency of 2%¹²⁹. However, the combination of both approaches can be interesting for the design of dye-sensitized cells.

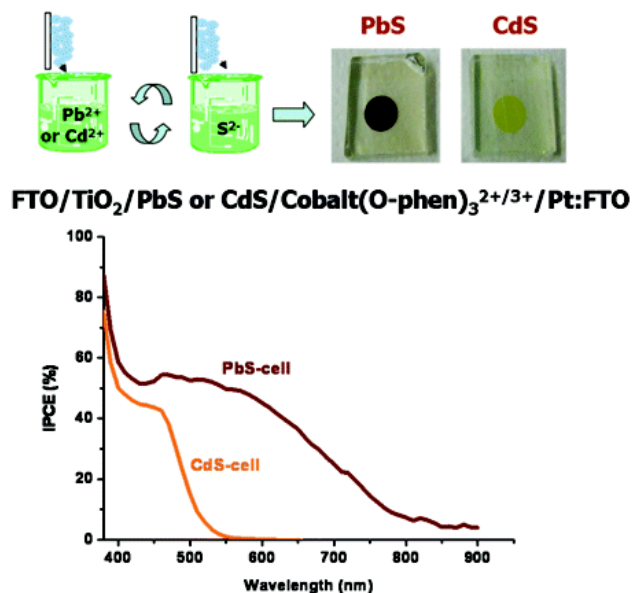


Figure 1-42 PbS and CdS quantum dots for solar cells

Application of binary chalcogenides in solar cells is not limited to A^{II}-B^{VI} materials. Other low band gap metal chalcogenides are also widely studied for both quantum dots with transparent oxide (TiO₂ or ZnO) and planar junctions, in particular PbS^{130,131}, PbSe^{132,133}, Sb₂Se₃¹³⁴, Sb₂S₃^{135,136}.

3.2.2. Ternary systems

Following cation cross-substitution trends^{137,138}, one can substitute one atom of 11 group and one atom of 13 group for two atoms of 12 group, obtaining A^IB^{III}C^{VI}₂ compound. These compounds show enhanced electronic properties suitable for solar energy applications, for instance ZnSe, with E_g=2.82eV, turns to CuGaSe₂ with E_g = 1.68eV upon the cation cross-substitution, which is favorable for efficient light absorption¹³⁹. A^IB^{III}C^{VI}₂ usually crystallizes in chalcopyrite structure, which contains A_nB^{III}_{4-n} tetrahedrons around common C atom (fig. 1-43 (a)).

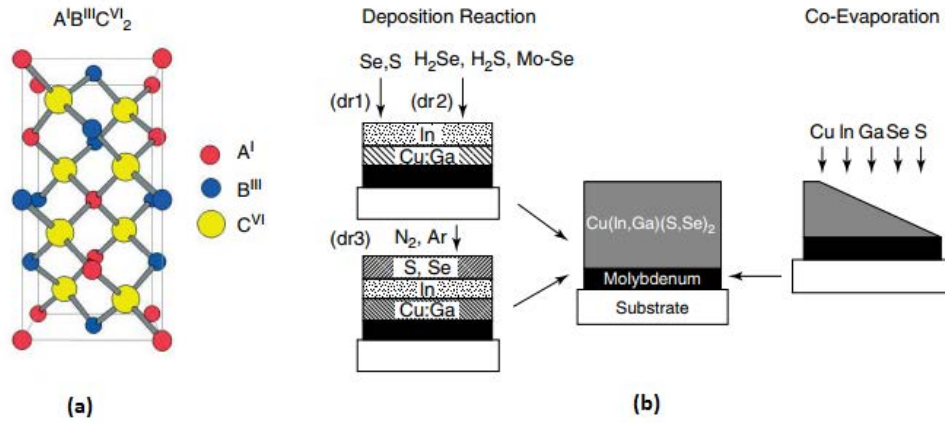


Figure 1-43 Chalcopyrite crystalline structure of $A^I B^III C^{VI}_2$ compounds (a), conventional methods of $A^I B^III C^{VI}_2$ absorbing layers preparation (b)¹³².

Due to p-d repulsion in the valence band, $A^I B^III C^{VI}_2$ shows gap shrinking compare $A^{II} B^{VI}$ crystals. Thus, their tenability in a vicinity of optimal gap energy ($\sim 1.4\text{eV}$) is higher. At the same time it can be tuned in sufficiently wide range of energies from 2.8eV for AgGaS_2 to 1eV for CuGaTe_2 , as shown in fig. 1-44.

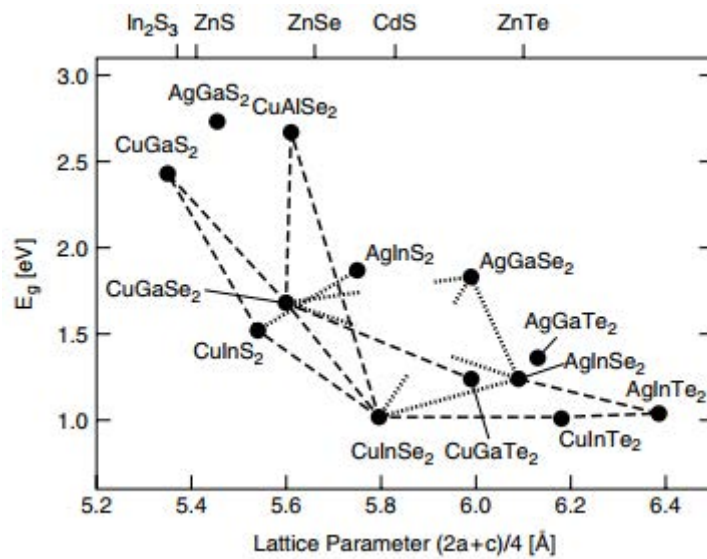


Figure 1- 44 Lattice parameters and gap energy distribution for $A^I B^III C^{VI}_2$ compounds¹³²

Prepared via co-evaporation or deposition reaction (fig. 1-43 (b)), CuInS_2 homojunction firstly reported in the literature¹⁴⁰. In past decades, CuInSe_2 (CIS) and chalcoperite $\text{CuIn}_{1-x}\text{Ga}_x\text{Se}_2$ films were used for the junctions with CdS showing more than 10% efficiency¹⁴¹. The same values were obtained recently for CuInS_2 homojunctions¹⁴².

CIS materials are probably the most widely studied because of their high absorption coefficient and low toxicity. They were also prepared in the form of nanocrystals¹⁴³, colloidal¹⁴⁴, and quantum dots using above described techniques¹⁴⁵. Being a promising and efficient absorber that allows producing μm -thick devices, CIS is still too costly for the market application. This is a common problem for $A^I B^III C^{VI}_2$ compounds since both Ga and In are expensive and rare metals. Thus, further developments of these

materials strongly depend on optimization processes and compromise between efficiency and price of the solar device.

3.2.3. Quaternary systems

The eager to reduce the price of $A^I B^{III} C^{VI}_2$ compounds opened a vast field of studies on cross-substitutions following the octet rule. Analogically with $A^{II}-B^{VI}$ compounds, it is possible to substitute an expensive metal of 13 group by a pair of metals from 12 and 14 group, obtaining $A^I_2-B^{II}-C^{IV}-D^{VI}_4$, or to replace one atom of 11 group and one atom of 13 group by two atoms of 12 group obtaining $A^I-B^{III}-C^{II}_2-D^{VI}_4$ ¹⁴⁶. A wide variety of materials with different stoichiometries was studied in past decades due to outstanding tuning capabilities and reduced cost because of the use of earth-abundant elements.

Upon the cross-substitution, crystalline structure undergoes modification from chalcopyrite to kesterite and from CuAu-like blend to Stannite and PMCA (fig. 1-45 (a)). Chen. et al showed that while valence band states are dominated by antibonding p-d coupling between A^I and C^{VI} atoms, analogically to $A^I B^{III} C^{VI}_2$, conducting band states are affected by the antibonding p-d coupling of B^{III} (C^{IV}) -s state and D^{VI} -s and -p states, which results in additional shrinking of the gap because of conducting band downshift, as it can be seen in fig. 1-45 (b)¹⁵⁶.

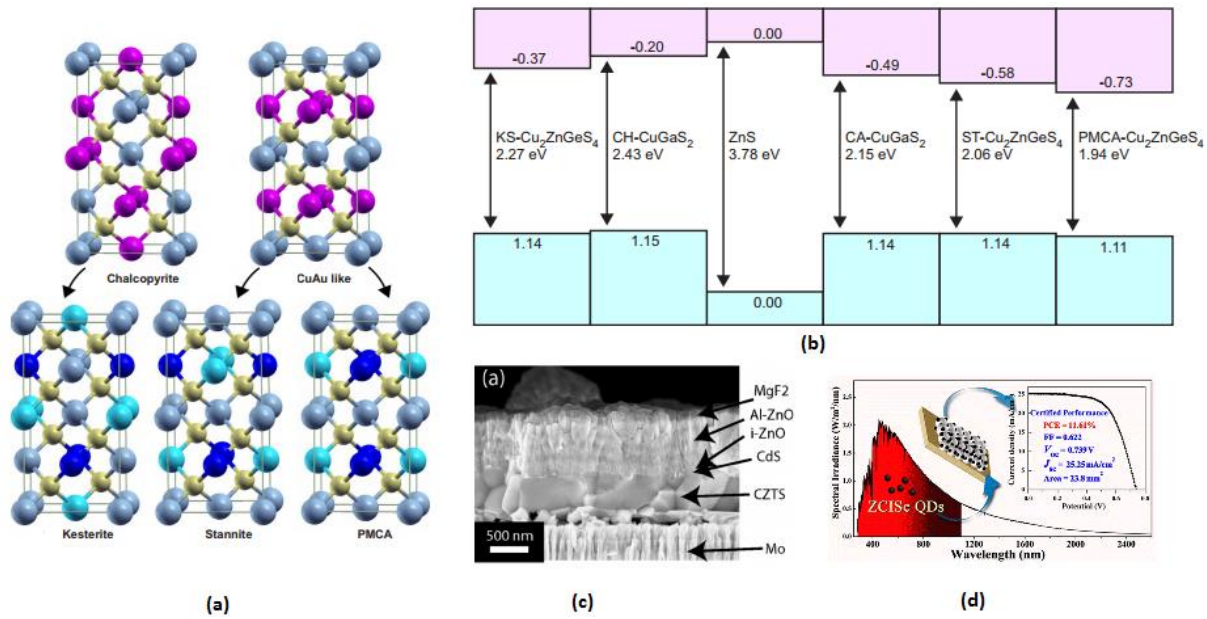


Figure 1- 45 Evolution of crystalline structure upon the cross-substitution of $A^I B^{III} C^{VI}_2$ to $A^I_2-B^{II}-C^{IV}-D^{VI}_4$ or $A^I-B^{III}-C^{II}_2-D^{VI}_4$ (a), band gap tuning (b), SEM image of planar heterojunction with CZTS as an absorber (c), quantum dots sensitizers fabrication based on CZTS (d). Compilation^{156,157,158}.

Being much cheaper than $CuInSe_2$, quaternary compound $Cu_2ZnSn(S,Se)_4$ shows a decent efficiency of 11% for bulk heterojunction, with CdS film as an n-type layer (fig. 1-45 (c))¹⁴⁷. Appropriate band alignment and near optimal gap favors charge generation and transfer towards transparent oxide (usually ZnO), as shown by Wang et al.¹⁴⁸.

$A^I-B^{III}-C^{II}_2-D^{VI}_4$ chalcogenides are used as quantum dots sensitizers. For instance, Zn-Cu-In-Se (fig. 1-45 (d)) showed facile tunability by controlling the Zn/Cu-In ratio, which permits to optimize the absorption spectra in the 860 - 980 nm range. Dye-sensitized cells obtained that way showed an efficiency of 11.61%, which is comparable to $A^I B^{III} C^{VI}_2$ best cells^{149,150}.

We gave a brief review of state-of-the-art in the domain of crystalline chalcogenides for solar cells application. As one can see, this is an enormously vast domain of material science which proposes different approaches for solar cell production from the very primitive planar heterojunctions based on binary compounds to highly sophisticated systems that involve non-conventional defect structures and multi-element compositions with high tenability of the key properties.

3.3. Chalcogenide glass-ceramics for photovoltaic applications

According to the ideas of Zachariasen, who was the first to discuss about atomic arrangement in glass¹⁵¹, the difference between crystalline and glassy structure is the absence of long range order. While for the crystal one can find a structural unit, which can be infinitely translated to represent the bulk material it is not possible for the glass. Beyond the first coordination sphere (first closest neighbors of a given atom) the order is absent in the glass, which makes atomic arrangement random and sometimes makes it possible to consider the whole glass as one molecule (“indefinitely large unit cell with indefinitely large number of atoms” by Zachariasen). Cases of crystalline and glassy structures are sketched in fig. 1-46. It is also worth to mention the effect of introduction of large ions in the glass matrix. As it is probably evident from the sketch it plays a role of chain-breaker and “depolymerize” well interconnected structure of the glass, which in its turn lead to the reduction of glass-transition temperature, because of the increased spatial disorder.

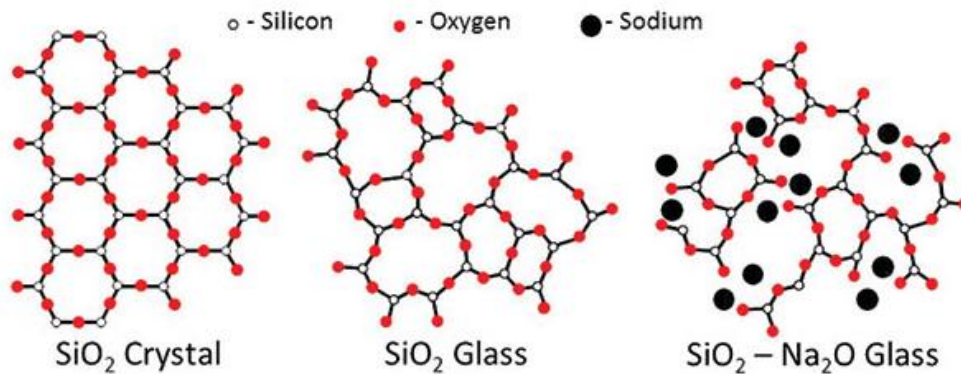


Figure 1- 46 Crystalline SiO_2 and glassy SiO_2 structures, signs of depolymerization are evident upon Na_2O introduction¹⁵²

To determine the case when it is possible to obtain a glass, we should consider several cooling patterns. Fig. 1-47 (a-1) describes a case when cooling of the melt down to melting temperature (T_m), leads to the intensive crystallization. In this case, crystallization heat compensates the external cooling, which results in constant temperature region (3-4) and forming of completely crystallized solid matter. In fig. 1-47 (a-2) a case of metastable state (2-3) is shown: here a crystalline phase here is undercooled below the thermodynamically stable state; after critical undercooling, spontaneous crystallization occurs, rising to the temperature due to crystallization heat (3-4) and, then, complete crystallization occurs (4-5). Fig. 1-47 (a-3) shows cooling without liberation of crystallization heat, leading to the formation of a solid body without crystallized fraction¹⁵³.

To understand why some liquid melts undergo crystallization and some turns to glass, Tammann studied the temperature dependence of nucleation rate and growth velocity. Tammann divided crystallization into two steps: nucleation J (growth of nuclei – crystalline precursors) and growth of crystal v (fig. 1-47 b1-b3). He showed that vitrification is possible if, in the T_g - T_x span (ΔT), no overlapping of these two curves occurs (fig. 1-47 b3). If J and v curves overlap on a wide range of

temperature (fig. 1-47 b1), crystallization will occur^{154,155}. Tammann showed that both of these parameters are connected with viscosity of the cooling melt and postulated that fast increase of viscosity is favorable for glass formation. An example of steep increase of viscosity for glassy selenium can be found in Nemilov et al.¹⁵⁶ and Rawson et al.¹⁵⁷.

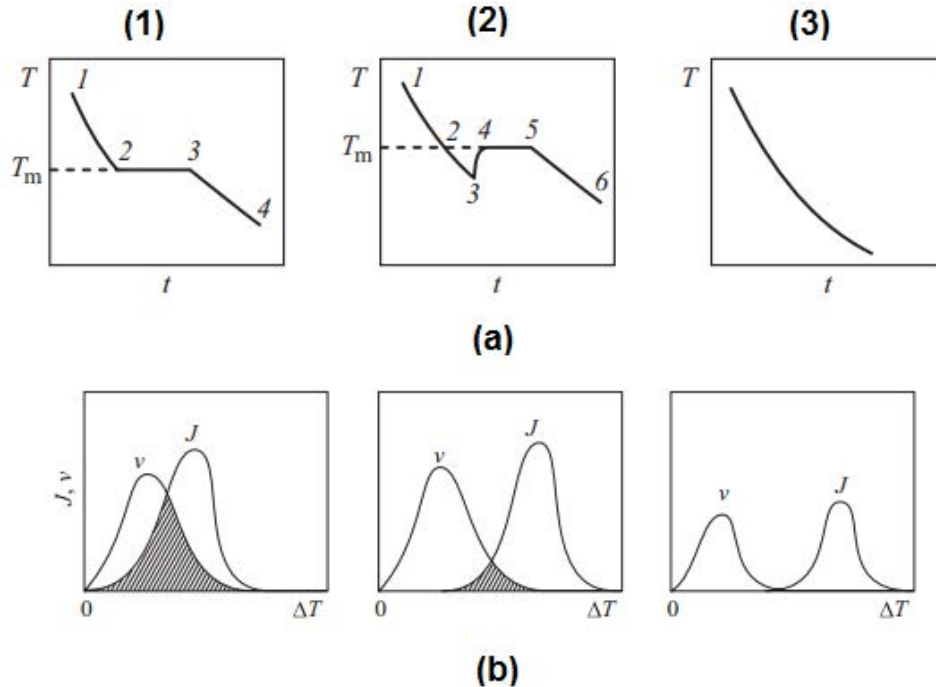


Figure 1-47 Glass-transition upon the cooling; (a-1) immediate crystallization, (a-2) significant crystallization in a certain temperature range (a-3) glass-transition without crystallization, viscosity-to-nucleation rate (b-1) weak glass-forming ability of the melt, (b-2) possible to form a glass, (b-3) strong glass-forming abilities of the melt¹⁶⁴

It makes understandable the absence of periodicity in the glass: quick increase of viscosity upon cooling and lack of energy for nucleation impede atomic regrouping and arrangement, and in consequence “freezes” the melt in the disordered liquid-like state.

3.3.1. Chalcogenide glasses and their application

Discovered by N.A. Goryunova and B.T.Kolomiets in 1956¹⁵⁸ chalcogenide glasses (ChGs) are nowadays represented by a colossal nomenclature of compositions with a variety of applications. Detailed discussion on physical and chemical properties of chalcogenide glass can be found elsewhere^{159,160,161}. Here we would like to underline only the major peculiarities of chalcogenide glasses.

As it was mentioned before glass can be described as a continuous network with random arrangement, isotropic in three dimensions. This description is not particularly correct for chalcogenide glasses, which have layer-like (As_2S_3 , GeS_2 , As_2Se_3 , $GeSe_2$) or chain-like (S, Se) structure. That brings to ChGs a considerable flexibility due to weak Van-der-Waals bonding between layers or chains.

Having a band gap of 1-3 eV, ChGs can be presented as amorphous semiconductor with generally hole-type conductivity. As we said before gap increases in the direction of increased electronegativity and thus larger band gaps are present in sulphide glasses. At the same time, telluride glasses with large amount of Te show decreased gap below 1eV with a pronounced metallic character. Ionic conductivity can be found in Ag-doped ChGs such as Ag-As-S or Ag-Ge-S.

While the influence of disorder on the optical gap width is relatively small, glasses show much higher density of traps with large energy distribution of trapping levels in amorphous solid, sketched in fig. 1-48 (a,b). This results in discrepancy between electrical and optical gap. For instance glassy As_2S_3 (presented in fig. 1- 48 (c)) has an electrical gap of 1.1eV, when the optical gap is equal to 1.9eV¹⁷².

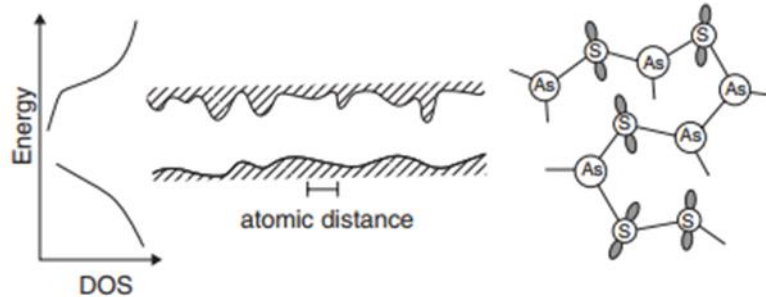


Figure 1-48 Density of states (a), the spatial potential fluctuations (b) and As_2S_3 glass structure (c)¹⁶²

Transmission spectra of different glasses are shown in fig. 1-49 (a). Chalcogenide glasses present a shorter transmission range in the visible region, but they are much more transparent in mid-IR, compared to oxides and fluorides. Absorption in material occurs due to several mechanisms. First is electronic absorption, when photon energy exceeds the material band gap (fig. 1-49(b)). In this case, photons are absorbed by electronic excitation. Usually, electronic absorption occurs in the visible or UV region ($14000\text{-}50000\text{ cm}^{-1}$) and in some cases in the near-IR, which is the case of most chalcogenide glasses. Multiphonon absorption, which limits transparency in long wavelength region, is due to molecular bonding oscillations¹⁶³. The simplest way to understand the nature of this process is to extrapolate dipole moment operator in Taylor series in the deviation of the atoms from their equilibrium positions¹⁶⁴. If one imagines a chemical bond as a harmonic oscillator, then one can quantize energies of its oscillation. The transition from one state to the other is accompanied with absorption or emission of energy (fig. 1-49 (c)). The presence of heavy atoms (Se, Te) in glass matrix of ChGs significantly reduces phonon absorption energies.

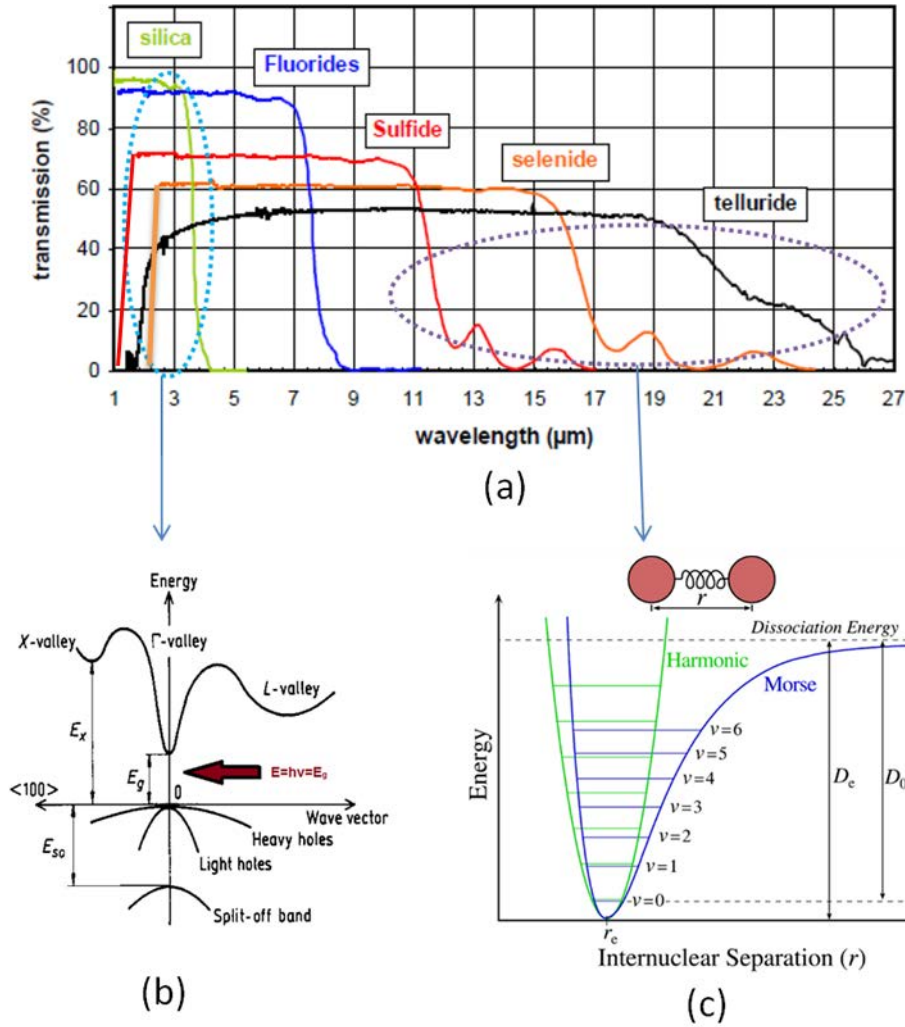


Figure 1-49 Transmission spectra of different glasses (a), absorption is caused by electronic excitation (b) or multiphonon absorption (c)^{165,166}

Low-energy fundamental phonon absorption opens a vast field of applications for ChGs, such as infrared sensing¹⁶⁷, biological sensing¹⁶⁸, fibers operating in mid-IR¹⁶⁹, etc. In the context of this study, it is interesting to pay attention to the domain of Infra-Red cameras made of ChGs.

Before we mentioned that ChGs are possessing wide transparency in mid-IR region, which is of particular interest for the devices operating in third atmospheric window 8-12μm. Most of infrared cameras made for these purposes use crystalline germanium, which is expensive, or ZnSe, which is extremely difficult to produce. Chalcogenide glasses propose cheap and efficient substitution of these costly materials. It is worth nothing that due to higher plasticity ChGs can be used for the molding of complex optics^{170,171}.

However despite some evident advantages, lenses made of glass suffer from poor mechanical properties. Especially, weak resistance to crack propagation and thermal shocks¹⁸¹.

To solve this problem glass compound can be crystallized above T_g. Viscosity is still very high in this span of temperatures, therefore crystallization via rearrangement still is not possible, because the

mobility of ions is low. However nucleation can occur, providing crystallization of the glass. On fig. 1-50 one can see transmission spectra of $5\text{GeS}_2\text{-1Sb}_2\text{S}_3\text{-2CsCl}$ glass annealed for different time at 290°C . We can notice appearance of Rayleigh scattering upon the annealing, increase of time leads to increase of the size of crystals which results in scattering region broadening. However one can notice that while transparency in visible and near-IR regions decreased due to Rayleigh scattering, zone of $8\text{-}12\mu\text{m}$ is not affected for most of ceramics.

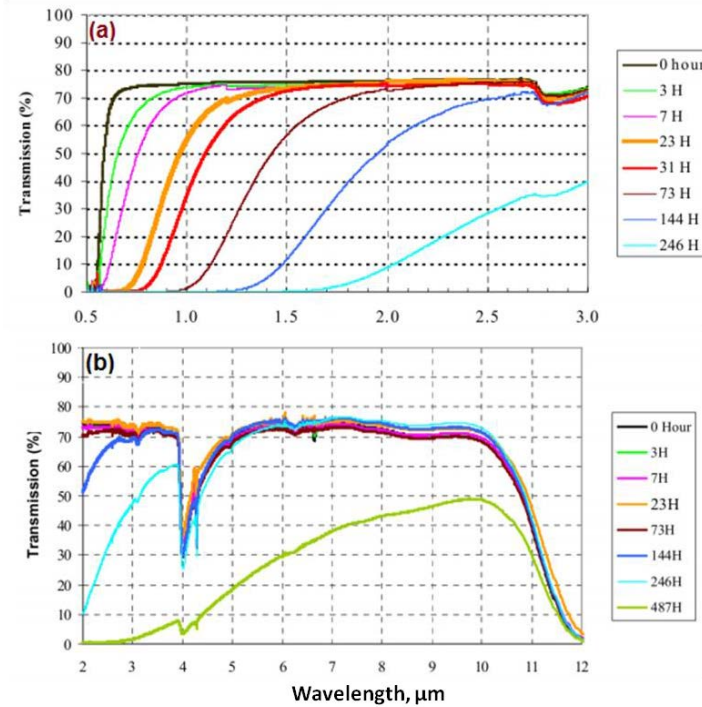


Figure 1- 50 Transmission spectra of different glass-ceramics, obtained by heating of $5\text{GeS}_2\text{-1Sb}_2\text{S}_3\text{-2CsCl}$ glass at 290°C for different time¹⁸¹

The bottom line is that controllable crystallization allows improving mechanical properties of the glass by means of introduction of small crystals in amorphous matter. It leads to the improvement of tenacity and hardness, prevents distribution of cracks^{171,184,185,186,187, 172,173,174,175,176,177}.

Pseudo-ternary system $\text{GeSe}_2\text{-Sb}_2\text{Se}_3\text{-CuI}$, similar to previously surveyed, was originally chosen as one of candidates for infrared imaging. However further investigations showed that its behavior significantly differs from other glass-ceramics in $\text{GeSe}_2\text{-Sb}_2\text{Se}_3$ family.

3.3.2. Photovoltaic effect in glass-ceramics of pseudoternary $\text{GeSe}_2\text{-Sb}_2\text{Se}_3\text{-CuI}$ system

Unlikely to other glass-ceramics of the $\text{GeSe}_2\text{-Sb}_2\text{Se}_3$ family, transmission of $\text{GeSe}_2\text{-Sb}_2\text{Se}_3\text{-CuI}$ shows absorption in the mid-IR and an overall reduction of transmission intensity, attributed to Mie scattering (fig 51). The broad absorption band in the $3\text{-}12\mu\text{m}$ region is associated with free charge carriers absorption¹⁷⁸.

This discover inspired the investigation of photoelectric properties of these glass-ceramics.

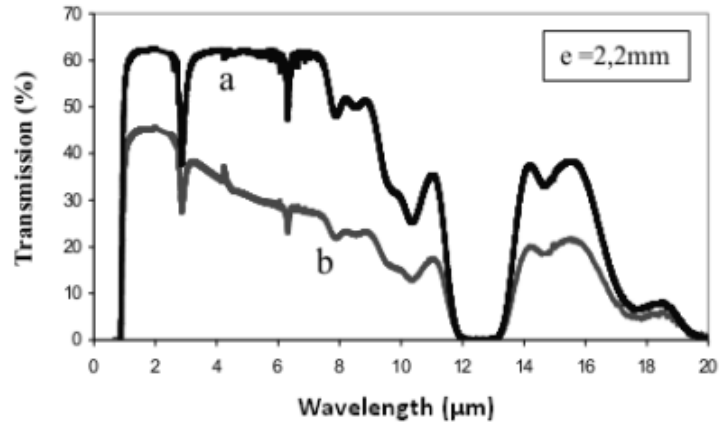


Figure 1-51 Transmission spectra of 60GeSe₂-30Sb₂Se₃-10CuI glass before annealing (a) and after annealing (b)¹⁷⁹

Studied by L. Calvez, glasses of the GeSe₂-Sb₂Se₃ system show large glass forming region and allows the introduction of big amounts of CuI, as shown in the phase diagram in fig. 1-52. First studies were carried out on several random samples from this system. Glasses were prepared by usual melting-quenching process, followed by annealing above T_g.

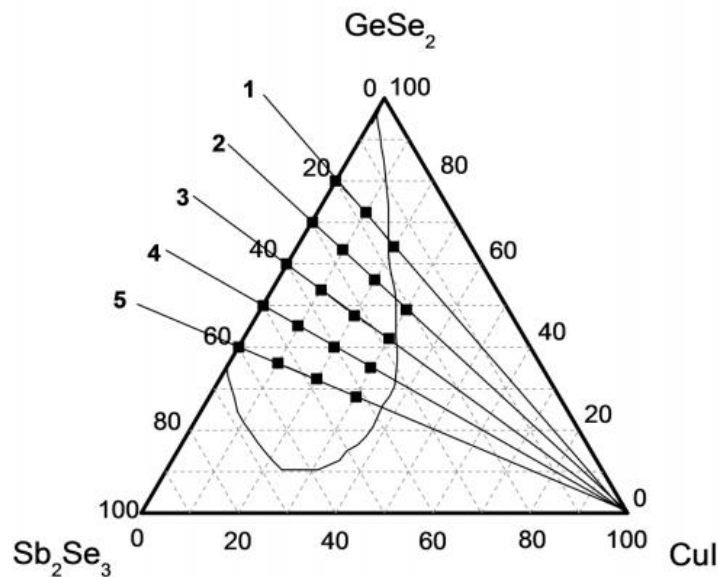


Figure 1-52 Glass-forming region in GeSe₂-Sb₂Se₃-CuI pseudo-ternary system¹⁸⁰

Several annealing processes were implemented. First was annealing under fixed temperature, normally T_g+50 °C (where T_g = [190 – 220 °C]), for different times. Second was the annealing for 1 hour under different temperatures. A careful systematic study showed that the annealing regime strongly influences the process of microstructuring (fig. 1-53(a,b)). Annealing at high temperatures lead to extensively fast growth of crystals and was found as non-efficient, while low-temperature treatment (T_g+50 °C) was more favorable for the growth of proper structure. However, the conductivity of the samples, which should increase with the crystallinity of the samples, is found to saturate after 3 hours of annealing (fig. 1-54). As one can see in fig. 1-53 (a), annealing for 1 hour is not sufficient to obtain significant crystallization with crystalline phases interconnected within the bulk, which results in poor

conductivity (fig. 1-54). However, after longer treatment (>3 hours), the crystalline phase is sufficiently extended to develop connected crystals (fig. 1-53 (b)) providing macroscopic conductivity¹⁸¹.

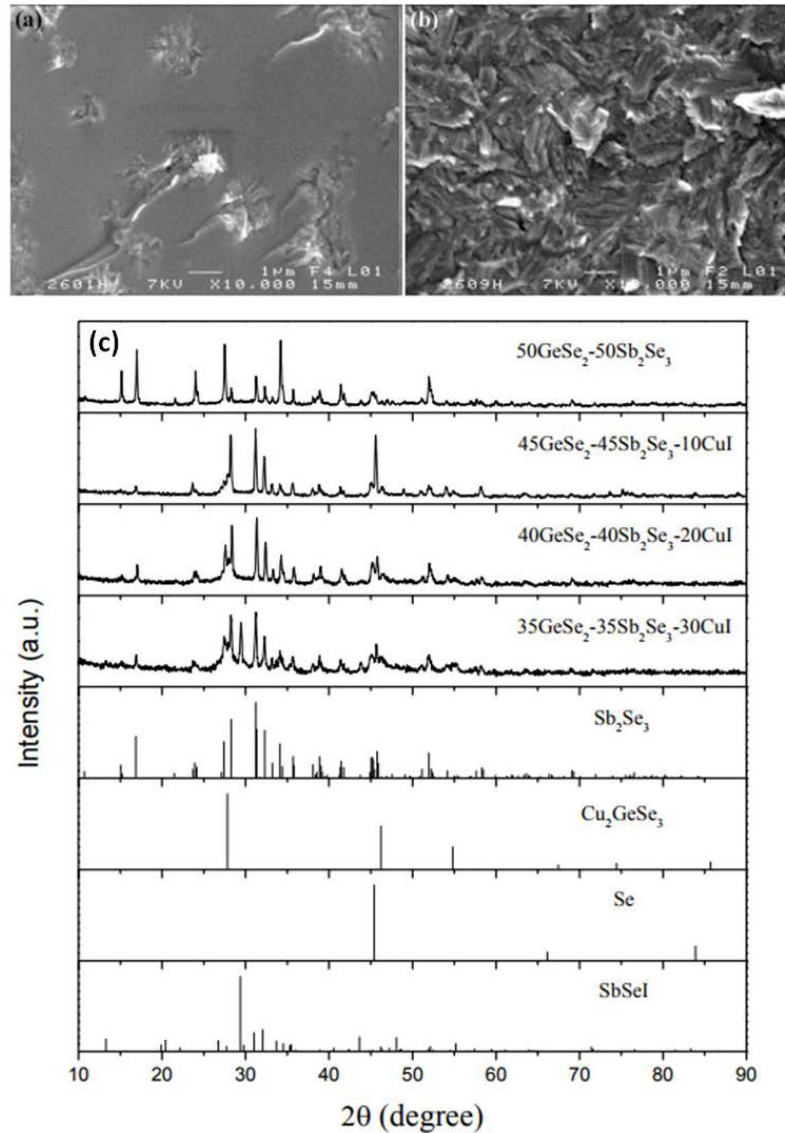


Figure 1-53 SEM images of 40GeSe₂-40Sb₂Se₃-20CuI glass-ceramics annealed for 1 hour at T_g+50 °C (a), 9 hours (b), X-ray diffraction patterns of obtained glass-ceramics (c)¹⁹⁴

Examination of the X-ray diffraction patterns indicates that the crystalline phases found within the bulk glass-ceramics were Cu₂GeSe₃ and Sb₂Se₃ with some signs of SbSeI phase appearance for CuI rich samples (fig. 1-53 (c)).

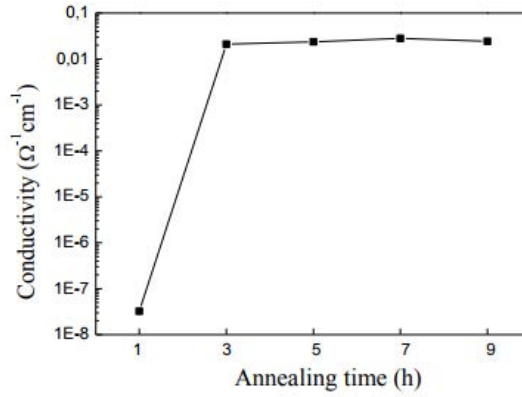


Figure 1-54 Dependence of conductivity of 40GeSe₂-40Sb₂Se₃-20CuI glass-ceramics on the annealing time¹⁹⁴

Examination of the microstructure of 40GeSe₂-40Sb₂Se₃-20CuI glass-ceramics showed that domains of intimately intermixed n-type Sb₂Se₃ and p-type Cu₂GeSe₃ exist inside the bulk. In fig. 1-55 a High Resolution Tunnel Electron Microscope image (HRTEM) is presented. In fig. 1-55 (a) needle-like Sb₂Se₃ can be seen (brighter regions), with Cu₂GeSe₃ crystals (darker regions). Closer investigation showed tight intermixing of these phase. In fig. 1-55 (b) one can see Sb₂Se₃ rod (1 2 0) covered by Cu₂GeSe₃ phase of two different orientations, namely (0 2 0), with lattice constant d = 0.1973 nm and (0 1 1) with d = 0.3203 nm

It became evident that Sb₂Se₃ rods connected within the bulk play a role of macroscopic continuous substrate for highly conductive Cu₂GeSe₃ crystals, which give rise to the conductivity when Sb₂Se₃ is sufficiently crystallized.

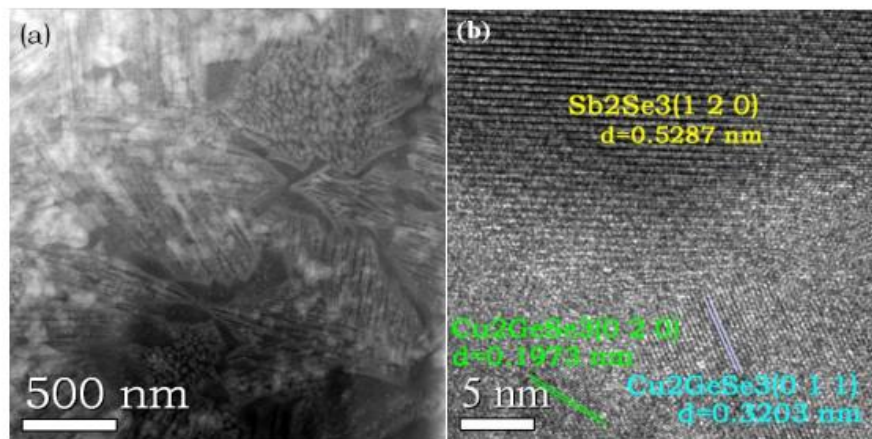


Figure 1-55 HRTEM of 40GeSe₂-40Sb₂Se₃-20CuI glass-ceramics

Elemental mapping depicted in fig. 1-56 shows close, but still separate, co-existence of Cu-rich and Sb-rich zones signifying no important diffusion of matter from one phase to another at the p-n junction interface. It is interesting to mention that iodine co-exists with Sb₂Se₃ phase rather than with Cu₂GeSe₃, which is clear from spatial overlapping of Sb- and I- rich zones

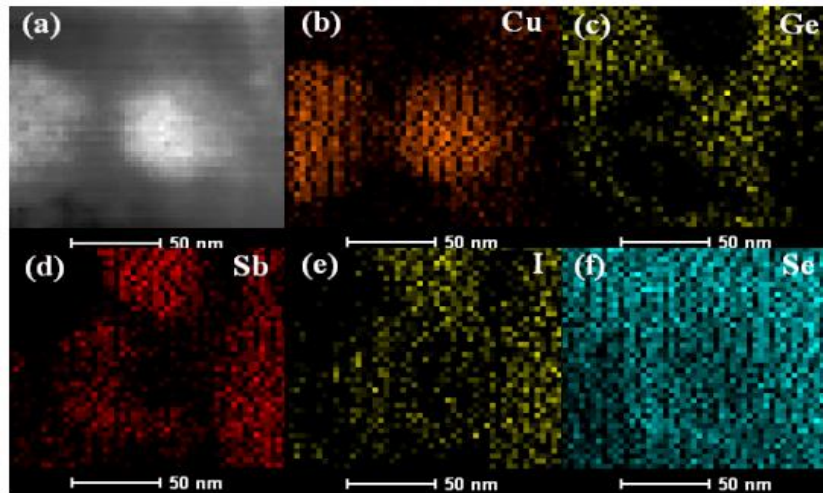


Figure 1-56 TEM image (a), elemental mapping of $40\text{GeSe}_2\text{-}40\text{Sb}_2\text{Se}_3\text{-}20\text{CuI}$ glass-ceramics(b-f)

Photoelectrochemical experiment (PEC) showed that $40\text{GeSe}_2\text{-}40\text{Sb}_2\text{Se}_3\text{-}20\text{CuI}$ possess both p- and n-type photo conducting crystals (fig. 1-57 (a)). If one compares the photoelectric response of glass-ceramics with the one of pure crystals¹⁸², it becomes evident that appearance of bulk p-n junctions promotes photo-charge generation and, which is probably more important, its separation and transfer towards electrodes. It is interesting to mention that $40\text{GeSe}_2\text{-}40\text{Sb}_2\text{Se}_3\text{-}20\text{CuI}$ glass-ceramics shows intense photocurrent under both positive and negative bias, which signifies co-existence of p – and n – type phases. On the other hand, $35\text{GeSe}_2\text{-}35\text{Sb}_2\text{Se}_3\text{-}30\text{CuI}$ glass-ceramics demonstrates intense photocurrent only under negative bias (Fig. 1- 57b), which corresponds to p-type semiconductor behavior. This effect can be due to an excessive amount of copper, which promotes the growth of p- Cu_2GeSe_3 phase with unfavorable conditions for Sb_2Se_3 growth.

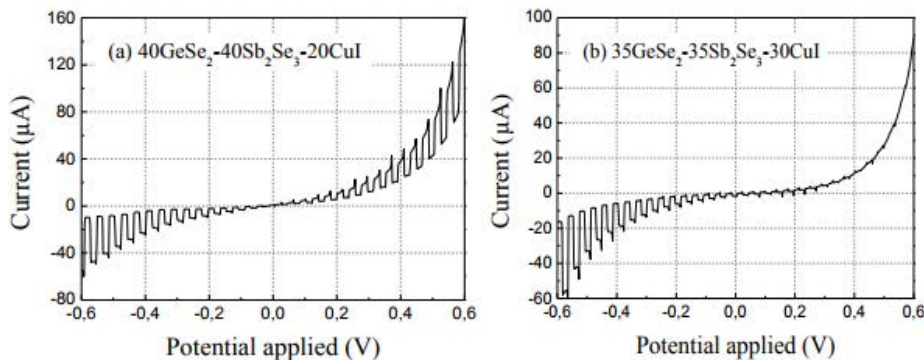


Figure 1-57 Photo-electric response of $\text{GeSe}_2\text{-Sb}_2\text{Se}_3\text{-CuI}$ glass ceramics obtained via controllable crystallization

The results on the microstructure of $\text{GeSe}_2\text{-Sb}_2\text{Se}_3\text{-CuI}$ glass-ceramics are illustrated in fig. 1-58. Upon annealing above T_g , microcrystalline domains appear. In addition, when the annealing time is sufficient, t interconnected rods of n- Sb_2Se_3 are obtained, and electrical conductivity rises. Sb_2Se_3 is not conductive by itself: the conductivity is provided by microcrystals of highly conductive p- Cu_2GeSe_3 , which covers n- Sb_2Se_3 rods. Spatial co-existence was proven by SEM images and elemental mapping. From HRTEM, we can conclude that very intimate intermixing of these two phases occur inside the bulk, without however significant atomic diffusion from one phase to another.

Thus, upon illumination, the thick layer of Sb_2Se_3 absorbs the light with electron-hole pair generation; holes are transferred to the Cu_2GeSe_3 phase through the p-n junction, where they become major charge carriers and contribute to the circuit current.

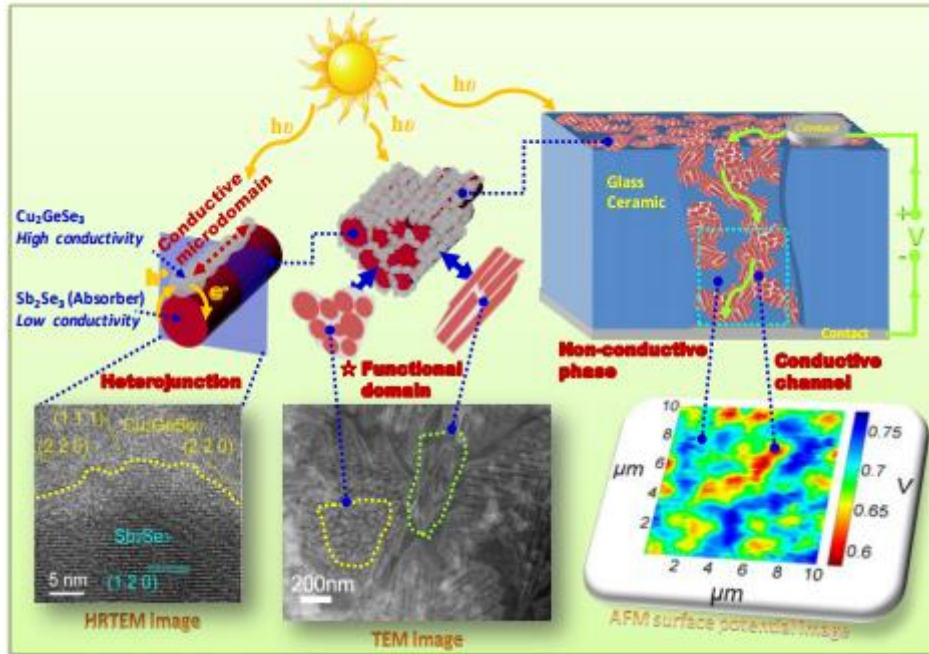


Figure 1-58 Percolating network of interconnected microscopic bulk p-n junctions, sketch

4. Conclusion

We gave a brief review of the state-of-the art in the domain of solar energy conversion, and particularly on up-to-date photovoltaics. Chalcogenides are one of the mostly studied materials for solar cells application mostly due to their suitable electronic and optical properties. However most of efficient solar cells contain rare and costly elements such as In or Ga, or elements that are relatively difficult to prepare.

Chalcogenide glass-ceramics of the $\text{GeSe}_2 - \text{Sb}_2\text{Se}_3 - \text{CuI}$ system possess the potential to become competitive, mostly because of its simple preparation. In $40\text{GeSe}_2 - 40\text{Sb}_2\text{Se}_3 - 20\text{CuI}$, the overall content of Ge is only 10% and it is the only costly element in this composition. Preparation of targets for magnetron sputtering is simple and relatively cheap also. Magnetron sputtering allows obtaining amorphous films of this composition; in addition, a simple and low temperature treatment permits to obtain bulk heterojunctions of $n\text{-Sb}_2\text{Se}_3/p\text{-Cu}_2\text{GeSe}_3$ inside a thin-film. Since glass-ceramics are highly-inhomogeneous materials, demand for crystalline purity is much less strict than those for CIS materials. Simplicity and low cost of the technique could allow using this technique in large scale fabrication.

Promising results for $40\text{GeSe}_2 - 40\text{Sb}_2\text{Se}_3 - 20\text{CuI}$ glass-ceramics inspired us to continue examination of this material in order to better understand its structure and properties on one hand, and to improve its performance by various modification of precursor composition on the other hand.

5. References

- ¹Energy Units, Retrieved from: <http://www.aps.org/policy/reports/popa-reports/energy/units.cfm>.
- ² Woledge, G., *History of the British Thermal Units*. Nature, 1942, **149** (149): p.613.
- ³Unit converter, International Energy Agency, Retrieved from : <http://www.iea.org/statistics/resources/unitconverter>.
- ⁴*Statistical Review of World Energy*, British Petroleum, 2016, Retrieved from : <http://www.bp.com/en/global/corporate/energy-economics/statistical-review-of-world-energy.html>.
- ⁵ *MAP: How much energy is the world using?*, BURN Energy Journal, 2010, Retrieved from : <http://burnanenergyjournal.com/how-much-energy-are-we-using>.
- ⁶ Jorgen Randers, *2052: A Global Forecast for the Next Forty Years*, Chelsea Green Publishing, 2012.
- ⁷ *Each Country's Share of CO2 Emissions*, Union of Concerned Scientists, 2014, Retrieved from : http://www.ucsusa.org/global_warming/science_and_impacts/science/each-countrys-share-of-co2.html#.WPdWAGnyiUk.
- ⁸ H. Damon Matthews et al., *National contributions to observed global warming*. Environ.Res.Lett, 2014, **9**, pp.1-9.
- ⁹ Frauke Urban, Tom Mitchell, *Climate change, disasters and electricity generation*. 2011. Archived September 20, 2012, at Wayback Machine. London: Overseas Development Institute and Institute of Development Studies, Retrieved from : <https://www.odi.org/sites/odi.org.uk/files/odi-assets/publications-opinion-files/7151.pdf>.
- ¹⁰ Worldwatch Institute, *Use and Capacity of Global Hydropower Increases*. 2012, Retrieved from: <http://www.worldwatch.org/use-and-capacity-global-hydropower-increases>.
- ¹¹ Robbins, Paul, *Hydropower. Encyclopedia of Environment and Society*. SAGE publications, 2007. 3.
- ¹² *WCD Findal Report*, World Commission of Dams, 2000, Retrieved from: <http://www.rivernet.org/general/wcd/welcome.htm>.
- ¹³ Moomaw, W., P. Burgherr, G. Heath, M. Lenzen, J. Nyboer, A. Verbruggen, In IPCC: *Special Report on Renewable Energy Sources and Climate Change Mitigation*. Annex II: Methodology, 2010, p.10.
- ¹⁴ Bargagli1, R.; Cateni, D.; Nelli, L.; Olmastroni, S.; Zagarese, B., *Environmental Impact of Trace Element Emissions from Geothermal Power Plants*. Environmental Contamination Toxicology, New York, 1997, **33** (2): pp. 172–181.
- ¹⁵ Wang, Feng, *Thermodynamic analysis of high-temperature helium heated fuel reforming for hydrogen production*. International Journal of Energy Research, 2015, **39** (3): pp.418–432.
- ¹⁶ Jones, J.C. *Energy-return-on-energy-invested for hydrogen fuel from the steam reforming of natural gas*. Fuel., 2015, **143**: p.631.
- ¹⁷ Altork, L.N. & Busby, J. R., *Hydrogen fuel cells: part of the solution*. Technology & Engineering Teacher, 2012, **70**(2): pp.22-27.
- ¹⁸ Eartha Jane Melzer, *Proposed biomass plant: Better than coal?*. The Michigan Messenger, 2010.
- ¹⁹ Zhang, J.; Smith, K. R., *Household Air Pollution from Coal and Biomass Fuels in China: Measurements, Health Impacts, and Interventions*. Environmental Health Perspectives, 2010, **115** (6): pp.848–855.
- ²⁰ IPCC Working Group III – *Mitigation of Climate Change*, Annex III: *Technology – specific cost and performance parameters*, IPCC, 2014. p. 10.
- ²¹ Hilsum, Lindsey, *Chinese pay toxic price for a green world*. London: The Sunday Times, 6 December 2009.

- ²² Par Fang Lin Luo, Hong Ye, *Advanced DC/AC Inverters: Applications in Renewable Energy*. CRC Press, 2013, p.284
- ²³ *Total Primary Energy Consumption*. Energy Information Administration, 2013 Retrieved from: <https://www.eia.gov/beta/international/data>.
- ²⁴ *Energy and the challenge of sustainability*. United Nations Development Program and World Energy Council, 2000.
- ²⁵ *France Electricity – consumption 2014*, Index Mundi, 2017, Retrieved from: http://www.indexmundi.com/france/electricity_consumption.html.
- ²⁶ Biello, David, *Sunny Outlook: Can Sunshine Provide All U.S. Electricity?*, 2008, Scientificamerican.com.
- ²⁷ *Kramer Junction (California) : La plus grande centrale Solaire Thermique du monde*, 2009, Retrieved from: <http://www.eco-conscient.com/art-53-centrale-solaire-thermique-de-kramer-junction-californie.html>.
- ²⁸ Boerema, Nicholas; Morrison, Graham; Taylor, Robert; Rosengarten, Gary, *High temperature solar thermal central-receiver billboard design*, Solar Energy, 2013, **97**: pp.356–368.
- ²⁹ Werner Luft, *High temperature storage - Solar thermal application*, U.S. Department of Energy, 1984, Retrieved from: <https://www.nrel.gov/docs/legosti/old/2294.pdf>.
- ³⁰ Xue Han, Chao Xu, Xing Ju, Xiaoze Du, Yongping Yang, *Energy analysis of a hybrid solar concentrating photovoltaic/concentrating solar power (CPV/CSP) system*. Science Bulletin, 2015, **60**(4): pp.460-469.
- ³¹ Public Photo, Retrieved from : https://en.wikipedia.org/wiki/Crescent_Dunes_Solar_Energy_Project#/media/File:Crescent_Dunes_Solar_December_2014.JPG
- ³² Apte, J. et al., *Future Advanced Windows for Zero-Energy Homes*. American Society of Heating, Refrigerating and Air-Conditioning Engineers, 2008.
- ³³ Murti Nugroho, Agung, Mohd Hamdan bin Ahmad, Makmal Sain Bangunan, *Possibility to Use Solar Induced Ventilation Strategies in Tropical Conditions by Computational Fluid Dynamic Simulation*, 6th Sustainable Environmental Architecture, at Institut Teknologi Bandung, Bandung, Indonesia, September, 2005
- ³⁴ Jeff Vail, *A Theory of Power*. New-York, ed. iUnivers, 2004 (ISBN 0-595-33030-4).
- ³⁵ Carlson, D., Wronski, C., *Topics in Applied Physics: Amorphous Semiconductors: Amorphous silicon solar cells*. Amorphous Silicon Solar Cells, TAP, volume **36**, pp. 287-329.
- ³⁶ D. M. Chapin-C. S, Fuller-G. L. Pearson, *Journal of Applied Physics—A New Silicon p–n Junction Photocell for Converting Solar Radiation into Electrical Power*. Journal of Applied Physics, 1954, **25**(5), p. 676.
- ³⁷ Bazilian, M., Onyeji, I., Liebreich, M., MacGill, I., Chase, J., Shah, J., Gielen, D., Arent, D., Landfear, D., Zhengrong, S., Re-considering the economics of photovoltaic power. Renewable Energy, 2013, 53: pp. 329–338.
- ³⁸ Nancy M. Haegel, Terawatt-scale photovoltaics: Trajectories and challenges. Science, 2017, 356 (6334): pp.141–143.
- ³⁹ *The World's Fastest Charging Station*. 2017, Retrieved from: <https://www.tesla.com/supercharger>
- ⁴⁰ *Calculation*. Based on Photovoltaic Geographical Information System (PVGIS), Geographical Assessment of Solar Resource and Performance of Photovoltaic Technology: <http://re.jrc.ec.europa.eu/pvgis>.
- ⁴¹ *Solar Electric Systems*. Ministry of Agriculture, Food and Rural Affairs, 2016, Retrieved from: http://www.omafr.gov.on.ca/english/engineer/facts/sol_elec.htm.
- ⁴² Michael Dale, Sally M. Benson, *Energy Balance of the Global Photovoltaic (PV) Industry - Is the PV Industry a Net Electricity Producer?*. Environ. Sci. Technol., 2013, **47** (7): pp.3482–3489.

- ⁴³ T. Mishima, M. Taguchi, H. Sakata, E. Maruyama, *Development status of highefficiency HIT solar cells*. Solar Energy Materials and Solar Cells, 2011, **95**: pp.18-21.
- ⁴⁴ Tom Markvart, Luis Castaner, *Principles of Solar Cell Operation*. Solar Cells, Materials, Manufacture and Operation, 2013, pp. 3-25.
- ⁴⁵ G.Cook, L.Billman, R.Adcock, *Photovoltaic fundamentals*. U.S. Department of Energy, 1995
- ⁴⁶ A. Lysenko, L.Mironenko, *Kratkaya Teoriya p-n perehoda*, MGU Moskva, 2002, Retrieved from: http://window.edu.ru/resource/861/55861/files/krat_teor_pn.pdf
- ⁴⁷ R. Kopecek, et al., *Large Area Screen Printed N-Type Silicon Solar Cells with Rear Aluminium Emitter: Efficiencies Exceeding 16%*. Photovoltaic Energy Conversion, Conference Record of the 2006 IEEE 4th World Conference on, 2006.
- ⁴⁸ J. E. Cotter, J. H. Guo, P. J. Cousins, M. D. Abbott, F. W. Chen, and K. C. Fisher, *P-Type Versus n-Type Silicon Wafers: Prospects for High-Efficiency Commercial Silicon Solar Cells*. IEEE TRANSACTIONS ON ELECTRON DEVICES, 2006, **53**(8), pp.1893-1901.
- ⁴⁹ D.E. Carlson, *Amorphous silicon solar cells*. IEEE Transactions on Electron Devices, 1977, **24**(4), pp. 449 – 453.
- ⁵⁰ D. E. Carlson, *Compensated amorphous silicon solar cell*. U.S. Patent 4 217 148, 1980.
- ⁵¹ D. E. Carlson and C. R. Wronski, *Amorphous silicon solar cell*. Appl. Phys. Lett. 1976, **28**: pp.671-673.
- ⁵² D.E. Carlson, *Amorphous-silicon solar cells*. IEEE Transactions on Electron Devices, 1989, **36**(12): pp. 2775 - 2780
- ⁵³ A. Catalano et al., *High performance, graded bandgap a-Si: H solar cells*. In Proc. 19th IEEE Photovoltaic Specialists Conf., 1987, pp.1506- 1507.
- ⁵⁴ K. Yang et al., *High efficiency multi-junction solar cells using amorphous silicon and amorphous silicon-germanium alloys*. In Proc. 20th IEEE Photovoltaic Specialists Conf, 1988, pp. 241-246.
- ⁵⁵ C. R. Wronski, D. E. Carlson, and R. E. Daniel, *Schottky-barrier characteristics of metal–amorphous-silicon diodes*. Appl. Phys. Lett., 1976, **29**: p. 602.
- ⁵⁶ K.NG. Kwok, *Complete guide to semiconductor devices*. SE, John Wiley and sons Inc, New York, 2002.
- ⁵⁷ Jasprit Singh, *Semiconductor Devices: Basic Principles*. WILEY, 2000, Chapter 7.
- ⁵⁸ V.G. Shinkarenko, *Materialy Lektsyi za 2010-2011 god*. pp. 90-111, Retrieved from: https://mipt.ru/drec/forstudents/study/studyMaterials/2kurs/eldev/f_50otza.pdf.
- ⁵⁹ P.E. Trojan, *Tverdotelnaya electronica*. Tomsk, 2006
- ⁶⁰ V.I.Gamana, *Fizika poluprovodnikovyh priborov*. Tomsk NTL, 2000
- ⁶¹ W. Fuhs, K. Niemann and J. Stuke, AIP Conf. Proc., *Heterojunctions of Amorphous Silicon and Silicon Single Crystals*. 1974, **20**: p.345
- ⁶² M. Taguchi, M. Tanaka, T. Matsuyama, T. Matsuoka, S. Tsuda, S. Nakano, Y. Kishi and Y. Kuwano, Tech. Digest 5th International Photovoltaic Science and Engineering Conference, Kyoto, Japan, 1990, p. 689.
- ⁶³ M. Tanaka, M. Taguchi, T. Matsuyama, T. Sawada, S. Tsuda, S. Nakano, H. Hanafusa and Y. Kuwano, *Development of new a-Si/c-Si heterojunction solar cells: ACJ-HIT (artificially constructed junction-heterojunction with intrinsic thin-layer)*. Jpn. J. Appl. Phys., 1992, **31**: p.3518
- ⁶⁴ T. Kinoshita, D. Fujishima, A. Yano, A. Ogane, S. Tohoda, K. Matsuyama, Y. Nakamura, N. Tokuoka, H. Kanno, H. Sakata, M. Taguchi and E. Maruyama, Proc. 26th European Photovoltaic Solar Energy Conference and Exhibition, Hamburg, Germany, 2011. p. 871.
- ⁶⁵ Stefaan De Wolf, et al., *High-efficiency Silicon Heterojunction Solar Cells: A Review*, Green, 2012, **2**: pp.7–24

- ⁶⁶ M. Boccard, et al., *Silicon-based heterojunction solar cells*, The Photovoltaics-Laboratory (PV-Lab) of IMT, Retrieved from : https://pvlab.epfl.ch/heterojunction_solar_cells.
- ⁶⁷ Corsin Battaglia, Silvia Martin De Nicolas, Stefaan De Wolf, Xingtian Yin, Maxwell Zheng, Christophe Ballif, and Ali Javey, *Silicon heterojunction solar cell with passivated hole selective moox contact*. Applied Physics Letters, 2014, **104**(11): p.113902
- ⁶⁸ Jens Meyer, Sami Hamwi, Michael Kröger, Wolfgang Kowalsky, Thomas Riedl, and Antoine Kahn, *Transition metal oxides for organic electronics: energetics, device physics and applications*. Advanced Materials, 2012, **24**(40): pp.5408–5427.
- ⁶⁹ Tadatsugu Minami, Yuki Nishi, and Toshihiro Miyata, *Heterojunction solar cell with 6% efficiency based on an n-type aluminum–gallium–oxide thin film and p-type sodium-doped Cu₂O sheet*. Applied Physics Express, 2015, **8**, 022301
- ⁷⁰ Wen S. Chen, Reid A. Mickelsen, *Thin film CdS /CuInSe₂ heterojunction solar cell*. SPIE, **248**, Role of Electro-Optics in Photovoltaic Energy Conversion, 1980, pp.62-69
- ⁷¹ Mikio Taguchi, et al., *24.7% Record Efficiency HIT Solar Cell on Thin Silicon Wafer* . IEEE JOURNAL OF PHOTOVOLTAICS, 2014, **4**(1): p.96
- ⁷² G. Prasad, O. Srivastava, *The high-efficiency (17.1%) wse₂ photo-electrochemical solar cell*. J Phys D: Appl Phys, 1988, **21**(6): p.1028
- ⁷³ P. Pérez-Higueras and E.F. Fernández (eds.), *High Concentrator Photovoltaics, Green Energy and Technology*, Springer International Publishing Switzerland 2015, pp.9-37
- ⁷⁴ Nikolay A. Kalyuzhnyy, *Multi-Junction Solar Cells, FTI IOFFE*, Retrieved from: <http://xen.ife.no/nordicpv/workshops/presentations-narvik/Nikolay-Kalyuzhnyy.pdf>
- ⁷⁵ Cotal H, Fetzer C, Boisvert J, Kinsey G, King R, Hebert P, Yoon H, Karam N, *III-V multijunction solar cells for concentrating photovoltaics*. Energy Environ Sci **2**(2): pp. 174–192.
- ⁷⁶ Masafumi Yamaguchi, et al., *Multi-junction III-V solar cells: Current status and future potential*. Solar Energy, 2005, **79** : pp. 78–85.
- ⁷⁷ King R, Shusari D, Larrabee D, Liu X-Q, Rehder E, Edmond-son K, Cotal H, Jones R, Ermer J, Fetzer C, Law D, Karam N, *Solar cell generations over 40 % efficiency*. Prog Photovolt Res Appl, 2012, **20**: pp. 801–815.
- ⁷⁸ Tanabe K., *A review of ultrahigh efficiency III-V semiconductor compound solar cells: multijunction tandem, lower dimensional, photonic up/down conversion and plasmonic nanometallic structures*. Energies, 2009, **2**: pp.504–530.
- ⁷⁹ B. O'Regan, M. Grätzel, *A low-cost, high-efficiency solar cell based on dye-sensitized colloidal TiO₂ films*. Nature, 1991, **353**: p.737
- ⁸⁰ M.A. Green, K. Emery, K. Bucher, D.L. King, S. Igari, Progress in Photovoltaics: Research and Applications **6**, 35.
- ⁸¹ Jan Kroon, Andreas Hinsch, *Dye-Sensitized Solar Cells*. Organic Photovoltaics, SSMATERIALS, **60**: pp. 273-290
- ⁸² Michael Grätzel, *Dye-sensitized solar cells*, Journal of Photochemistry and Photobiology C: Photochemistry Reviews, 2003, **4**(2): pp.145-153
- ⁸³ Michael Grätzel, *Photoelectrochemical cells*, Nature, 2001, **414**: pp.338-344
- ⁸⁴ K. Tennakone, G.R.R. Kumara, I.R.M. Kottegoda, V.S.P. Perera, *Dye-Sensitized Photoelectrochemical Cells Based on Porous SnO₂/ZnO Composite and TiO₂ Films with a Polymer Electrolyte*. Chem. Mater., 1999, **11**(9), pp. 2474–2477.
- ⁸⁵ K. Sayama, H. Suguhara, H. Arakawa, *Photoelectrochemical Properties of a Porous Nb₂O₅ Electrode Sensitized by a Ruthenium Dye*. Chem. Mater., 1998, **10**, pp.3825-3832
- ⁸⁶ Anders Hagfeldt, et al., *Dye-Sensitized Solar Cells*. Chem. Rev., 2010, **110** (11): pp 6595–6663
- ⁸⁷ M.K. Nazeeruddin, I. Kay, A. Rodicio, R. Humphry-Baker, E. Müller, P. Liska, N. Vlachopoulos, M. Grätzel, *Conversion of light to electricity by cis-X₂bis(2,2'-bipyridyl)-4,4'*

dicarboxylate)ruthenium(II) charge-transfer sensitizers ($X = Cl^-$, Br^- , I^- , CN^- , and SCN^-) on nanocrystalline titanium dioxide electrodes. *J. Am. Chem. Soc.*, 1993, **115**: p.6382.

⁸⁸ Arthur J Nozik, Gavin Conibeer and Matthew C. Beard, *Advanced Concepts in Photovoltaics*. 2014, pp.242-257

⁸⁹ Mitzi, D. B., *Synthesis, Structure and Properties of OrganicInorganic Perovskites and Related Materials*. Prog. Inorg. Chem., 1999, **48**: pp.1–121.

⁹⁰ Mitzi, D. B. *Templating and Structural Engineering in OrganicInorganic Perovskites*. J. Chem. Soc., Dalton Trans., 2001, pp.1–12.

⁹¹ Green, M. A., Emery, K., Hishikawa, Y., Warta, W. and Dunlop, E. D., *Solar cell efficiency tables (version 39)*. Prog. Photovoltaics: Res. Appl., 2012, **20**: pp.12–20.

⁹² Yang, W. S., *High-performance photovoltaic perovskite layers fabricated through intramolecular exchange*. Science, 2015, **348** : pp. 1234–1237.

⁹³ Nam-Gyu Park, *Perovskite solar cells: an emerging photovoltaic technology*. Materials Today, in press.

⁹⁴ D.B. Mitzi, et al., *Conducting tin halides with a layered organic-based perovskite structure*. Nature, 1994, **369** : pp.467–469.

⁹⁵ A. Kojima, et al., *Organometal Halide Perovskites as Visible-Light Sensitizers for Photovoltaic Cells*. J. Am. Chem. Soc., 2009, **131**: pp.6050–6051.

⁹⁶ J.-H. Im, C.-R. Lee, J.-W. Lee, S.-W. Park and N.-G. Park, *6.5% efficient perovskite quantum-dot-sensitized solar cell*. Nanoscale, 2011, **3**: pp.4088–4093.

⁹⁷ H.-S. Kim, C.-R. Lee, J.-H. Im, K.-B. Lee, T. Moehl, A. Marchioro, S.-J. Moon, R. Humphry-Baker, J.-H. Yum, J. E. Moser, M. Gratzel and N.-G. Park, *Lead iodide perovskite sensitized all-solid-state submicron thin film mesoscopic solar cell with efficiency exceeding 9%*. Sci. Rep., 2012, **2**: p.591.

⁹⁸ Lee, M. M., Teuscher, J., Miyasaka, T., Murakami, T. N. and Snaith, H. J., *Efficient hybrid solar cells based on mesosuperstructured organometal halide perovskites*. Science, 2012, **338**: pp.643–647.

⁹⁹ M. Liu, M. B. Johnston and H. J. Snaith, *Efficient planar heterojunction perovskite solar cells by vapor deposition*. Nature, 2013, **501**: pp.395–398.

¹⁰⁰ Seelam Prasanthkumar and Lingamallu Giribabu, *Recent advances in perovskite-based solar cells*, CURRENT SCIENCE, 2016, **111**(7): pp.1173-1181.

¹⁰¹ Ameen, S. et al., *Perovskite solar cells: influence of hole transporting materials on power conversion efficiency*. ChemSusChem., 2016, **9**: pp.10–27.

¹⁰² Sweta, T. and Singh, S. P., *Perovskite solar cells based on small molecule hole transporting materials*. J. Mater. Chem. A, 2015, **3**: pp.18329–18344.

¹⁰³ W.A. Laban, L. Etgar, *Depleted hole conductor-free lead halide iodide heterojunction solar cells*. Energy Environ. Sci., 2013, **6** : pp.3249–3253.

¹⁰⁴ S. Aharon, et al., *Depletion region effect of highly efficient hole conductor free CH₃NH₃PbI₃ perovskite solar cells*. Phys. Chem. Chem. Phys., 2014, **16**: pp.10512–10518.

¹⁰⁵ W.-J. Yin, T. Shi, Y. Yan, *Unique Properties of Halide Perovskites as Possible Origins of the Superior Solar Cell Performance*. Adv. Mater., 2014, **26**(27): pp. 4653–4658

¹⁰⁶ Mirtat Bouroushian, *Chalcogens and Metal Chalcogenides*, Electrochemistry of Metal Chalcogenides, Springer, 2010, pp.1-56.

¹⁰⁷ Fischer W, *A second note on the term “Chalcogen”*. J Chem Educ, 2001, **78**: p.1333.

¹⁰⁸ Mihai A. Popescu, *Non-Crystalline Chalcogenides*. Springer Netherlands, 2002, pp. 4-102.

¹⁰⁹ Mirtat Bouroushian, *Electrochemistry of Metal Chalcogenides*, Springer, 2010, pp.1-56.

¹¹⁰ Urii Isaakovich Ravich, *Semiconducting Lead Chalcogenides*, Springer, 1970.

¹¹¹ Gurinder Kaur Ahluwalia, *Application of Chalcogenides. S, Se, Te*. Springer International Publishing, 2017.

- ¹¹² R.D. Schaller, M.A. Petruska, V.I. Klimov, *Tunable Near-Infrared Optical Gain and Amplified Spontaneous Emission Using PbSe Nanocrystals*. J. Phys. Chem., 2003, **107**: p.13765
- ¹¹³ R.D. Schaller, V.I. Klimov, *High efficiency carrier multiplication in PbSe nanocrystals: Implications for solar energy conversion*. Phys. Rev. Lett., 2004, **92**: p.186601–1
- ¹¹⁴ F.W. Wise, *Lead Salt Quantum Dots: the Limit of Strong Quantum Confinement*. Acc. Chem. Res., 2000, **33**: p.773
- ¹¹⁵ T.D. Krauss, F.W. Wise, D.B. Tanner, *Observation of coupled vibrational modes of a semiconductor nanocrystal*. Phys. Rev. Lett., 1996, **76**: p.1376
- ¹¹⁶ T.D. Krauss, F.W. Wise, *Coherent Acoustic Phonons in a Semiconductor Quantum Dot*. Phys. Rev. Lett., 1997, **79**: p.5102
- ¹¹⁷ A. Olkhovets, R.-C. Hsu, A. Lipovskii, F.W. Wise, *Size-Dependent Temperature Variation of the Energy Gap in Lead-Salt Quantum Dots*. Phys. Rev. Lett., 1998, **81**: p.3539
- ¹¹⁸ M. Wolf, *Introduction to solid state physics*, WS 2005/06, Retrieved from: https://www.fhi-berlin.mpg.de/~wolf/femtoweb/teaching/WS0506-wolf-festk/WS0506/material/extfields_12_13.pdf
- ¹¹⁹ G. Zoppi, I. Forbes, R.W. Miles, P.J. Dale, J.J. Scragg, L.M. Peter, *Cu₂ZnSnSe₄ thin film solar cells produced by selenisation of magnetron sputtered precursors*. Prog. Photovoltaics Res. Appl., 2009, **17**: p.315.
- ¹²⁰ H. Katagiri, K. Jimbo, W.S. Maw, K. Oishi, M. Yamazaki, H. Araki, A. Takeuchi, *Deep defects in Cu₂ZnSnS₄ monograin solar cells*. Thin Solid Films, 2009, **517**: p.2455.
- ¹²¹ T.K. Todorov, K.B. Reuter, D.B. Mitzi, *High-efficiency solar cell with Earth-abundant liquid-processed absorber*. Adv. Mater., 2010, **22**: E156.
- ¹²² Roland Scheer and Hans-Werner Schock, *Chalcogenide Photovoltaics: Physics, Technologies, and Thin Film Devices*. WILEY-VCH Verlag GmbH & Co. KGaA, 2011, p.175-235.
- ¹²³ D. Bonnet, H. Rabenhorst, in Proceedings of the 9th IEEE Photovoltaic Specialist Conference, 129, 1972.
- ¹²⁴ Lukas Kranz, et al., *Doping of polycrystalline CdTe for high-efficiency solar cells on flexible metal foil*. Nature Communications, 2013, **4**.
- ¹²⁵ J. Britt and C. Ferekides, *Thin film CdS/CdTe solar cell with 15.8% efficiency*. Appl. Phys. Lett., 1993, **62**: p.2851.
- ¹²⁶ Sigurd Wagner, J. L. Shay, K. J. Bachmann, and E. Buehler, *p-InP/n-CdS solar cells and photovoltaic detectors*. Applied Physics Letters, 1975, **26**: p.229 .
- ¹²⁷ Hyo Joong Lee, et al., *CdSe Quantum Dot-Sensitized Solar Cells Exceeding Efficiency 1% at Full-Sun Intensity*. J. Phys. Chem. C, 2008, **112** (30): pp. 11600–11608.
- ¹²⁸ Pralay K. Santra and Prashant V. Kamat, *Tandem-Layered Quantum Dot Solar Cells: Tuning the Photovoltaic Response with Luminescent Ternary Cadmium Chalcogenides*. J. Am. Chem. Soc., 2013, **135**(2): pp. 877–885.
- ¹²⁹ Hyo Joong Lee, et al., *Regenerative PbS and CdS Quantum Dot Sensitized Solar Cells with a Cobalt Complex as Hole Mediator*. Langmuir, 2009, **25**(13): pp. 7602–7608.
- ¹³⁰ Joseph M. Luther, et al., *Stability Assessment on a 3% Bilayer PbS/ZnO Quantum Dot Heterojunction Solar Cell*. Advanced materials, 2010, **22** (33): pp. 3704–3707.
- ¹³¹ Serap Günes, et al., *Hybrid solar cells using PbS nanoparticles*. Solar Energy Materials and Solar Cells, 2007, **91** (5): pp. 420-423.
- ¹³² R. D. Schaller and V. I. Klimov, *High Efficiency Carrier Multiplication in PbSe Nanocrystals: Implications for Solar Energy Conversion*. Phys. Rev. Lett., 2004, **92**: 186601.
- ¹³³ Joshua J. Choi, et al., *PbSe Nanocrystal Excitonic Solar Cells*. Nano Lett., 2009, **9** (11): pp 3749–3755

- ¹³⁴ Meiyong Leng, et al., *Selenization of Sb₂Se₃ absorber layer: An efficient step to improve device performance of CdS/Sb₂Se₃ solar cells*. Appl. Phys. Lett., 2014, **105**: 083905 .
- ¹³⁵ Soo-Jin Moon, et al., *Sb₂S₃-Based Mesoscopic Solar Cell using an Organic Hole Conductor*. J. Phys. Chem. Lett., 2010, **1** (10): pp. 1524–1527.
- ¹³⁶ Yafit Itzhaik, et al., *Sb₂S₃-Sensitized Nanoporous TiO₂ Solar Cells*. J. Phys. Chem. C, 2009, **113** (11): pp. 4254–4256.
- ¹³⁷ C. H. L. Goodman, *The prediction of semiconducting properties in inorganic compounds*. J. Phys. Chem. Solids, 1958, **6**: p.305-314.
- ¹³⁸ B. R. Pamplin, *A systematic method of deriving new semiconducting compounds by structural analogy*. J. Phys. Chem. Solids, 1964, **25**: p.675-684.
- ¹³⁹ O. M. Madelung, *Semiconductors: Data Handbook*, 3rd ed. Springer, New York, 2004.
- ¹⁴⁰ L.L. Kazmerski, *CuInS₂ thin-film homojunction solar cells*. J. Appl. Phys., 1977, **48**: p. 3178.
- ¹⁴¹ Viljay K. Kapur, et al., *Low cost methods for the production of semiconductor films for CuInSe₂/CdS solar cells*. Solar Cells, 1987, **21**(1-4): pp. 65-72.
- ¹⁴² R.Klenk, *Solar cells based on CuInS₂—an overview*. Thin Solid Films, 2005, **480**: p. 509-514
- ¹⁴³ Qijie Guo, et al., *Development of CuInSe₂ Nanocrystal and Nanoring Inks for Low-Cost Solar Cells*. Nano Lett., 2008, **8** (9): pp. 2982–2987
- ¹⁴⁴ Haizheng Zhong, et al., *Controlled Synthesis and Optical Properties of Colloidal Ternary Chalcogenide CuInS₂ Nanocrystals*. Chem. Mater., 2008, **20** (20): pp 6434–6443
- ¹⁴⁵ Zhenxiao Pan, *High-Efficiency “Green” Quantum Dot Solar Cells*. J. Am. Chem. Soc., 2014, **136** (25): pp. 9203–9210.
- ¹⁴⁶ Shiyu Chen and X. G. Gong, *Electronic structure and stability of quaternary chalcogenide semiconductors derived from cation cross-substitution of II-VI and I-III-VI₂ compounds*. PHYSICAL REVIEW B, 2009, **79**: p.165211.
- ¹⁴⁷ Teodor Todorov, et al., *Progress towards marketable earth-abundant chalcogenide solar cells*. Thin Solid Films, 2011, **519**: pp. 7378–7381.
- ¹⁴⁸ K. Wang, et al., *Thermally evaporated Cu₂ZnSnS₄ solar cells*. APPLIED PHYSICS LETTERS, 2010, **97**: p.143508.
- ¹⁴⁹ Jun Du, et al., *Zn–Cu–In–Se Quantum Dot Solar Cells with a Certified Power Conversion Efficiency of 11.6%*. J. Am. Chem. Soc., 2016, **138**(12): pp. 4201–4209.
- ¹⁵⁰ Yanyan Cao, et al., *High-Efficiency Solution-Processed Cu₂ZnSn(S,Se)₄ Thin-Film Solar Cells Prepared from Binary and Ternary Nanoparticles*. J. Am. Chem. Soc., 2012, **134** (38): pp. 15644–15647.
- ¹⁵¹ W. H. Zachariasen, *THE ATOMIC ARRANGEMENT IN GLASS*. J. Am. Chem. Soc., 1932, **54** (10): pp. 3841–3851.
- ¹⁵² Public image. Retrieved from: http://www.ceramicindustry.com/ext/resources/Issues/2015_03/CI0315-fusion-slide3-615px.jpg.
- ¹⁵³ Jürn W.P. Schmelzer and Ivan S. Gutzow, *Glasses and the Glass Transition*. First Edition, WILEY-VCH Verlag GmbH & Co. KGaA, 2011.
- ¹⁵⁴ Tammann, G. *Der Glaszustand*. 1933, Leopold Voss Verlag, Leipzig.
- ¹⁵⁵ Tammann, G. *Die Aggregatzustände*. 1922, Leopold Voss Verlag, Leipzig.
- ¹⁵⁶ Nemilov, S.V., *Thermodynamic and Kinetic Aspects of the Vitreous State*. Zh.Prikl.Khimii, 1964, **37**: p.1020.
- ¹⁵⁷ Rawson, H., *Inorganic Glass-forming Systems*. 1967, Academic Press, London, New York.
- ¹⁵⁸ NA Goryunova, BT Kolomiets - Izv. Akad. nauk SSSR, ser. fiz, 1956.
- ¹⁵⁹ ZU Borisova, *Halkogenidyie stekloobraznye poluprovodniki*. SPBGU, 1983.
- ¹⁶⁰ GZ Vinogradova, *Stekloobrazovaniye i fazovye ravnovesiya v halkogeninyh sistemah*. Nauka, Moskwa, 1984, p.176.
- ¹⁶¹ J-L Adam, X. Zhang , *Chalcogenide Glasses: Preparation, Properties and Applications*. Woodhead, 2014.

- ¹⁶² A. Zakery S. R. Elliott, *Optical Nonlinearities in Chalcogenide Glasses and their Applications*. Springer, **135**: pp. 1-28.
- ¹⁶³ F. V. Kusmartsev, *Multiphonon absorption of light in nonpolar crystals*. Phys. Rev., 1991, B **43**: p.1345.
- ¹⁶⁴ Shashanka S. Mitra, Bernard Bendow, *Optical Properties of Highly Transparent Solids*. Springer, 1975, p. 3-19.
- ¹⁶⁵ Shuo Cui, et al. *From Selenium- to Tellurium-Based Glass Optical Fibers for Infrared Spectroscopies*. Molecules, 2013, **18**(5): p.5373-5388.
- ¹⁶⁶ Public image, Graphical depiction of the Morse potential with a harmonic potential for comparison. Created by Mark Somoza, March 26 2006.
- ¹⁶⁷ Rajan Jha, et al., *High-performance sensor based on surface plasmon resonance with chalcogenide prism and aluminum for detection in infrared*. Optics Letters, 2009, **34**(6): pp. 749-753
- ¹⁶⁸ Jas S. Sanghera, *Infrared Evanescent Absorption Spectroscopy of Toxic Chemicals Using Chalcogenide Glass Fibers*. JACS, 1995, **78**(8): pp. 2198–2202
- ¹⁶⁹ T. Kanamori, et al., *Chalcogenide glass fibers for mid-infrared transmission*. Journal of Lightwave Technology, 1984, **2**(5): pp.607-613.
- ¹⁷⁰ X.H. Zhang, *Applications of chalcogenide glass bulks and fibers*. Journal of Optoelectronics and Advanced Materials, 2003, **5**(5): pp. 1327 - 1333
- ¹⁷¹ X.H. Zhang, *A new class of infrared transmitting glass-ceramics based on controlled nucleation and growth of alkali halide in a sulphide based glass matrix*. Journal of Non-Crystalline Solids, 2004, **337**(2): pp. 130-135.
- ¹⁷² Changgui Lin, et al., *Crystallization behavior of 80GeS₂·20Ga₂S₃ chalcogenide glass*. Appl Phys A, 2009, **97**: pp.713–720
- ¹⁷³ C. Lin, et al., *Controllability study of crystallization on whole visible-transparent chalcogenide glasses of GeS₂-Ga₂S₃-CsCl system*. Journal of Optoelectronics and Advanced Materials, 2010, **12** (8): pp.1684-1691
- ¹⁷⁴ Laurent CALVEZ, et al., *Controlled crystallization in Ge-(Sb/Ga)-(S/Se)-MX glasses for infrared applications*. Journal of the Ceramic Society of Japan, 2008, **116** (1358): pp.1079-1082
- ¹⁷⁵ Mathieu Roze, et al., *Optical and Mechanical Properties of Glasses and Glass–Ceramics Based on the Ge–Ga–Se System*. J. Am. Ceram. Soc., 2008, **91**(11): pp.3566–3570
- ¹⁷⁶ Guang Yang, et al. *Glass Formation and Properties of Chalcogenides in a GeSe₂–As₂Se₃–PbSe System*. J. Am. Ceram. Soc., 2007, **90** (5): pp. 1500–1503.
- ¹⁷⁷ Hongli Ma, et al. *Infrared transmitting chalcogenide glass ceramics*. Journal of Non-Crystalline Solids, 2003, **317**: pp. 270–274.
- ¹⁷⁸ A. H. Kahn, *Theory of the Infrared Absorption of Carriers in Germanium and Silicon*. Phys. Rev., 1955, **97**: p. 1647.
- ¹⁷⁹ Yang Xu, *Les propriétés photoélectriques de vitrocéramiques de chalcogénures*. Thesis, 2014.
- ¹⁸⁰ Laurent Calvez, *Nouveaux verres et vitrocéramiques transparents dans l'infrarouge pour l'imagerie thermique*. Thesis, 2006.
- ¹⁸¹ Yang Xu, et al., *Crystallization optimization of the 40GeSe₂–40Sb₂Se₃–20CuI glass for improvement of photoelectric properties*. Journal of Non-Crystalline Solids, 2016, **431**(1): pp. 61-67.
- ¹⁸² Xianghua Zhang, et al. *Enhancement of charge photo-generation and transport via an internal network of Sb₂Se₃/Cu₂GeSe₃ heterojunctions*. J. Mater. Chem. A, 2014, **2**: pp. 17099-17106

Chapter II

Investigations on charge photo generation and charge transfer mechanism in 40GeSe₂-40Sb₂Se₃-20CuI bulk glass-ceramics.

Table of contents

1. Establishing of iodine crucial role in charge photogeneration and transfer in $40\text{GeSe}_2\text{-}40\text{Sb}_2\text{Se}_3\text{-}20\text{CuI}$ glass-ceramics.	54
1.1. Effect of iodide introduction on the chalcogenide glass structure	54
1.2. Glass precursor preparation and characterization	55
1.2.1. Glass synthesis	55
1.2.2. Thermal properties	56
1.3. Controlled crystallization of glass.....	59
1.3.1. Characterization by XRD.....	59
1.3.2. Observation by SEM.....	61
1.3.3. Surface potential measurement	62
1.3.4. Photoelectrochemical (PEC) measurements	65
2. Influence of Iodine doping on the electrical properties of Sb_2Se_3	69
2.1. Influence on the structure and the electric conductivity	69
2.2. On the photoelectric properties	74
3. Fine tuning of the $40\text{GeSe}_2\text{-}40\text{Sb}_2\text{Se}_3\text{-}20\text{CuI}$ glass precursor	76
3.1. On fine tuning in this system	76
3.2. Glass precursor preparation and characterization.	77
3.3. Preparation and characterization of glass-ceramics.	79
3.4. Optimization of annealing procedure of $\text{Ge}_{11}\text{Sb}_{22}\text{Cu}_5\text{I}_5\text{Se}_{58.8}$ glass-ceramic.....	83
4. Influence of stoichiometric deviations on Sb_2Se_3 electrical properties.....	86
5. Conclusion	96
6. References.....	97

1 Establishing of iodine crucial role in charge photogeneration and transfer in 40GeSe₂-40Sb₂Se₃-20CuI glass-ceramics.

1.1 Effect of iodide introduction on the chalcogenide glass structure

Previous studies on controllable crystallization of glass-ceramics showed that it is extremely difficult to obtain optically transparent glass-ceramics from highly covalent glass¹. Therefore, introduction of ionic compounds could be utilized in order to control the process of nucleation and crystal growth. For instance, the introduction of CuI is known for glass depolymerisation which is the result of bridge bonding breaking. It is supposed that halogens take the place of chalcogen atoms in Ge-Se, Sb-Se or Se-Se bonds, which is the reason of the bond rupture. Therefore some negative charges are accumulated on the site of non-bridged chalcogen atoms and the positively charged Cu⁺ ions will be located nearby for charge compensation. It leads to the appearance of ionic bonding between negatively charged chalcogenide and positively charged Cu⁺ ion. The structure is schematically represented in fig. 2-1.

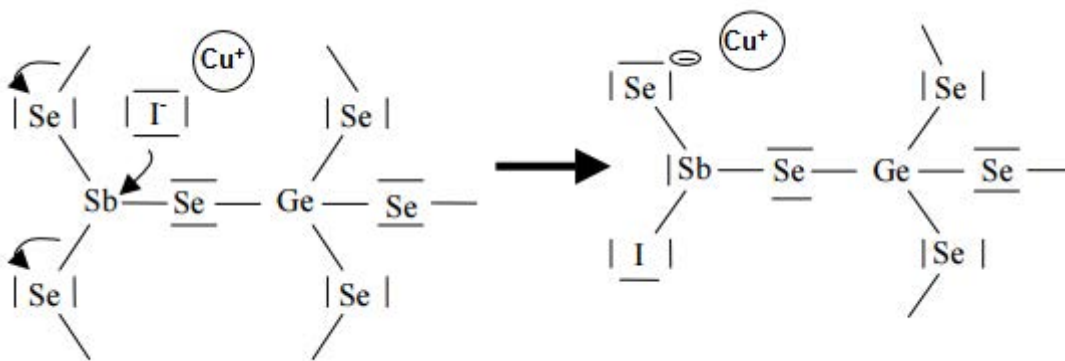


Figure 2-1 Modification of chalcogenide glass structure upon the introduction of CuI³

Therefore, the introduction of CuI in chalcogenide glasses has a double effect. Firstly, the introduction of a large atom (iodine) expands the glass-forming region and reduces the melting and glass transition temperatures due to bridge bonds breaking². Secondly, the Cu⁺ ions are not directly incorporated in the glass network and serve only as a charge compensator for non-bridged Se⁻ atoms³. The Cu introduction increases the ionicity of the compound and will promote phase separation⁴, which is favorable for homogenous nucleation.

Table 2-1 Table of prepared glassy precursor samples

Composition
40GeSe ₂ -40Sb ₂ Se ₃ -20CuI
40GeSe ₂ -40Sb ₂ Se ₃ -20CuI _{1.1}
40GeSe ₂ -40Sb ₂ Se ₃ -20CuI _{1.2}
40GeSe ₂ -40Sb ₂ Se ₃ -20CuI _{1.4}
40GeSe ₂ -40Sb ₂ Se ₃ -20CuI _{1.5}
40GeSe ₂ -40Sb ₂ Se ₃ -20CuI _{0.9}
40GeSe ₂ -40Sb ₂ Se ₃ -20CuI _{0.75}
40GeSe ₂ -40Sb ₂ Se ₃ -20CuI _{0.5}

40GeSe ₂ -40Sb ₂ Se ₃ -20CuI _{0.25}
40GeSe ₂ -40Sb ₂ Se ₃ -20Cu
40GeSe ₂ -40Sb ₂ Se ₃ -30Cu
40GeSe ₂ -40Sb ₂ Se ₃ -10Cu
40GeSe ₂ -40Sb ₂ Se ₃ -6Cu

Previous study has demonstrated the critical importance of the iodine presence in the chalcogenide glass-ceramics, on its photoelectric properties. In order to elucidate the precise role of iodine, we have designed a series of glass compositions listed in table 2.1, with different iodine content.

1.2 Glass precursor preparation and characterization

1.2.1 Glass synthesis

For the glass synthesis highly pure raw materials stored in glove box under argon atmosphere are used: Ge (UMICORE, 5N), Se (UMICORE, 5N), Sb (Alfa Aesar, 99.999%), CuI (Sigma Aldrich, 98%). To avoid contamination silica tube, utilized for glass synthesis, is thoroughly cleaned with HF, rinsed in deionized water and then dried under vacuum pumping. Being under vacuum, silica tube is brought to the glovebox, where raw materials are weighted and inserted into the tube. Then the tube with raw materials is pumped again to the pressure of 10^{-5} mbar. The schema of vacuum pumping is presented in fig. 2-2.

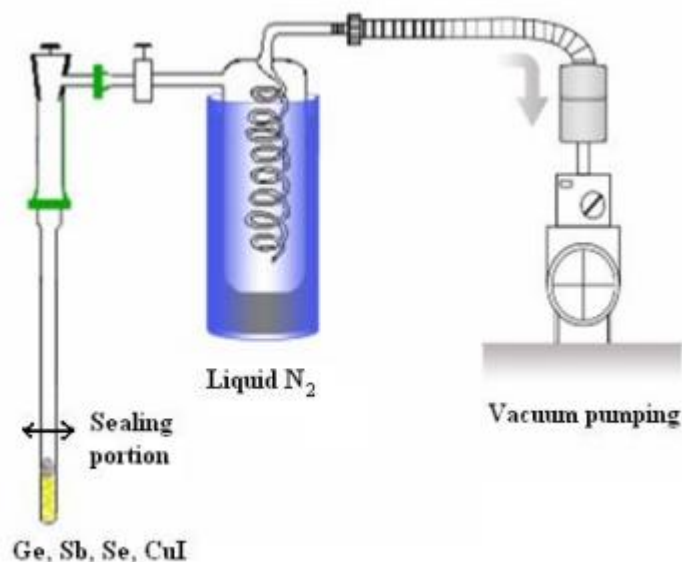


Figure 2-2 Setup used for preparation of chalcogenide glasses

For preparing the above-mentioned composition with different copper and iodine content, metallic Cu (STREM, 99.999%) and I (Sigma Aldrich, 99.9%) were directly added in the tube. Considering the fact that iodine has a significant partial pressure at room temperature, the tube containing the raw elements was emerged in ice water during the vacuum pumping in order to limit the iodine loss.

Sealed silica tube is then heated in rocking furnace to 700-800 °C and synthesized at this temperature for 10 hours to provide homogeneous intermixing. The obtained melt is then cooled down to 650 – 700 °C without rocking to reduce the pressure over the melt and avoid bubbles in the bulk material. The melt is then quenched in water. Rocking furnace utilized for synthesis and typical synthesis profile are presented in fig. 2-3.

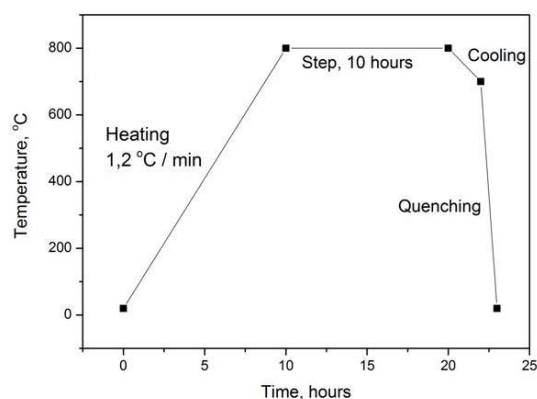


Figure 2-3 Photograph of a rocking furnace and typical synthesis profile for glass-precursor preparation

Silica tube is then quenched in water for several seconds in order to solidify the melt without crystallization. Obtained glass is then annealed at $T_g - 10$ (usually about 200 °C) for 3 hours for 3 hours in order to reduce mechanical stresses accumulated due to quenching procedure.

Extracted glass rod is then sliced into discs of 2 mm in thickness and polished to obtain optically flat surface, as shown in fig. 2-4.

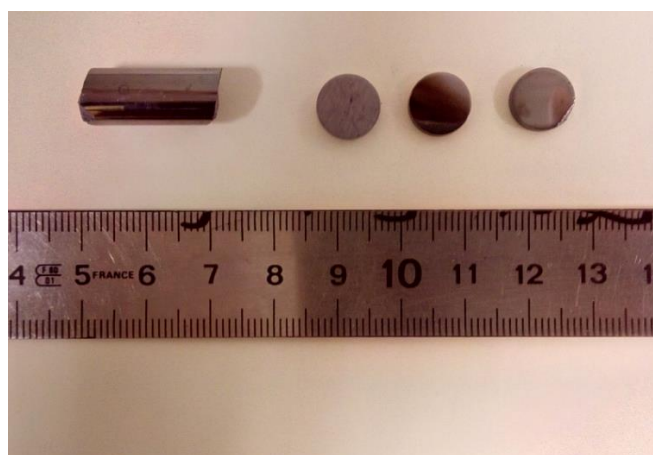


Figure 2-4 Photograph of chalcogenide glass rod and obtained discs before and after polishing

1.2.2 Thermal properties

The characteristic temperatures of different glasses have been measured by using differential scanning calorimetry (DSC) using a typical heating rate of 10°C/minute. The examination of all the results presented in fig. 2-5 leads to the following comments:

- The introduction of Cu and I in the Sb₂Se₃ – GeSe₂ pseudo binary system has a quite complex effect. The iodine content has a limited effect on the glass transition temperature until it reaches the stoichiometry with copper. An excess of iodine compared to copper will then lead to a significant decrease of the glass transition temperature, as shown in fig. 2-5 (a, b) and summarized in fig. 2-5 (e). From this point, the iodine will break the Ge-Se or Sb-Se bonding without charge compensation by Cu, as proposed in fig. 2-6. The dimensionality of the glass network will decrease, leading to decreasing T_g. This effect of halogen is observed, in Ge-S-Br glass or Ge-S-Br(I) glass for example^{5,6}.
- The introduction of copper, without the presence of iodine leads to a continuous decrease of T_g and an increasing tendency of crystallization as shown in fig. 2-5(c). The difference between the T_g and T_x (crystallization temperature) decreases with increasing Cu content. Tokihiro et al.³ observed electron transfer from alkali metal to Se and Ge atoms in case of GeSe₂ based glass. This can probably also happen with copper ions. The only way to maintain electrical neutrality in this case is to isolate some of chalcogene atoms by bridge bond breaking, leading therefore to decreasing T_g.

We could also notice appearance of multiple crystallization peaks for the glass with CuI_{1.5} in fig. 2-5 (a). Several crystalline phases are in competition and can appear successively as the temperature increases.

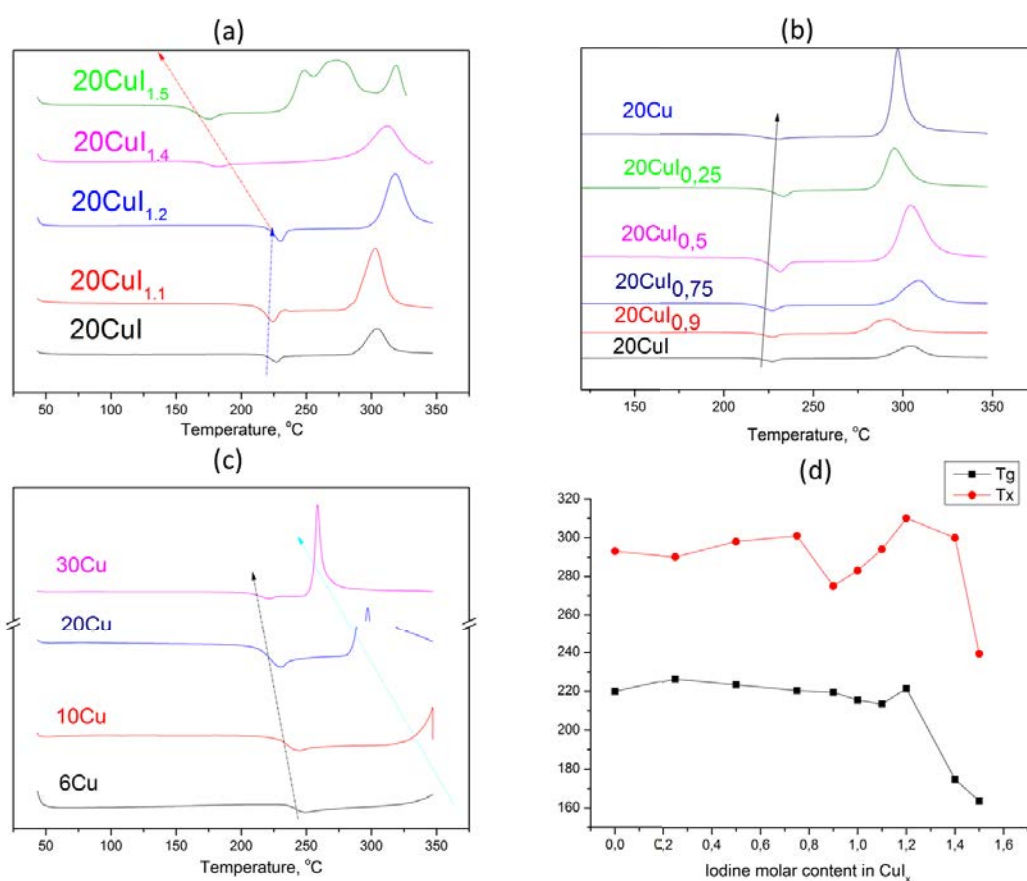


Figure 2-5 DSC curves: (a) Iodine excess in 40GeSe₂ – 40 Sb₂Se₃ – 20CuI_{1+x} glass (b) iodine deficiency in 40GeSe₂ – 40 Sb₂Se₃ – 20CuI_{1-x} glass ,(c) variation of copper content in the absence of iodine in XGeSe₂ – YSb₂Se₃ – (1-X-Y)Cu glass, (d) T_g and T_x plotted against iodine molar content in 20CuI_x compound

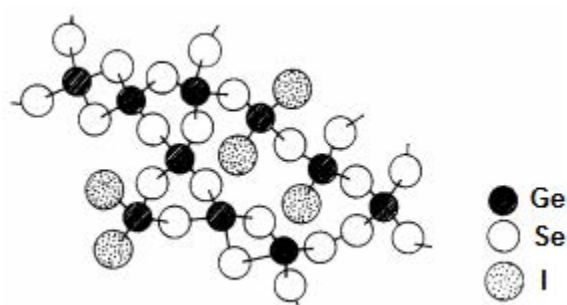


Figure 2 6 Structure of GeSe₄ sites upon Iodine introduction. Modified from⁵

1.2.3. Optical properties

The optical transmission has been measured using a Fourier Transform infrared (FTIR) spectrometer with polished samples having a thickness around 1 mm. Even the objective of this work is to develop materials for photoelectric application; this property is still very interesting for assessing the quality of the samples as it is very sensitive to the presence of crystals, impurities as well as free charge carriers. The results of all measurements are collected in fig. 2-7. It is clear that most of the glasses present a flat transmission curve with a maximum transmission limited by the reflection due to the relatively high refractive index, indicating a homogenous precursor glass. More or less OH⁻ groups and H₂O molecules along with Ge-O impurities are present in these glasses and it seems that the oxygen impurity is introduced with iodine or/and copper. Three glasses show significantly lower transmission. This is due to the presence of relatively big crystals inside the glass matrix. Even their quantity is small, typically <5%, it reduces optical transparency significantly. In case of more important amount of crystalline fraction, the sample would not have any noticeable transmission.

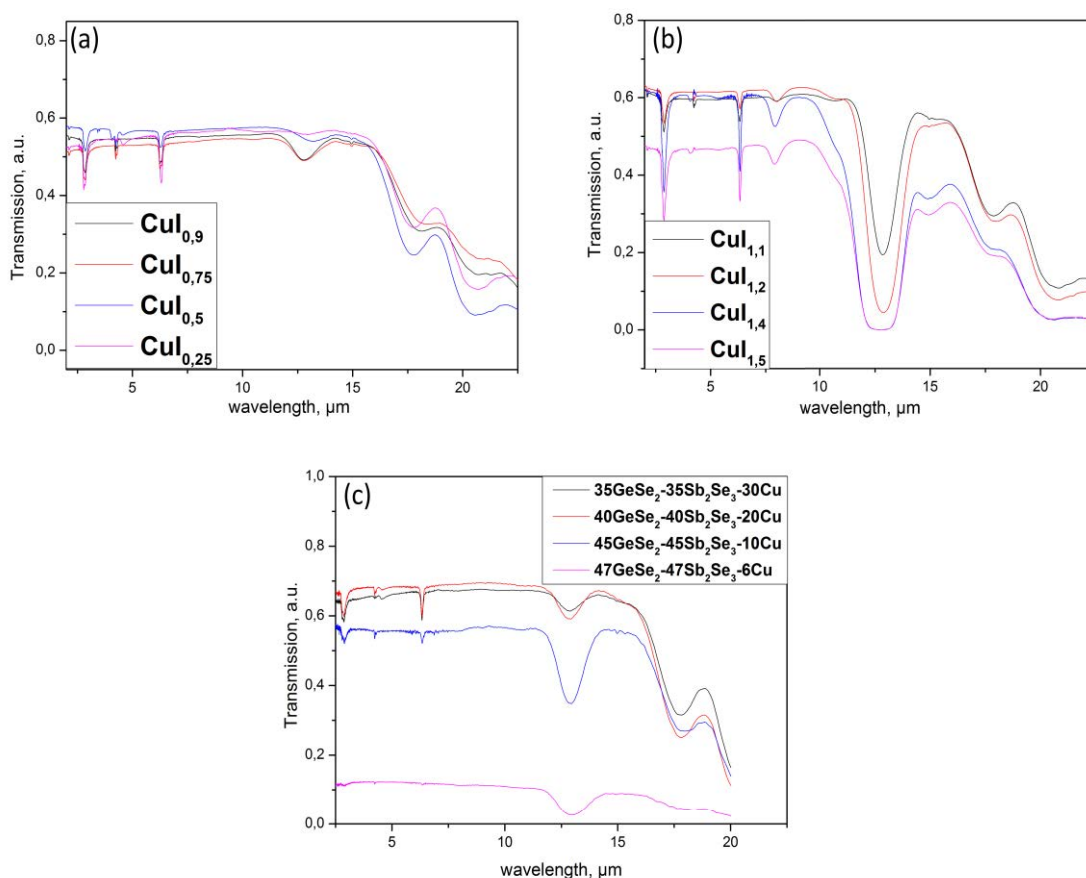


Figure 2- 7 IR transmission spectra for different glass precursors: (a) glass precursors $40\text{GeSe}_2\text{-}40\text{Sb}_2\text{Se}_3\text{-}20\text{CuI}_x$ with deficiency of iodine, (b) glass precursors $40\text{GeSe}_2\text{-}40\text{Sb}_2\text{Se}_3\text{-}20\text{CuI}_x$ with excess of iodine, (c) different variations of copper content for the precursor prepared in the absence of iodine

1.3 Controlled crystallization of glass.

No glass sample shows any significant electric conductivity. Tested via 4-probe-method, all the precursors showed resistivity above $10^8 \Omega \times \text{cm}^2$. To prepare glass-ceramics all the glass precursors were annealed at T_x , the crystallization temperature, for 1 hour. In case of multiple crystallization peaks on the DSC curves, samples with different annealing temperatures were prepared.

1.3.1 Characterization by XRD

In fig. 2-8 the XRD patterns are presented. We established that with increase of iodine content (fig. 2-8a) beyond the above mentioned threshold, crystallization properties change drastically. Glasses saturated with iodine possess higher amount of terminated chains $[\text{Se-Sb-Se}]_n$ with iodine atom at the end, which is, apparently, favorable for SbISe phase crystallization with its intense peak at 29.445° (1 1 2). It crystallizes in orthorhombic phase with cell parameters $a = 8.698 \text{ \AA}$, $b = 4.127 \text{ \AA}$, $c = 10.412 \text{ \AA}$. As it can be seen from the relative intensities, SbISe is the dominant phase to crystallize. At lower temperature (fig. 2-8c) one can only observe the SbISe phase crystallization, while upon the increase of the annealing temperature to 258°C , the appearance of Cu_2GeSe_3 related peak at 27.7° (0 1 1) and

Sb₂Se₃ peak at 27.394° (2 3 0) can be observed. We can conclude that SbISe requires less energy for crystallization due to its lower coordination in iodine saturated glassy phase.

In fig. 2-8b, we can notice a weak shift of Sb₂Se₃ peaks towards higher 2 θ values. This could be explained by the decrease of large iodine atom content, leading to a decrease of the lattice parameters due to decrease of I_(Se) defects quantity. The decrease of the lattice parameters leads to increase in 2 θ diffraction angle. Diffraction peak appeared in 20Cu glass-ceramics at 29.2° could be attributed to CuSe cubic phase with lattice parameters a=b=c=6.116 Å (PDF 26-1115).

With reduction of Cu content (fig. 2-8d), the Cu₂GeSe₃ (0 1 1) peak at 27.7° continuously decreases. This can also serve as a clear evidence of this particular Cu₂GeSe₃ polymorphic crystal structure existence inside the glass ceramics, since this peak in 40GeSe₂-40Sb₂Se₃-20CuI is in superposition with Sb₂Se₃ neighbor peaks. No Cu₂GeSe₃ related peak in 47GeSe₂-47Sb₂Se₃-6Cu composition is observed. Surprisingly (0 0 2) orientation with XRD peak at 45.5° becomes preferential for Sb₂Se₃ phase.

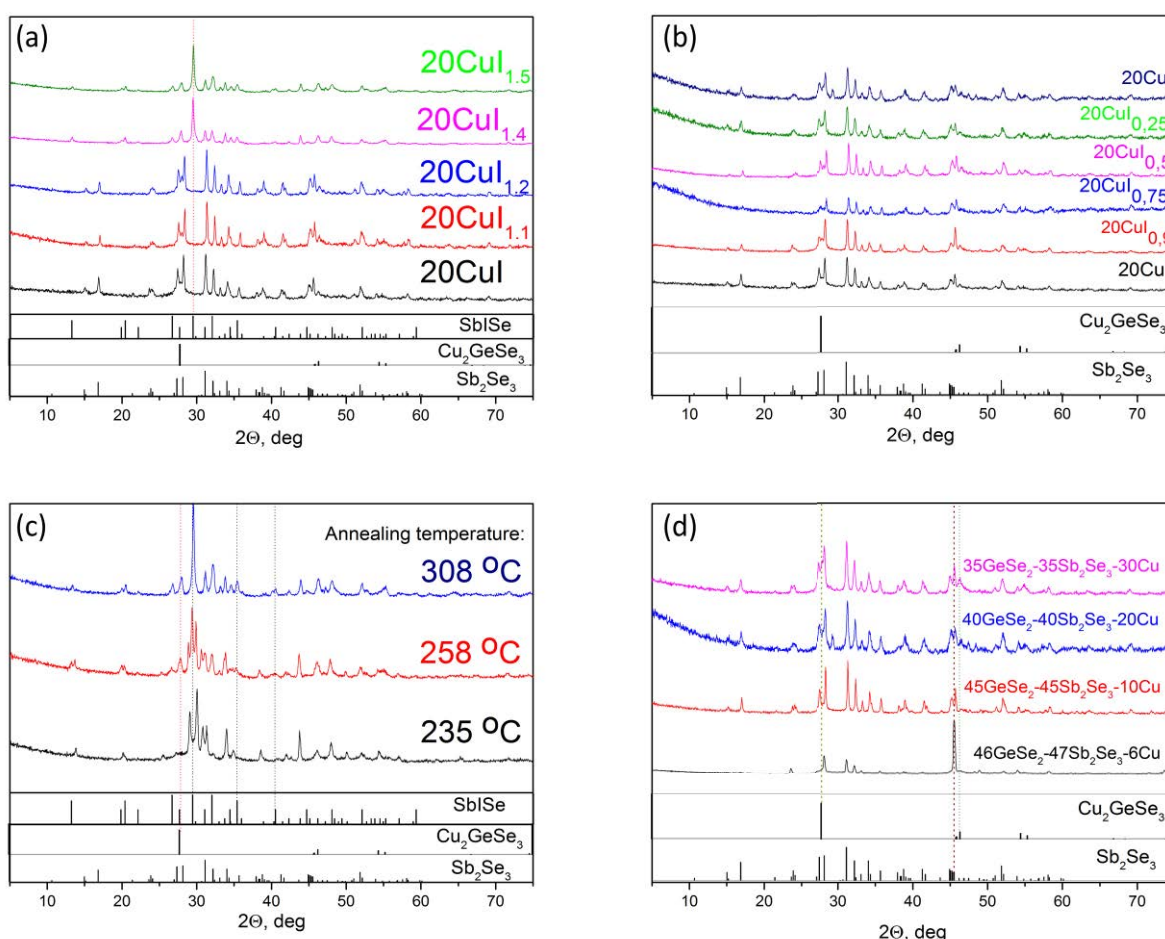


Figure 2-8 XRD diffractograms for glass-ceramics with different iodine content: increased amount of iodine (a), decreased amount of iodine (b), different annealing temperatures for iodine excess 40GeSe₂-40Sb₂Se₃-20CuI_{1.5} sample (c) and variations of copper content in the absence of iodine (d)

1.3.2 Observation by SEM

The influence of iodine and copper content on the microstructure of different glass-ceramics has been studied by using SEM. The results are shown in fig. 2-9 and fig. 2-10. From fig. 2-9a to fig. 2-9f we are showing the influence of iodine, the morphology change is observable with however non-clear tendency. In fact, as confirmed by the XRD, discussed previously, without excess, the iodine content does not induce noticeable change on the crystallized phases in the glass-ceramics. The iodine will be incorporated partially in the Sb₂Se₃ as confirmed in previous study. With excess of iodine, a new crystallized phase, the SbISe phase will appear.

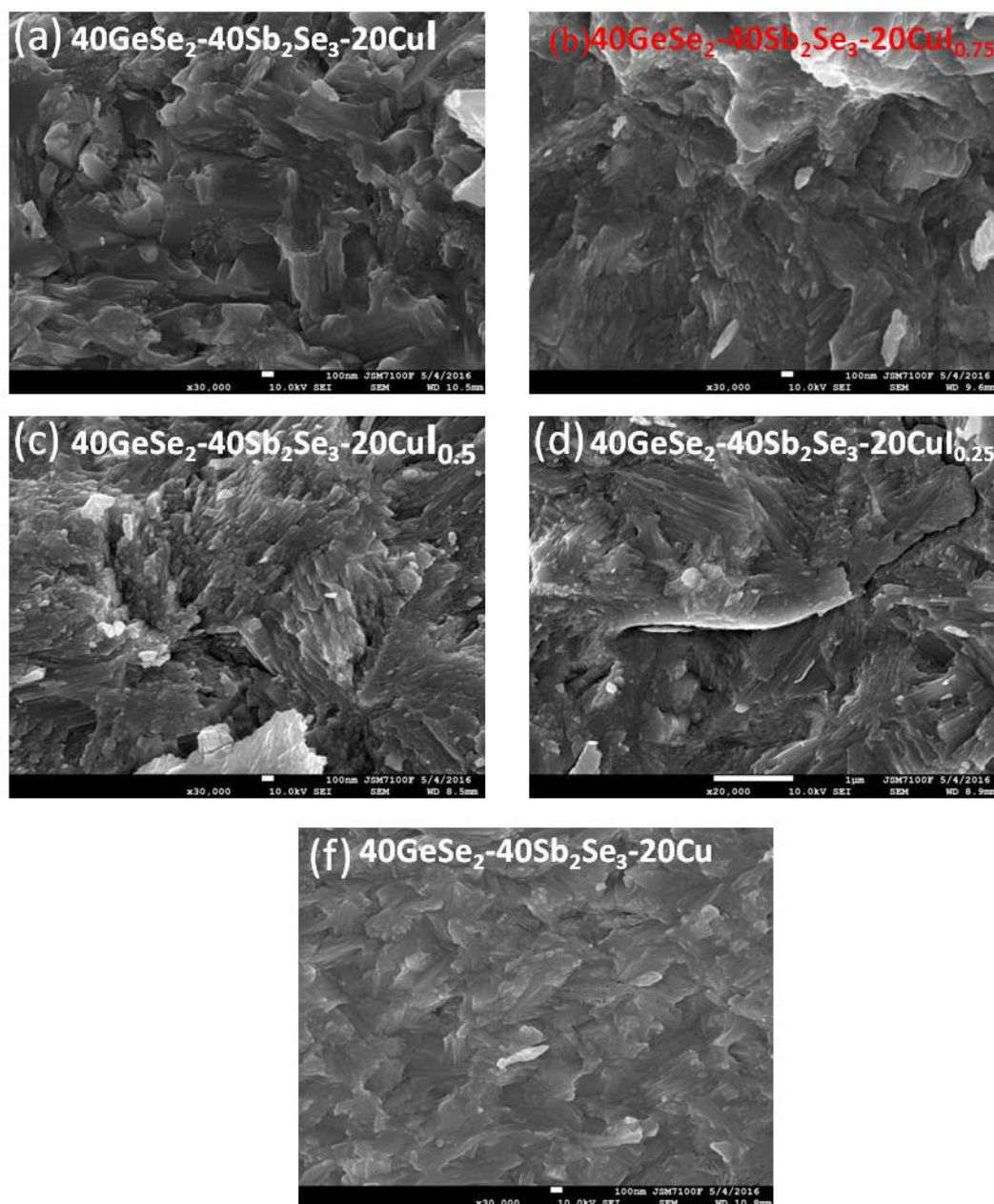


Figure 2-9 SEM image of (a) 40GeSe₂-40Sb₂Se₃-20CuI, (b) 40GeSe₂-40Sb₂Se₃-20CuI_{0.75}, (c) 40GeSe₂-40Sb₂Se₃-20CuI_{0.5}, (d) 40GeSe₂-40Sb₂Se₃-20CuI_{0.25}, (f) 40GeSe₂-40Sb₂Se₃-20Cu.

The influence of copper content is important, as shown in fig. 2-10. Copper-rich glass-ceramic contain nanoscale Cu₂GeSe₃ crystals covering the whole surface. As the Cu content decreases, the

proportion of Sb₂Se₃ increases progressively. In case of the sample with 6 mol. % of Cu, only needle-like Sb₂Se₃ can be observed with oriented crystalline structure, which is in good correspondence with XRD pattern for this glass-ceramics (fig. 2-8d).

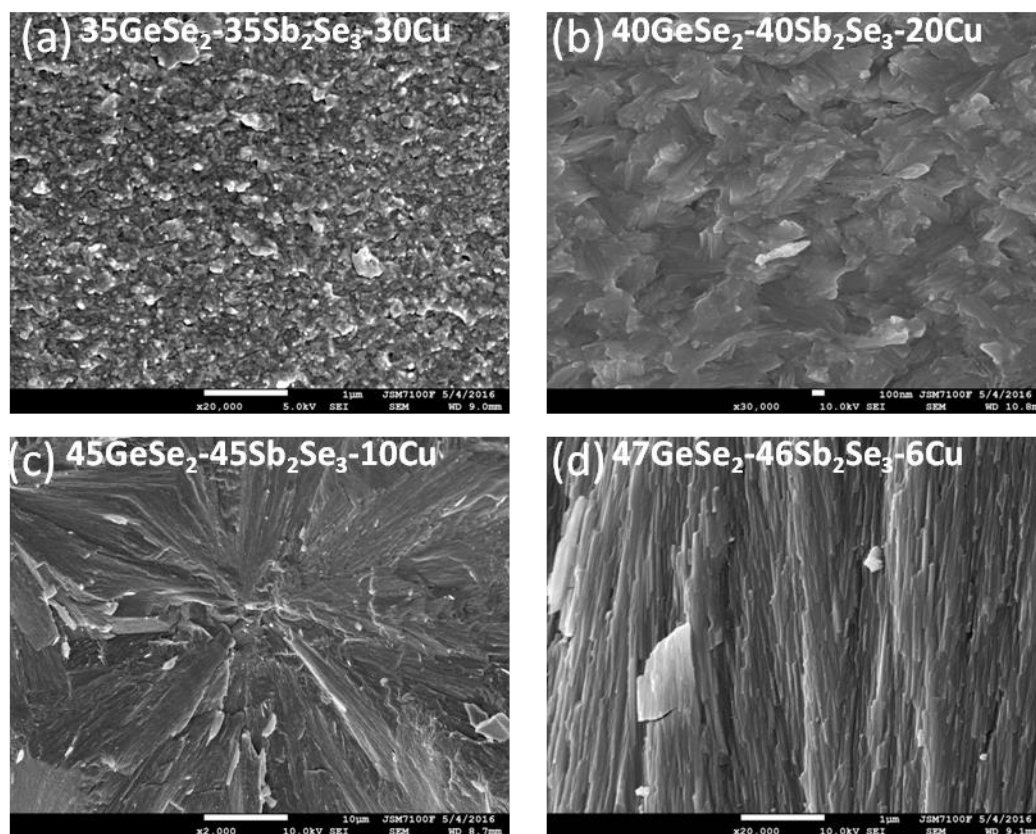


Figure 2-10 SEM image of (a) 35GeSe₂-35Sb₂Se₃-30Cu, (b) 40GeSe₂-40Sb₂Se₃-20Cu, (c) 45GeSe₂-45Sb₂Se₃-10Cu, (d) 47GeSe₂-46Sb₂Se₃-6Cu

1.3.3 Surface potential measurement

Kelvin probe force microscopy (KPFM) enables high-resolution imaging of the surface potential of a given material, which is extremely useful for characterization of inhomogeneous materials with a variable bulk composition.

The KPFM measure contact potential difference (CPD) between the surface of the sample and conducting tip (crystalline silicone in our case). CPD can be defined as the difference of work functions between the tip and the sample, and expressed in simple formula⁷:

$$V_{\text{CPD}} = \frac{\phi_{\text{tip}} - \phi_{\text{sample}}}{-e}, \quad (2.1)$$

where ϕ_{tip} is a work function of a tip, ϕ_{sample} work function of a sample, e – elementary charge.

Before the contact: both KPFM tip and the sample are characterized by their work functions, which depend only on their chemical nature (fig. 2-11 (a)). After the contact the electrons will flow from the material with lower work function ϕ_1 to the material with higher work function ϕ_2 , since the electrons are trying to occupy lower energy states. At the same time, Fermi level of both materials will equalize. Due to the accumulation of positive charge in the material with ϕ_1 and negative charge in the material with ϕ_2 an energy barrier will be established equal to V_{CPD} . When Fermi levels are equalized, considering that ϕ_1 and ϕ_2 are constants, contact potential difference will describe the difference of potential energy of 2 electrons existing in a vicinity of the surface of the material with ϕ_1 and ϕ_2 . The case when ϕ_{sample} is higher than ϕ_{tip} is shown in fig. 2-11 (b)

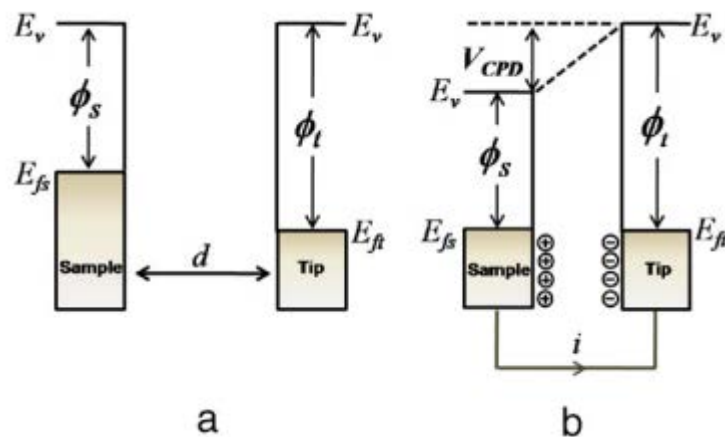


Figure 2-11 Interaction between conductive tip and surface of the sample: before (a) and after contact (b)⁷

Thus, KPFM gives as a result, the V_{CPD} mapping, where we can estimate the work function of different spatial areas of the sample, considering that the work function of crystalline silicone is known. And, what is even more important in our case, estimate chemical inhomogeneity of the sample since the work function depends only on the composition.

KPFM images depicted in fig. 2-12 clearly show that the decrease of iodine content leads to the loss of contrast between highly conductive (bright) and low conductive (dark) regions. It is much less pronounced for 20CuI_{0.75} composition and almost completely disappears in the case of 20CuI_{0.5} samples. The analysis of these pictures leads to the following comments:

- Even the presence of two crystallized phases, Sb₂Se₃ and Cu₂GeSe₃, is confirmed by XRD, the inhomogeneous contrast is associated to the Sb₂Se₃ which is more or less doped by I. This doping is essential for increasing the conductivity of the glass-ceramics, as shown in Fig. 2-13.
- As discussed before, the iodine content does not change the crystallization of the Cu₂GeSe₃ phase. This highly conductive phase is not efficient for increasing the conductivity of the glass ceramics, because of its high symmetry, which is not efficient for creating an interconnected network.

Based on this analysis, it is reasonable to conclude that the contrast of work function, shown in fig. 2-12 is induced by the more or less iodine-doped Sb₂Se₃. The crystallization of the precursor glass is realized at relatively low temperature where the viscosity of the glass is still high, the crystal growth

will be controlled by the diffusion of atoms. The diffusion of big atoms like iodine is more difficult, possibly leading to a concentration of inhomogeneities in microscopic level. With low iodine content, the contrast logically disappears.

Using these measurements, it is possible to estimate the Fermi level of different phases. Taking silicon tip work function $E_f = 4.83\text{eV}$ ⁸ and using formula 2.1, one can estimate non-doped Sb_2Se_3 $E_f = 4.788\text{eV}$ and iodine doped Sb_2Se_3 $E_f = 4.800 - 4.805\text{ eV}$.

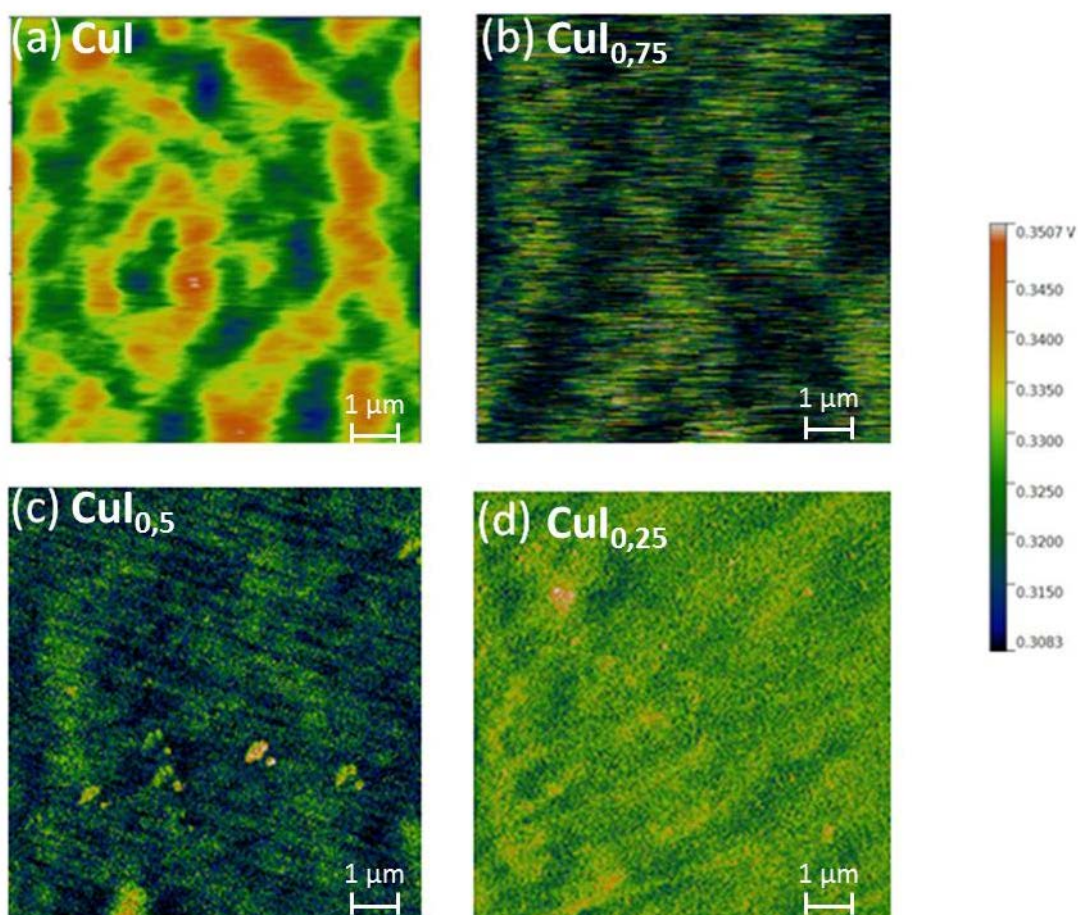


Figure 2-12 AFM Kelvin probe microscopy images (a) 40GeSe₂-40Sb₂Se₃-20CuI, (b) 40GeSe₂-40Sb₂Se₃-20CuI_{0.75}, (c) 40GeSe₂-40Sb₂Se₃-20CuI_{0.5}, (d) 40GeSe₂-40Sb₂Se₃-20CuI_{0.25}

It can be seen in fig. 2-13 that despite the same quantity of Cu_2GeSe_3 phase for all the samples, the conductivity of the glass-ceramics decreases exponentially with reduction of iodine content. Therefore, it is likely that iodine-doped Sb_2Se_3 phase is responsible for the appearance of bulk conductivity. It is worth mentioning that stoichiometric CuI compound looks the most suitable from the point of view of Iodine molar content. Further increase in iodine content leads to preferential formation of SbISe phase, which is highly resistive with $\sigma < 1\mu\text{S/cm}$ ⁹. That leads to overall loss in conductivity.

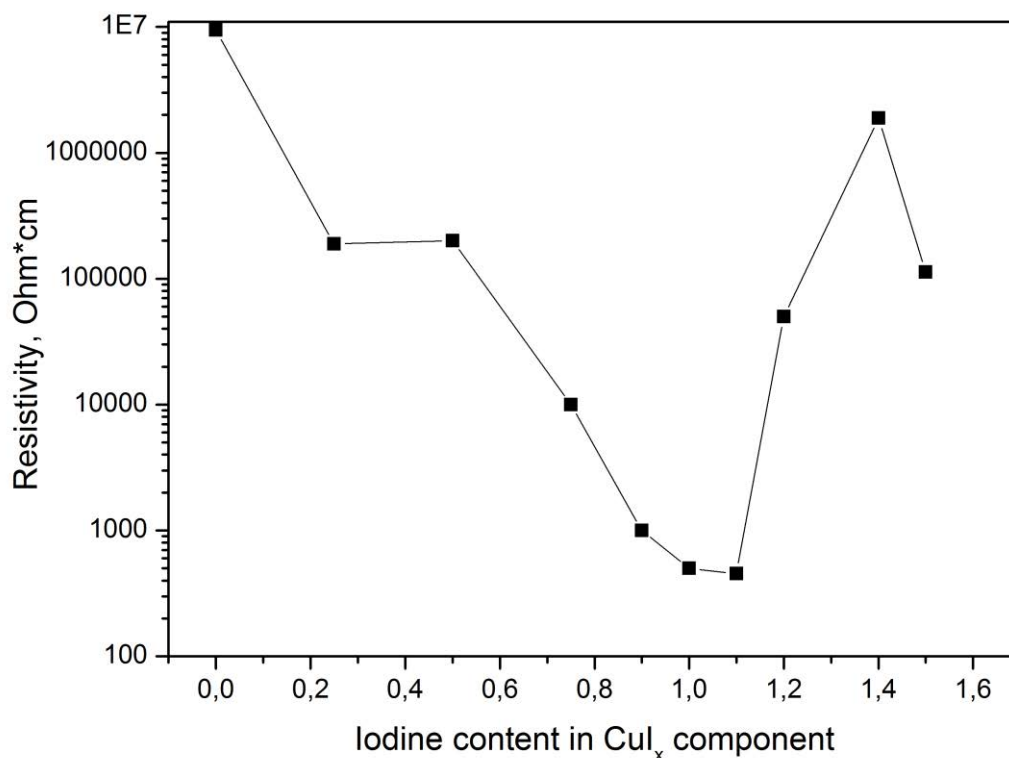


Figure 2-13 Dependence of conductivity of the glass ceramics on iodine content

1.3.4 Photoelectrochemical (PEC) measurements

The equilibrium between semiconductor and electrolyte has a lot in common with the contact of two semiconductors. Immediately after contact, on the interface occurs equalization of Fermi level of semiconductor and RedOx energy level of the electrolyte, which is accompanied by the bending of energy levels. Forward and reverse currents become balanced as in the case of two semiconductors. Thus, the dynamic equilibrium is characterized by the absence of net current¹⁰.

We can express the net current for the semiconductor – electrolyte interface as:

$$I_c = -eAk_{et}c_{ox}(n_s - n_{s0}), \text{ where } (2.2)$$

k_{et} is the constant for electron transfer, c_{ox} is the concentration of empty states in redox electrolyte, n_s surface concentration of electrons and n_{s0} surface concentration of electrons in the equilibrium state.

Since for the equilibrium $n_s = n_{s0}$, the net current turns to zero, this case for n-type semiconductor is depicted in fig. 2-14 (a).

Applying voltage it is possible to vary n_s/n_{s0} ratio, which results in the flow of anodic or cathodic current. Rewriting the n_s as a function of major charge carrier concentration (n) and applied bias (V), we obtain:

$$n_s = n \exp\left(\frac{e(V_{sc}+V)}{kT}\right), \text{ where (2.3)}$$

V_{sc} is a parameter of semiconductor, which depends on its nature and depletion region width.

And n_{s0} as :

$$n_{s0} = n \exp\left(\frac{-eV_{sc}}{kT}\right), \quad (2.4)$$

Merging formulas (2.2, 2.3, 2.4) one can obtain :

$$I_c = -e_0 A k_{ct} c_{ox} n_{s0} \times \left[\exp\left(\frac{-eV}{kT}\right) - 1 \right], \quad (2.5)$$

As shown in fig. 2-14 (b), if one applies positive bias (reverse bias) for n-type semiconductor, electrons will leave the vicinity of junction interface. The current from semiconductor to electrolyte will be possible only due to minor charge carriers (holes) flow, however their concentration is low. The current from electrolyte to semiconductor will be provided by occupied redox states in the electrolyte, however the potential barrier for those electrons is significant. Indeed, looking at (2.5), we can conclude that in case of positive bias, the contribution of exponent is negligible. At the same time application of positive bias results in downwards shift of E_F and increase V_{sc} and in consequence reduce n_{s0} . This results in very weak dark current flow in reverse bias regime, which is reflected in fig. 2-15.

The case of negative bias application for n-type semiconductor is shown in fig. 2-14 (c). In this case electrons are pushed from the conductive band of semiconductor to electrolyte. Negative sign of voltage value makes exponent in (2.5) very important. As a consequence, one can observe an exponential growth of dark current as shown in fig. 2-15.

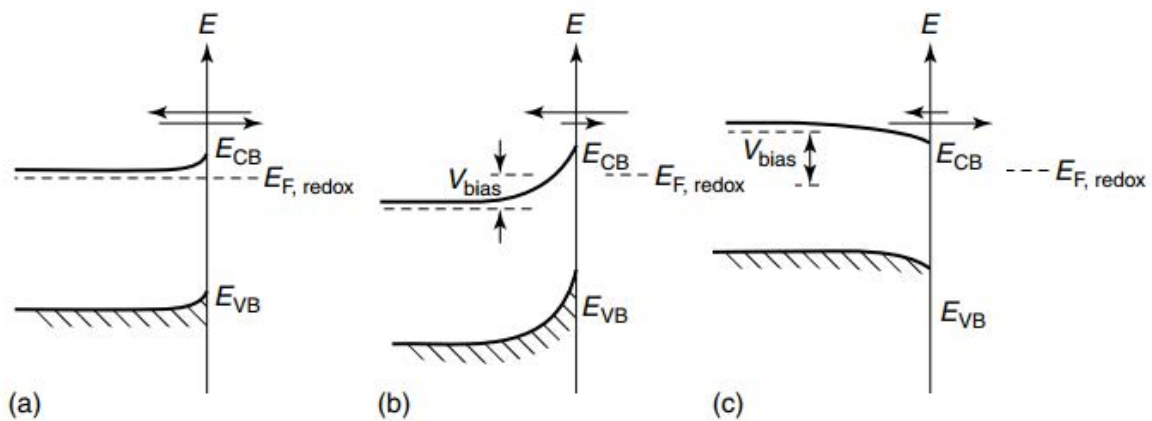


Figure 2-14 n-type semiconductor – electrolyte interface at dynamic equilibrium (a), reverse (positive) bias (b), forward (negative) bias (c)¹⁰

Thus light induced charge carriers can substantially contribute only in reverse bias regime, when the dark current is saturated at low values and no electronic interaction between electrolyte and semiconductor occurs. For n-type semiconductor we are expecting to see light induced charge carriers contribution at positive bias, as it is demonstrated in fig. 2-15

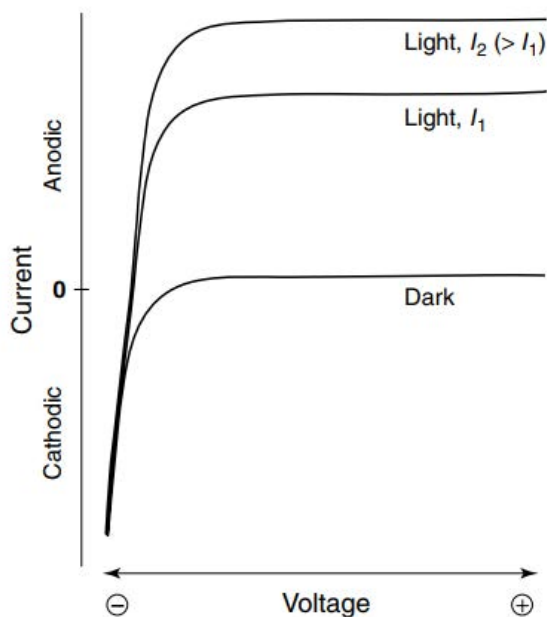


Figure 2-15 Current density in case of forward (left side) and reverse bias (right side) for the electric junction between electrolyte and n-type semiconductor¹⁰

Analogous expressions and graphics may be derived for p-type semiconductor taking into account the position of fermi level and conductivity via valence band. Fig. 2-16 summarizes theoretical expectation on the behavior of n-type and p-type semiconductor in the electrolyte under chopped illumination. If both p-type and n-type phases co-exist in the sample we expect to observe a superposition of these two cases.

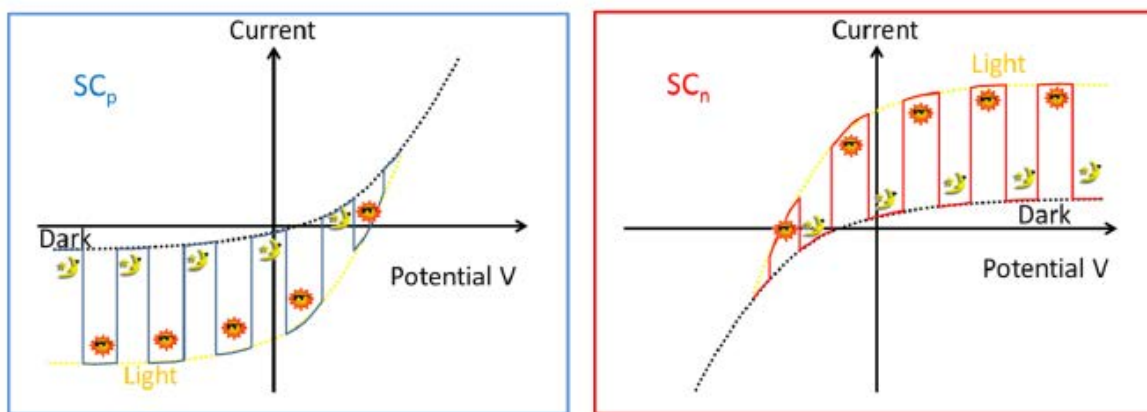


Figure 2-16 Electric behavior of the junction between p-type (left) and n-type (right) semiconductor and electrolyte under chopped illumination¹¹

Current density eventually depends on illumination power density, which for our PEC experiments is equal to $250 \text{ W} \times \text{m}^{-2}$.

PEC experiments also demonstrate the crucial role of iodine on the photoelectric response. Without iodine, very weak p-type response can be observed on fig. 2-17 (a,b), associated with the p-type Cu_2GeSe_3 crystals. With further reduction of Cu content and, therefore, Cu_2GeSe_3 proportion, very weak p-type and n-type photocurrent associated probably with Sb_2Se_3 as well as Cu_2GeSe_3 can be observed.

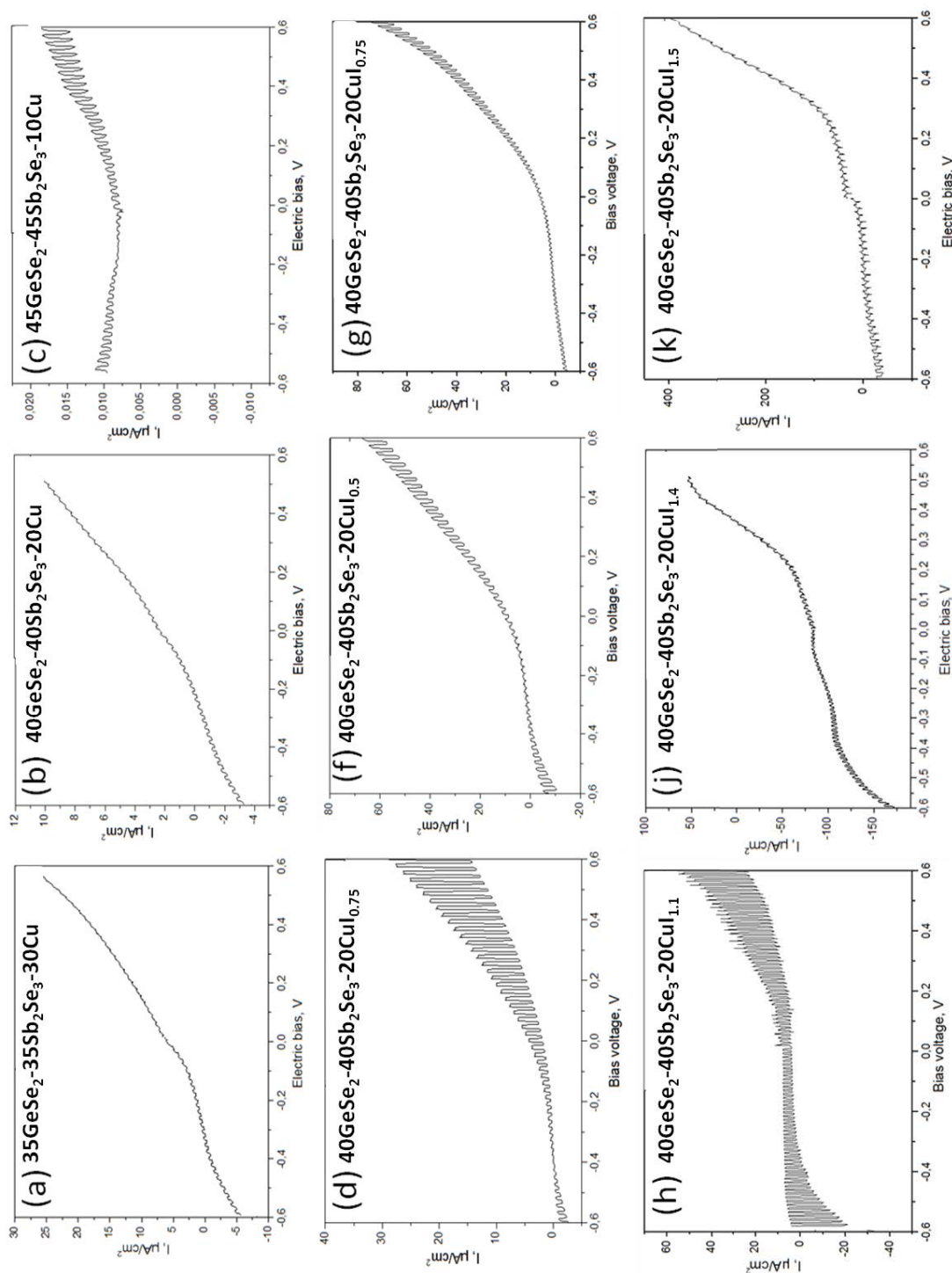


Figure 2-17 PEC curves of obtained glass-ceramics: $35\text{GeSe}_2\text{-}35\text{Sb}_2\text{Se}_3\text{-}30\text{Cu}$ (a), $40\text{GeSe}_2\text{-}40\text{Sb}_2\text{Se}_3\text{-}20\text{Cu}$ (b), $45\text{GeSe}_2\text{-}45\text{Sb}_2\text{Se}_3\text{-}10\text{Cu}$ (c), $40\text{GeSe}_2\text{-}40\text{Sb}_2\text{Se}_3\text{-}20\text{CuI}_{0.75}$ (d), $40\text{GeSe}_2\text{-}40\text{Sb}_2\text{Se}_3\text{-}20\text{CuI}_{0.5}$ (f), $40\text{GeSe}_2\text{-}40\text{Sb}_2\text{Se}_3\text{-}20\text{CuI}_{0.25}$ (g), $40\text{GeSe}_2\text{-}40\text{Sb}_2\text{Se}_3\text{-}20\text{CuI}_{1.1}$ (h), $40\text{GeSe}_2\text{-}40\text{Sb}_2\text{Se}_3\text{-}20\text{CuI}_{1.4}$ (j), $40\text{GeSe}_2\text{-}40\text{Sb}_2\text{Se}_3\text{-}20\text{CuI}_{1.5}$ (k).

As for the conductivity, the iodine content has a critical effect on the photoelectric response for the glass ceramics. More iodine-contained samples show dominantly n-type behavior, associated to the iodine-doped Sb₂Se₃. Samples with near stoichiometric CuI content can show simultaneous p- and n-type behaviors. They are also the samples showing the highest photocurrent density, as demonstrated in fig. 2-18.

In summary, we have found out that iodine role is crucial for the appearance of photoelectric response and bulk conductivity for the glass-ceramics. The optimum iodine content is close to the CuI stoichiometry. An excess of iodine is undesirable because of the SbISe phase formation, which is highly resistive.

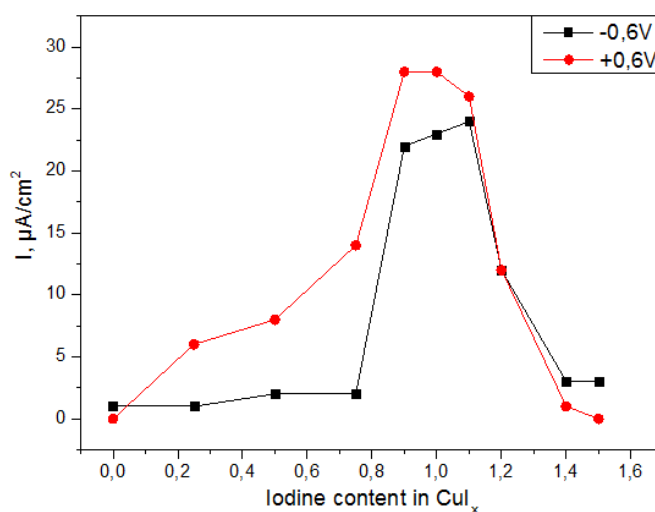


Figure 2-18 Photocurrent density of glass-ceramics with different iodine content

2 Influence of Iodine doping on the electrical properties of Sb₂Se₃.

It has been demonstrated earlier that the iodine plays a key role on the electric and photoelectric properties of the GeSe₂-Sb₂Se₃-CuI glass ceramics. To elucidate the conduction mechanism of these glass ceramics and to confirm the incorporation of iodine inside Sb₂Se₃, the influence of iodine doping on different properties of Sb₂Se₃ has been studied in details.

All the samples were prepared by melting-quenching process from purified raw materials stored and weighted in a glove box. The technique of synthesis has been described in detail earlier in this chapter. The fast quenching is used for limiting the crystal size of the obtained sample.

2.1 Influence on the structure and the electric conductivity

XRD spectra of samples with different iodine contents are depicted in fig. 2-19. All obtained samples are well crystallized. It is observed that, in addition to the Sb₂Se₃, SbISe secondary phase appears for the samples with iodine content above 8 mol. %. The Peak at 29.45° corresponding to the (1 1 2) orientation of the orthorhombic SbISe grows proportionally to iodine concentration.

In fig. 2-20 the orthogonal projection of Sb₂Se₃ crystal unit cell on (0 0 1) plane is presented¹². It can be seen that Sb₂Se₃ crystal consists of infinite chains parallel to c-axis, which are bonded together through sets of Sb-Se bonds.

Concerning the doping mechanism, the most likely possibility is that iodine takes the place of selenium in Sb₂Se₃. The difference of their ionic radius is important ($r_{\text{Se}^{2-}} = 184\text{pm}$, $r_{\text{I}^-} = 220\text{pm}$) that a direct substitution is difficult and cannot take place in a large scale without changing the structure. Such direct substitution would increase the lattice parameters, leading to a shift of Sb₂Se₃ related peaks towards lower 2θ values. Such shift is not observed even for the sample with 20 mol. % of iodine.

Previous discussion indicates that without excess, iodine doping will lead to the co-existence of doped or un-doped (or poorly doped) Sb₂Se₃ with different conductivity. It is likely that the diffraction peak shift is very small with slight iodine doping and this is not observable with our experimental condition. With more than 8 mol. % of iodine, the excessive iodine will be crystallized in a new phase, which is SbISe. Possible doping mechanism is depicted in fig. 2-21.

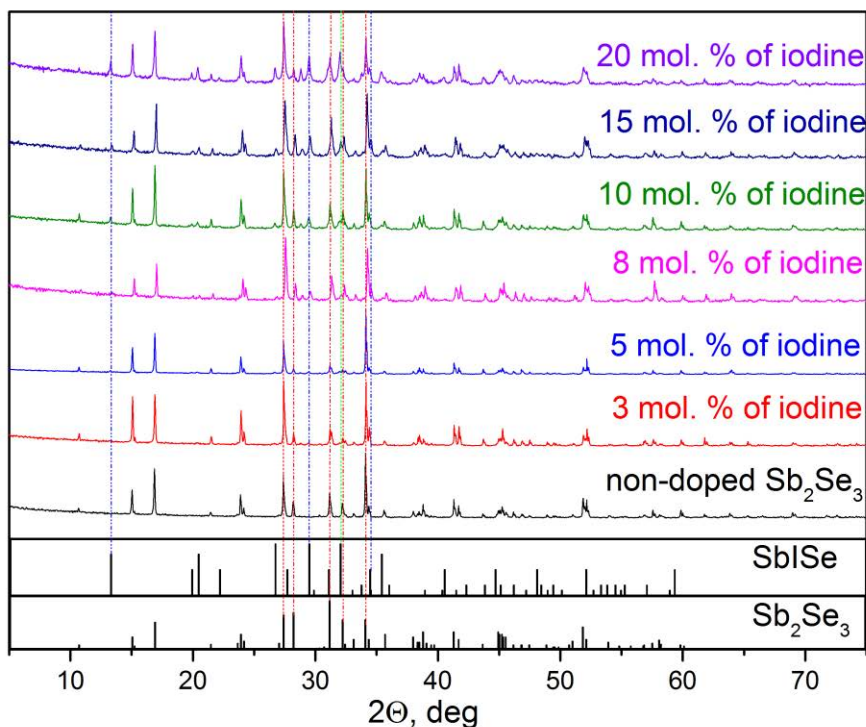
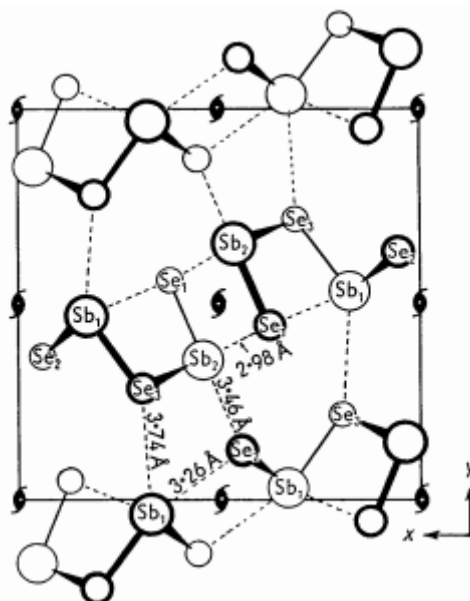
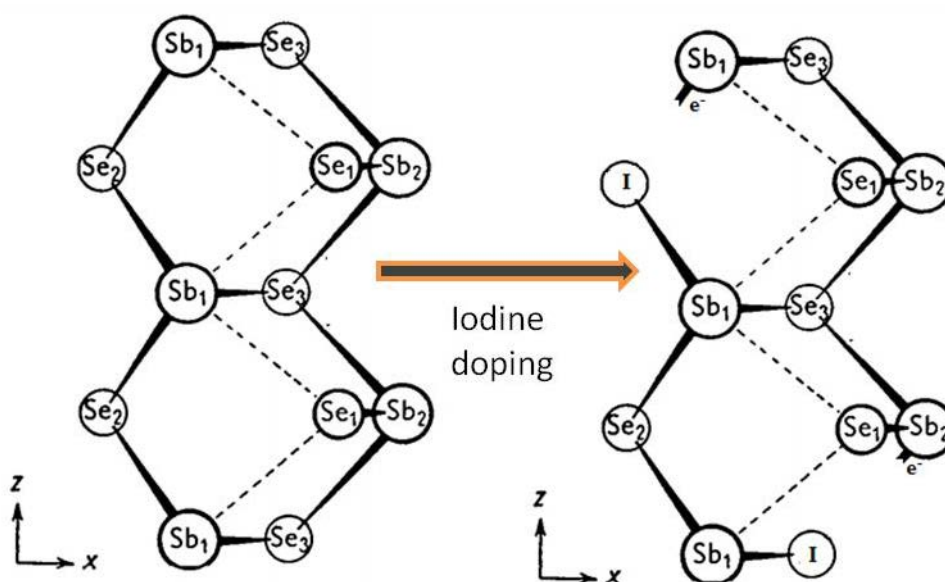


Figure 2-19 XRD diffractogram of iodine doped Sb₂Se₃_x

Figure 2- 20 Projection of Sb₂Se₃ unit cell on (0 0 1) plane¹²Figure 2- 21 Possible mechanism of Sb₂Se₃ iodine doping. Modified from¹².

AFM and KPFM images (fig. 2-22 (a, b)) show a homogenous and equipotential surface of non-doped Sb₂Se₃. One can find weak photocurrent density under negative bias, usually attributed to p-type materials. This can be explained by certain compositional inhomogeneity which will be discussed further. Similar photoresponse was obtained for Sb₂Se₃ nanowires by Choi et al.¹³. The resistivity of the obtained Sb₂Se₃ bulk is equal to $2 \times 10^9 \Omega \times \text{cm}$.

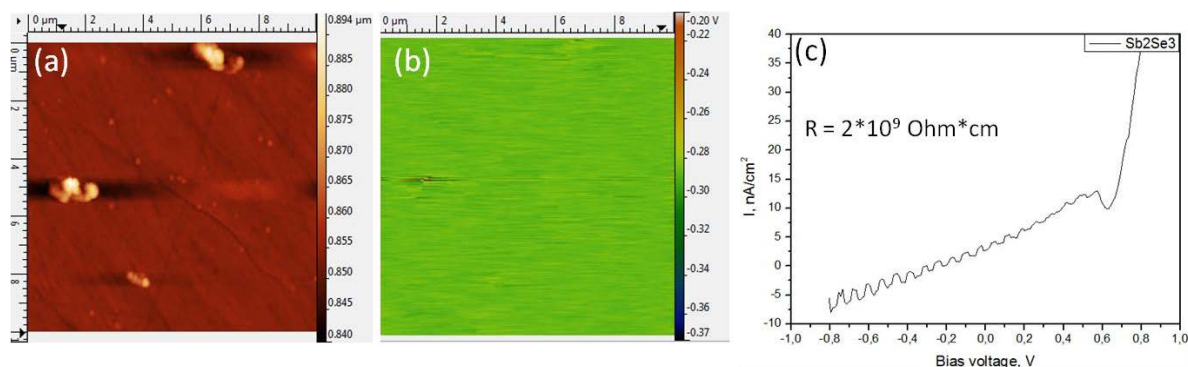


Figure 2-22 Non-doped Sb₂Se₃ AFM image (a), Kelvin probe microscopy image (b), and PEC curve with resistivity measurement (c)

Introduction of iodine inside Sb₂Se₃ results in the appearance of some microscopic rod-like loose agglomerations fig. 2-23(a, b) that can be distinguished from Sb₂Se₃ bulk rods, which have larger scale. For the sample with 20 mol. % of selenium (fig. 2-23c) two types of crystalline structure can be observed: microscopic separated rods and sintered sheet-like structure which consist of some needle-like crystals. Energy-dispersive X-ray spectroscopy (EDS) analysis (fig. 2-24) shows very different compositions. While separated rods contain more than 20 at. % of iodine, there are only 10 at. % at the site of sheet-like crystalline aggregates. The composition analysis is performed over a domain and the high iodine content can be the result of some mixture of Sb₂Se₃ (doped or not) and SbISe, as suggested by the XRD.

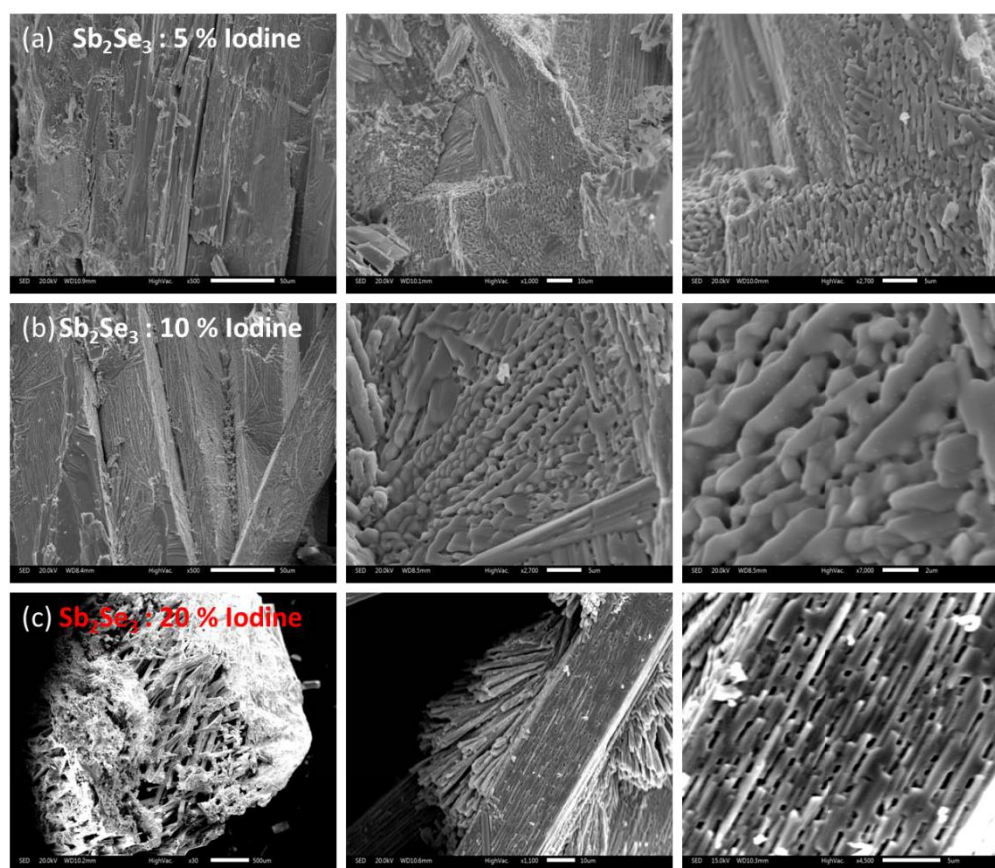


Figure 2- 23 SEM images of Sb₂Se₃ doped with Iodine (a) - 5 mol. % Iodine, (b) - 10 mol. % Iodine, (c) - 20 mol. % iodine

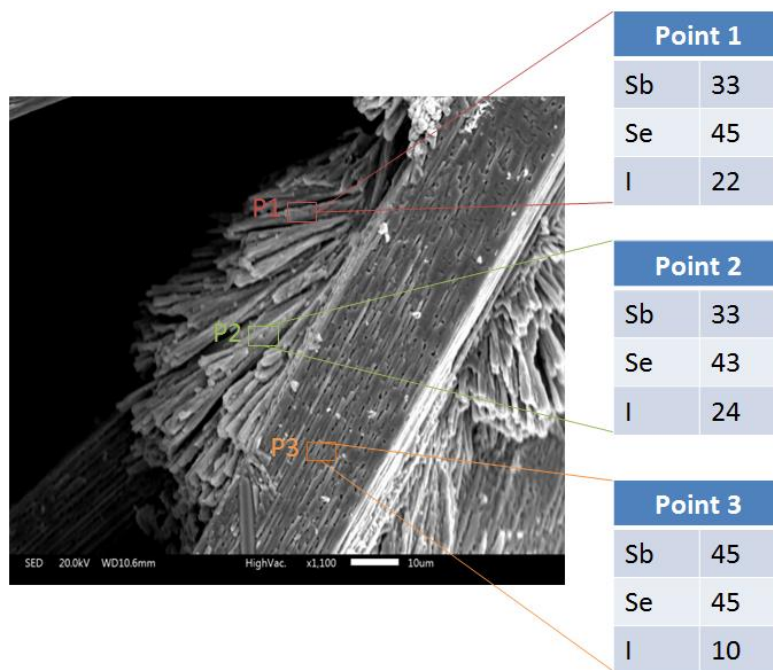


Figure 2-24 EDS spectra of 20 mol. % iodine sample.

In fig. 2-25 the dependence of the electrical resistivity on iodine content is depicted for Sb₂Se₃. One can observe a rapid ($>10^5$) decrease of resistivity upon the introduction of 3 mol. % of iodine. Further decrease is much slower and obtain its minimum for the sample with 15 mol. % of iodine, where the resistivity is equal to 68 $\Omega \times \text{cm}$. It slightly increases for 20 mol. % of iodine.

If we consider that iodine plays a role of electronic dopant, we can apply the formula:

$$\sigma = ne\mu_e \quad (2.6)$$

where n is charge carriers concentration, μ_e is mobility of charge carriers, e is elementary charge.

In this case, iodine can bring a large number of free-charge carriers which leads to rapid increase in conductivity. At the same time:

$$\mu_e = \frac{e\tau}{m_e} \quad (2.7), \text{ where}$$

τ is scattering time, m_e is effective mass of charge carrier,

$$\tau = \frac{1}{SN_s v_{th}} \quad (2.8), \text{ where}$$

S is scattering cross – section, v_{th} – thermal velocity, N_s – number of scatters per volume unit

Then, we obtain:

$$\sigma = \frac{ne^2}{meSN_s v_{th}} \quad (2.9)$$

Therefore we are dealing with two opposite forces. On one hand introduction of iodine increases charge carrier concentration due to modification of Sb₂Se₃ structure and disengagement of antimony-

associated electrons (see fig. 2-21). However, on the other hand charge carriers scattering rate also increases due to increase of non-conductive SbISe phase content. As the dominant scattering centers we can consider following: impurities (dopants) itself, variety of crystalline imperfections and formation of non-conductive SbISe phase, which can be also represented as a major scattering center. Thus these two opposite forces meet each other in the equilibrium for the sample with 15 mol. % of iodine. Further increase of iodine content makes scattering components dominant compare to new charge carriers injection. Hence, further doping is useless and will apparently lead to the conductivity reduction.

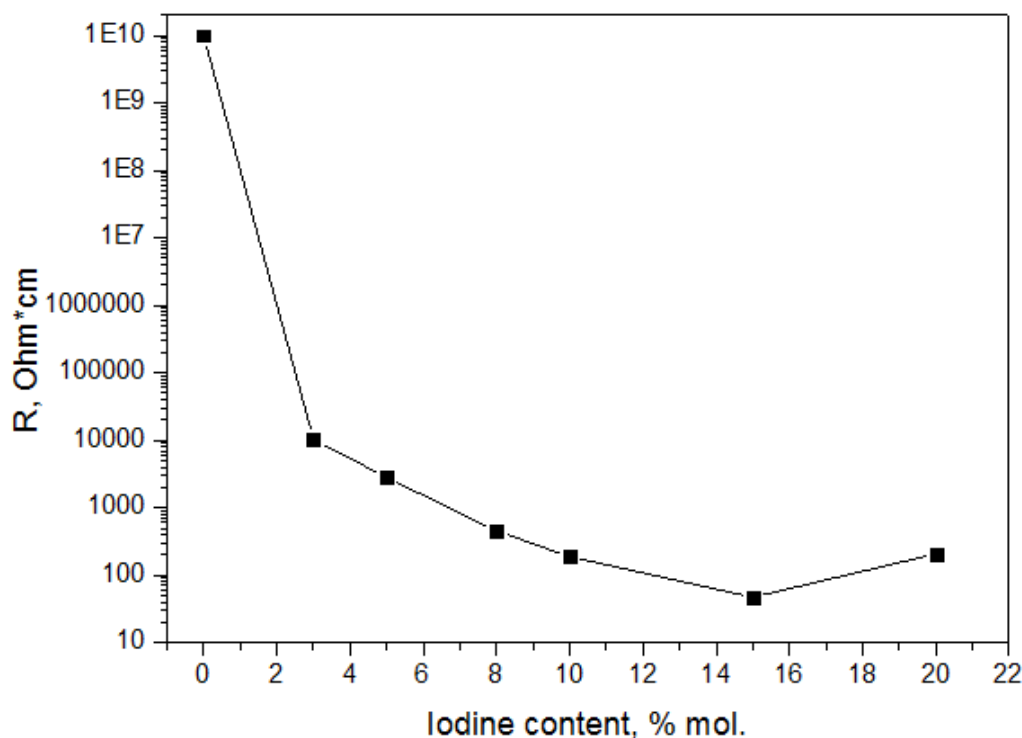


Figure 2-25 Dependence of resistivity of Sb₂Se₃ : I bulk crystals on iodine content

2.2 On the photoelectric properties

PEC measurement (fig. 2-26) confirms that iodine doped Sb₂Se₃ is an n-type semiconductor, with strong photoconductive effect pronounced under positive bias. Maximal photocurrent density obtained under positive bias curve changes similarly with the change of the resistivity vs iodine content, which is expected since photogenerated charge carriers undergo the same scattering process. 650 $\mu\text{A}/\text{cm}^2$ under the positive bias +0.6V with illumination of 250 $\text{W}\times\text{cm}^{-2}$ is obtained for the sample with 15 mol. % of iodine. It is useful to underline that the samples obtained via melting-quenching process did not undergo any additional heating treatment. The sample is directly crystallized even with fast quenching. As a comparison, the maximal photocurrent density obtained for glass-ceramics under the same positive bias +0.6V is equal to 160 $\mu\text{A}/\text{cm}^2$.

One could also mention the presence of p-type photogenerated current, which continues to increase even with high iodine content. The appearance of p-type photocurrent indicates possible local inhomogeneities within the bulk, containing other phases with different doping mechanism. This will be discussed in details in paragraph 2.5.

Obtained photocurrent densities under maximal positive (+0.6V) and maximal negative (-0.6V) bias for different content of iodine are summarized in fig. 2-27.

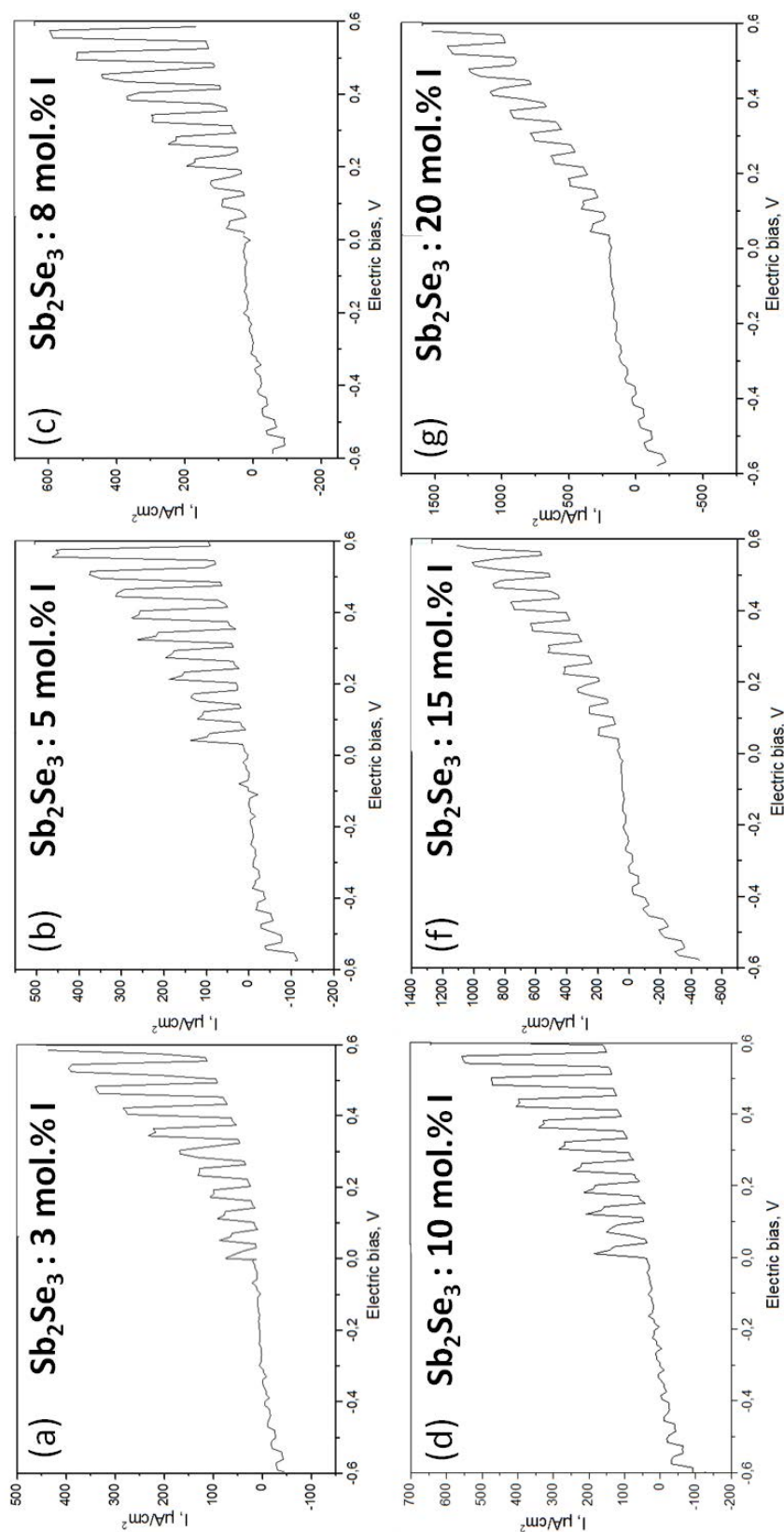


Figure 2-26 PEC curves of iodine doped Sb₂Se₃ crystals with different amount of iodine.

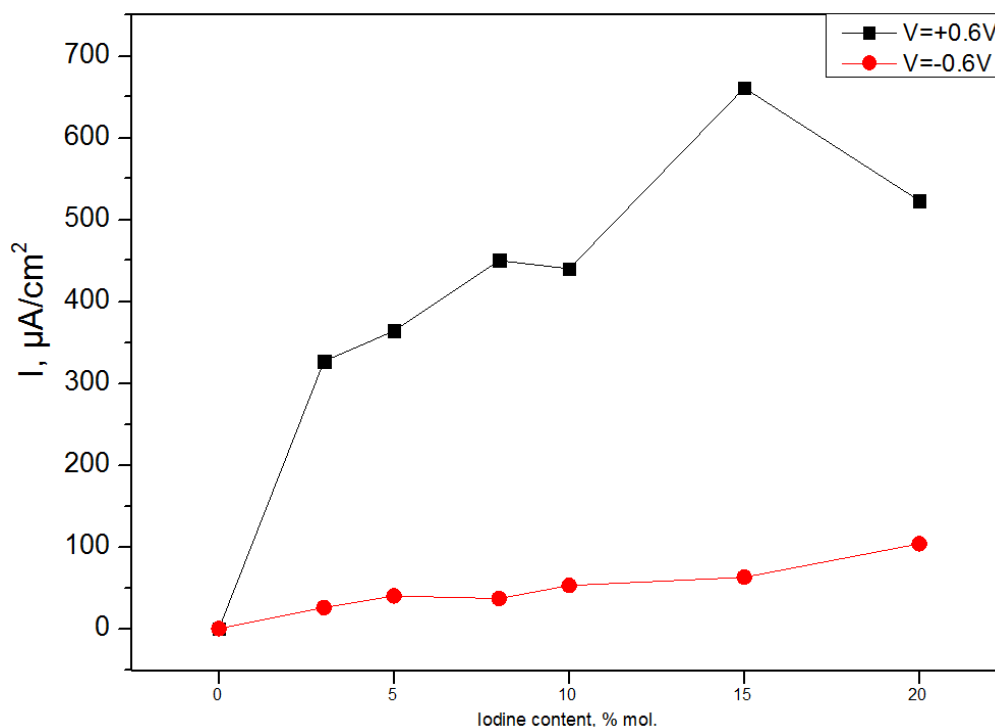


Figure 2-27 Maximal photocurrent obtained for bulk crystals with different content of iodine

In summary for this paragraph, we have synthesized a series of Iodine doped Sb₂Se₃ crystals. We have demonstrated significant morphological changes associated with the formation of iodine doped Sb₂Se₃ and SbISe crystalline aggregates. Despite that the doping mechanism is not totally evidenced, it is likely that iodine takes the place of selenium in the crystalline structure of Sb₂Se₃. Serving as a strong electron donor, it makes charge carrier concentration to increase fast, which leads to drastical increase of electrical conductivity. On the other hand, further augmentation of iodine content increases charge carrier scattering rate by giving rise to resistive SbISe phase. We have found that 15 mol. % of iodine is the optimal doping concentration, which provides the lowest resistivity of 68 Ω×cm and the maximal photocurrent of 650μA/cm² at +0.6V bias.

3 Fine tuning of the 40GeSe₂-40Sb₂Se₃-20CuI precursor glass

3.1 On fine tuning in this system

As we mentioned in the Introduction section, the composition 40GeSe₂-40Sb₂Se₃-20CuI was studied as a material for infrared transmission. Presence of free charge carriers and photoelectric effect was found by chance. Thus, we could barely believe that this composition is optimal. However with more and more experience we were persuaded that it is either optimal or very close to optimal composition for our purposes. We will show the possibility to slightly reduce GeSe₂ content without affecting photoelectric properties in Chapter III. However our initial goal was to improve photocurrent intensity. Therefore we tried to tune precursor composition varying selenium quantity with a very small step.

For nomenclature reasons we will rewrite 40GeSe₂-40Sb₂Se₃-20CuI to Ge₁₁Sb₂₂Cu₅I₅Se₅₆. In this paragraph we will observe structural and electric properties of Ge₁₁Sb₂₂Cu₅I₅Se_{56-x}, where x = 2.8, 5.6 and of Ge₁₁Sb₂₂Cu₅I₅Se_{56+x}, where x = 0.56, 1.12, 1.68, 2.24, 2.8, 3.36, 3.92, 4.48, 5.04, 5.6, 11.2.

3.2 Glass precursor preparation and characterization.

Obtained precursors were glasses with pronounced glass-transition peak (fig. 2-28). One can mention that glass with stoichiometric content of selenium Ge₁₁Sb₂₂Cu₅I₅Se₅₆ is the less stable through the whole set of samples. Reduction of selenium quantity leads to slight decrease of T_g and increase in T_x at the same time. The same is observed during the increase of selenium content; however T_g decrease is more pronounced (fig. 2-29). Optical transmission measurement shows that all these glasses are transparent and do not present any significant scattering loss due to the presence of crystals (fig. 2-30).

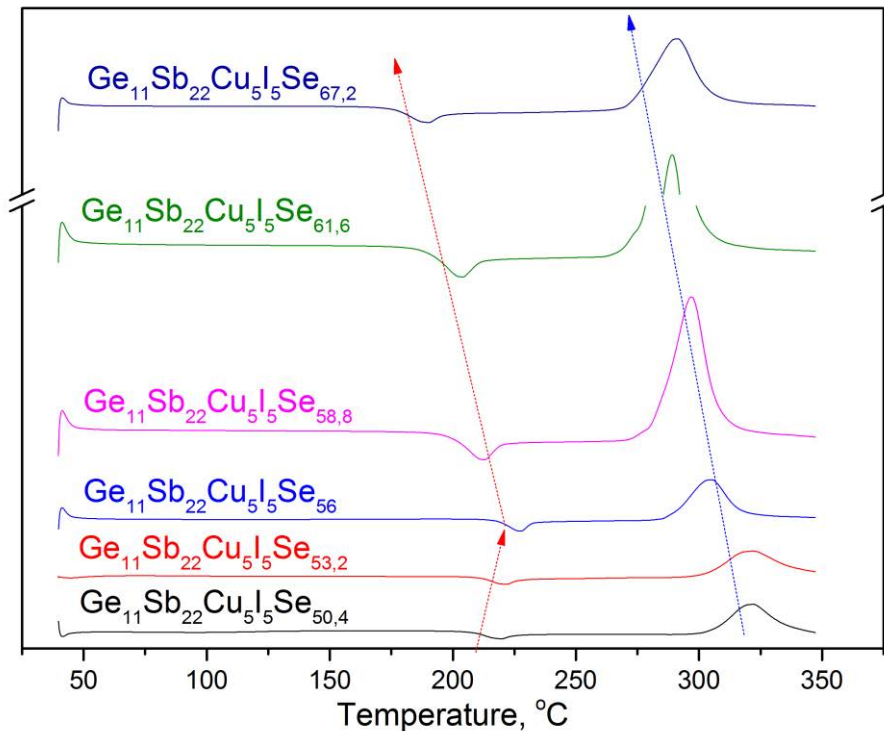


Figure 2-28 DSC spectra of glassy precursors

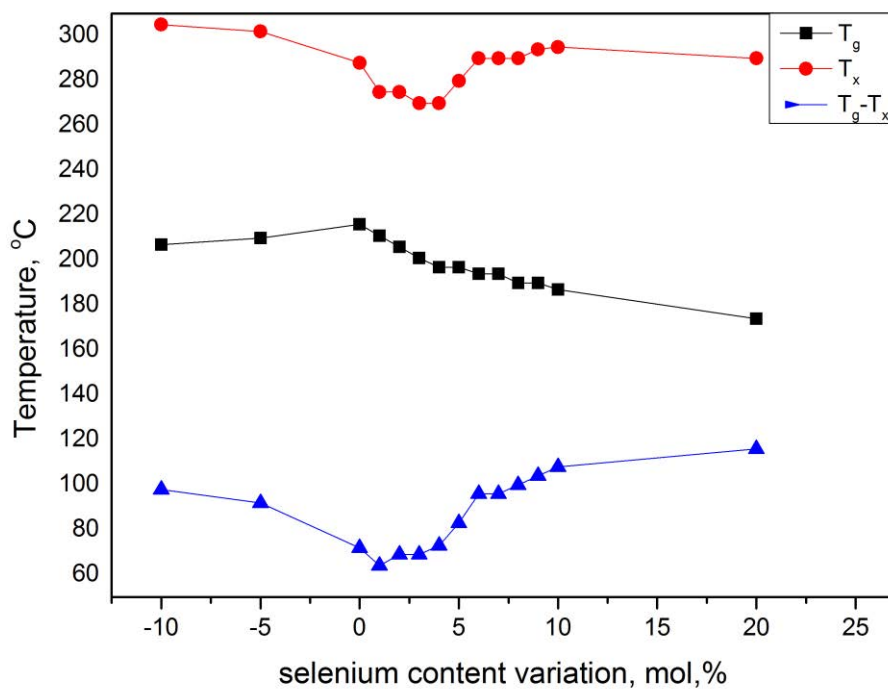


Figure 2-29 Glass precursor glass transition (T_g), crystallization temperature (T_x), and thermal stability ($T_x - T_g$) as a function of selenium content

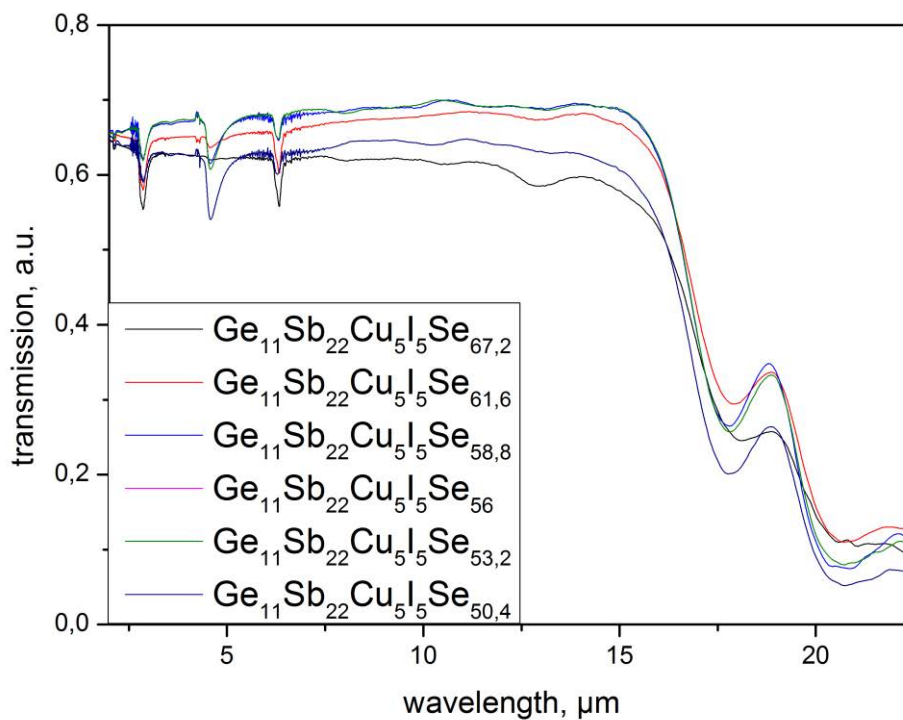


Figure 2-30 IR transmission spectra for glass precursors with different amount of selenium

3.3 Preparation and characterization of glass-ceramics.

Glass-ceramics were obtained by annealing of glass precursor at T_x for 1 hour and re-polished after.

XRD spectra of obtained glass-ceramics are shown in fig. 2-31. With decrease of selenium content, a relative intensity growth of the orthorhombic Cu_2GeSe_3 crystalline phase (0 1 1) is observed. It is possible that with decrease of Se content the amount of stable GeSe_4 tetrahedrals within the glassy phase decreases also making Ge more available for Cu_2GeSe_3 formation. At the same time, we are observing shift of Sb_2Se_3 and Cu_2GeSe_3 related peaks towards higher 2θ values, which signs shrinking of lattice parameters. This could be explained by appearance of some void-type defects within the crystal cell upon the lack of selenium.

It can also be explained by the fact that Cu_2GeSe_3 is more favorable to grow under slightly higher temperature. In this case T_x shift on the DSC curves is only associated with Sb_2Se_3 crystallization temperature upon the variation of Se content in glass-precursor. As T_x increases in both cases (reduction and augmentation of Se content) and the annealing temperature is T_x , therefore, the annealing conditions are more favorable for Cu_2GeSe_3 growth. This could explain appearance of more pronounced Cu_2GeSe_3 peak for Se rich samples also.

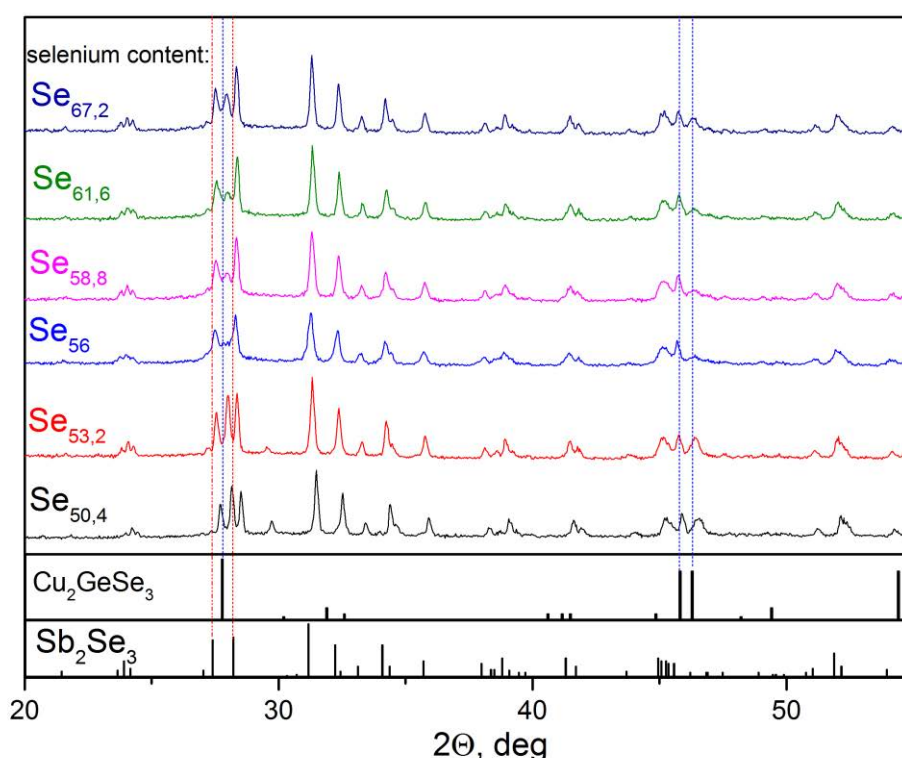


Figure 2-31 XRD spectra of glass-ceramics with different Selenium content

As one can see in fig. 2-32 slight increase of selenium content leads to improvement of resistivity compare to the stoichiometric composition. Lowest resistivity is observed for sample with 6

mol. % excess of selenium. This can be explained by increase of bridge bondings in glass precursor, where iodine is capable to end the chain, and in consequence the amount of Sb₂Se₃ doped iodine increases. Further increase of selenium content leads to slight reduction of conductivity, which further maintains on the same values. This could sign that iodine doping distribution reaches its optimum. At the same time reduction of selenium content leads to fast increase in resistivity. We cannot suppose severe morphological changes, or dramatic reduction of iodine doped Sb₂Se₃ crystals. (This can happen but not at such severe extent). However as it was described in paragraph 2.4.1, formula 2.9, conductivity is defined by concentration of injected charge carriers and scattering probability. Last one, apparently, increases because of excessive Cu₂GeSe₃ phase crystallization which plays role of scattering centers. One could suppose that XRD peaks shift related to Se-poor glass-ceramics connected with appearance of some void-type defect as we mentioned before. This type of defects could also serve as recombination centers.

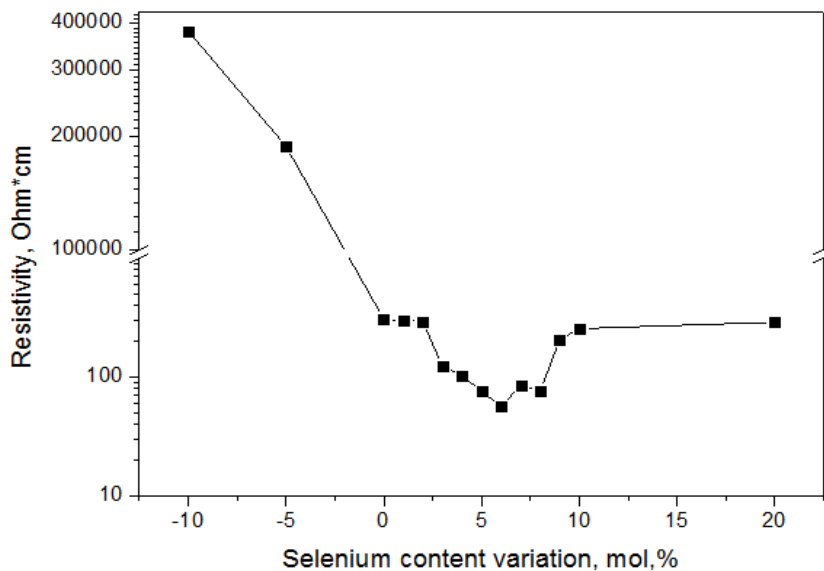


Figure 2- 32 Dependence of resistivity of glass-ceramics on selenium content

Set of PEC measurement is presented in fig. 2-34. We can mention complete loss of photoresponse for the glass-ceramic with 10 mol. % of Se deficiency (fig. 2-34(a)). This sample is, in fact, too resistive. With slight increase of conductivity, a weak photoresponse of p-type semiconductor behavior is observed, probably due to the presence of Cu₂GeSe₃ (fig. 2-34(b)). The maximum photocurrent density is reached for the sample with 5 mol. % of Se excess, is equal to $J = 128 \mu\text{A}/\text{cm}^2$ (fig. 2-34(g)). This composition has also the lowest resistivity. Photocurrent densities obtained for glass-ceramics with different amount of Se are summarized in fig. 2-33.

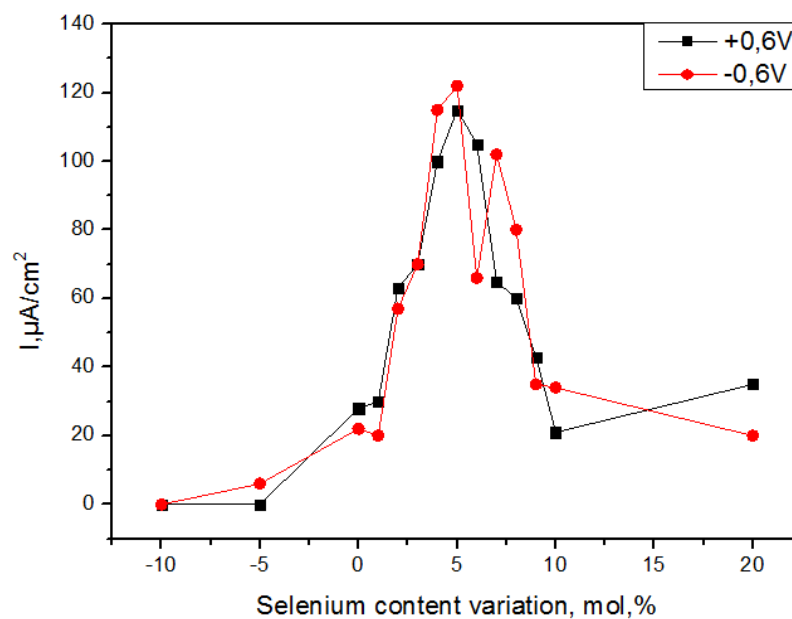


Figure 2-33 Maximal photocurrent obtained as a function of selenium molar content

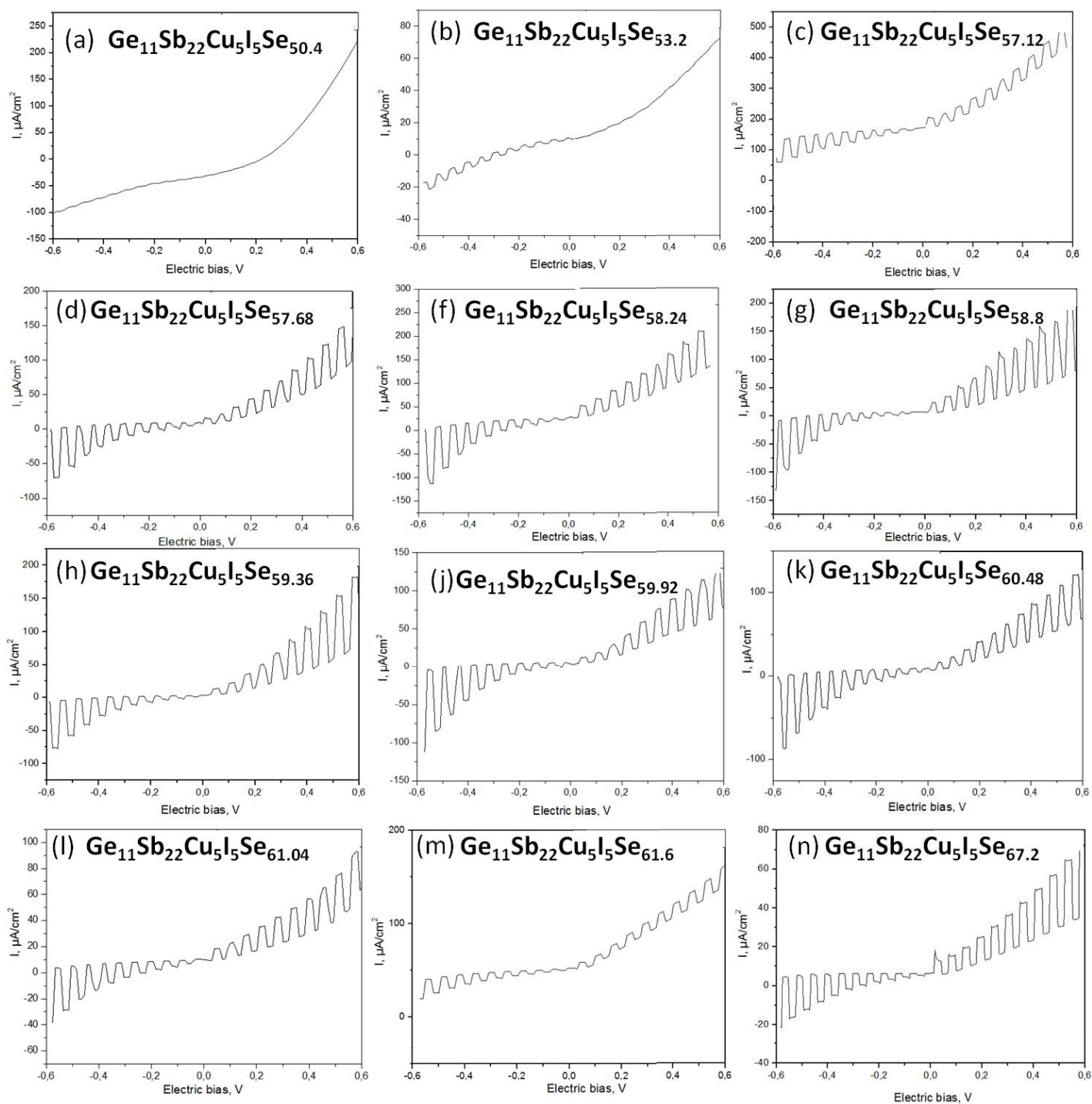


Figure 2-34 PEC curves of glass-ceramics with different molar content of selenium

3.4 Optimization of annealing procedure for Ge₁₁Sb₂₂Cu₅I₅Se_{58.8} glass-ceramic.

Considering the above-discussed results, a more detailed study has been performed on glass-ceramics with 5 mol. % excess of Se, in relationship with the microstructure. Thus, we tried to optimize annealing process to find out the optimal configuration. In fig. 2-35 are presented the XRD diffractograms for a set of glass ceramics annealed at T_x for different durations. We can establish that 30 min. annealing is sufficient for obtaining above discussed structure with well-defined Sb₂Se₃ and Cu₂GeSe₃ diffraction peaks. Further annealing does change neither relative intensity of peaks, nor its position. It is possible to confirm this from resistivity dependence on annealing time, where it reaches its optimum for 30 min. annealed glass-ceramics (fig. 2-36). The excessive annealing temperature very slightly decreases the overall conductivity.

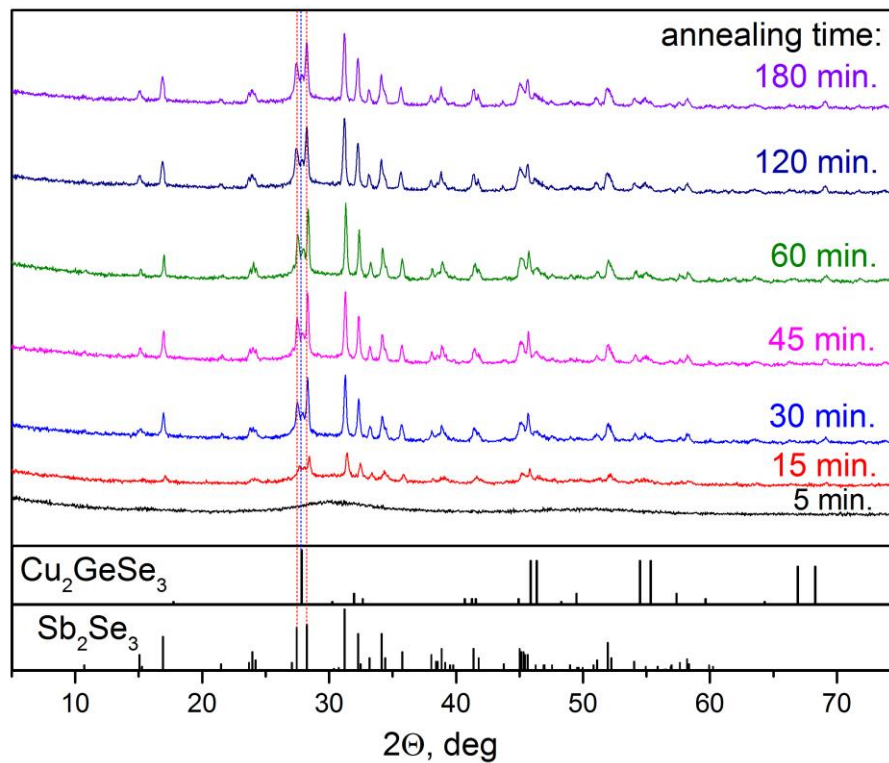


Figure 2-35 XRD diffractogram of Ge₁₁Sb₂₂Cu₅I₅Se_{58.8} glass-ceramics annealed at T_x for different time (0-180 min.)

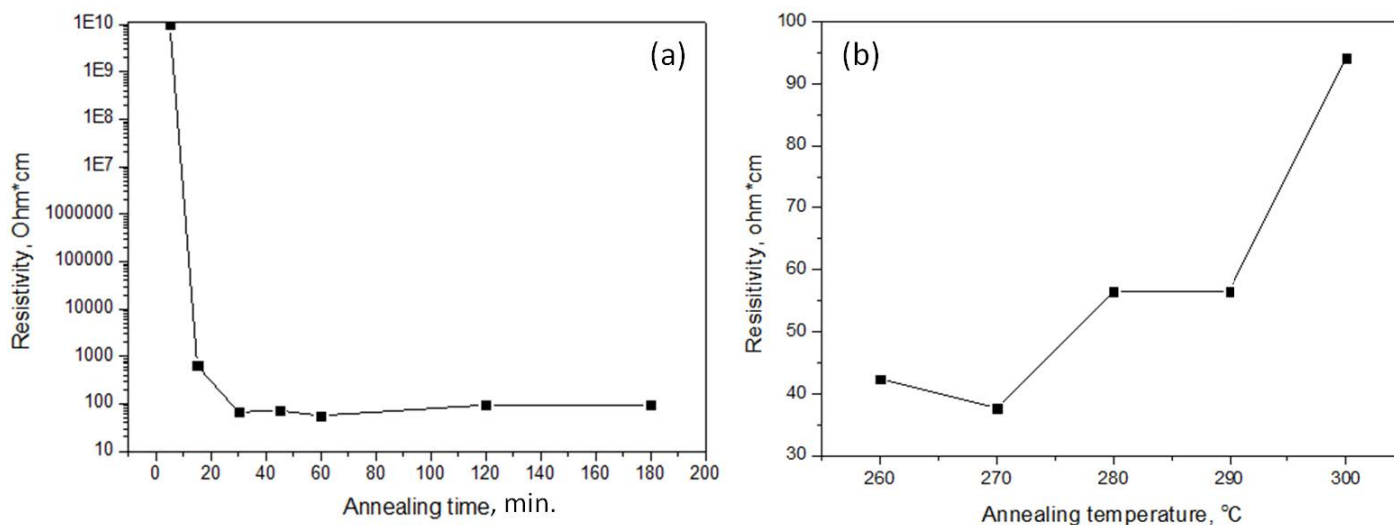


Figure 2-36 Dependence of resistivity of Ge₁₁Sb₂₂Cu₅I₅Se_{58.8} glass-ceramic on annealing time (annealed at T_x) (a) and temperature (annealed for 60 min.) (b).

Fig. 2-37 and fig. 2-38 show PEC curves of glass-ceramics obtained at different annealing times and temperatures. We can mention that a significant photoresponse can be obtained even for 15 min. annealed glass-ceramics with $j|_{V=+0.6(-0.6)} = 70$ (45) $\mu\text{A}/\text{cm}^2$. It reaches its maximum after 60 min. of annealing. Further annealing is not favorable for microstructural crystalline organization and leads to the reduction of photocurrent.

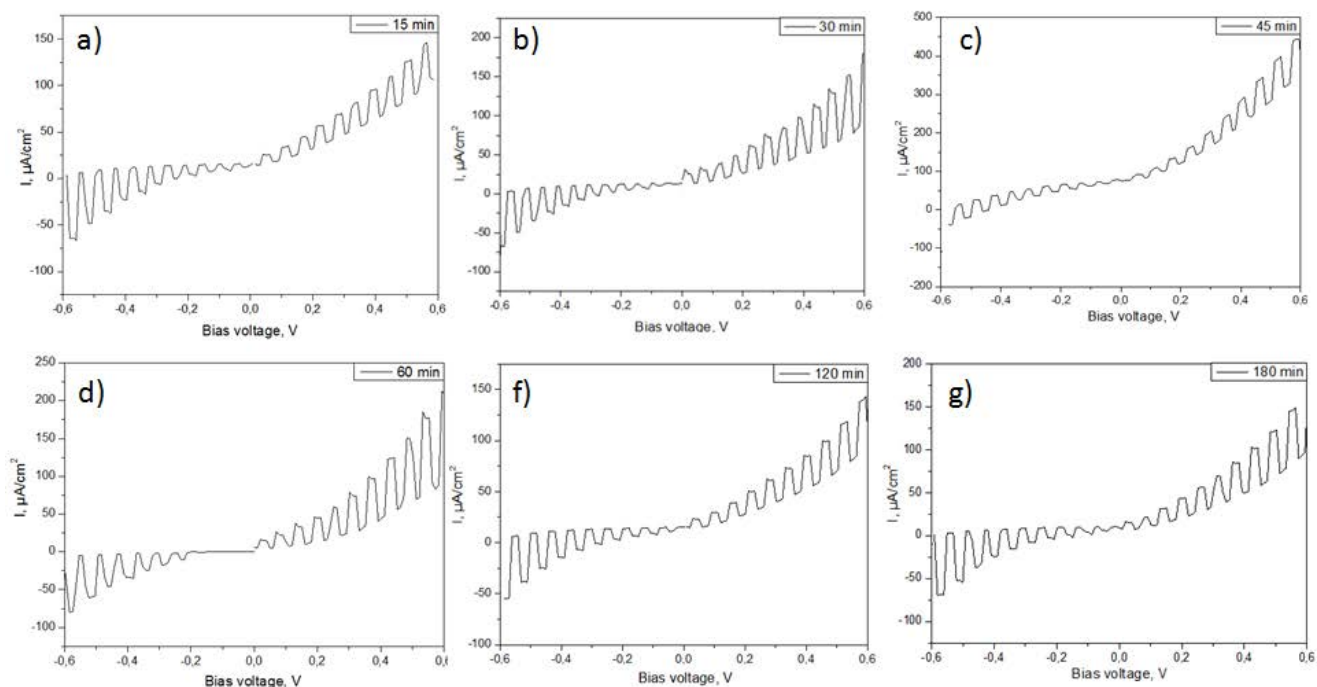


Figure 2-37 PEC curves of glass-ceramics annealed for different time at T_x

We can observe that with increase of annealing temperature, photocurrent density follows resistivity dependence trend and reduces (fig. 2-39). The optimal annealing temperature is $260\text{ }^\circ\text{C}$, where photocurrent reaches $160\text{ (}78\text{)}\ \mu\text{A}/\text{cm}^2$ at $+0.6\text{ (-}0.6\text{)}\text{V}$ bias (fig. 2-38 a)). The overall photocurrent reduction is probably associated with the reduction of conductivity caused by some undesirable excessive crystallization, that leads to less favorable arrangement of photoconductive phases ($\text{Sb}_2\text{Se}_3\text{:I}$) and phases serving as scattering centers (SbISe , Cu_2GeSe_3).

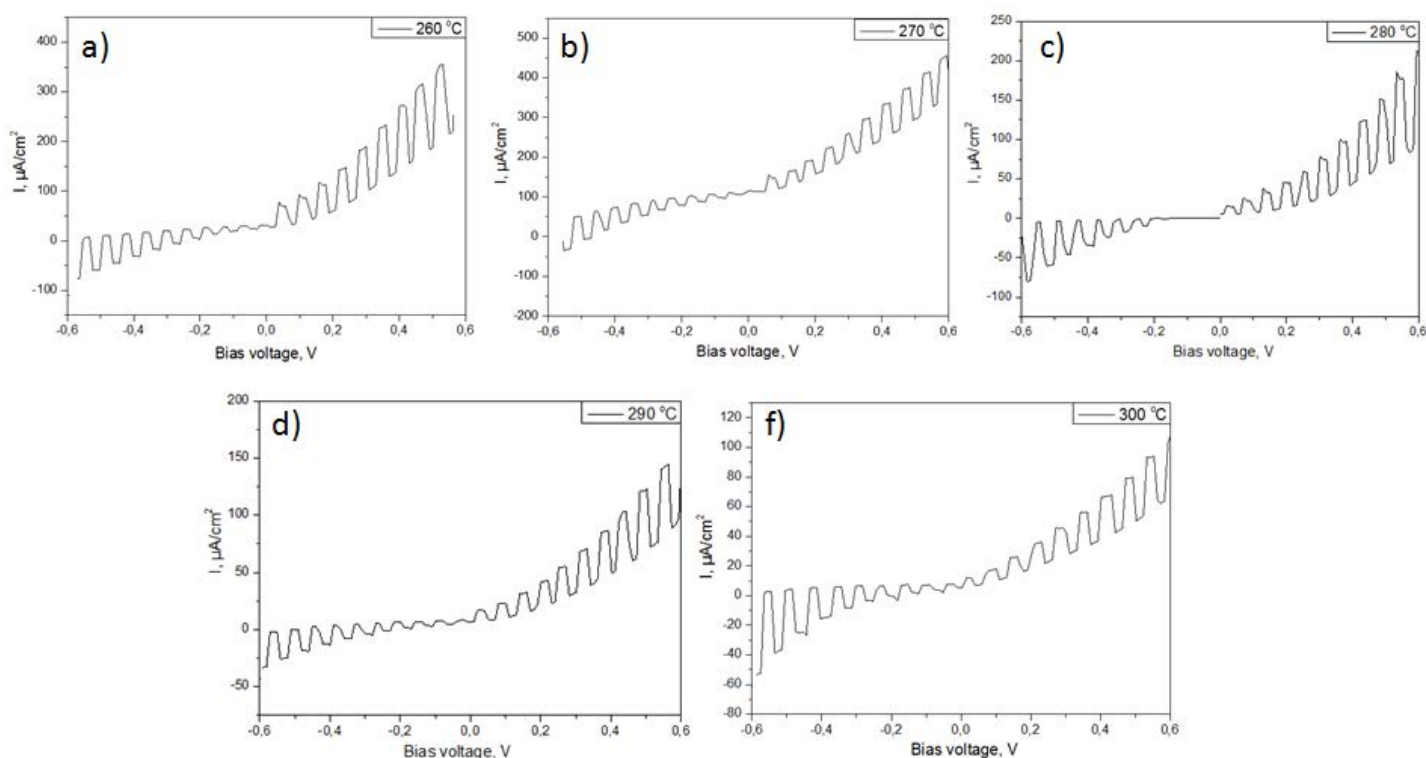


Figure 2-38 PEC curves of $\text{Ge}_{11}\text{Sb}_{22}\text{Cu}_5\text{I}_5\text{Se}_{58.8}$ glass-ceramic annealed at different temperatures.

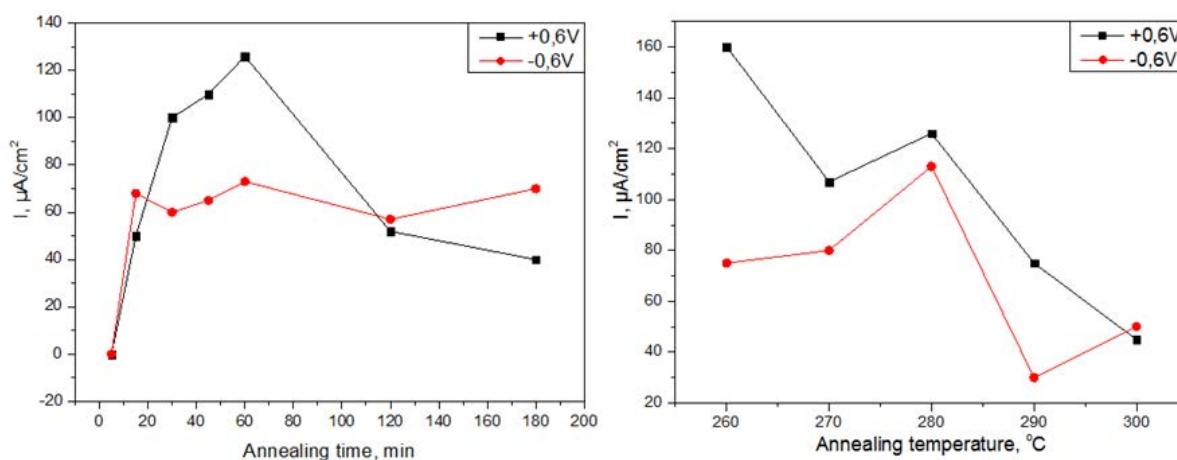


Figure 2-39 Maximal photocurrent density obtained for $\text{Ge}_{11}\text{Sb}_{22}\text{Cu}_5\text{I}_5\text{Se}_{58.8}$ glass-ceramics as a function of annealing time (annealed at T_x) (left) and temperature (annealed for 1 hour) (right)

In summary for this paragraph, we observed an improvement of conductivity upon the introduction of excessive selenium quantity in glass precursor to a certain extent -6 mol. %. We concluded that excessive selenium positively influence on internal bulk microstructure and improves the photogeneration and transport of charge carriers. It was found that the sample with 5 mol. % of Se excess demonstrates the most intense photocurrent. Further, a detailed study for optimizing the annealing conditions shows that the increase of annealing temperature or duration is undesirable since it leads to degraded photoelectric properties. We have obtained glass-ceramics with photocurrent of 160 (78) $\mu\text{A}/\text{cm}^2$ at +0.6 (-0.6) V for illumination density equal to $250 \text{ W}\times\text{cm}^{-2}$. For the moment this is the best result obtained for glass-ceramics in this pseudo-ternary system $\text{GeSe}_2 - \text{Sb}_2\text{Se}_3 - \text{CuI}$.

4 Influence of stoichiometric deviations on Sb_2Se_3 electrical properties.

It has been demonstrated that the stoichiometry has an important influence on the electric and photoelectric properties of glass-ceramics. Consequently, we have decided to study the influence of stoichiometry on the properties of crystalline Sb_2Se_3 , which is a key component of the glass ceramics.

It was unexpected to find p-type semiconductor response under negative bias for iodine doped Sb_2Se_3 (fig. 2-26). Presence of significant concentration of holes in preferentially n-type semiconductor made us think about certain compositional inhomogeneity. Inhomogeneous crystallization looks possible since crystals were prepared by melting quenching process where viscosity increases very fast and appearance of microscopic domains with excess or deficiency of certain elements is highly possible. However appearance of p-type semiconducting zones in any case cannot be associated with iodine which is for sure an electronic dopant. To find out the reason of such behavior we prepared pure Sb_2Se_3 crystals with certain deficiency or excess of Selenium.

In fig. 2-40 are presented the XRD spectra of selenium – poor compositions. We can observe slight shift towards higher 2Θ values of the diffraction peak located at about 28.6° during the reduction of Se molar content. This peak is associated with hexagonal antimony (0 1 2) with cell parameters $a=b=4.307 \text{ \AA}$, $c = 11.273 \text{ \AA}$. We can conclude that Sb_2Se_3 maintains its structure but Sb does not take place of Se, since this would cause a shift toward lower 2Θ values (atomic radius of Sb (140pm) larger than one of Se (103pm)). In contrary here, a shift in a different direction is observed, which could signify that lack of Se leads to the formation of selenium vacancies within the crystalline structure of Sb_2Se_3 presented in fig. 2-20 and fig. 2-21 (left). At the same time, we remark the precipitation of excessive Sb in above mentioned hexagonal phase. These two processes co-exist simultaneously.

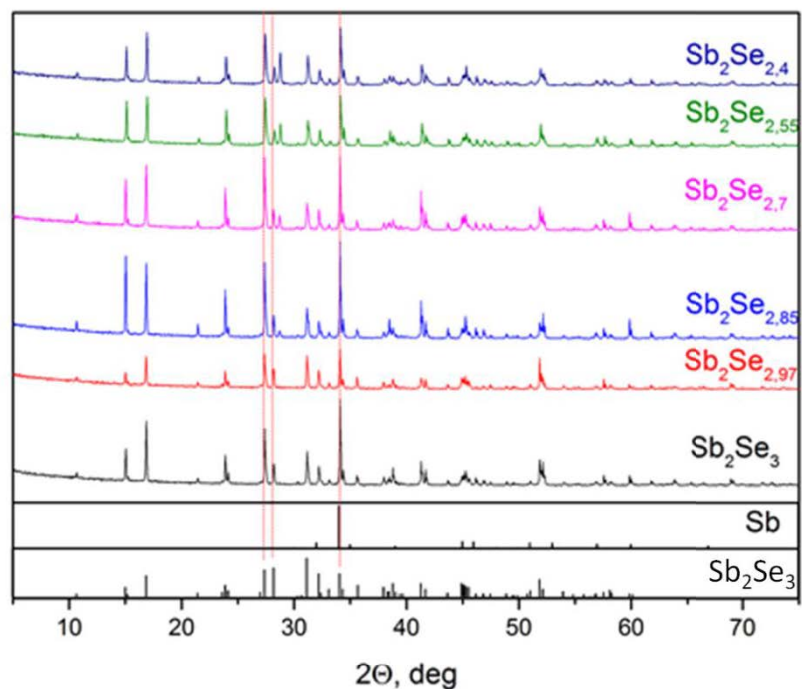


Figure 2-40 XRD spectra of Se-poor Sb₂Se₃ crystals

A set of SEM images is depicted in fig. 2-41. We can mention that, in general, morphology does not undergo significant changes. We do not find any traces of major secondary phase neither. One can observe aggregates of rod and sheet-like crystals typical for bulk Sb₂Se₃.

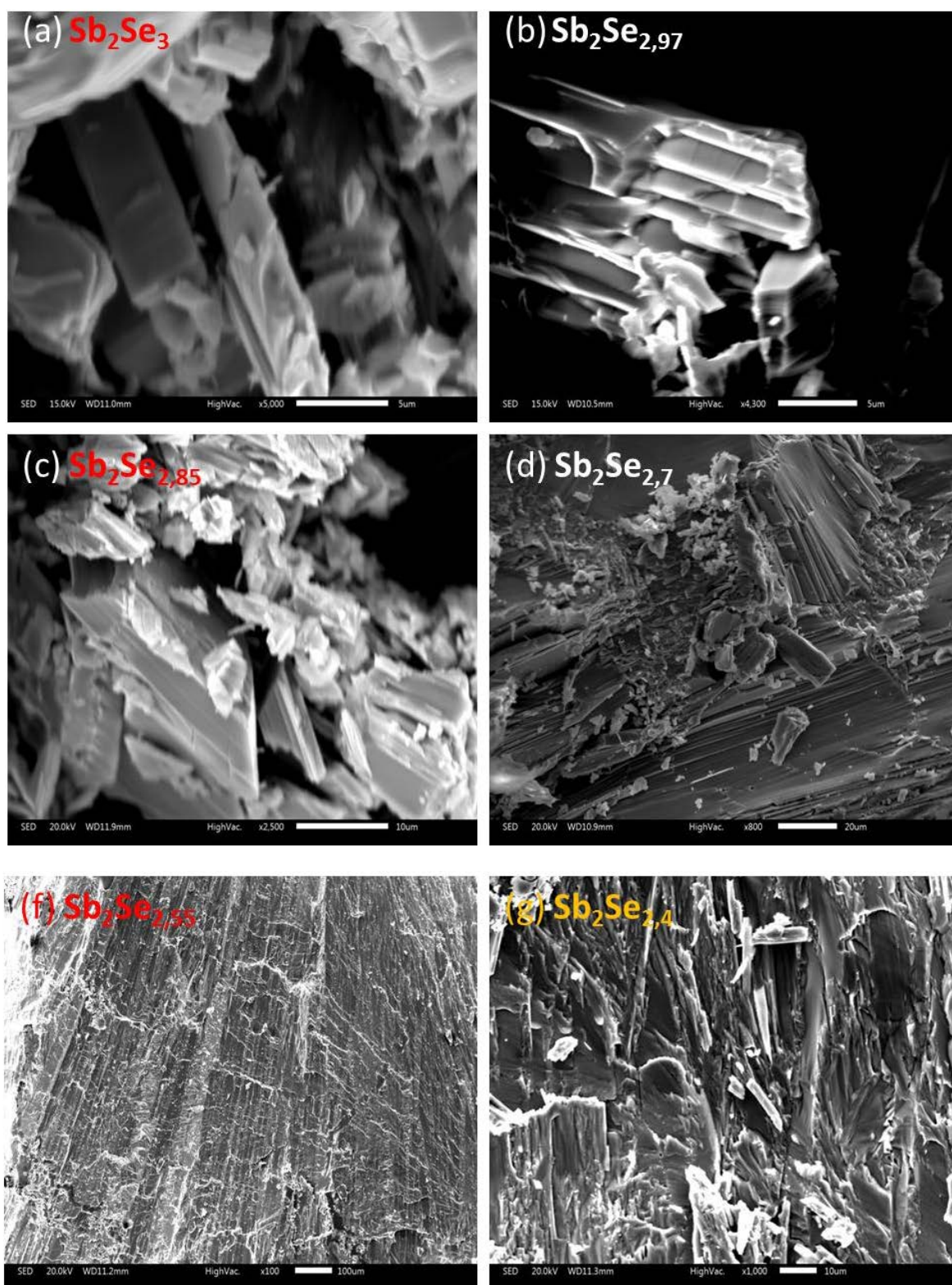


Figure 2-41 SEM images of (a)Sb₂Se₃, (b)Sb₂Se_{2.97}, (c)Sb₂Se_{2.85}, (d)Sb₂Se_{2.7}, (f)Sb₂Se_{2.55}, (g)Sb₂Se_{2.4} crystals

In fig. 2-42 the EDS analysis of Sb₂Se_{2.7} is presented. We have found severe inhomogeneity of composition, as expected. While sintered sheet-like aggregates show excess of selenium compare to stoichiometry with ration close to 50/50 (point 2, point 4), loose rod-like structure shows excess of antimony which corresponds to Sb₇Se₃ proportion (point 3).

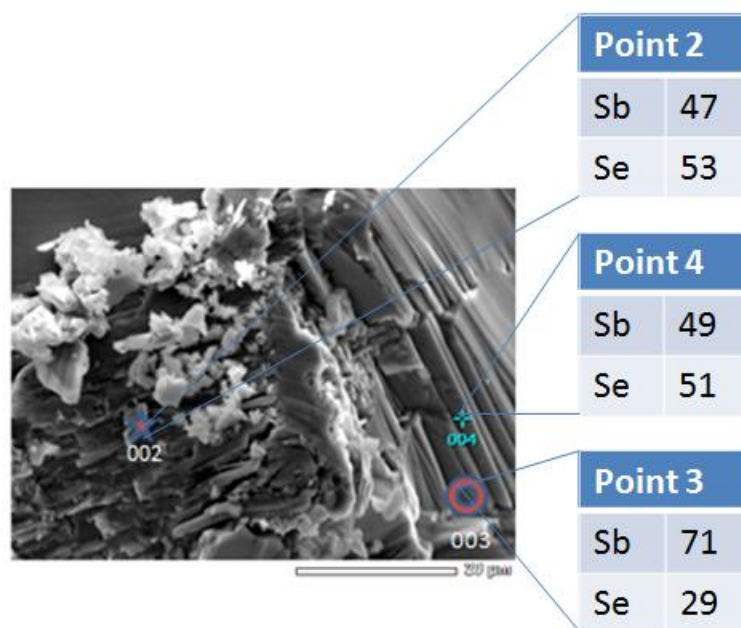


Figure 2- 42 SEM image and EDS analysis of several spatial zones.

Further PEC measurements confirmed our suggestion concerning the influence of composition inhomogeneity on the formation of p-type and n-type micro domains within Sb₂Se₃ crystalline structure. As one can see in fig. 2-43, with the reduction of Se quantity, the overall resistivity decreases.

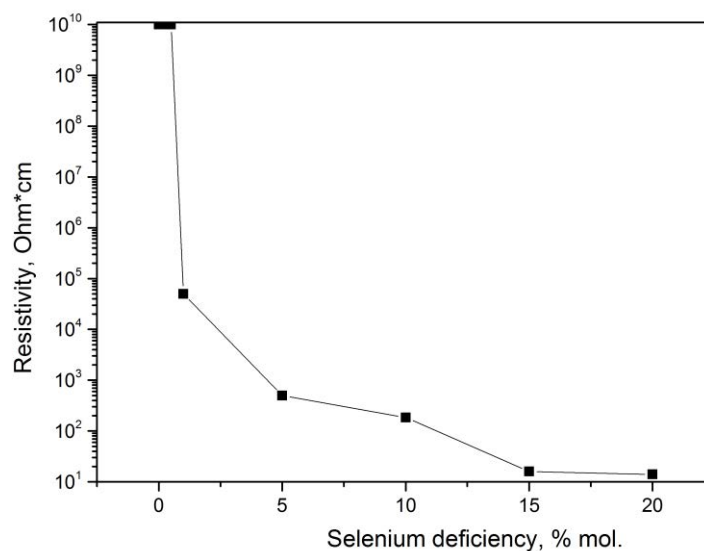


Figure 2-43 Dependence of resistivity on the selenium deficiency rate in Sb₂Se₃ crystals

The non-stoichiometric Sb₂Se₃ crystals obtain distinctly pronounced n-type semiconducting properties and demonstrate photoconductive properties. With increase of Sb/Se ratio, the conductivity and photocurrent under positive bias increases (fig. 2-44). At the same time for all

samples with deficiency of selenium above 1 mol. % (fig. 2-44(d)) we are observing pronounced photoresponse under negative bias associated with p-type semiconducting phase. It is worth mentioning that p-type photocurrent increases upon the reduction of Se quantity, which signs that inhomogeneity becomes more important upon the increase of selenium deficiency. The excessive Sb amount precipitates in secondary phase.

Therefore we can conclude that with reduction of Selenium quantity, the crystalline structure becomes more 'flexible' for compositional variations and severe difference in element content could be found in different micro domains as shown in fig. 2-42. This induces increase of electronic conductivity (charge carriers concentration) due to Se vacancies and at the same time increase of hole conductivity (p concentration), apparently due to Se-Sb defects, where Se²⁻ atom approaches Sb³⁺ atom in the lattice and partially attracts its electronic density creating non-compensated positively charged areas. Two cases are represented in fig. 2-46.

The photocurrent is quite important and reaches 380 (95) $\mu\text{A}/\text{cm}^2$ at +0.6 (-0.6)V bias for Sb₂Se_{2.4} sample under illumination density of 250 $\text{W}\times\text{m}^{-2}$. This could also be considered as one of mechanisms of photoelectric properties appearance within bulk glass-ceramics. Maximal photocurrent values obtained for different Se deficiency rate summarized in fig. 2-45

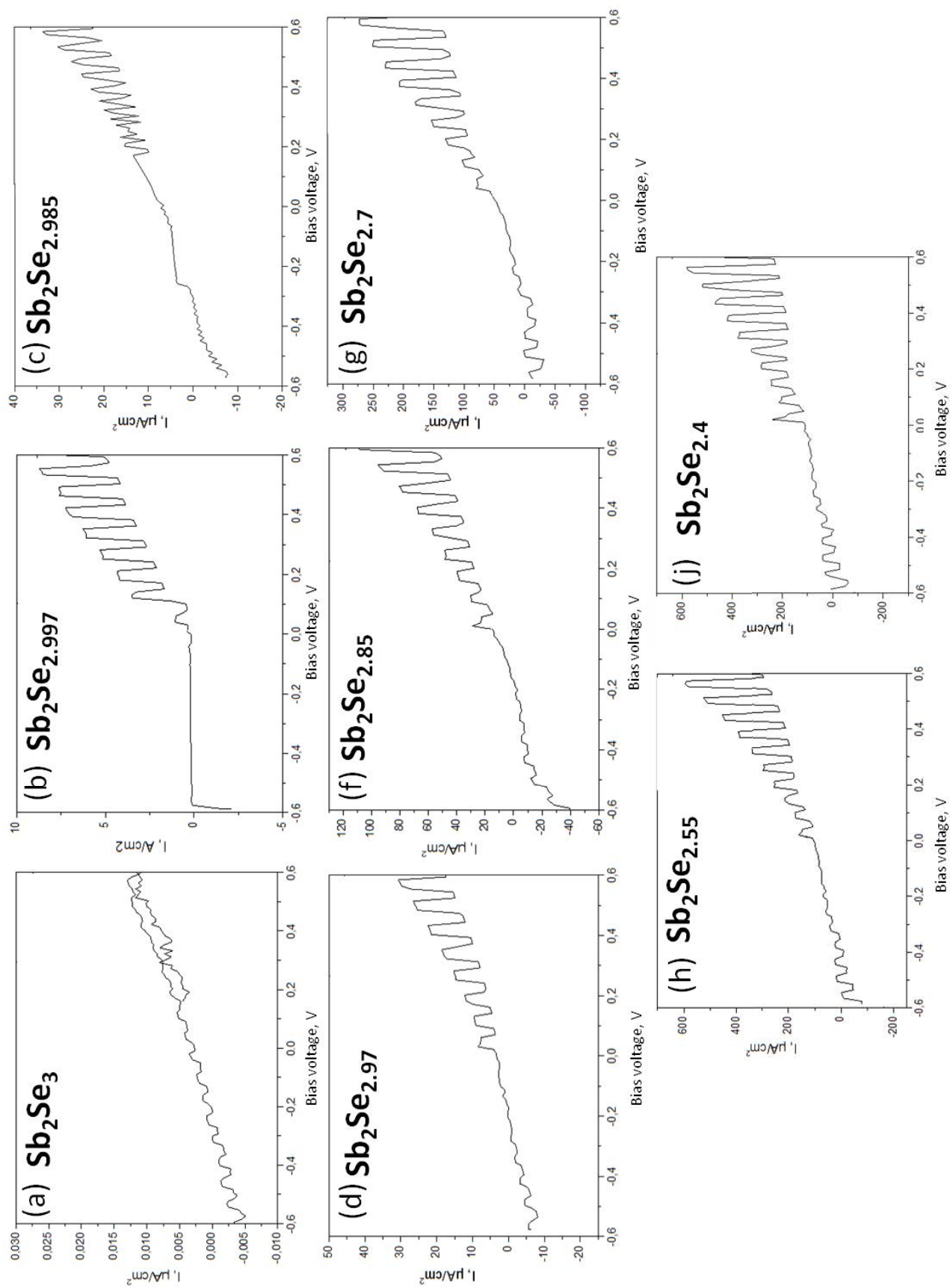


Figure 2- 44 Set of PEC curves for different selenium content

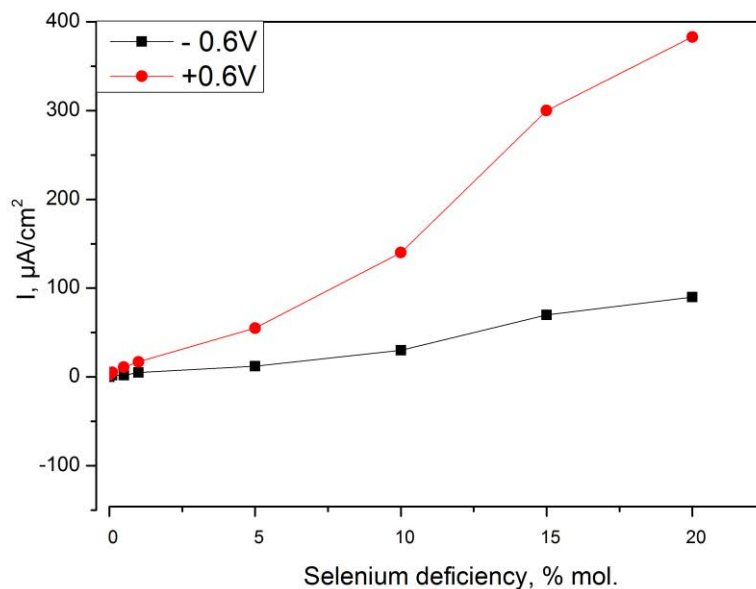


Figure 2-45 Maximal photocurrent obtained for different selenium rate in Sb_2Se_3 crystals

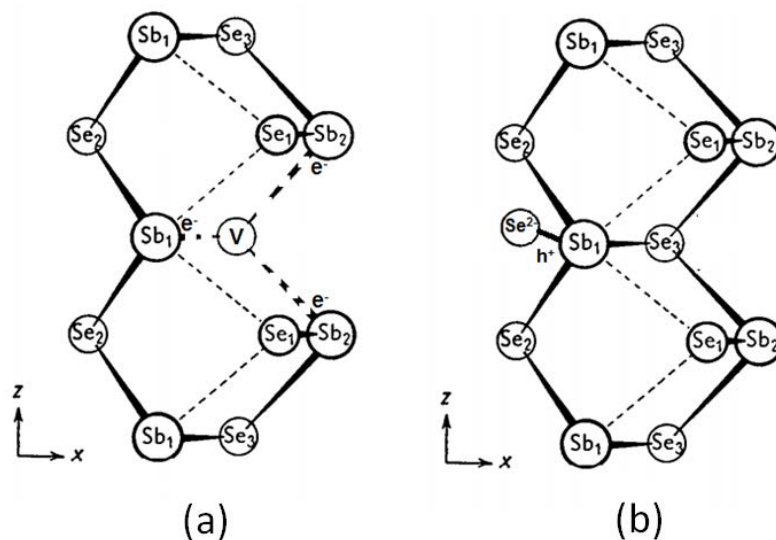


Figure 2-46 Schematic representation of influence of selenium deficiency (left) and selenium excess (right). Modified from¹²

With introduction of 1 mol. % of selenium in excess, the Sb_2Se_3 crystal switches its conductivity type from N to P. This is confirmed by both PEC curve and SEMILAB p/n tester, depicted in fig. 2-47. This device generates electron-hole pairs on the surface of the material under coherent chopped light. Being capacitively coupled with the sample surface p/n probe measures the difference of surface potential under illumination and in the dark. Comparing these values it is possible to determine conductivity type with high precision.

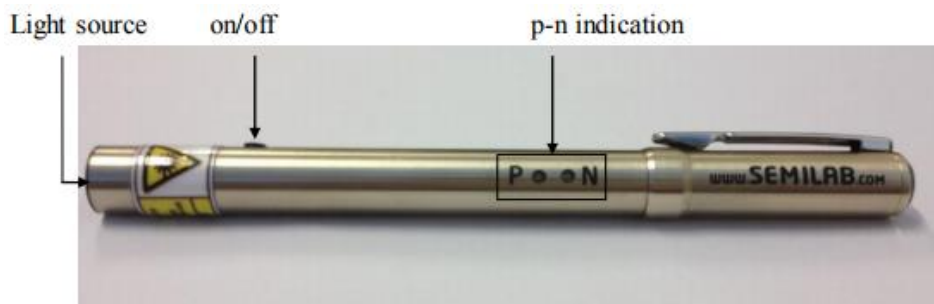


Figure 2-47 Photograph of SEMILAB p/n tester.

On XRD spectra showed in fig. 2-48 one can find out slight shift toward higher 2θ values for Sb_2Se_3 major peaks, which is understandable if we suppose substitution of Sb by Se or Sb-vacancy. At the same time, precipitation of monoclinic selenium with cell parameter $a = 9.05 \text{ \AA}$ $b = 9.07 \text{ \AA}$ $c = 11.61 \text{ \AA}$ is obvious with its main XRD peak at 29.454° , corresponding to the (0 0 1) orientation. We can find selenium precipitations also on SEM images (fig. 2-49).

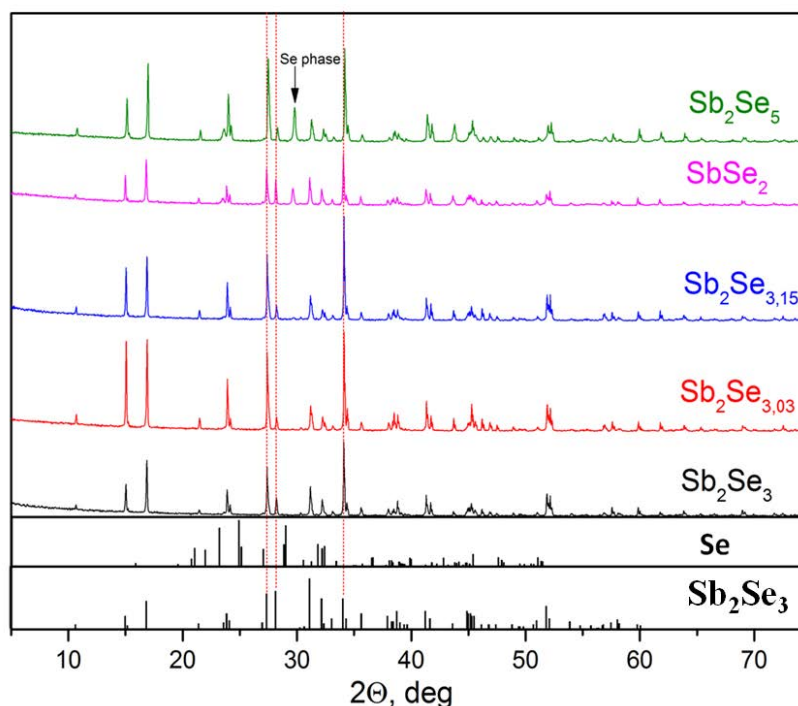


Figure 2-48 XRD diffractograms of selenium-rich Sb_2Se_3 crystals

Consequently, we can conclude that for nonstoichiometric Sb_2Se_3 , with Sb or Se excess, microscopic composition inhomogeneity can exist in the bulk sample obtained with the melt-quenching technique. P-type and N-type micro domains can co-exist within a macroscopically homogenous bulk sample.

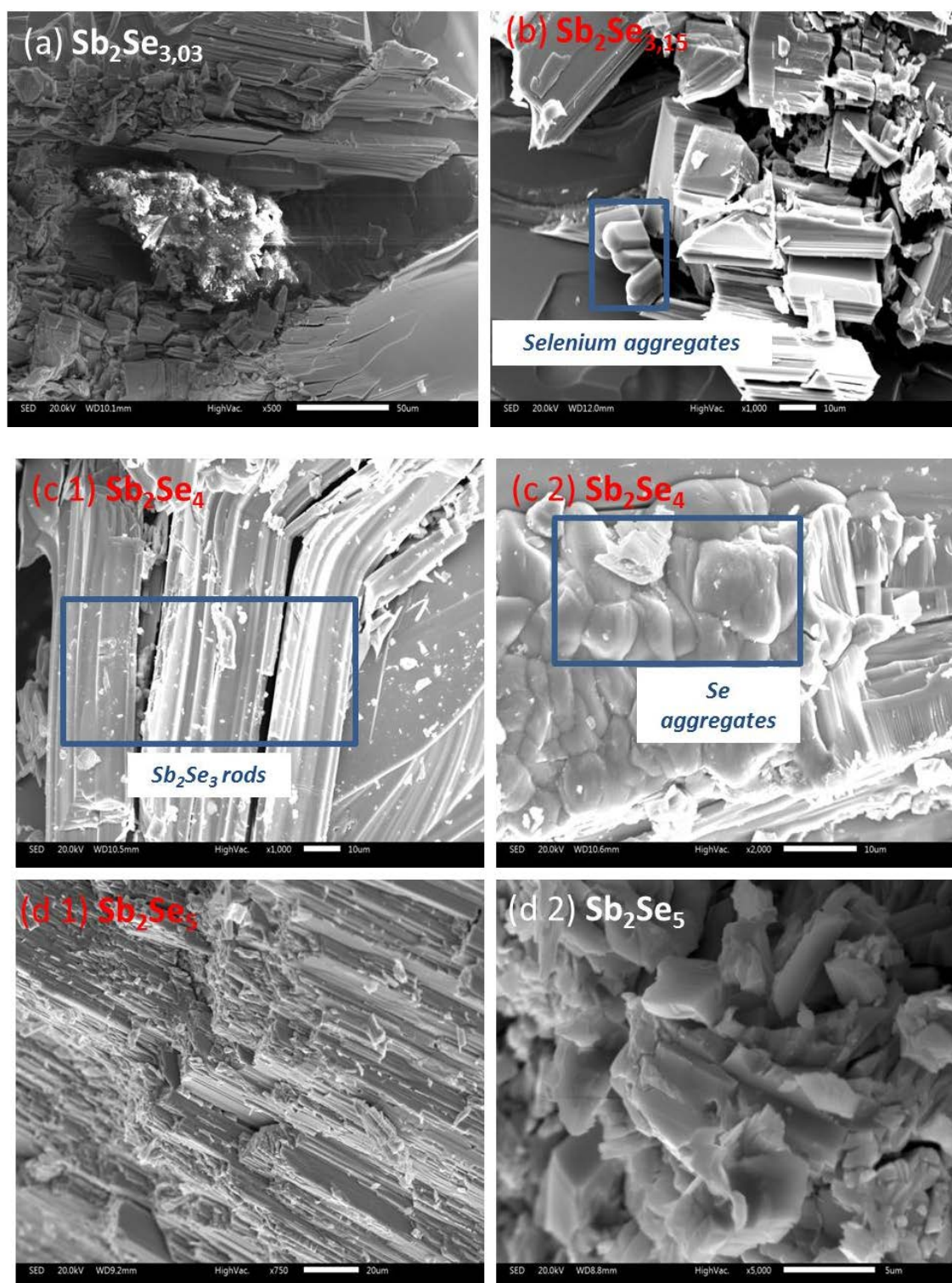


Figure 2-49 SEM images of (a)Sb₂Se_{3,03}, (b)Sb₂Se_{3,15}, (c)Sb₂Se₄, (d)Sb₂Se₅

It is interesting to mention some sort of switching effect for Sb₂Se₅ crystal (fig. 2-50). We found out fully reversible and reproducible switching from low conductive state (LCS) to high conductive state (HCS) at potential bias +0.4V. During the reduction of bias voltage to +0.1V switching back to LCS occurs. Further it switches to high conductive state (HCS) at -0.6V, and in reverse direction it switches to LCS at -0.2V. This circle was reproduced for 50 times without significant shift in

switching voltage and current density. One can also notice weak photoconductive effect at negative bias, expected for p-type semiconductor

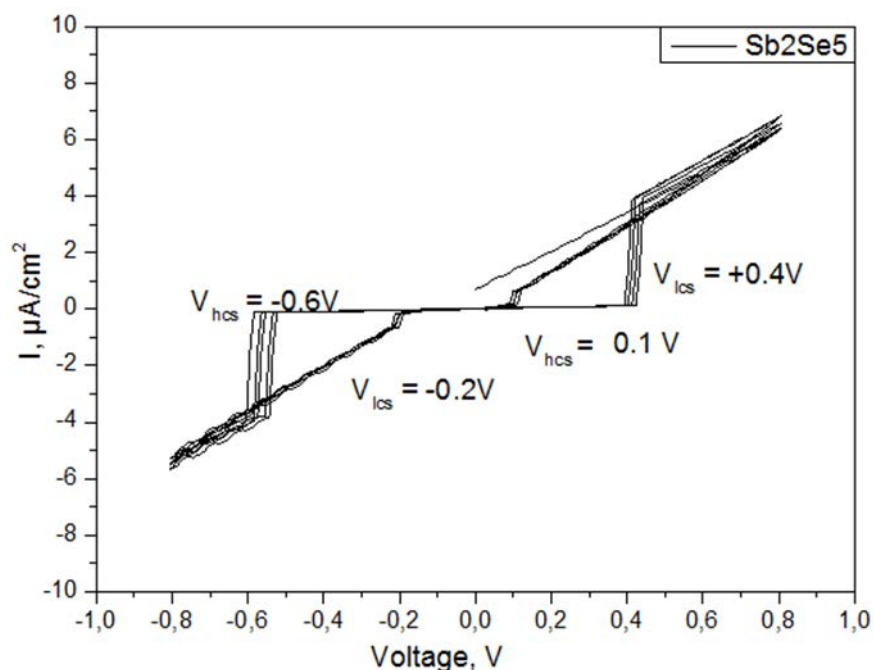


Figure 2-50 PEC curve of selenium-rich Sb₂Se₅ crystal

Table 2-2 Resume on selenium-rich and selenium-poor Sb₂Se₃ crystals bulk resistivity and major charge carriers type.

Composition	Resistivity, Ω×cm	Conductivity type (p/n tester)
Sb ₂ Se ₃	>10 ⁹	n
Sb ₂ Se _{3,03}	>10 ⁹	p
Sb ₂ Se _{3,15}	10 ⁸	p
Sb ₂ Se ₄	10 ⁸	p
Sb ₂ Se ₅	45×10 ⁶	p
Sb ₂ Se _{2,997}	>10 ⁹	n
Sb ₂ Se _{2,985}	>10 ⁹	n
Sb ₂ Se _{2,97}	5×10 ³	n
Sb ₂ Se _{2,85}	500	n
Sb ₂ Se _{2,7}	184	n
Sb ₂ Se _{2,55}	16	n
Sb ₂ Se _{2,4}	14	n

To summarize, we analyzed the behavior of Sb₂Se₃ crystals in non-stoichiometric conditions. We synthesized selenium poor and selenium rich crystals in wide range of compositions. It is possible to

conclude that non-stoichiometric crystals are capable of crystallization of microscopic inhomogeneous domains. We observed both selenium rich and selenium poor zones upon reduction of selenium quantity. Based on the PEC results, we conclude that these zones are p-type (excess of selenium) and n-type (deficiency of selenium) bulk semiconductors which co-exist within the same crystalline form of Sb₂Se₃ with Se-Sb defects (p-type) and V_{se} vacancies defects (n-type). We confirmed p-type character of selenium-rich Sb₂Se₃ by means of PEC and surface potential photovoltaic tester. Conductivity type and bulk conductivity values are summarized in table 2-2.

5 Conclusion

We have found out that iodine doped Sb₂Se₃ is responsible for the photoelectric properties of 40GeSe₂-40Sb₂Se₃-20CuI glass-ceramics. It was shown that in the absence of iodine the resistivity of samples is equal to 10⁻⁵ Ω×cm and PEC response is very weak, while the amount of Cu₂GeSe₃ phase in the iodine-poor glass ceramics is the same. Thus, we can conclude that Cu₂GeSe₃ phase participate weakly in conductive network formation, which is mostly due to iodine doped Sb₂Se₃. However exceeding amount of iodine is not favorable neither because of the excessive formation of highly resistive SbSeI phase.

It was demonstrated that insertion of iodine in Sb₂Se₃ crystals is favorable for the conductivity and photocurrent density to the extent of 15 % mol. Further increase of iodine concentration leads to the SbISe phase formation and degradation of photoelectric performance. Sb₂Se₃ doped with 15 % mol. of iodine shows photocurrent density equal to 650 μA/cm² at the positive bias +0.6V. So far this is the best result obtained within the study.

Results obtained for glass-ceramics and crystals are in correlation and confirm the key role of iodine in appearance of photoelectric features.

We found out that deviations from stoichiometry are capable to improve electric properties of glass-ceramics. Slightly varying concentration of selenium we succeeded to increase conductivity and photocurrent density up to 160 μA/cm² (+0.6V). This improvement is apparently due to increase of Se associated bridge-bondings, which allow more efficient incorporation of higher amount of iodine compare to stoichiometric composition. At the same time we established that deficiency of Se drastically affects overall conductivity, which is related to the extensive crystallization of Cu₂GeSe₃ phase. This phase does not contribute positively to the conductivity but, apparently, plays a role of strong scattering center for charge carriers.

It was shown that deviation from stoichiometry has a great influence on Sb₂Se₃ electric properties. Deficiency of Se leads to the increase of conductivity and appearance of photoconductive effect, those crystals demonstrate strongly pronounced n-type, and high chemical inhomogeneity on a microscopic scale. At the same time excess of Se switches Sb₂Se₃ to p-type conductivity with, however, relatively high resistivity and weak photocurrent densities.

We suppose that presence of both p-type and n-type phases in iodine doped Sb₂Se₃ and Sb₂Se₃ with deficiency of Se is due to high spatial inhomogeneity, which leads to formation of p-type Se-rich areas. These areas contribute to p-type related photocurrent observable via PEC.

6 References

- ¹ Guang Yang, *Effects of Pb on Thermal Stability and Crystallization Kinetics of GeS₂-Sb₂S₃-PbS Glasses*. International Journal of Applied Glass Science, 2016, **7** (3) : pp. 337–344.
- ² A. B. Seddon and M. A. Hemingway, *Thermal properties of chalcogenide-halide glasses in the system: Ge-S-I*. Journal of Thermal Analysis, 1991, **37** : pp. 2189- 2203.
- ³ L. Calvez, *Nouveaux verres et vitrocéramiques transparents dans l'infrarouge pour l'imagerie thermique*, Thesis, 2006.
- ⁴ Tokihiro Ueno and Akira Odajima, *X-Ray Photoelectron Spectroscopy of Ag- and Cu-Doped Amorphous As₂Se₃*. Jpn. J. Appl. Phys., 1982, **21**: p.230
- ⁵ Jong HEO, *Vibrational spectra of Ge-S-Br glasses*. Journal of Non-Crystalline Solids, 1989, **113** : pp. 1-13.
- ⁶ Jong HEO, *Vibrational spectra of Ge-S-I glasses*. Journal of Non-Crystalline Solids, 1989, **113** : pp 246-252.
- ⁷ Wilhelm Melitz, et al., *Kelvin probe force microscopy and its application*. Surface Science Reports, 2011, **66**: pp. 1–27.
- ⁸ F. G. Allen and G. W. Gobe, *Work Function, Photoelectric Threshold, and Surface States of Atomically Clean Silicon*. Phys. Rev., 1962, 127: p.150
- ⁹ Algirdas Audzijonis, et al., *Dielectric and electrical properties of SbSI and SbSeI single crystals in the region of antiferroelectric phase transition*. Journal of Physics and Chemistry of Solids, 2015, **83**: pp. 117 - 120
- ¹⁰ Krishnan Rajeshwar, *Fundamentals of Semiconductor Electrochemistry and Photoelectrochemistry*. Wiley-VCH, 2007, pp. 3 – 18.
- ¹¹ Y. Wu, *Céramiques semi-conductrices à base de séléniures pour des applications photovoltaïque et thermoélectrique*. Thesis, 2016, p.62
- ¹² N. W. Tideswell, F. H. Kruse and J. D. McCullough, *The crystal structure of antimony selenide, Sb₂Se₃*. Acta Cryst., 1957, **10**: pp. 99-102.
- ¹³ Donghyeuk Choi, et al., *Diameter-Controlled and Surface-Modified Sb₂Se₃ Nanowires and Their Photodetector Performance*. Scientific Reports 4, 2014, Article number: **6714**.

Chapter III

Improvement of photoelectric properties of glass-ceramics in pseudo-ternary system $x\text{GeSe}_2$ - $y\text{Sb}_2\text{Se}_3$ -(1-x-y)CuI

Table of contents

1 Introduction.....	98
2 Influence of small additives of sulphur on electric properties of 40GeSe ₂ -40Sb ₂ Se ₃ -20CuI glass-ceramics.	101
2.1. On Fermi level tuning in Sb ₂ Se ₃	101
2.2. Synthesis peculiarities of sulphur containing glass precursor	103
2.3. Glass precursor characterization	105
2.4. Controllable crystallization of sulphur-containing precursors.....	108
2.5. Electric properties of sulphur-containing glass-ceramics.	111
3 Variety of cation substitutions in 40GeSe ₂ -40Sb ₂ Se ₃ -20CuI glass precursor.....	113
3.1. On the cation substitutions in glass-ceramics.	113
3.2 Glass precursors preparation	114
3.3. Structural and electric properties of 40GeSe ₂ -40Sb _{2-x} Bi _x Se ₃ -20CuI glass-ceramics.....	115
3.4. Structural and electric properties of 40GeSe ₂ -40Sb _{2-x} Sn _x Se ₃ -20CuI glass-ceramics.	119
3.5. Structural and electric properties of xGeSe ₂ -(1-x)Sb ₂ Se ₃ -20CuI glass-ceramics.....	130
4. Study of xGeSe ₂ – ySb ₂ Se ₃ – (1-x-y)Cu(Br,Cl) system	136
4.1 On the utilization of CuBr and CuCl.	136
4.2 Glass precursor preparation	137
4.3 Glass precursor analysis. Controllable crystallization. Electric properties.....	139
5. Conclusion	145
6. References.....	146

1 Introduction

It was discussed previously, that the microstructure of 40GeSe₂-40Sb₂Se₃-20CuI glass-ceramics and therefore its electric properties strongly depend on the annealing conditions^{1,2}. While upon the optimization of crystallization process a photocurrent of 178 μA/cm² was obtained, a small difference in Fermi level (E_f) of Sb₂Se₃ and Cu₂GeSe₃ is an obstacle for obtaining higher open circuit voltage.

We have already discussed the structure of Sb₂Se₃ crystals and estimated its Fermi level as $E_f = 4.778\text{eV}$. Cu₂GeSe₃ density of state is composed of Cu-d, Se-p, Ge-s and Ge-p states with total span of energies between -10eV to 4eV. Its conductive zone is mainly composed of Ge-s and Se-p states³. Therefore, we can estimate E_f as 4eV with respect to vacuum level. Thus, a small difference in E_f of Cu₂GeSe₃ and Sb₂Se₃ causes serious doubts for obtaining higher V_{oc} and in consequence achieving of a decent fill factor (FF) and power conversion efficiency (η), which can be described as following (see fig. 3-1 for illustration)⁴

$$FF = \frac{I_m V_m}{I_{sc} V_{oc}}, \text{ where (3.1)}$$

I_m and V_m – current density and voltage corresponding to the maximal power P_m , I_{sc} – short circuit current ($V = 0$ under illumination), V_{oc} – open circuit voltage ($I = 0$ under illumination).

$$\eta = \frac{FF * I_{sc} V_{oc}}{P_i}, \text{ where (3.2)}$$

P_i - input solar power.

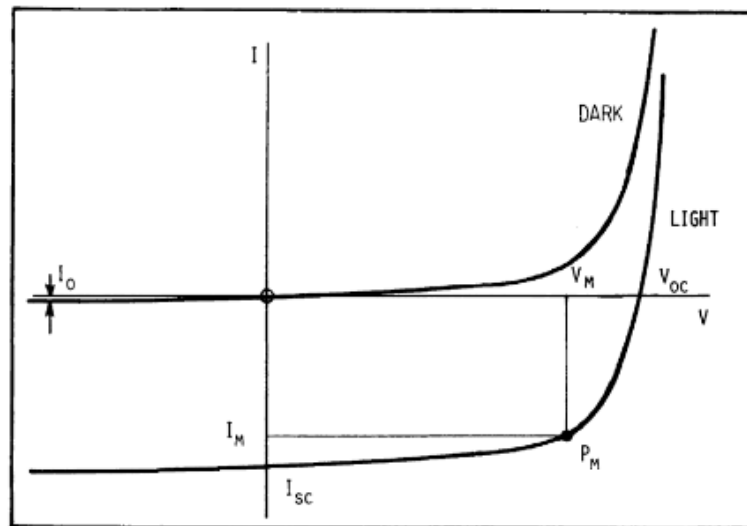


Figure 3-1 Typical I-V curves of the solar cell in the dark and under illumination⁴

The analysis of basic photovoltaic cell properties leads to the conclusion that I_{sc} and V_{oc} are the most important and determinant properties. Their improvement is the main goal of the presented thesis.

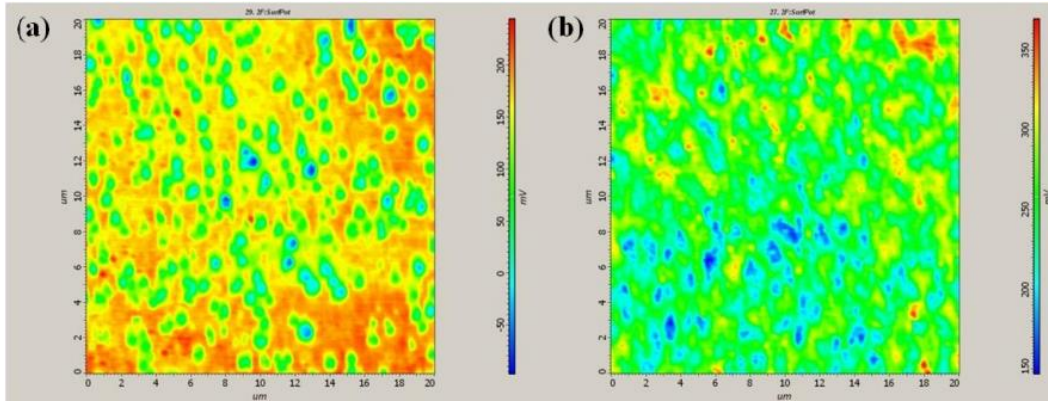


Figure 3-2 Kelvin probe microscopy images (a) - low conductive glass-ceramics (insufficient annealing), (b) - highly conductive glass-ceramics of 40GeSe₂-40Sb₂Se₃-20CuI composition⁵.

As it can be seen from the Kelvin probe microscopy experiment for conductive glass-ceramics (fig. 3-2 (b))⁵ the difference between lower potential zone which is attributed to Sb₂Se₃ and higher potential zone, which stays for iodine doped Sb₂Se₃ (as we have shown before), can be estimated as 10-20 mV.

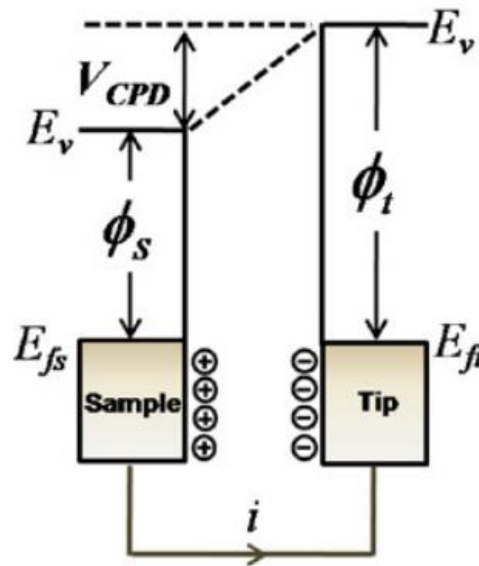


Figure 3-3 Interaction between scanning AFM tip and sample surface⁶

Fig. 3-3 depicts the interaction between silicon tip with known work function ($\phi_{tip} = 4.83\text{eV}$) and the surface of studied matter. The work function of surface therefore could be calculated as⁶

$$V_{cpd} = \frac{\phi_{tip} - \phi_{sample}}{-e} \quad (3.3)$$

Hence,

$$\phi_{sample} = \phi_{tip} + eV_{cpd} \quad (3.4)$$

Thus, we succeeded to improve Fermi level shift between Cu₂GeSe₃ and Sb₂Se₃ by not more than for 0.02 eV! At the same time it is known that for the bulk heterojunction, V_{oc} can be absolutely determined by the difference of electron and hole electrochemical potentials (E_{fn} and E_{fp}) in the corresponding materials, and can be described with a simple formula⁷

$$qV_{oc} = E_{Fn} - E_{Fp} \quad (3.5)$$

Thus, the output voltage characterizes the relative E_f (Fermi level position inside the gap) and, in consequence, charges carrier concentration^{8,9}.

The charge carrier concentration in its turn determines also the current density¹⁰. In non-equilibrium state, where

$$np \neq n_{int}^2, \text{ where } (3.6)$$

np – charge carriers concentration and n_{int} – concentration of charge carries in the intrinsic semiconductor. The quasi-Fermi level potential describes the deviation from equilibrium of the system (separately for electrons and holes) under an external force (light, bias voltage, etc.).

$$n(p) = n_{int} \exp \left[\left(- \frac{\varphi_p - \varphi_n}{V_t} \right) \right], \text{ where } (3.7)$$

$n(p)$ concentration of electrons (for n-type semiconductor) or holes (for p-type semiconductor), V_t – applied bias, φ_n, φ_p – Quasi-fermi level energies for semiconductors on n-type and p-type respectively.

Thus, for total charge carrier concentration one obtains

$$np = n_{int} \exp \left[\left(- \frac{\varphi_p - \varphi_n}{V_t} \right) \right] \quad (3.8)$$

If the current is determined by diffusion and drift components

$$J_{n(p)} = J_{n(p) \text{ drift}} + J_{n(p) \text{ diff}}, \text{ where } (3.9)$$

$J_{n(p) \text{ drift}}$ - density of drift current component, $J_{n(p) \text{ diff}}$ – diffusion current density.

As the drift component is determined by the differential form of Ohms law:

$$J = \sigma E \quad (3.10)$$

and diffusion component by the Fick's first law of diffusion:

$$F = -D \frac{dn}{dx}, \text{ where } (3.11)$$

D – diffusion coefficient or diffusivity, dn/dx – gradient of charge carrier concentration.

we obtain

$$J_{n(p)} = qn(p)\mu_{n(p)}E + qD_{n(p)} \frac{dn(p)}{dx}, \text{ where } (3.12)$$

q - elementary charge, $n(p)$ – concentration of electrons (holes), $\mu_{n(p)}$ – mobility of electrons (holes), E – electric field, $D_{n(p)}$ – diffusion coefficient of electrons (holes).

And for the non-equilibrium state we obtain

$$J_{n(p)} = qn(p)\mu_{n(p)} \frac{d\varphi_{n(p)}}{dx} \quad (3.13)$$

Fig. 3-4 depicts two semiconductors in equilibrium (a) and non-equilibrium (b) states.

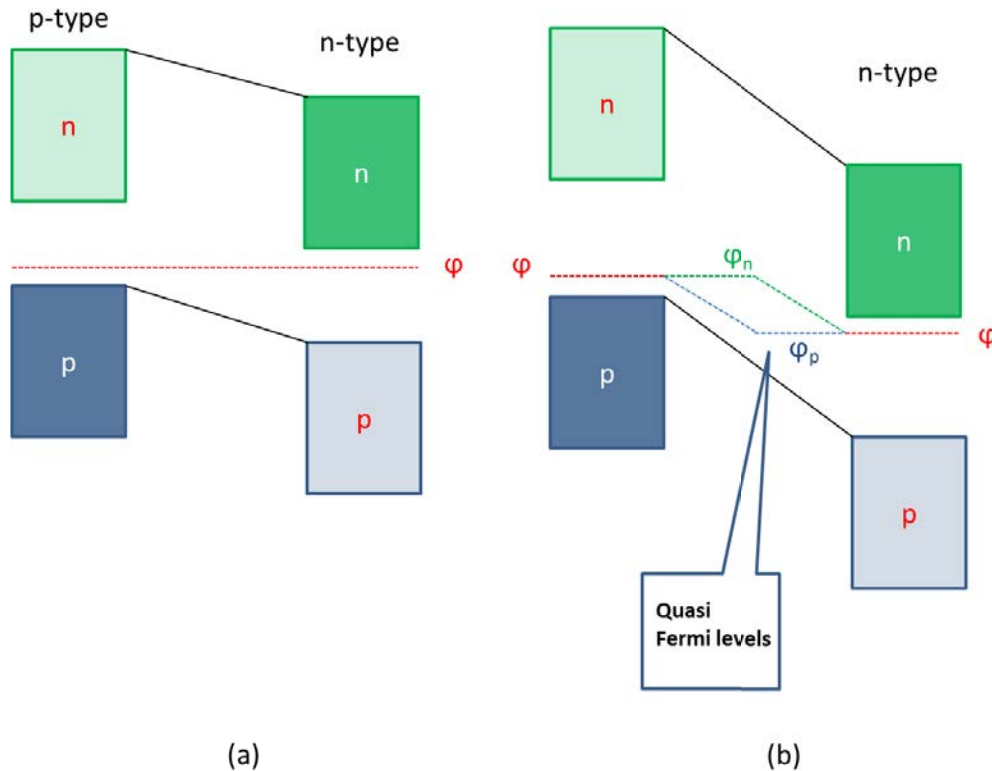


Figure 3-4 p-n junction in equilibrium (a) and non equilibrium (under illumination) (b) states

Summarizing, two semiconductors with extended difference between Fermi levels of its p- and n- type would demonstrate higher V_{oc} and higher J_{sc} since both of these parameters strongly depend on the electrochemical potential and charge carrier concentration.

In this chapter various modifications of 40GeSe₂-40Sb₂Se₃-20CuI glass precursor are presented. They were made lining on the concept that precursor modification allows doping of Sb₂Se₃ and Cu₂GeSe₃ crystalline phases upon the annealing with more electronegative (electropositive) chemical elements, and therefore could lead to the extension of the gap between E_{fn} of Sb₂Se₃ and E_{fp} of Cu₂GeSe₃ and increase charge carriers concentration n (p).

2 Influence of small additives of sulphur on electric properties of 40GeSe₂-40Sb₂Se₃-20CuI glass-ceramics.

2.1. On Fermi level tuning in Sb₂Se₃.

Antimony selenide (Sb₂Se₃) is a well known n-type semiconductor¹¹ with high absorption coefficient in the visible region ($>10^5 \text{ cm}^{-1}$)¹² and a band gap of 1.17 eV¹², which makes this material suitable for the single junction solar cell preparation. Various attempts to use Sb₂Se₃ as an active layer in solar cells have been recently made¹³. Cu₂GeSe₃ has a direct band gap of 0.78 eV¹⁴. As it can be seen these two materials possess complementary direct band gaps. As it was shown⁴, low conductivity of

Sb₂Se₃ (10⁻⁶ Ω⁻¹·cm⁻¹) demands a percolating network of Cu₂GeSe₃ crystals which being highly conductive (10¹ Ω⁻¹·cm⁻¹), insures the separation and transfer of charge towards the electrode^{15,16}. Thus, our goal was to modify the electronic structure of Sb₂Se₃, in terms of the band gap E_g, and Fermi level E_F position, which could improve a photovoltaic performance.

The refinement of Sb₂Se₃ structure shows that it crystalizes in orthorhombic lattice with cell parameters a=1.113 nm, b=1.142 nm and c=0.385 nm of P_{bnm} space group¹⁷. It is also interesting to take into account the results of Mustafa et al., where the structural behavior of Sb₂Se₃ crystal upon the introduction of sulphur was refined¹⁸. Upon the introduction of Sulphur the crystal cell has a tendency to shrink, which can be explained by smaller atomic size of sulphur (1.84 Å) compared to Selenium (1.98 Å). While the stereo-configuration of the structure was not affected by the atomic replacement.

The enhancement of electrochemical performance of sulphur doped Sb₂Se₃ nanosheets without significant structural changes was presented as well¹⁹. Analysis of optical transmission spectra shows blue shift upon the introduction of sulphur²⁰. It is explained by the difference in a band gap for Sb₂Se₃ (1.17 eV) and Sb₂S₃ (1.62 eV). Yang et al. applied Vegard's law of approximation to establish the relation between the sulphur content and the band gap²¹

$$E_g(x) = x E_g(\text{Sb}_2\text{Se}_3) + (1-x) E_g(\text{Sb}_2\text{S}_3) - x(1-x)b, \text{ where } (3.14)$$

b is a coefficient describing non-linear relation between the gap and the sulphur content. Expressing this law as a numerical equation, one can obtain:

$$E_g(x) = 0.118x^2 - 0.662x + 1.621\text{eV} (3.15)$$

On the other hand, there is a direct correlation between Fermi level position (E_f) and electronegativity of the elements comprising the crystal cell given by Nethercot for binary oxides in 1974²², and applicable for most of covalent oxides such as P₂O₅, SeO₃, XeO₃, Re₂O₇, OsO₄ and others. Chalcogenides are materials with strongly covalent bonding which co-exist with a weak intermolecular (Van-der-Waals) interaction²³. In particular; Se possesses two s-electrons and four p-electrons, two of four p-electrons occupy p_x and p_y orbitals creating covalent bond with their neighbors. The same reasoning can be applied for sulphur. Therefore it is possible to consider Nethercot approach as a fair for the case of chalcogenide binary components with, however, certain peculiarities.

$$E_F = (\chi_M^m \chi_{Ch}^n)^{\frac{1}{m+n}} (3.16),$$

where χ_M^m is the electronegativity of the element M with stoichiometry m , χ_{Ch}^n is the electronegativity of chalcogenide element with stoichiometry n

To resolve the ambiguity caused by various oxidation numbers and, in consequence, various electronegativities, we use the approach proposed by Campet et al. for oxides²⁴:

$$E_F = ((\chi_M^{z+})^m (\chi_{Ch}^{z-})^n)^{\frac{1}{m+n}} (3.17)$$

To convert Pauling units to electronvolts, Huheey equation can be used²⁵

$$\chi (eV) = 2.976 \chi (P. u.) + 0.615 (3.18),$$

Therefore, for Sb_2Se_3 one can obtain the following:

$$E_F = ((\chi_{\text{Sb}})^2(\chi_{\text{Se}})^3)^{\frac{1}{2+3}} \times 2.976 + 0.615 = 7.37 \text{ eV}$$

And in the same manner for Sb_2S_3 :

$$E_F = ((\chi_{\text{Sb}})^2(\chi_{\text{S}})^3)^{\frac{1}{2+3}} \times 2.976 + 0.615 = 7.54 \text{ eV}$$

Considering the coexistence of Se and S, we can propose to use Vegard's law of approximation in general form. In fig. 3-5 the idea of Fermi level tuning is presented graphically

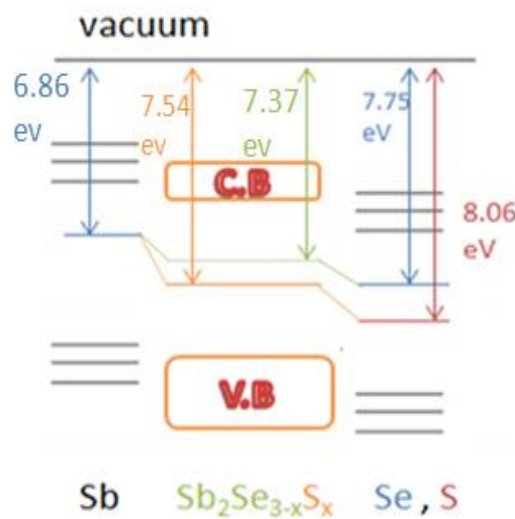


Figure 3-5 Equalization of electronegativity in $\text{Sb}_2(\text{Se},\text{S})_3$ compound.

Thus, by varying sulphur content we should be able to tune both the band gap and Fermi level of the binary $\text{Sb}_2\text{Se}_{3-x}\text{S}_x$ compound due to equalization of electronegativity.

2.2. Synthesis peculiarities of sulphur containing glass precursor

To synthesize this type of glass precursors we utilized metallic germanium, antimony, copper iodine, selenium and sulphur. Before the synthesis selenium and sulphur were distilled to eliminate residual impurities. All the elements were stored and weighed in the glovebox under Argon atmosphere.

The usual procedure for synthesising sulphur-containing glass precursors based on $40\text{GeSe}_2-40\text{Sb}_2\text{Se}_3-20\text{CuI}$ composition is depicted in fig. 3- 6

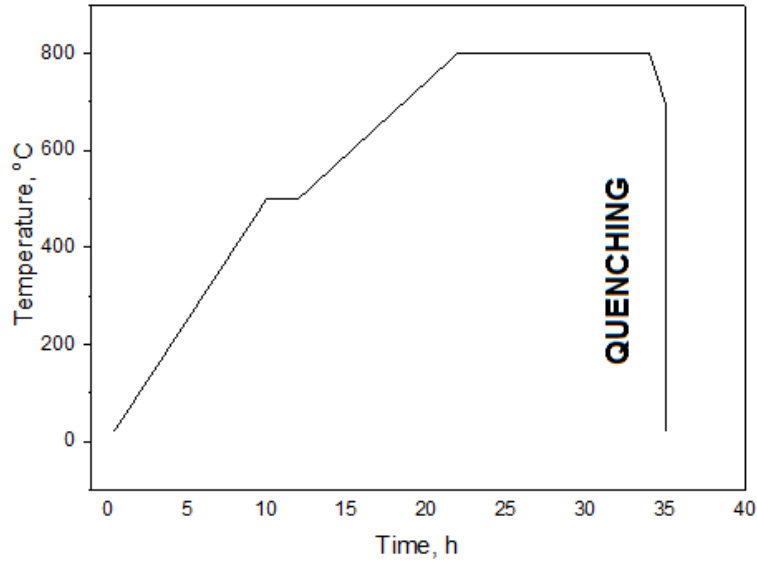


Figure 3-6 Synthesis profile for sulphur containing precursors

The increase of synthesis time and appearance of « hold » step at 550 °C is explained by the excessive, compared to selenium, vapour pressure of Sulphur. While vapour pressure of selenium is described with formula²⁶

$$\text{Log P (atm.)} = -5043/T + 5.265 \quad (3.19)$$

giving $\text{Log P (atm.)} = 0.565$ at 800 °C, and $P = 3.67$ atm.,

The pressure of sulphur vapours changes non-linearly, as it is shown in fig. 3-7, and can achieve $\text{log P(atm.)} = 1.8$ at a temperature of 800 °C and $P = 63.1$ atm.²⁷

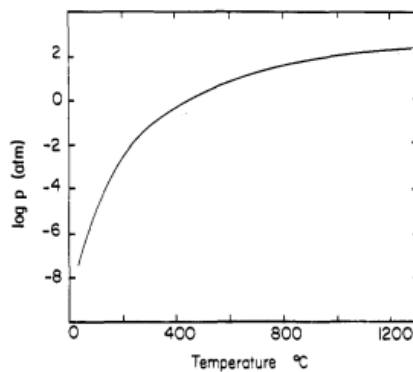


Figure 3-7 Dependence of sulphur vapor pressure on temperature²⁸

Therefore, usual synthesis route often leads to the explosion of the tube during the excessive internal pressure over the melt. While the above presented profile allows the chemical reaction under lower temperature between low melting-point elements reducing the overall pressure inside the tube. It is worth mentioning that fast quenching is very undesirable because it leads to internal stresses in the bulk, which cannot be eliminated during the annealing, since in most cases the bulk has already a number of major defaults (i.e. cracked after quenching). According to our experience, slow immersion in water with a slight clockwise rotation of the tube can be recommended.

All the samples containing sulphur were then annealed at 200 °C for 3 hours in order to reduce the essential stresses produced because of quenching.

2.3. Glass precursor characterization

To prove or refute the above described hypothesis a number of sulphur containing composition based on 40GeSe₂-40Sb₂Se₃-20CuI glass were prepared :

40Ge(S_e_{1-x}S_x)₂-40Sb₂(S_e_{1-x}S_x)₃-20CuI, where x = 0, 0.00025, 0.001, 0.005, 0.01, 0.02, 0.05, 0.1, 0.15, 0.2

The obtained bulk rods were cut to obtain discs of 0.8 cm in diameter and thickness of 2.2 mm. After, they were thoroughly polished to obtain perfectly flat surface with low diffusion scattering due to the mechanical imperfections (scratches, roughness).

DSC curves of obtained glasses are presented in fig. 3-8. As one can see even 0.1 mol. % substitution of Se for S leads to crystallization peak splitting, which shifts towards lower temperatures reducing the stability of precursor. The stability of glass can be described as the difference between glass-transition temperature (T_g) and lowest crystallization temperature (T_x). It is graphically represented in fig. 3-11. The reduction of stability can explain the increase of Mie scattering intensity and transmission attenuation. The change of DSC curve profile for the precursor with 5 mol. % of sulphur could be a sign of occurred volume crystallization. This suggestion is supported by IR transmission spectrum (fig. 3-9) where Rayleigh scattering is pronounced for 5 mol. % of sulphur compound. In this case, it is not completely correct to speak about glass stability, since presented compound comprises of glass and crystallized fracture, i.e. it is already a glass-ceramic.

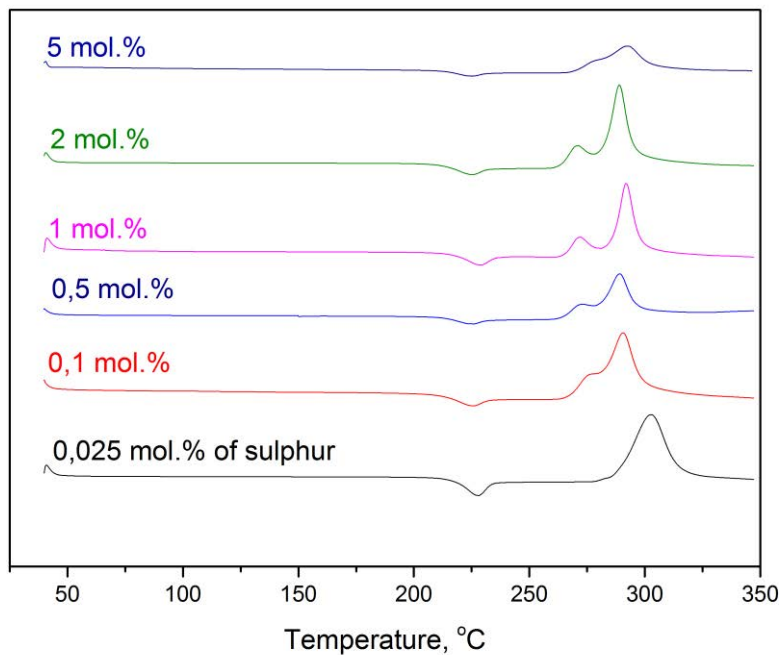


Figure 3-8 DSC spectra of glass-precursor with various content of sulphur, crystallization peak splitting occurs for sulphur contacting precursors.

The infrared transmission spectra in fig. 3-9 shows typical features for Ge and Se containing chalcogenide glass with absorptions at 2.77 μm and 6.32 μm assigned to H_2O molecule and OH^- group vibrational modes respectively, 4.59 μm and 4.12 μm for Se-H and S-H vibrational modes respectively and Ge-O group absorption at 13.5 μm ²⁸. It is interesting that upon introduction of sulphur Se-H absorption band at 4.59 μm decreases, while S-H associated absorption peak at 4.12 μm increases. Apparently, due to its higher electronegativity sulphur attracts hydrogen atoms more actively compared to selenium, which results in absorption peak shift. Difference in relative intensity of impurities absorption can be assigned to non-equal purity of the starting elements. All the compositions show strong Mie scattering associated with a certain amount of crystallized matter inside the glass precursor. As it can be seen, upon the introduction of sulphur, the amount of crystallized fracture increases and the transmission attenuates. Glass with 5 mol. % shows a sign of Rayleigh scattering exhibiting the presence of crystals with the size compatible to IR-wavelengths inside the precursor. Composition with a sulphur content above 5 mol. % were severely crystallized and show the absence of transmission, probably due to the massive Rayleigh scattering.

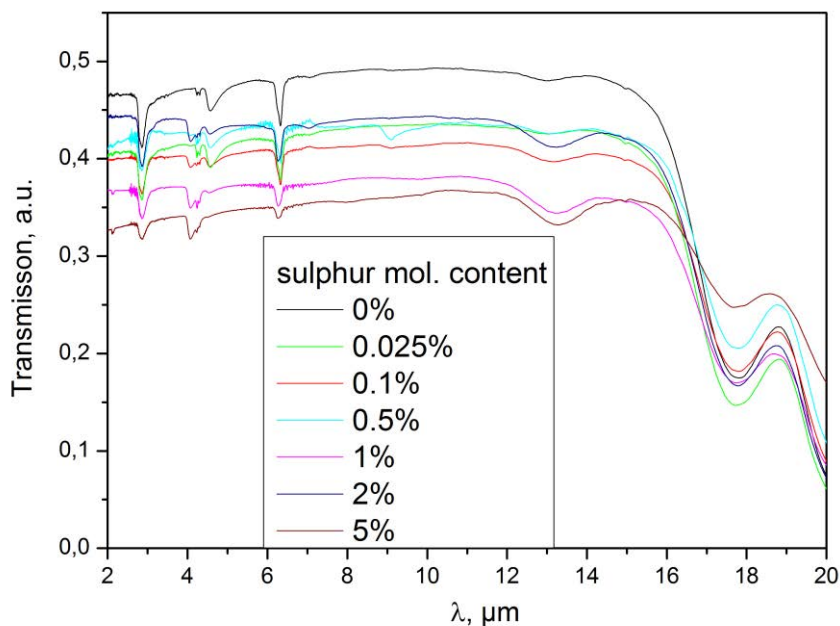


Figure 3-9 Infra-Red transmission spectra of transparent sulphur containing precursors, $e = 1 \text{ mm}$

In the fig. 3-10 one can compare X-ray diffractograms of the transparent glass precursor and the precursors with significant amount of crystallized matter. While precursors with 0 mol. % and 5 mol. % of sulphur show typical features for glassy state (without long-range order) diffraction pattern, precursor with 10 mol. % of sulphur demonstrates clear signs of volume crystallization however the amount of amorphous fraction is still very important. Further, increase of sulphur content to 15 and 20 mol. % leads to the reduction of glassy phase and appearance of bulk phase crystallization. The shift towards higher 2Θ values stays for crystalline cell shrinking and appears to be in precise correspondence with reported by Mustafa et al.¹⁸. At the same time, Cu_2GeSe_3 peak at 28.9° is not pronounced, apparently, because this phase requires higher energy to be crystallized.

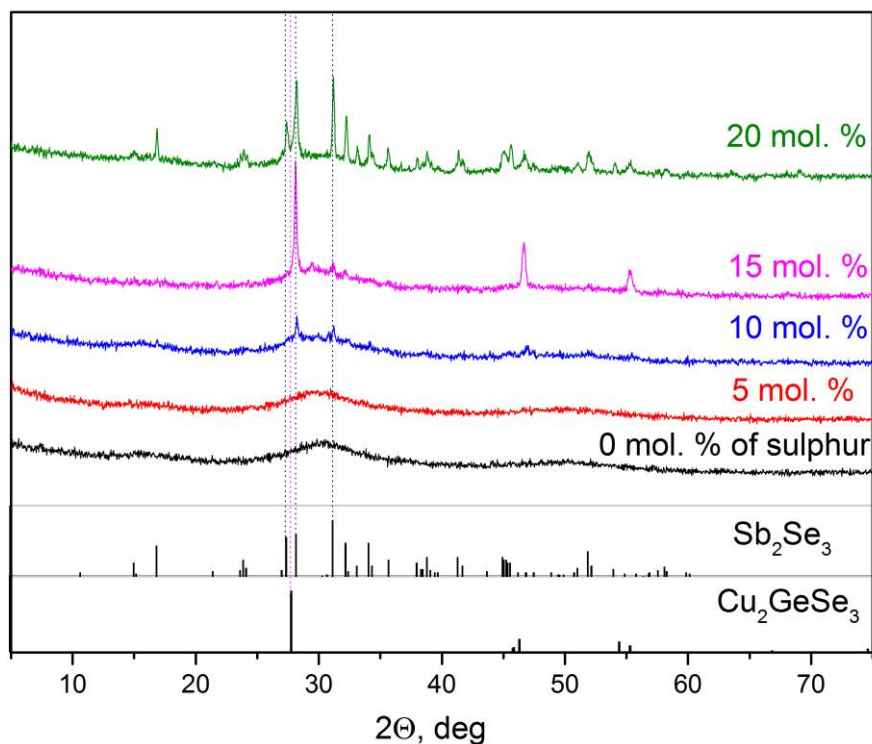


Figure 3-10 X-Ray patterns of as-prepared precursor with different molar content of sulphur without any additional heat treatment.

We do not discuss composition with 10, 15 and 20 mol. % in terms of stability since they are already significantly crystallized

Most probably, the presence of sulphur causes decrease of the Sb_2Se_3 crystallization temperature, since it is the first phase that appears on X-Ray pattern upon the increase of sulphur content, while no signs of Cu_2GeSe_3 phase were found in as-prepared samples without additional annealing.

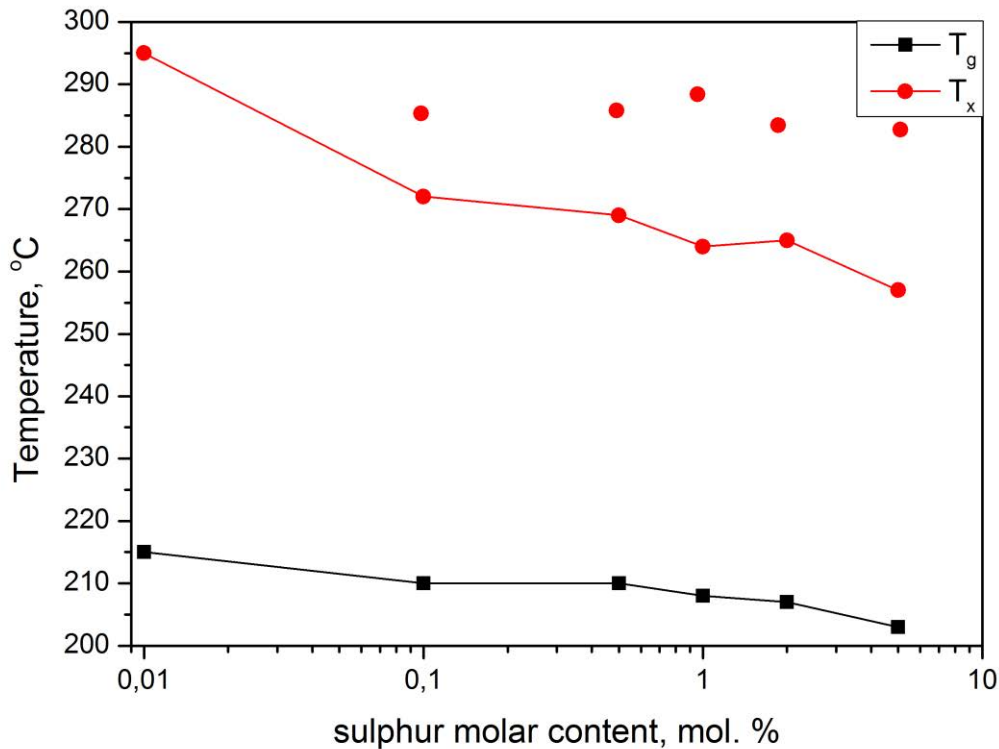


Figure 3-11 Dependence of glass-transition and crystallization temperatures of glassy-precursor on sulphur content. Several red dots stay for different crystallization peaks (see fig. 3-8).

2.4. Controllable crystallization of sulphur-containing precursors.

All the precursors were controllably crystallized via annealing at T_x for 1 hour. Since certain samples show two crystallisation peaks they were annealed at two different temperatures. As we can see in fig. 3-12, compounds with sulphur content less than 1 mol. % do not show any significant difference compared to non-doped 40GeSe₂-40Sb₂Se₃-20CuI composition. Clearly pronounced Sb₂Se₃ orientations with Cu₂GeSe₃ orientation can be seen at both crystallization temperatures.

There are no clearly pronounced difference between X-ray patterns of glass-ceramics annealed at lower T_{x1} and higher T_{x2} crystallization temperatures as shown in fig. 3-13. However attenuation of Cu₂GeSe₃ peak with increase of sulphur content is a quite clear trend. At the same time, by examination of SEM images in fig. 3-14, we cannot underline any significant morphological differences between two glass-ceramics annealed at different temperatures.

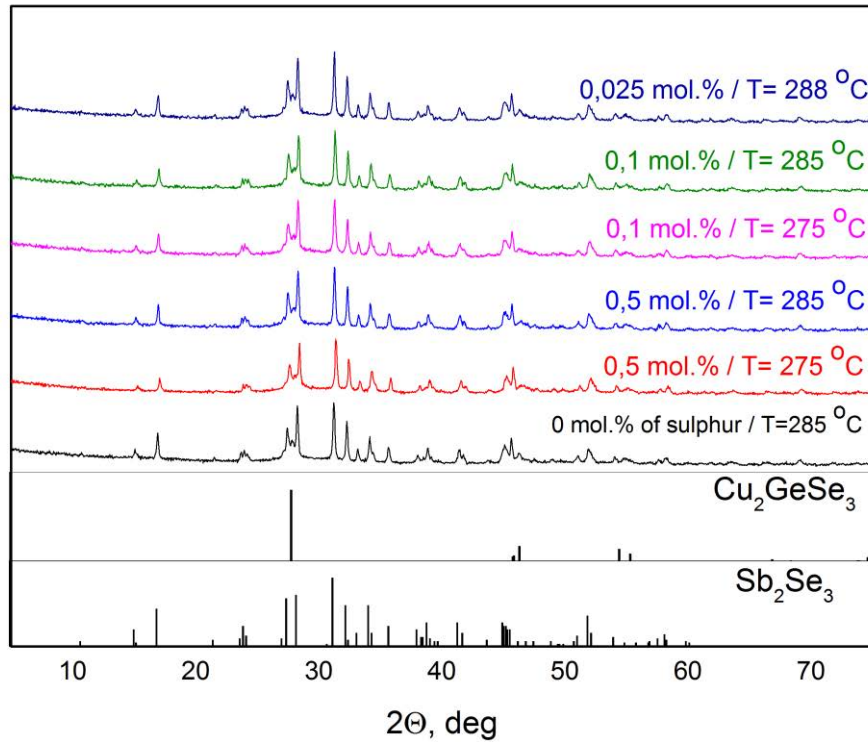


Figure 3-12 XRD diffractogram of glass-ceramics with different molar content of sulphur, annealed at different crystallization temperatures in comparison with non-doped $40\text{GeSe}_2\text{-}40\text{Sb}_2\text{Se}_3\text{-}20\text{CuI}$

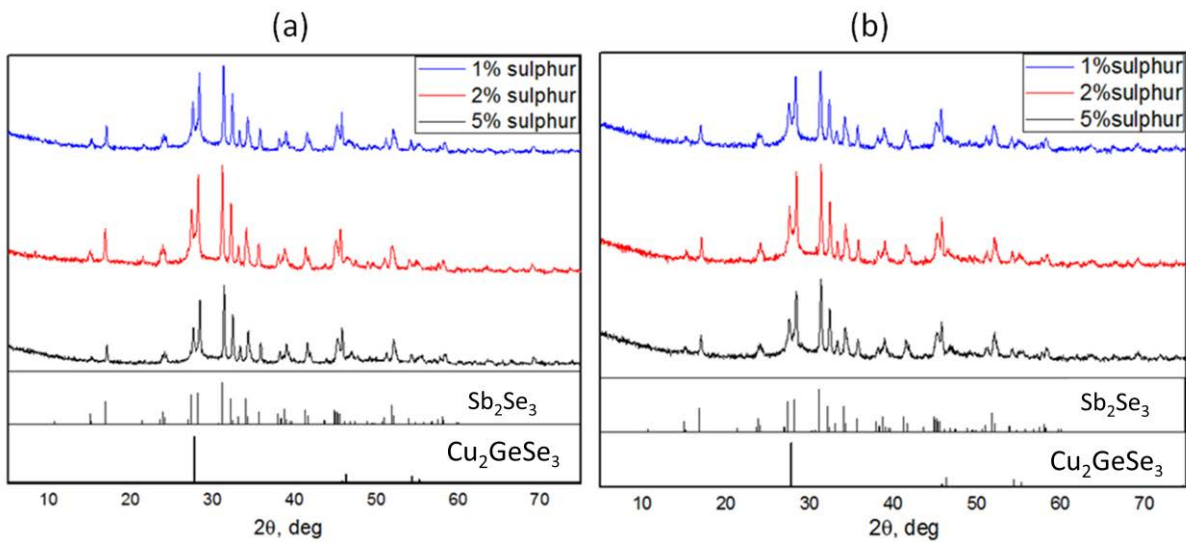


Figure 3-13 Comparison of XRD diffractograms of annealed glass-ceramics with different sulphur content at lower crystallization temperature T_{x1} (left) and higher crystallization temperature T_{x2} (right)

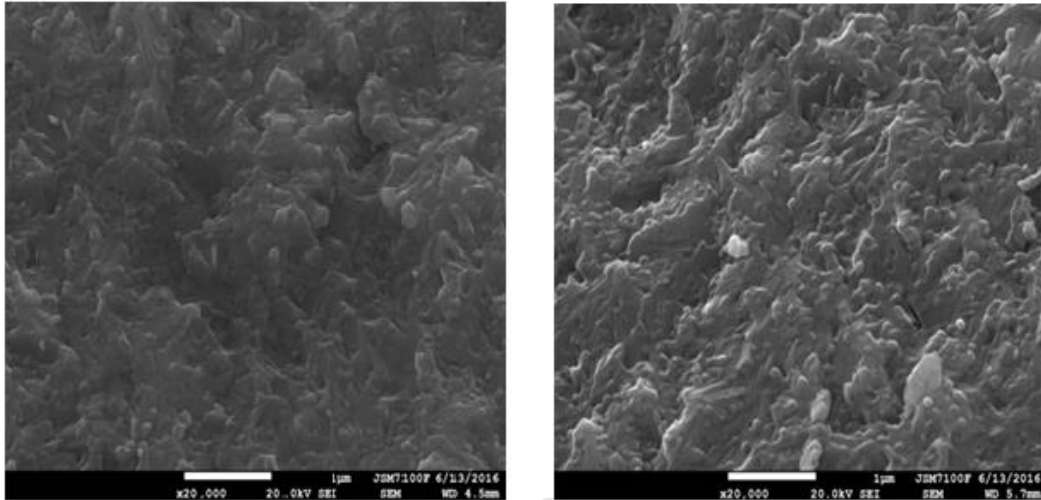


Figure 3-14 SEM images of 5 mol. % sulphur containing glass-ceramics annealed at $T_{x1} = 260$ °C(left) and $T_{x2} = 285$ °C (right)

It is also interesting to compare samples containing 5 mol. % and 20 mol. % of sulphur with non-doped $40\text{GeSe}_2\text{-}40\text{Sb}_2\text{Se}_3\text{-}20\text{CuI}$ glass-ceramic (fig. 3-15). One can mention that compared to the non-doped sample, we can suppose that there is no pronounced Cu_2GeSe_3 peak at 27.8° for the sample with 5 mol. % of sulphur. At the same time the absence of Cu_2GeSe_3 peak is absolutely clear in case of 20 mol. % sample. It is also interesting to mention the peak at 29.44° , present in the 20 mol. % sample only, which can be assigned to Sb_2S_3 orthorhombic Pbnm phase with (2 1 1) orientation.

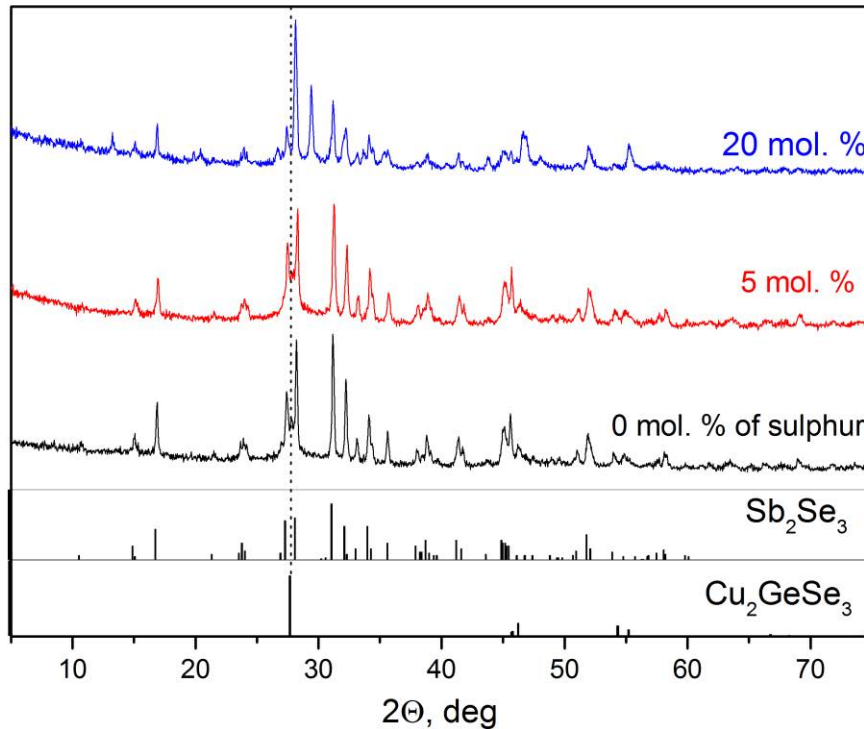


Figure 3-15 X-ray diffraction diagrams of glass-ceramics with 5 mol. % and 20 mol. % of sulphur in comparison with non-doped $40\text{GeSe}_2\text{-}40\text{Sb}_2\text{Se}_3\text{-}20\text{CuI}$ glass-ceramic (0 mol. % of sulphur).

2.5. Electric properties of sulphur-containing glass-ceramics.

The dependence of conductivity on sulphur content shows that even 0.1 mol. % doping leads to almost complete loss of conductivity, as depicted in fig. 3-16. Since there are no clear morphology changes upon the introduction of sulphur and, as previously was reported, sulphur doping does not lead to structural deviations from the conventional rod-like structure of Sb_2Se_3 , the possible explanation of this rapid decrease in conductivity could be:

- Insufficient crystallization of conductive Cu_2GeSe_3 due to lower annealing temperature, that we observe on DRX patterns in fig. 3-13 and fig. 3-15. It was found that Cu_2GeSe_3 peak intensity at 27.8° decreases with introduction of sulphur. For the sample with 20 mol. % of sulphur this peak is completely absent.

- Substantial change of Sb_2Se_3 electronic properties upon the introduction of sulphur. As it was found in chapter II, iodine doped Sb_2Se_3 phase is responsible for the conductivity of glass ceramics rather than Cu_2GeSe_3 phase. Introduction of sulphur may affect Sb_2Se_3 doping with iodine upon the annealing. Co-doping of Sb_2Se_3 with both iodine and sulphur could be unfavorable for appearance of conductive network as well.

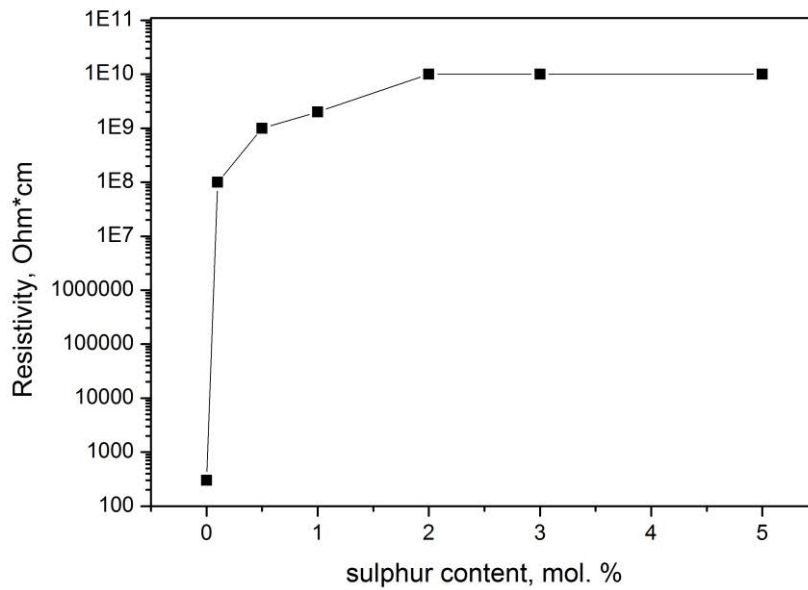


Figure 3-16 Dependence of resistivity on sulphur content in glass-ceramics with different (0-5 mol. %) molar content of sulphur

PEC curve represented in fig. 3- 17 shows that 0.025 mol. % doped glass-ceramic demonstrates similar to non-doped sample response reaching $32 \mu\text{A}/\text{cm}^2$ at $+0.6\text{V}$ bias and $-24\mu\text{A}/\text{cm}^2$ under -0.6V bias (compare to $28.8 \mu\text{A}/\text{cm}^2$ and $16 \mu\text{A}/\text{cm}^2$ respectively for non-doped $40\text{GeSe}_2\text{-}40\text{Sb}_2\text{Se}_3\text{-}20\text{CuI}$). This difference can be considered as negligible since PEC experiment is very sensitive to the sample surface quality. Glass-ceramics containing more than 0.1 mol. % of sulphur do not show any distinguishable photoelectric response due to their extremely high resistivity.

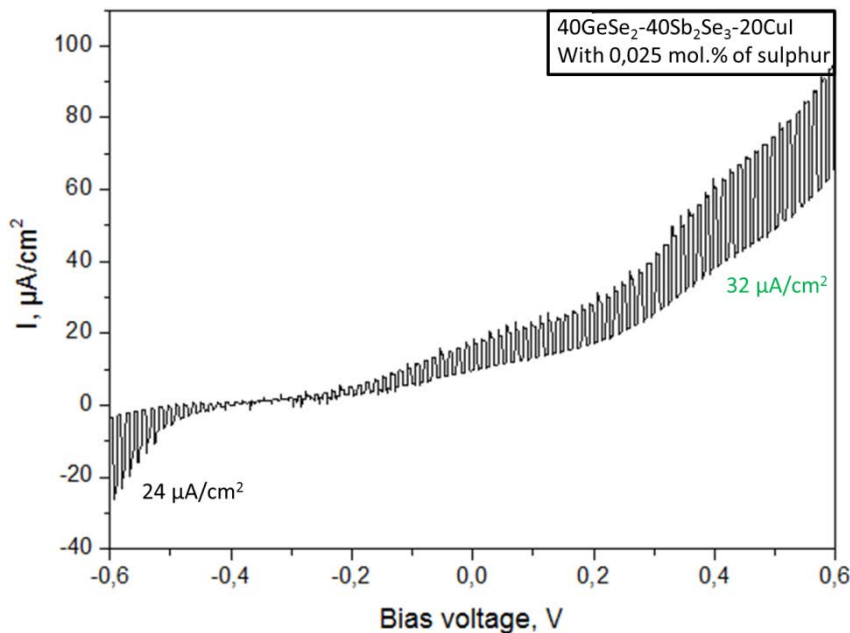


Figure 3-17 PEC measurement of $40\text{GeSe}_2\text{-}40\text{Sb}_2\text{Se}_3\text{-}20\text{CuI}$ glass-ceramic with 0.025 mol. % of sulphur.

In summary for this paragraph, we found that sulphur doping of glass-ceramics does not lead to the desired improvement of photoelectric performance. Furthermore, the presence of small amount of

sulphur (0.1 mol. %) leads to the dramatic change of resistivity. Typical for the 40GeSe₂-40Sb₂Se₃-20CuI glass-ceramic resistivity value of 3×10² Ω×cm increases up to 10⁸ Ω×cm with introduction of only 0.1 mol. % of sulphur. Neither substantial morphologic nor structural changes were found to explain such rapid loss of bulk conductivity. It is possible that co-doping of Sb₂Se₃ crystals with iodine and sulphur not favorable for conductive domains formation, since, as it was shown before in Chapter II, iodine doped Sb₂Se₃ is responsible for appearance of bulk conductivity in 40GeSe₂-40Sb₂Se₃-20CuI glass-ceramics.

3 Variety of cation substitutions in 40GeSe₂-40Sb₂Se₃-20CuI glass precursor.

3.1. On the cation substitutions in glass-ceramics.

Discourse developed earlier in paragraph 2.1 concerning the substitution of chemical elements with electronegativity χ_1 with an element with higher (lower) electronegativity is fair not only for chalcogenide elements but also for cation metals (or semi-metal). Thus, behind the idea of substitution of bismuth (with $\chi = 6.87$ eV) for antimony (with $\chi = 6.26$ eV) stays the same motivation of Fermi level (E_F) tuning via equalization of electronegativity as for the substitution of sulphur for selenium. Thus, utilizing formula 3.17, one can obtain:

$$E_F = ((\chi_{Bi})^2((\chi_{Se})^3)^{\frac{1}{2+3}} \times 2.976 + 0.615 = 7.10 \text{ eV}$$

Bi₂Se₃ is known as topological insulator^{29,30}, where conductivity is achieved via surface states (dirac electrons)^{30,31,32}. Being a non-trivial semiconductor it shows possibility to form trivial – non-trivial heterojunction interfaces. In particular with Sb₂Se₃, where it shows the migration of topological states towards trivial Sb₂Se₃ semiconductor in depth more than 6 nm, where they are delocalized in a vicinity of grain boundary³³

Bi₂Se₃ is also known for its narrow band gap of 0.35eV³⁴. Thus the combination of Sb₂Se₃ with Bi₂Se₃ could allow tuning of the gap, which could improve charge photogeneration and photoconductive properties of Sb₂Se₃ and positively influence the overall performance of 40GeSe₂-40Sb_{2-x}Bi_xSe₃-20CuI ceramics.

Surveyed in literature, co-deposition of Sb₂Se₃ and Bi₂Se₃ is capable of forming rectifying type of junction with efficiency η of 0.02. This low efficiency was attributed to the presence of surface states on the grain boundaries which are serving as recombination (scattering) centres³⁵. In our case we do not eager to obtain topological insulator or internal trivial – non-trivial heterojunction and the scattering of charge carriers is very undesirable. Thus we tried to avoid phase separation inside the bulk, but insure a certain level of Sb₂Se₃ doping.

Another promising type of precursor modification is tin for antimony substitution. Sn_xSb_{1-x}Se_{1-x-y} system shows the formation of hexagonal SnSe₂ and orthorhombic Sn₂Sb₄Se₈ crystal phases upon annealing³⁶. At the same time SnSe₂ is a direct band n-type semiconductor with $E_g = 1.08$ eV (slightly inferior compared to Sb₂Se₃ with $E_g = 1.17$ eV), low resistance of 10 Ω×cm, and charge carriers concentration of 2×10¹⁷ cm⁻³, which makes this particular phase interesting in case of its coupling with

p-type Cu_2GeSe_3 ³⁶. It is also interesting to mention that Sn doping of Sb-Se based materials showed a capability to improve its electrical properties which was demonstrated in Sb-Sb-Se based thin films for RAM by Lee et al.³⁷

The other type of performed substitutions was financially motivated. It is obvious that the majority of utilized elements are earth abundant and low cost, but germanium. Thus, it is essential that we tried to reduce the amount of germanium. As it was mentioned before, the light-harvesting percolating network formed in the bulk ceramics consist of n-type Sb_2Se_3 and p-type Cu_2GeSe_3 . Analysing the glass composition one can mention that there is only 20 atoms of Cu and 40 atoms of Ge. Regarding the crystalline stoichiometry we can mention that considering 100% of Cu utilized for the phase crystallisation (20 atoms) we will use only 10 atoms of Ge. Thus, 25% of Ge existing inside the glass matrix. The residual Ge-Se-I compound is capable of forming stable glassy phase, which role in forming the bulk heterojunction was not clear and supposed to be negligible. Therefore we tried to substitute excessive amounts of GeSe_2 with Sb_2Se_3 .

3.2 Glass precursors preparation

For synthesizing of glass precursors, we utilized metallic germanium, antimony, copper iodine, selenium, bismuth (99.999% Sigma Aldrich) and tin (99.999% Sigma Aldrich). Standard procedure of glass precursor synthesis described in chapter II paragraph 1.2.1, fig. 3-3. The following compositions were prepared (table 3-2):

Table 3-2 Compositions of synthesized precursors for glass-ceramic preparation

Content	GeSe_2	Sb_2Se_3	CuI	Bi_2Se_3	Sn_2Se_3
1	40	40	20	0	0
2	40	36	20	4	0
3	40	30	20	10	0
4	40	20	20	20	0
5	40	0	20	40	0
6	40	39.6	20	0	0.4
7	40	36	20	0	4
8	40	30	20	0	10
9	40	20	20	0	20
10	40	0	20	0	40
11	40	0	20	0	40 SnSe_2
12	38	42	20	0	0
13	36	44	20	0	0
14	32	48	20	0	0
15	30	50	20	0	0
16	26	54	20	0	0

3.3. Structural and electric properties of $40\text{GeSe}_2\text{-}40\text{Sb}_{2-x}\text{Bi}_x\text{Se}_3\text{-}20\text{CuI}$ glass-ceramics.

All the precursors containing bismuth show a glass transition. They remain glassy with a certain quantity of crystallized matter in case of samples with 25 and 50 mol. % of bismuth, which is evident from IR transmission spectra where we observe Rayleigh scattering (fig. 3-18). While for the precursor with 25 mol. % of bismuth Rayleigh is weak and expressed only in near-IR (fig. 3-18 (b)), sample with 50 mol. % of bismuth demonstrates intensive scattering in wide range of wavelengths (fig. 3-18 (c)).

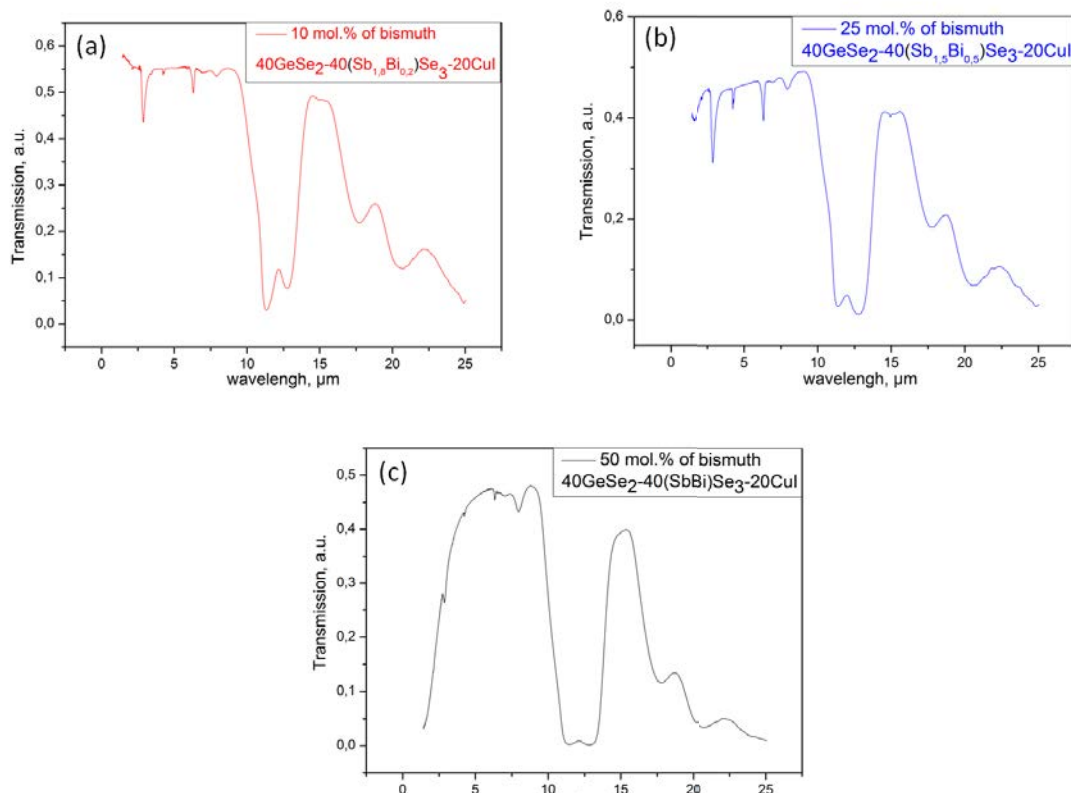


Figure 3-18 IR transmission spectra of glass precursors containing 10 mol. % of bismuth (a), 25 mol. % (b), 50 mol. % (c).

The attenuation of transparency and increase of scattered component evidences reduction of glass stability. We had mentioned previously that $40\text{GeSe}_2\text{-}40\text{Sb}_2\text{Se}_3\text{-}20\text{CuI}$ matrix barely can be assigned to be stable, however it is quite tolerant to the introduction of 10 mol. % of bismuth, that does not cause any crystallization (fig. 3-18 (a)).

On the other hand, precursor with complete substitution of bismuth for antimony was completely crystallized after quenching. It shows the absence of transparency and strongly pronounced crystal peaks on XRD diffractogram (fig. 3-19 (a)), which correspond to hexagonal lattice of R-3m space group with cell parameters $a = b = 4.1396 \text{ \AA}$, $c = 29.636 \text{ \AA}$. It is interesting to mention that melting – quenching synthesis process leads to (0 0 6) preferential orientation of crystal plane with XRD peak at 18.56° . While for Bi_2Se_3 crystals obtained by self-assembling, it is (0 1 5) orientation with XRD peak at 29.35° , with respect to JSCPDS 033-0214 card (fig. 3-20)³⁸.

In fig. 3-19 (b) one can see a typical for bismuth-based topological insulator image of surface³⁹, where we can observe “sintered” dense matter of Bi_2Se_3 (dark background) and white flakes of Cu_2GeSe_3 on top of it. Possessing metallic conductivity $\rho = 1.7 \times 10^{-2} \Omega \times \text{cm}$, it does not show any photoresponse in PEC experiment and can be consider as useless for our purposes.

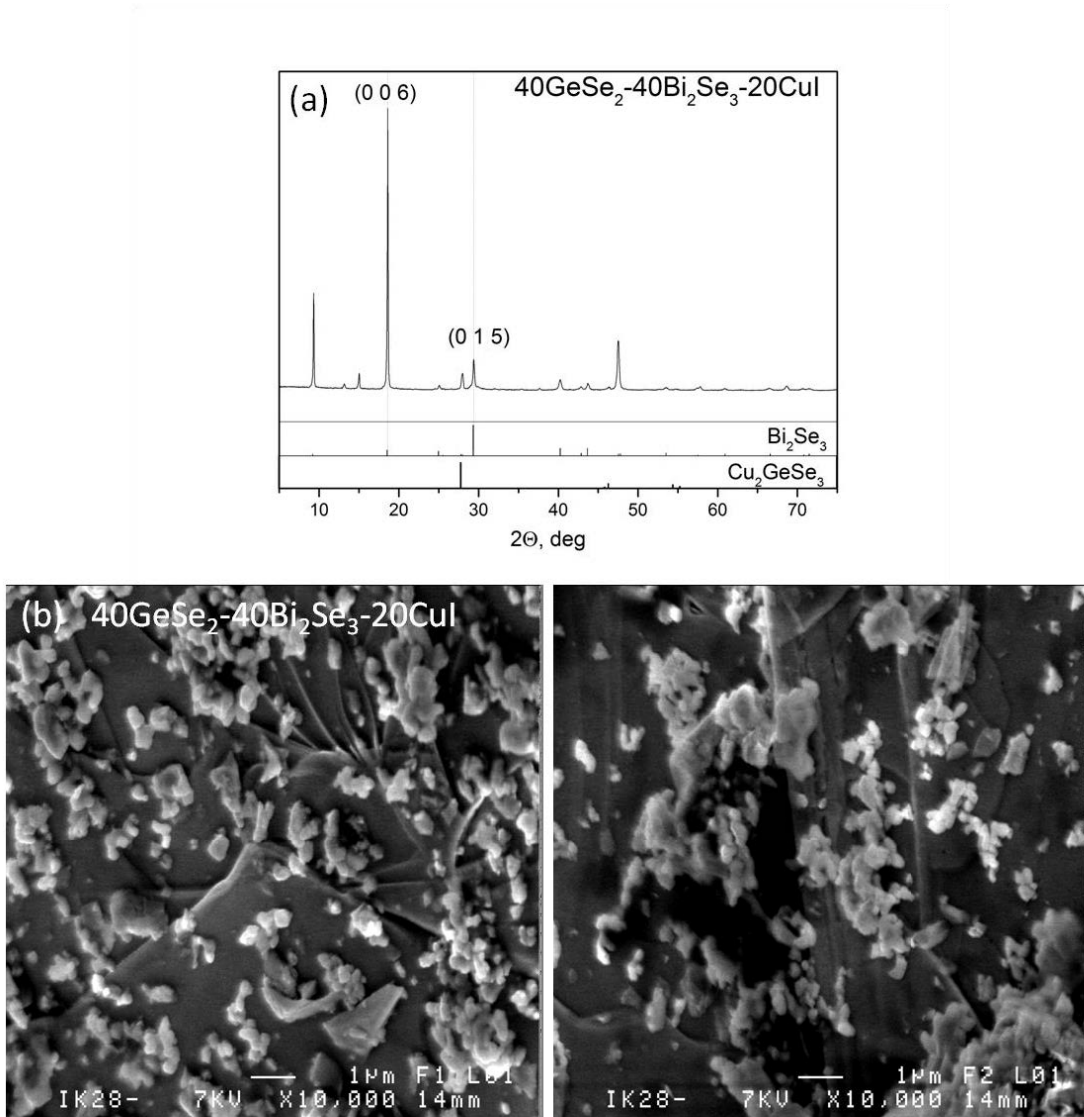


Figure 3-19 XRD diffractogram for as-prepared 40GeSe₂-40Bi₂Se₃-20CuI precursor (a), and its SEM image (b)

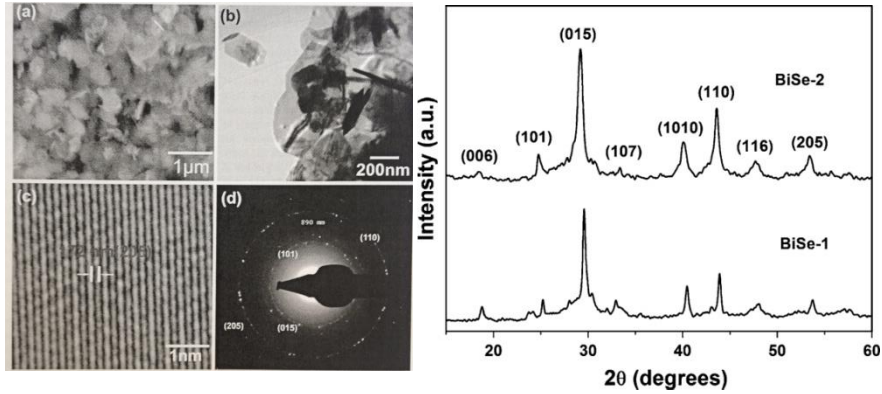


Figure 3-20 Bi_2Se_3 self-assembling nanoplates crystallization⁴¹

Other glassy precursors were annealed at T_x for one hour and further analyzed by X-ray diffraction and SEM. In fig. 3-21 one can see that XRD pattern is very similar to the spectra of pure $40\text{GeSe}_2\text{-}40\text{Sb}_2\text{Se}_3\text{-}20\text{CuI}$ glass-ceramics (fig. 3-15 black curve) with strongly pronounced peaks of Sb_2Se_3 and Cu_2GeSe_3 phases. The presence of Bi_2Se_3 phase can be found for sample with 25 mol. % concentration of bismuth and more pronounced for glass-ceramics with 50 mol. % of bismuth. This secondary phase peak at 29.35° is attributed to (0 1 5) orientation, certain amount of (0 0 6) oriented crystals could also be supposed at 18.56° . However, looking at the SEM images, presented in fig. 3-22, we can conclude that even 10 mol. % of bismuth changes drastically the morphology. One can see that compared to $40\text{GeSe}_2\text{-}40\text{Sb}_2\text{Se}_3\text{-}20\text{CuI}$ (fig. 3-21 (a)) Sb_2Se_3 maintain its rod-like structure on nanometer scale, but on micrometer scale material undergoes severely different crystallization with larger crystalline domains and higher symmetry (fig. 3-21 (b-d)). With increase of bismuth content one could mention that Sb_2Se_3 rods “sinters” (fig. 3-21 (c,d)) with the transition from rod-like to sheet-like structure .

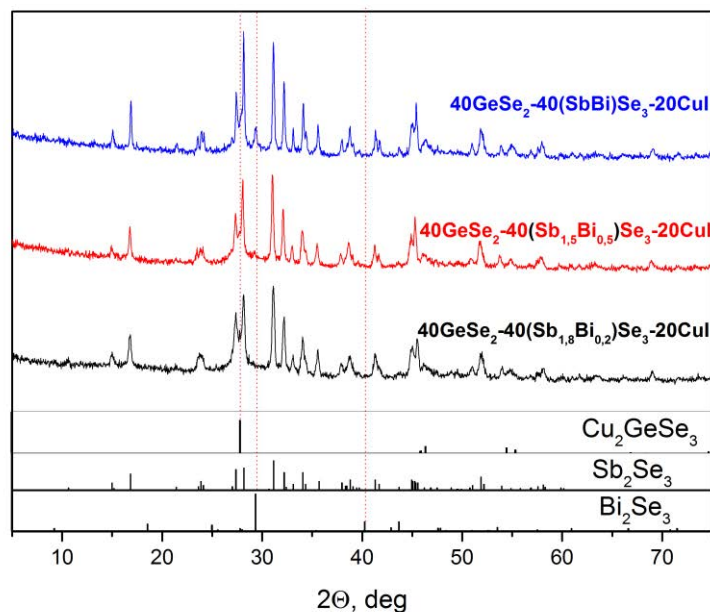


Figure 3-21 XRD diffractogram of obtained glass-ceramics with different content of bismuth.

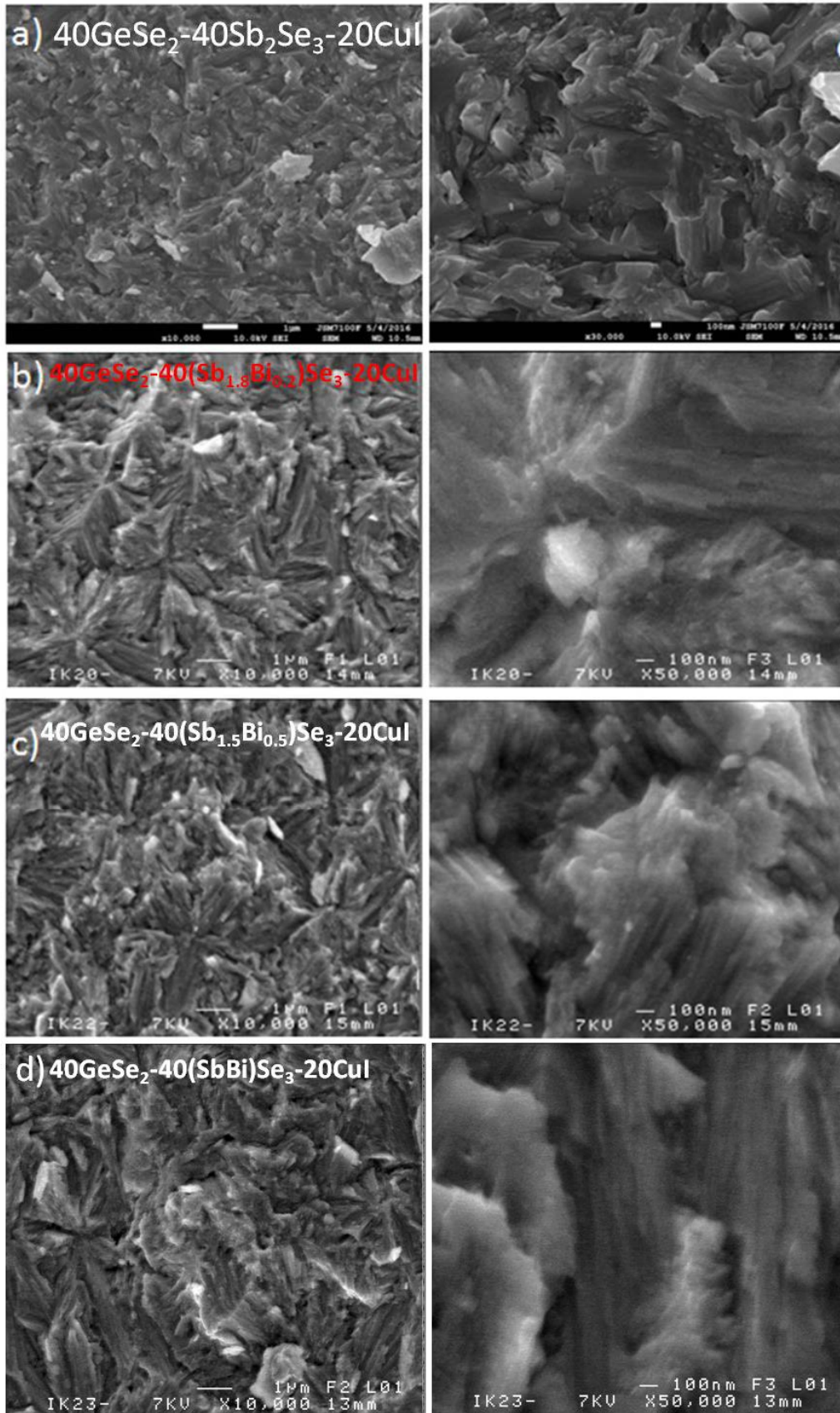


Figure 3-22 SEM images of obtained glass-ceramics a) $40\text{GeSe}_2\text{-}40\text{Sb}_2\text{Se}_3\text{-}20\text{CuI}$, b) $40\text{GeSe}_2\text{-}40\text{Sb}_{1.8}\text{Bi}_{0.2}\text{Se}_3\text{-}20\text{CuI}$, c) $40\text{GeSe}_2\text{-}40\text{Sb}_{1.5}\text{Bi}_{0.5}\text{Se}_3\text{-}20\text{CuI}$, d) $40\text{GeSe}_2\text{-}40\text{SbBiSe}_3\text{-}20\text{CuI}$

PEC experiment (fig. 3-23) shows that introduction of 10 mol. % of Bi increases photocurrent at positive bias, which is probably associated with Bi-doping of Sb_2Se_3 . Photocurrent up to $50\mu\text{A}/\text{cm}^2$ under $+0.6\text{V}$ electric bias can be obtained. However no p-type phase was formed inside this glass-ceramics, since the response of p-type semiconductor under negative bias is absent. With increase of Bi content, we observe the reduction of photocurrent by several orders of magnitude. Thus, for 25 mol. % of Bi photocurrent reaches $4\mu\text{A}/\text{cm}^2$ at $+0.6\text{V}$ bias, and $0.4\mu\text{A}/\text{cm}^2$ at $+0.6\text{V}$ for 50 mol. %. This decrease of photocurrent density can be explained by unfavorable morphology of obtained glass-ceramic. First, the increase of crystal size could negatively affect charge separation properties and increase the recombination probability. Second, the presence of secondary phase of Bi_2Se_3 could increase the amount of grain boundaries, which serve as charge carrier scattering centers.

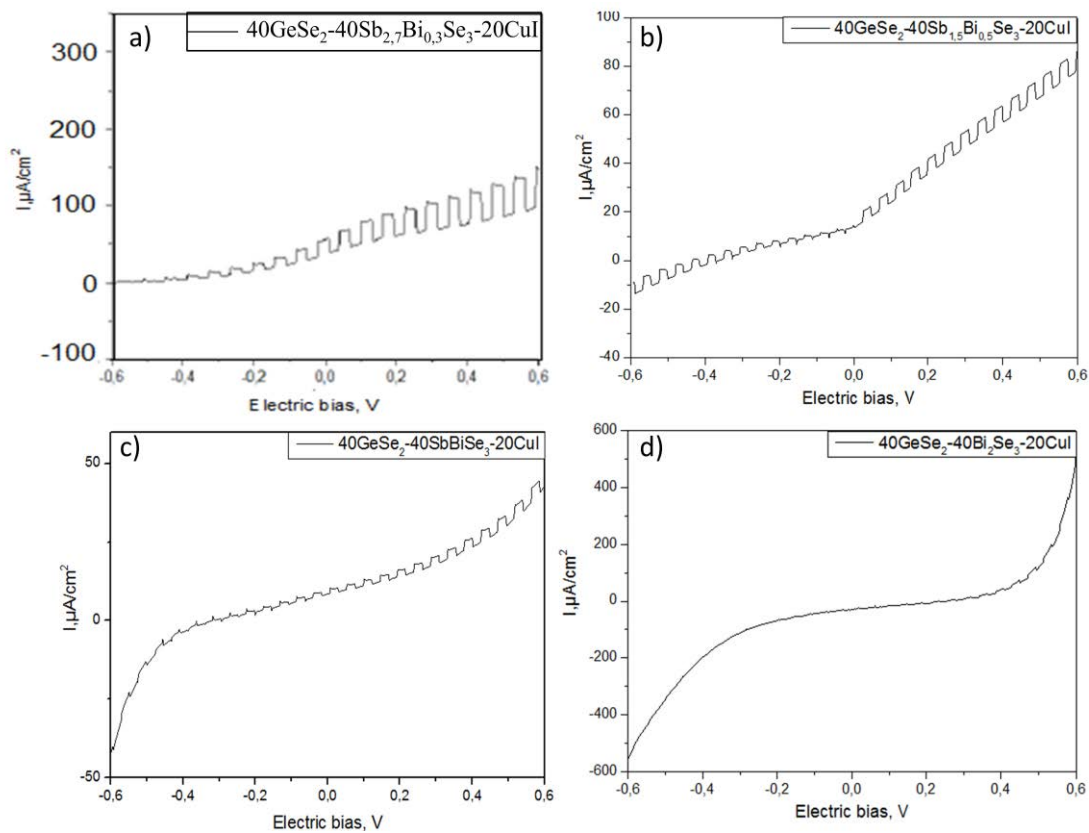


Figure 3-23 PEC curves of obtained glass-ceramics with different molar content of bismuth (a) $40\text{GeSe}_2-40\text{Sb}_{2.7}\text{Bi}_{0.3}\text{Se}_3-20\text{CuI}$, (b) $40\text{GeSe}_2-40\text{Sb}_{1.5}\text{Bi}_{0.5}\text{Se}_3-20\text{CuI}$, (c) $40\text{GeSe}_2-40\text{SbBiSe}_3-20\text{CuI}$, (d) $40\text{GeSe}_2-40\text{Bi}_2\text{Se}_3-20\text{CuI}$

3.4. Structural and electric properties of $40\text{GeSe}_2-40\text{Sb}_{2-x}\text{Sn}_x\text{Se}_3-20\text{CuI}$ glass-ceramics.

As a result of substitution, in fig. 3-24 one can observe a slight reduction of glass-transition temperature with increase of tin content. At the same time, crystallization peak splitting occurs for a glass with 10 mol. % of tin (red curve). It is clearly pronounced for precursors with 25 mol. % and 50 mol. % of tin (blue curve, pink curve). The stability of precursor reduces due to migration of lower crystallization temperature peak towards glass-transition temperature with increase of tin molar

content. This can be explained by appearance of the phase, which requires less energy to be crystallized compared to Sb_2Se_3 . This effect can be assigned to SnSe_2 phase appearance and, probably reduction of Sb_2Se_3 crystallization temperature because of Sn doping. We observe that the precursor with complete substitution of tin for antimony $40\text{GeSe}_2\text{-}40\text{Sn}_2\text{Se}_3\text{-}20\text{CuI}$ shows first crystallization peak at higher temperature compared to compounds where two elements co-exist (green curve). This compound reaches maximal concentration of tin within the set of prepared compositions. It shows the absence of transparency (see fig. 3-27, red line), some X-ray reflections assigned to SnSe_2 phase on XRD diffractogram (fig. 3-26) and weak glass-transition peak (fig. 3-24, green curve) immediately after melting-quenching without any additional heat treatment. That leads to the conclusion that severe quantity of low temperature phase SnSe_2 is already crystallized. On DSC curve (fig. 3-24, green curve) we are dealing with residual glass (amorphous background on XRD diffractogram in fig. 3-26). Thus, crystallization peak shift towards higher temperatures is understandable.

Precursor $40\text{GeSe}_2\text{-}40\text{SnSe}_2\text{-}20\text{CuI}$ was completely crystallized and does not show neither glass-transition nor SnSe_2 phase crystallization peaks on DSC curve (fig. 3- 24, navy curve).

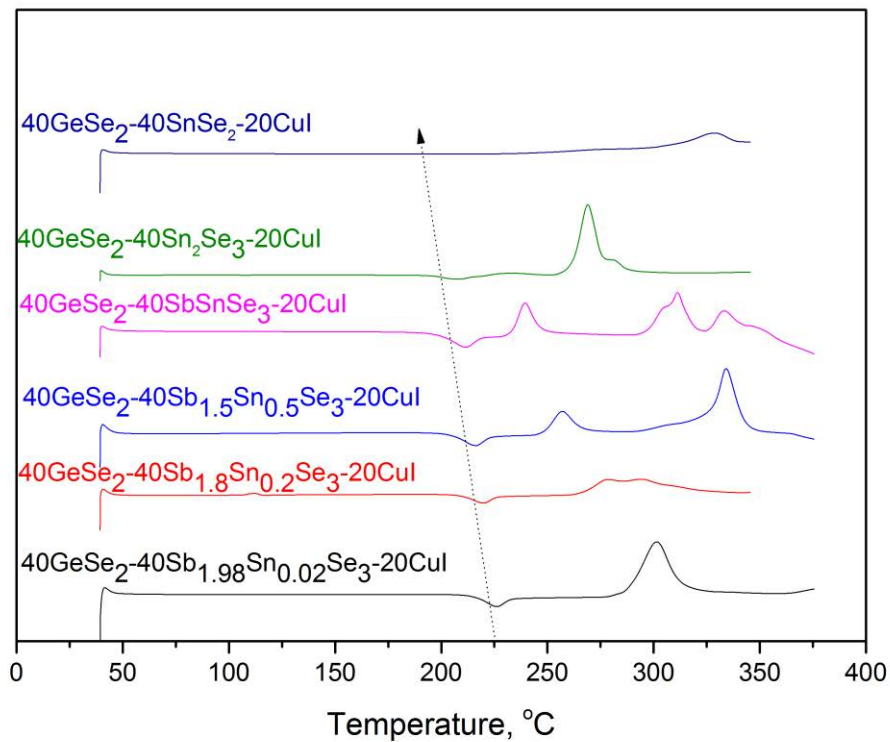


Figure 3-24 DSC curves of obtained precursors with different molar content of tin.

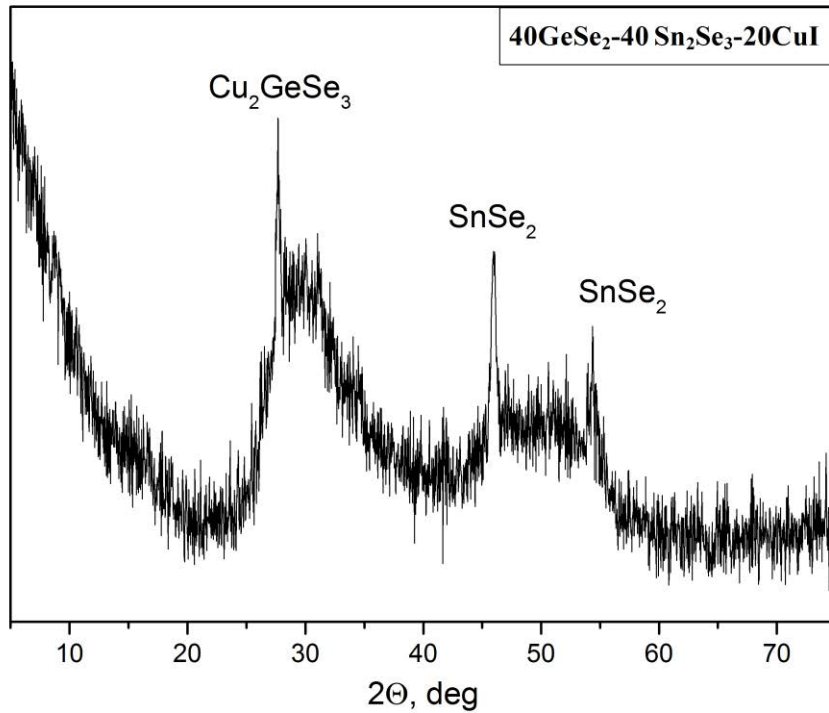


Figure 3-25 XRD diffractogram of 40GeSe₂-40Sn₂Se₃-20CuI as prepared sample

In fig. 3-26 glass transition and crystallization temperatures evolution as a function of tin for antimony substitution is shown. Certain compositions possess several crystallization peaks marked with several red dots. Here we would like to underline that only low-temperature phase can be taken into account to estimate the stability of precursor. As a result of reduced stability, sample with 25 mol. % of Sn shows certain crystallization leading to pronounced Rayleigh scattering, as it is shown on IR transmission spectrum in fig. 3-27 (blue line). Precursors with higher quantity of Sn (> 25 mol. %) have been already severely crystallized after preparation and show the absence of transparency. On the other hand, precursors with a 1 mol. % and 10 mol. % of tin show descent transparency comparable to 40GeSe₂-40Sb₂Se₃-20CuI precursor without any sign of Rayleigh scattering, as shown in fig. 3-27 (orange line, green line).

Since certain precursor show several distinguished crystallization peaks several series of ceramics with different annealing temperatures were prepared. Samples were annealed for 1 hour at different Tx temperatures, summarized in fig. 3-26.

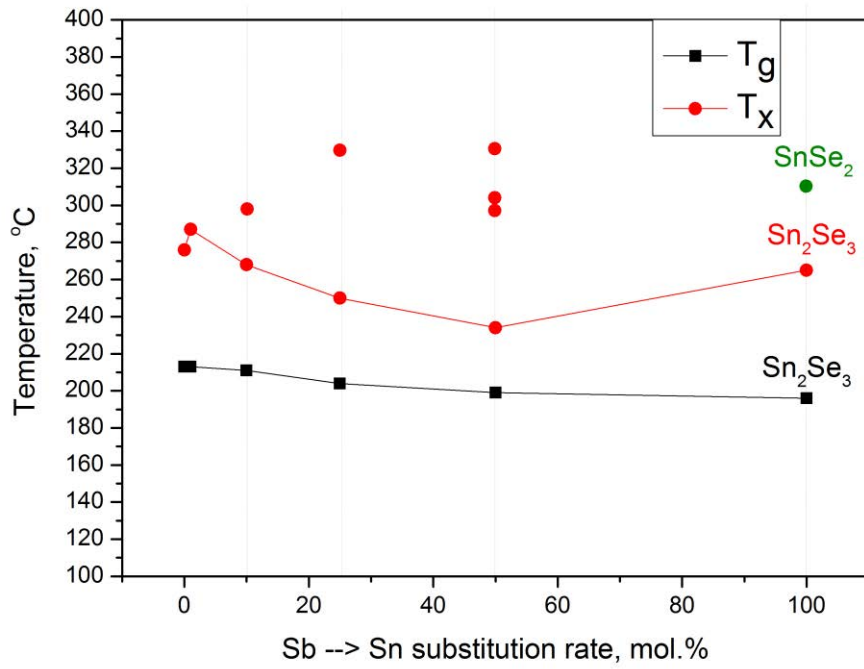


Figure 3-26 Glass-transition (black) and crystallization (red) temperatures as a function of tin for antimony substitution. Several dots mean several crystallization peaks. Sn_2Se_3 labeled dots stay for $40\text{GeSe}_2\text{-}40\text{Sn}_2\text{Se}_3\text{-}20\text{CuI}$ precursor. SnSe_2 green dot stay for $40\text{GeSe}_2\text{-}40\text{SnSe}_2\text{-}20\text{CuI}$ composition.

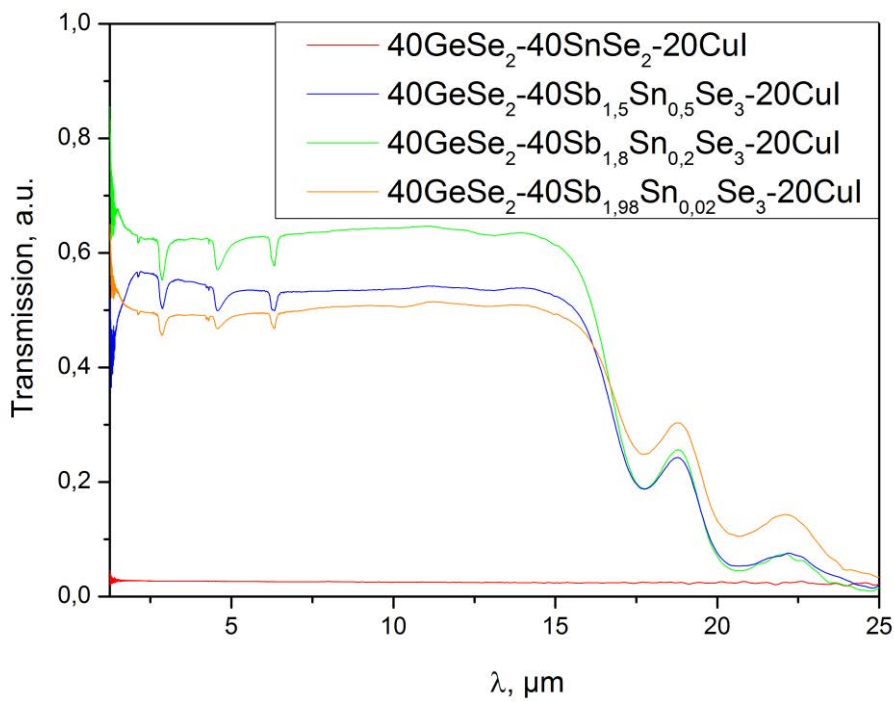


Figure 3-27 IR spectra of glass precursors with different molar content of tin.

XRD diffractograms of glass-ceramics prepared at lowest crystallization temperature are summarized in fig. 3-29. For the sample with 1 mol. % of tin (violet line) X-ray pattern shows a weak shift of Sb_2Se_3 peaks towards lower 2θ values, which may stay for stretching of crystal lattice with tin atoms. However, there are no SnSe_2 phase signature and no changes in relative peak intensities, which could stay for the absence of atomic occupation rate change. Appearance of SnSe_2 phase could be supposed for compounds with 50 mol. % of Sn (navy line), where XRD peak at 30.69° is related to (1 0 1) orientation of hexagonal crystal lattice of SnSe_2 with cell parameters 3.81 nm x 3.81 nm x 6.14 nm. At the same time one can observe a significant change in relative intensities of Sb_2Se_3 related peaks at 27.39° (2 3 0) and 28.19° (2 1 1). With increase of Sn content signs of R-centered hexagonal polymorph of SnSe_2 phase with 3.8 nm x 3.8 nm x 55.229 nm cell parameters could be supposed referring XRD peak at 14.27° (blue line, red line). In particular, 40GeSe₂ - 40SnSe₂ - 20CuI crystal demonstrates multiple signatures of monoclinic GeSe₂ secondary phase with $a = 7.0716 \text{ \AA}$, $b = 16.769 \text{ \AA}$, $c = 11.831 \text{ \AA}$ cell parameters. It is characterized by various crystal planes reflections in a vicinity of $2\theta = 30^\circ$ (with respect to PDF 30-0595).

We established that annealing of 40GeSe₂ - 40SnSe₂ - 20CuI and 40GeSe₂ - 40Sn₂Se₃ - 20CuI precursors at higher temperatures does not lead to new phases formation, as demonstrated in XRD diffractograms in fig. 3-29 (a,b). It results only in increase of crystal size (more narrow XRD peaks with higher intensity) and promotes certain crystalline orientations weakly pronounced at lower temperatures, as SnSe_2 orientation (1 0 1) at 30.69° and (1 0 2) orientation at 40.04° .

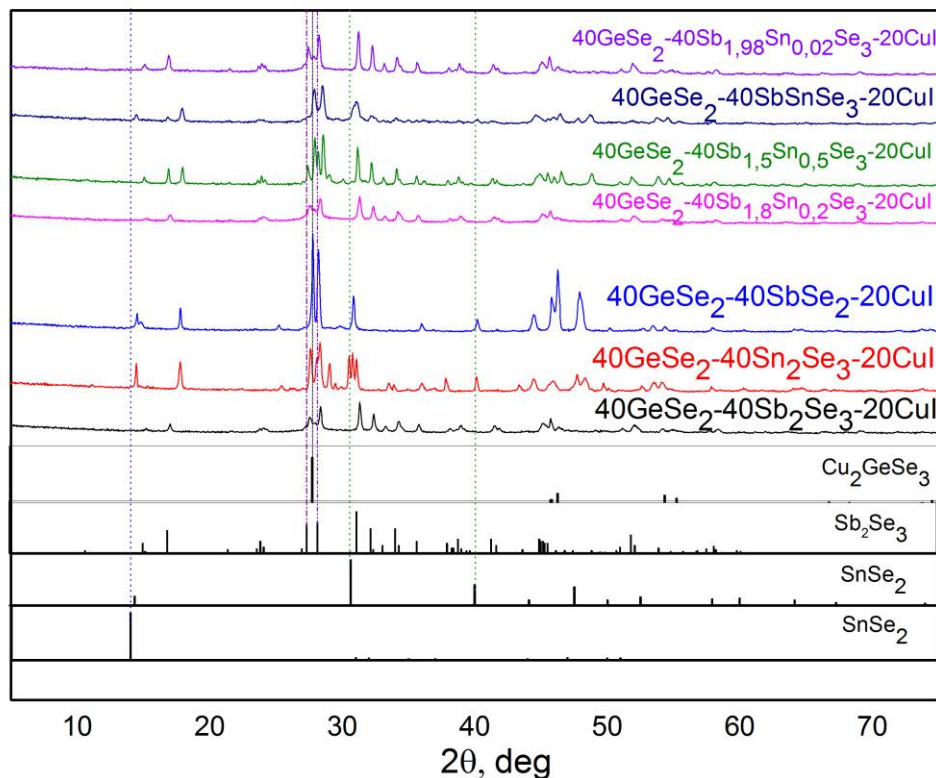


Figure 3-28 XRD diffractogram of tin doped glass-ceramics

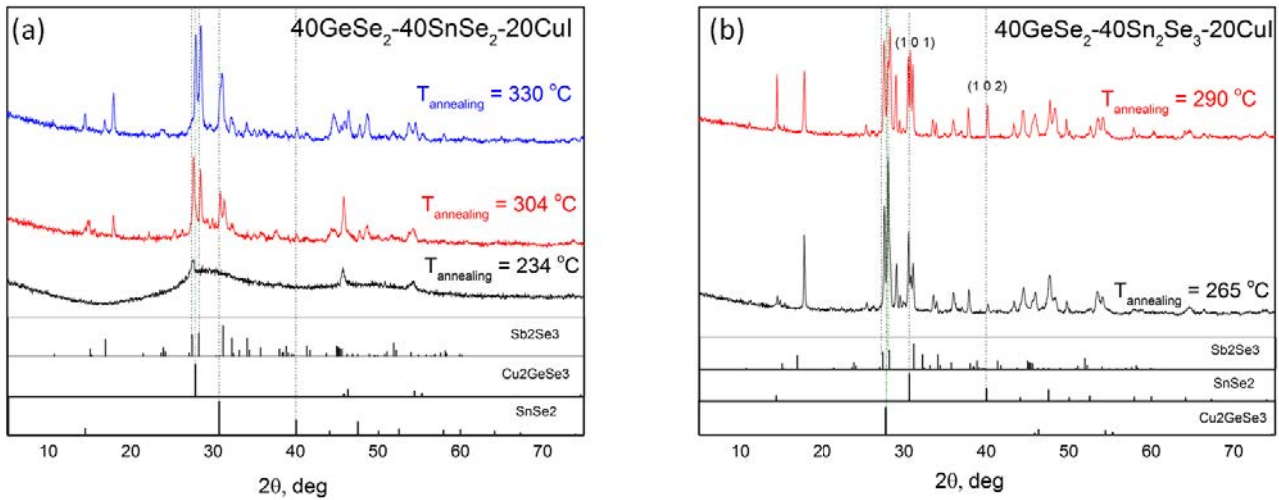


Figure 3-29 XRD diffractogram of compounds with complete substitution of Sb by Sn : 40GeSe₂-40SnSe₂-20CuI (a), 40GeSe₂-40Sn₂Se₃-20CuI (b).

Resistivity of glass-ceramics annealed at different temperatures is summarized in fig. 3-30. Concerning low resistance of SnSe₂, it is not surprising that samples with complete substitution of tin for antimony, which are crystallized to the certain extent without any additional annealing, show resistivity of 20 Ω×cm, which is comparable to the annealed 40GeSe₂-40Sb₂Se₃-20CuI glass-ceramics. Further annealing does not improve the resistivity of these samples and even leads to its increase up to 10³ Ω×cm, in case of 40GeSe₂ - 40SnSe₂ -20CuI. Since the conductivity is determined by the most conductive phase, which in our case is SnSe₂ and this phase is first to crystallize, other phases formed upon additional annealing (especially secondary phases represented by a vast amount of smaller size crystals) could serve only as scattering centers. For glassy precursors low temperature annealing (below T_x) leads to weak conductivity, probably, because of insufficient crystallization of SnSe₂ or Cu₂GeSe₃ phases. Increase of annealing temperature reduces resistivity. However, further augmentation of temperature leads to the increase of resistivity, because of the above mentioned reasons. This can be clearly seen in case of glass-ceramics with 50 mol. % of Sn (green line).

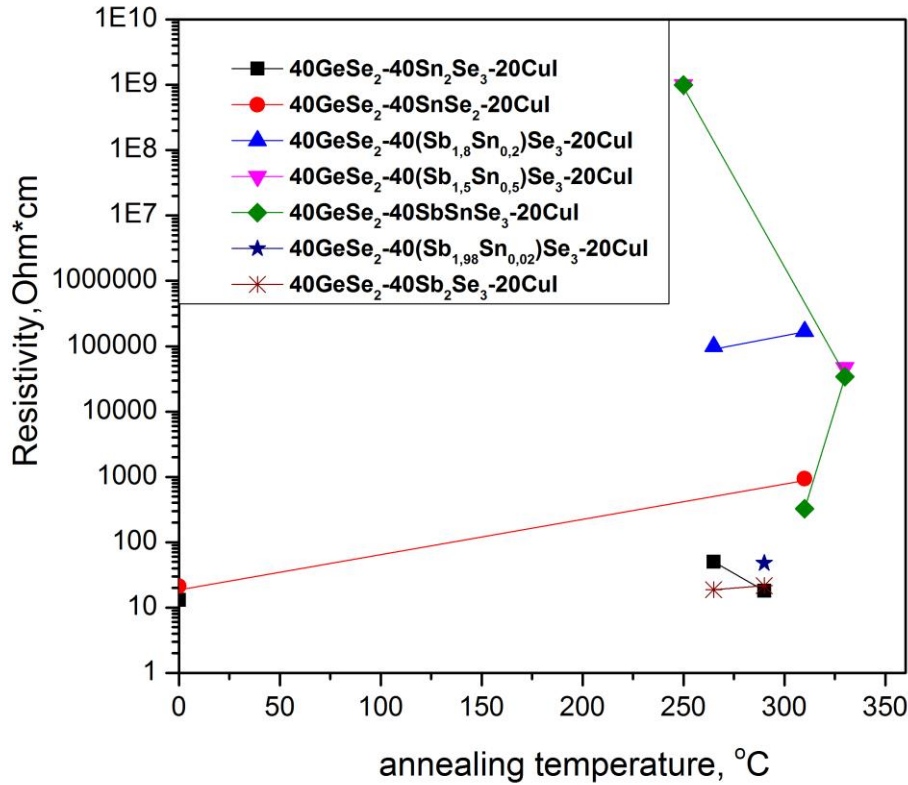


Figure 3- 30 Influence of annealing temperature and composition on electrical resistivity of glass ceramics obtained. Annealing for 1 hour.

In fig. 3-31 lowest achieved resistivity for each glass-ceramics composition is represented. Pure 40GeSe₂-40Sb₂Se₃-20CuI (0 mol. % of Sn) glass-ceramics annealed at 275°C and as-prepared 40GeSe₂ - 40Sn₂Se₃ -20CuI (100 mol. % of Sn) without additional treatment shows similar resistivity. However, it is evident that while the origin of 40GeSe₂-40Sb₂Se₃-20CuI glass-ceramics conductivity is iodine doped Sb₂Se₃ macroscopic rods, the conductivity of Sn-based ceramics is provided by SnSe₂ phase. Other phases are not sufficiently crystallized in as-prepared compound without additional thermal treatment and, therefore, cannot take part in electrical charge transport. The amount of amorphous phase is still significant for untreated 40GeSe₂ - 40Sn₂Se₃ -20CuI ceramics. For the compounds where Sb and Sn co-exist, we can observe rapid augmentation of resistivity with increase of Sn content. It is associated, probably, with rupture of rod-like Sb₂Se₃ structure upon the incorporation of Sn. Reaching its maximum for composition with 10 mol. % of Sn, we observe further decrease of resistivity with Sn content, explained by the bulk formation of microscopic SnSe₂ crystals, which is in good correspondence with XRD results.

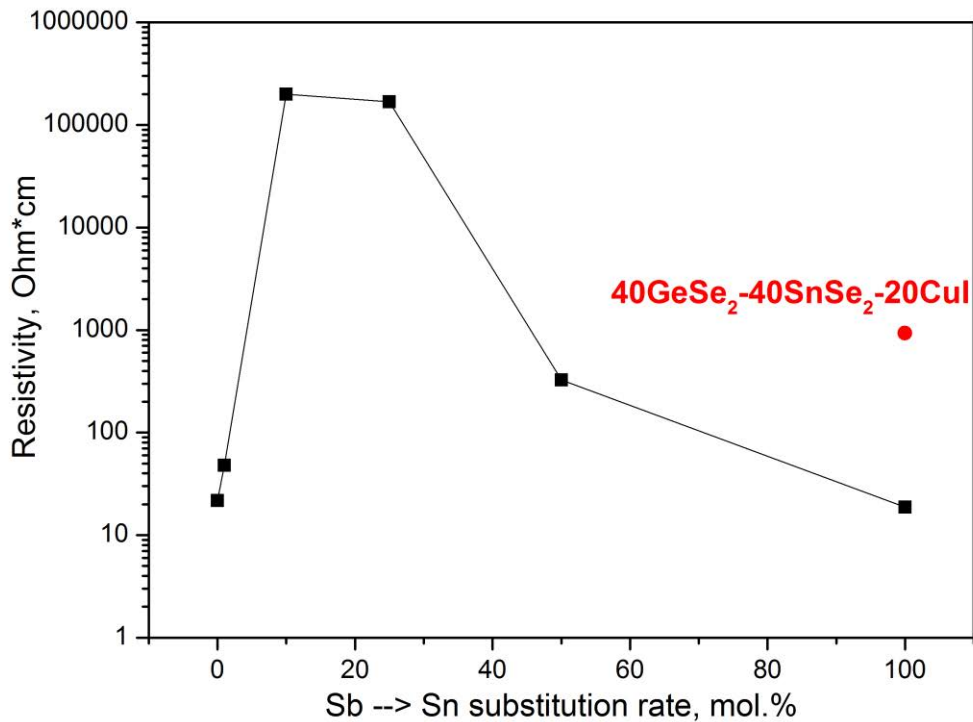


Figure 3-31 Highest achieved electrical conductivity for tin doped glass-ceramics. Red dot stays for composition $40\text{GeSe}_2\text{-}40\text{SnSe}_2\text{-}20\text{CuI}$.

Indeed in fig. 3-32 we observe substantially different morphology for tin doped glass-ceramics with different molar content of Sn. For the glass-ceramics with 1 mol. % of Sn (fig. 3-32 (c)) we observe rough crystallized surface with small crystal size, while for 10 mol. % the size of rod-like crystals reach dozens of micrometers (fig. 3-32 (d)). This significantly different microstructure could stay for poor conductivity of glass-ceramics with 10 mol. % of tin. For the samples with complete substitution of tin for antimony one can observe leaf-like or sheet-like structure conventional for SnSe_2 phase (fig. 3-32 (a,b)). It is evident that conductivity mechanism for these ceramics differs from one for $40\text{GeSe}_2\text{-}40\text{Sb}_2\text{Se}_3\text{-}20\text{CuI}$.

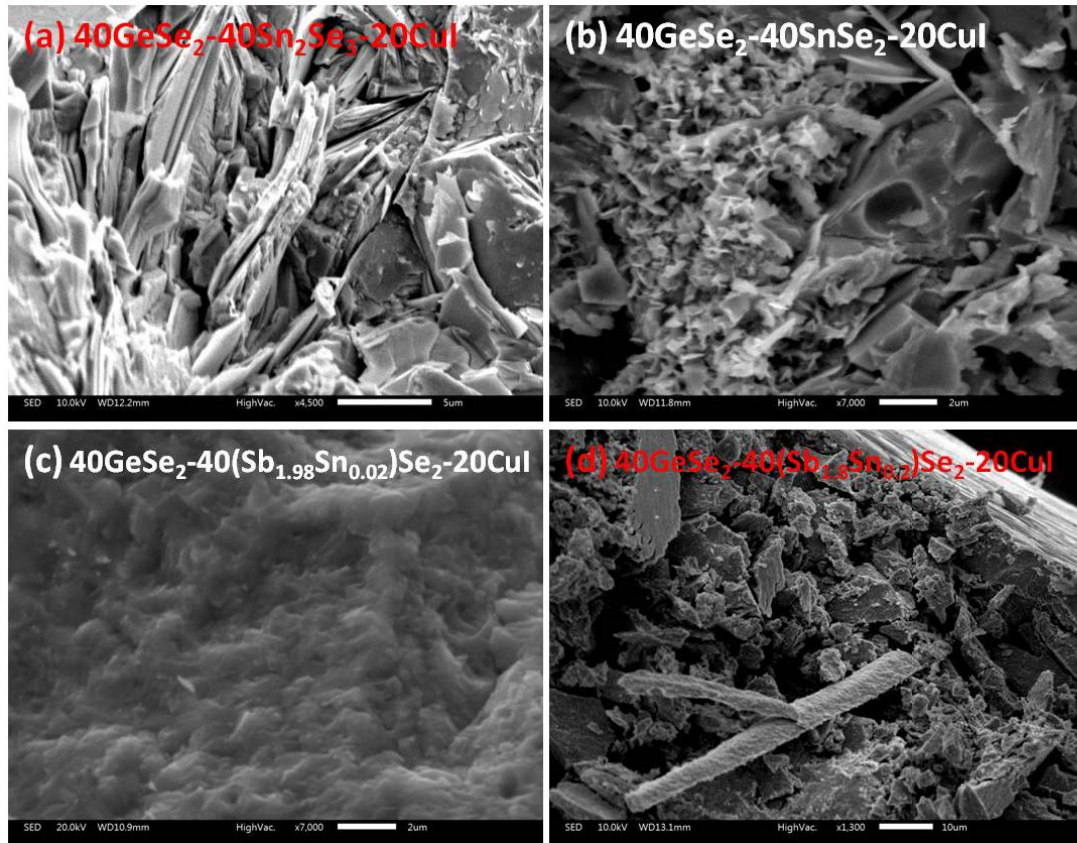


Figure 3-32 SEM image of glass-ceramics with different molar content of tin.

A set of PEC measurements for obtained glass-ceramics is shown in fig. 3-33. In fig. 3-33 (a) and fig. 3-33 (b) one could observe a weak photo response of p-type SnSe_2 pronounced at negative electric bias. Light induced photocurrent reaches $12 \mu\text{A}/\text{cm}^2$ under -0.6V bias for both sample annealed at lower and higher temperatures. As we can conclude, despite a decent conductivity, this compound is much less performant photoconductor compare to $40\text{GeSe}_2 - 40\text{Sb}_2\text{Se}_3 - 20\text{CuI}$ glass-ceramics (up to $22 \mu\text{A}/\text{cm}^2$).

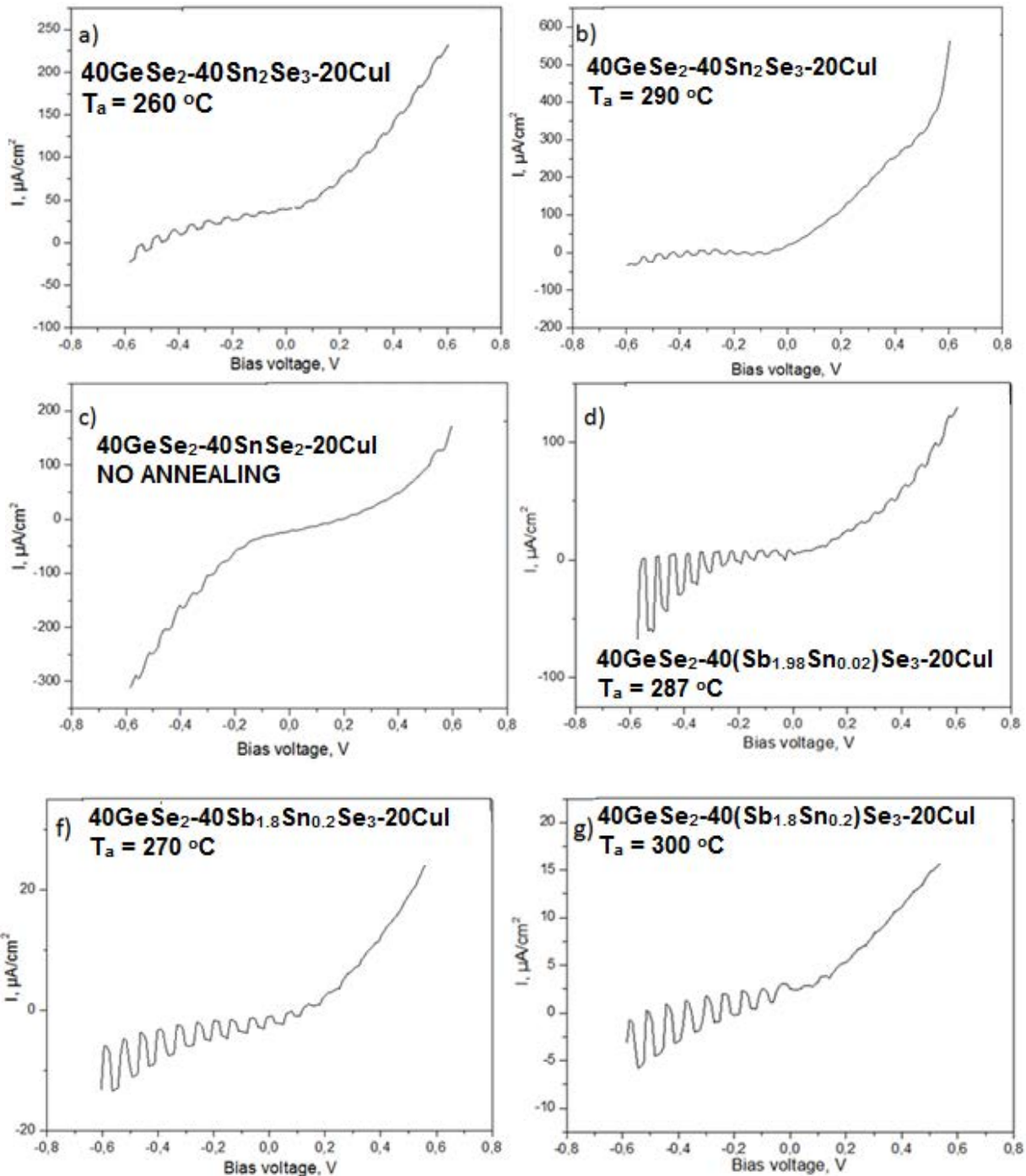
In fig. 3-33 (c) $40\text{GeSe}_2 - 40\text{SnSe}_2 - 20\text{CuI}$ crystal without additional thermal treatment shows a diode behavior with weak photoconductive effects under stronger negative voltage.

On the other hand photovoltaic response of glass-ceramics with 1 mol. % of Sn depicted in fig. 3-33 (d) deserves attention. We can observe a very weak photo response under positive bias. It means that n-type phase is not formed in sufficient quantity. It is known that Sb_2Se_3 doped with a small amount of Sn ($\sim 1-2$ mol. %) is a p-type semiconductor^{40,41}. One can suppose that either iodine doped Sb_2Se_3 is not crystallized sufficiently (or in a proper way) in the presence of Sn, or the presence of Sn change severely the morphology of glass ceramics, which leads to unfavorable spatial distribution of iodine dope Sb_2Se_3 phase. However the photoconductive performance of Sn doped Sb_2Se_3 in glass-ceramics under negative bias ($81 \mu\text{A}/\text{cm}^2$ at -0.6V) is better compared to non-doped $40\text{GeSe}_2 - 40\text{Sb}_2\text{Se}_3 - 20\text{CuI}$ glass-ceramics ($22 \mu\text{A}/\text{cm}^2$ at -0.6V), where Cu_2GeSe_3 phase and non-stoichiometric phase of Sb_2Se_3 are responsible for p-type phase formation. We can notice that upon the increase of Sn content PEC response does not vary qualitatively (we observe p-type photoconductive phase under

negative bias) as shown in fig. 3-33 (g,j,l). However quantitatively, the intensity of photocurrent is directly proportional to conductivity, which decreases with increase of tin content.

$$J = n\mu\sigma E \quad (3.20)$$

Fig. 3-33 (h, k) show PEC curves for glass-ceramics with 25 mol. % and 50 mol. % of tin annealed at lower temperatures. It is possible to make a conclusion that annealing temperature was too low to assure sufficient bulk crystallization, therefore its conductivity is weak and photoelectric properties are not pronounced.



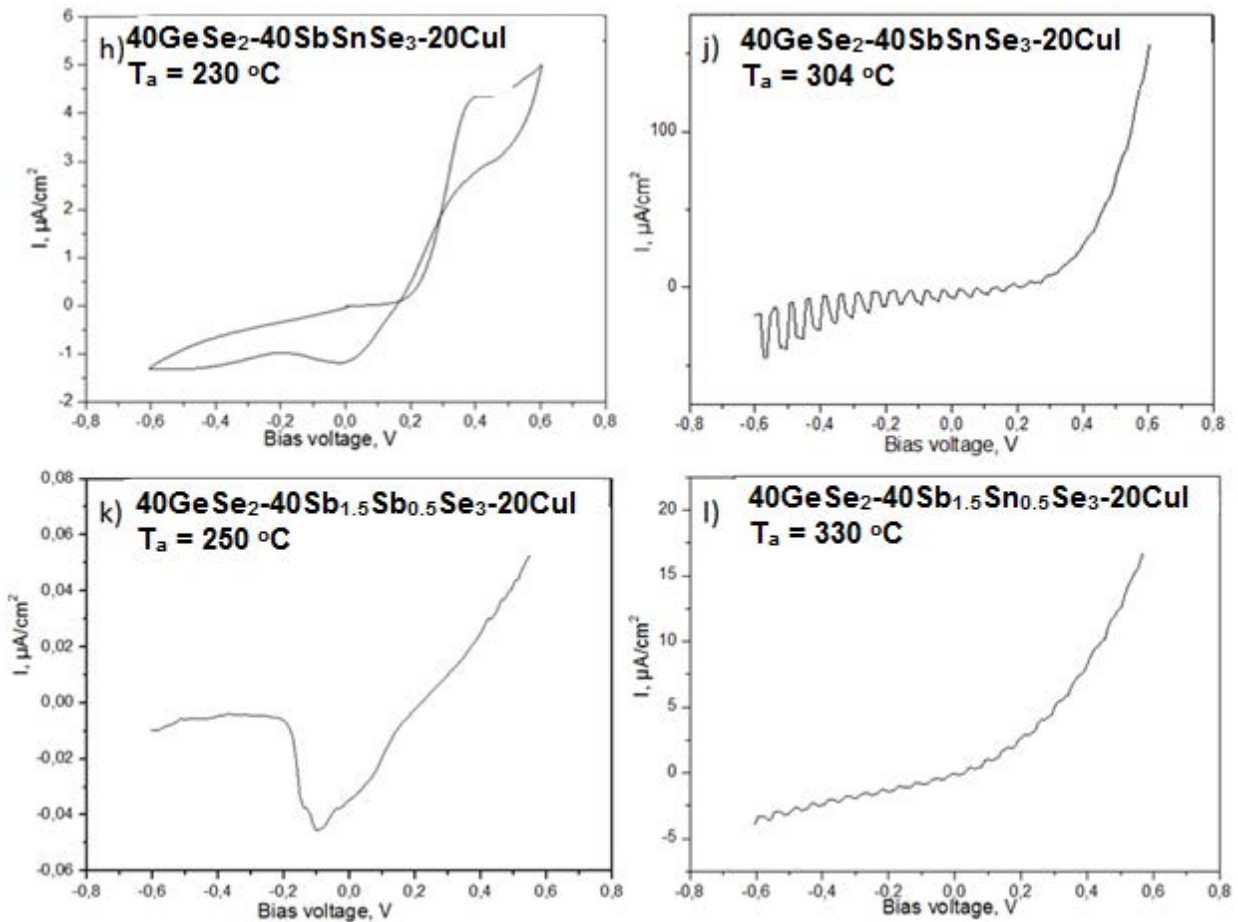


Figure 3-33 PEC curves of glass-ceramics with different molar content of tin annealed at different temperatures.

Maximal photocurrent obtained under positive and negative bias for glass-ceramics with different molar content of tin is summarized in fig. 3-34. We can observe that with introduction of Sn photocurrent under positive bias vanishes, signifying the absence of sufficiently conductive n-type phase. At the same time photocurrent density under negative bias increases, which stays for photoconductive p-type phase formation.

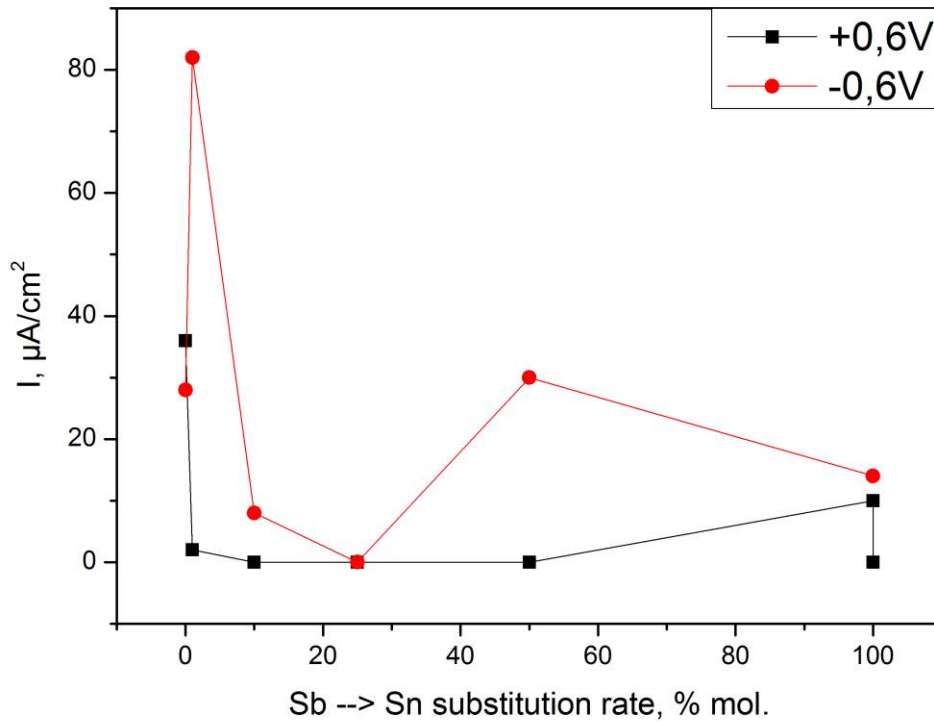


Figure 3-34 Maximal obtained photocurrent density under positive and negative bias of tin doped glass-ceramics

To put a bottom line under these experiments, we can mention that Sn doping could cause the change of conductivity type of Sb_2Se_3 , which normally is n-type in case of $40\text{GeSe}_2 - 40\text{Sb}_2\text{Se}_3 - 20\text{CuI}$ glass-ceramics. Sn doped p-type Sb_2Se_3 demonstrates higher photocurrent compared to Cu_2GeSe_3 phase and non-stoichiometric Sb_2Se_3 . However, with introduction of substantial quantities of Sn (>10 mol. %) photocurrent density decreases because of the increase in bulk resistivity.

Tin doped Sb_2Se_3 , being p-type phase, could be a promising material for pairing with iodine doped Sb_2Se_3 to prepare planar p-n junction.

3.5. Structural and electric properties of $x\text{GeSe}_2-(1-x)\text{Sb}_2\text{Se}_3-20\text{CuI}$ glass-ceramics

Since the only costly element in glass-ceramics is germanium we tried to reduce its quantity. We studied the influence of GeSe_2 component reduction on thermal and optical properties of glassy precursor and its influence on photoelectric performance of obtained glass-ceramics.

Since germanium is one of the main glass formers in pseudo-ternary system $\text{GeSe}_2-\text{Sb}_2\text{Se}_3-\text{CuI}$ we expected reduction of glass stability with decrease of GeSe_2 component. In order to obtain more stable glass-precursor, we utilized a tube with 6 mm internal diameter for $30\text{GeSe}_2-50\text{Sb}_2\text{Se}_3-20\text{CuI}$ and $24\text{GeSe}_2-56\text{Sb}_2\text{Se}_3-20\text{CuI}$ compositions instead of usually utilized 9 mm tube. It leads to increase of the cooling rate and reduces the probability of crystallized phase formation.

In fig. 3-35 (a,b) IR transmission spectra are presented. One can mention that glass-precursors with reduced molar content of GeSe_2 (fig. 3-35 (a)): $38\text{GeSe}_2\text{-}42\text{Sb}_2\text{Se}_3\text{-}20\text{CuI}$, $36\text{GeSe}_2\text{-}44\text{Sb}_2\text{Se}_3\text{-}20\text{CuI}$ and $32\text{GeSe}_2\text{-}48\text{Sb}_2\text{Se}_3\text{-}20\text{CuI}$ have similar optical properties and do not demonstrate strong Rayleigh scattering. At the same time, molar content of GeSe_2 below 32 mol. % leads to the formation of important crystallized fraction, which results in strong Rayleigh scattering in a range of wavelengths 1.25 – 8 μm , as it is shown in fig. 3-35 (b).

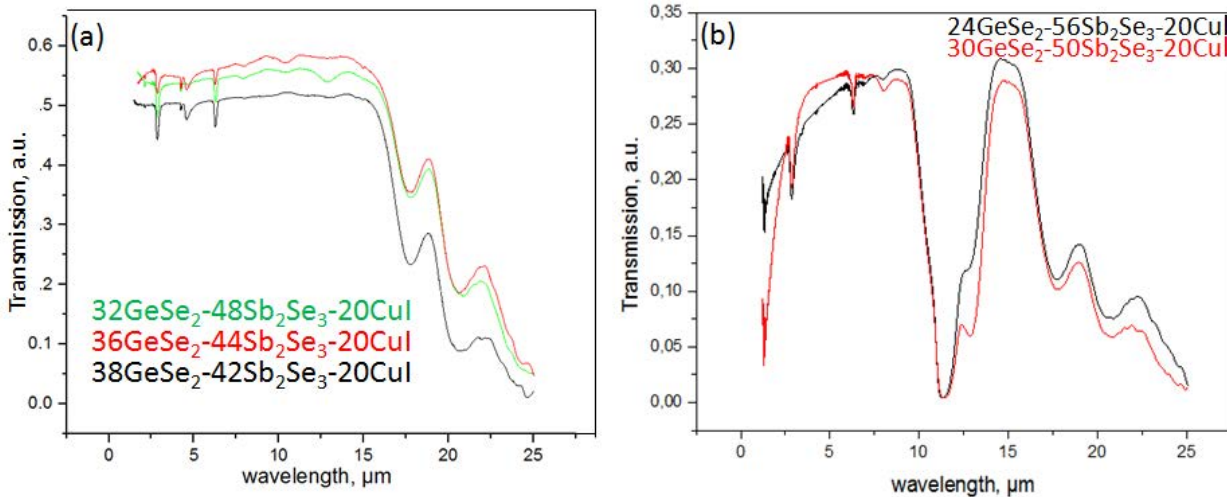


Figure 3-35 IR transmission spectra of (a) glass-precursors, (b) initially crystallized precursors (glass-ceramics)

In fig. 3-38 (a,b) DSC curves of obtained glass precursors are presented. We observe weak reduction of T_g with decrease of GeSe_2 molar content. At the same crystallization temperature slightly increases. For the precursor of $24\text{GeSe}_2\text{-}56\text{Sb}_2\text{Se}_3\text{-}20\text{CuI}$ composition (fig. 3-38 (b), blue line) glass-transition peak is less pronounced compared to samples with higher molar content of GeSe_2 . Simultaneously the crystallization temperature of this precursor increases. Apparently, less stable fraction of precursor is already crystallized, causing Rayleigh scattering (in fig. 3-35 (b)), that makes the residual phase more stable against crystallization.

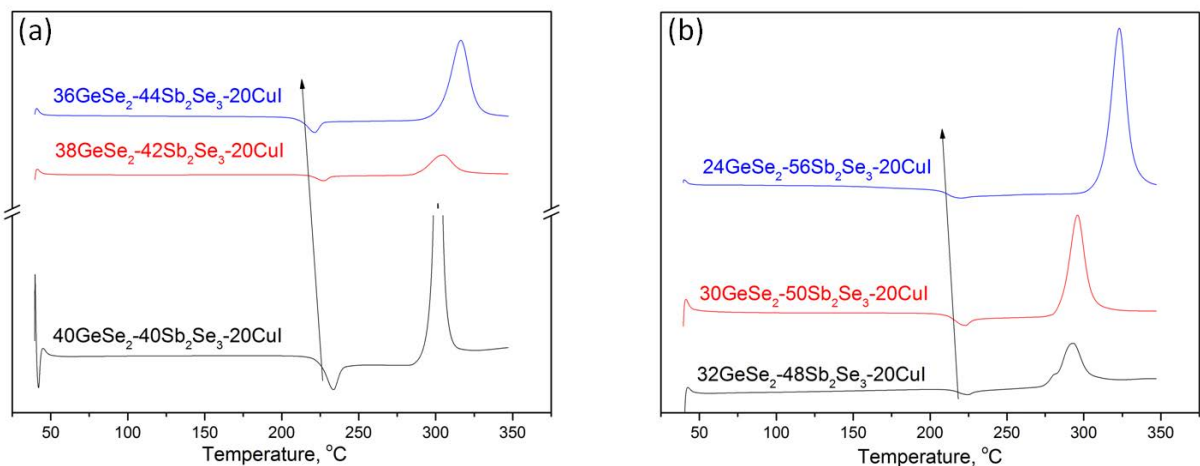


Figure 3- 36 DSC curves of GeSe_2 reduced quantity compounds

We also made an attempt to prepare $20\text{GeSe}_2\text{-}60\text{Sb}_2\text{Se}_3\text{-}20\text{CuI}$ precursor. However with usual melting-quenching process in was not possible. Probably the increase of Cu/Ge molar ratio leads to higher wetting capabilities of the melt; therefore, during quenching the liquid adheres to the internal side of the tube. Possible schema is proposed in fig. 3-37.

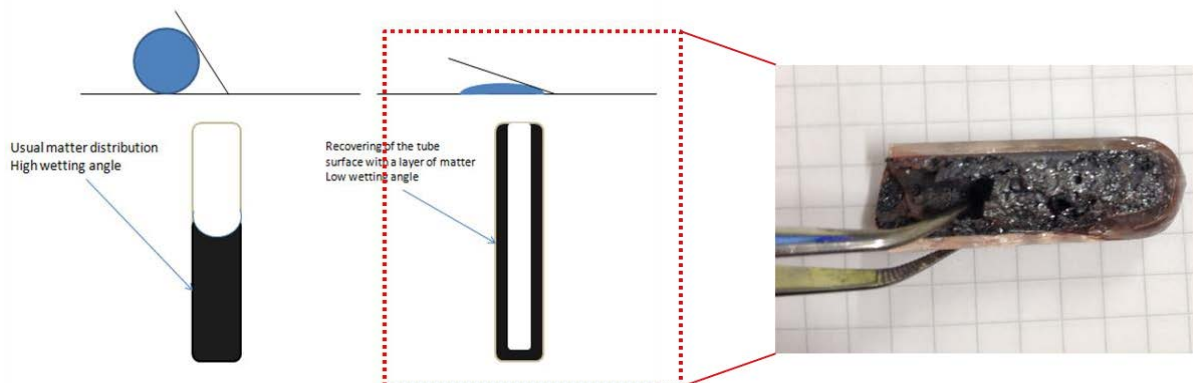


Figure 3-37 Distribution of matter inside the tube for high and low wetting angles (left), photograph of the tube with $20\text{GeSe}_2\text{-}60\text{Sb}_2\text{Se}_3\text{-}20\text{CuI}$ compound adhesion (right).

With this type of quenched matter distribution, it is not possible to extract any intact pieces of material from the tube.

Fig. 3-38 presents X-ray diffraction patterns of glass-ceramics with different molar content of GeSe_2 annealed for 1 hour at Tx. We cannot underline any difference in crystal structure upon the composition variations. XRD curves perfectly fit Sb_2Se_3 (PDF 15-0861) orthorhombic phase of Pnbn (62) space group with cell parameters $a= 1.1163 \text{ nm}$, $b = 1.178 \text{ nm}$, $c = 0.3985 \text{ nm}$ and orthorhombic Cu_2GeSe_3 (PDF 26-0516) space group Imm2 with cell parameters $a= 1.186 \text{ nm}$, $b = 0.396 \text{ nm}$, $c = 0.5485 \text{ nm}$.

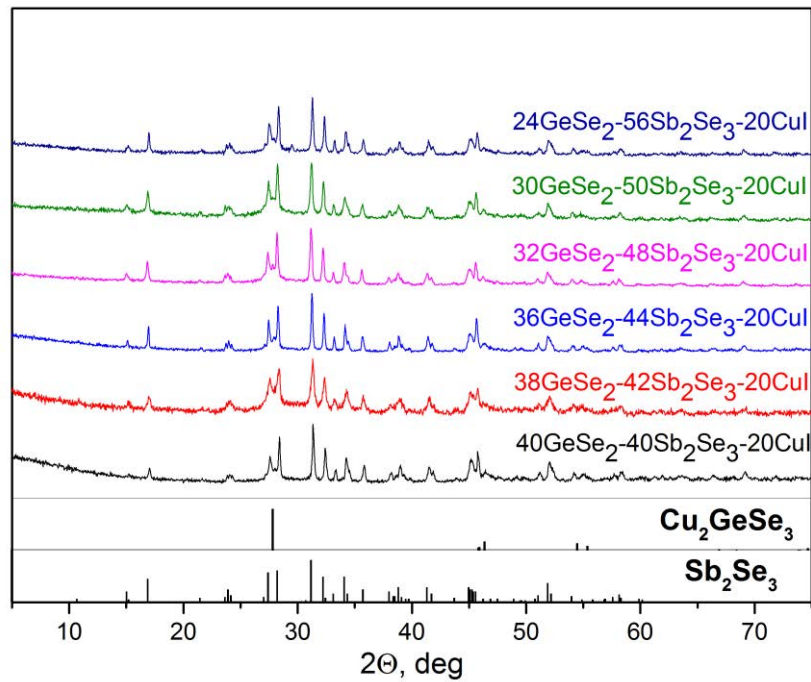


Figure 3-38 XRD diffractogram of obtained glass-ceramics

In fig. 3-39 the dependence of resistivity is presented as a function of GeSe₂ molar content in glass-ceramics. It can be seen that it slowly reduces in the span between 30 mol. % and 40 mol. % of GeSe₂ and significantly goes down for 24-56-20 composition. Without any information from XRD diffractogram it is difficult to point the reason of such behavior; however it is evident that efficiency of formed conductive network decreases. Since the content of copper does not change, quantitative lack of Cu₂GeSe₃ crystals can be explained only if we suppose that certain quantity of Ge is confined in residual glassy phase and cannot be extracted from it for Cu₂GeSe₃ formation (in applied annealing conditions). In this case an excess of Ge is obviously needed. Another possibility is that Sb₂Se₃ component introduced in larger molar quantity stays for crystallization of higher microscopic amount of Sb₂Se₃ phase. In this case the amount of iodine doped Sb₂Se₃ could be insufficient to provide bulk conductivity. Excessive amount of non-doped Sb₂Se₃ crystals can serve as a strong scattering center.

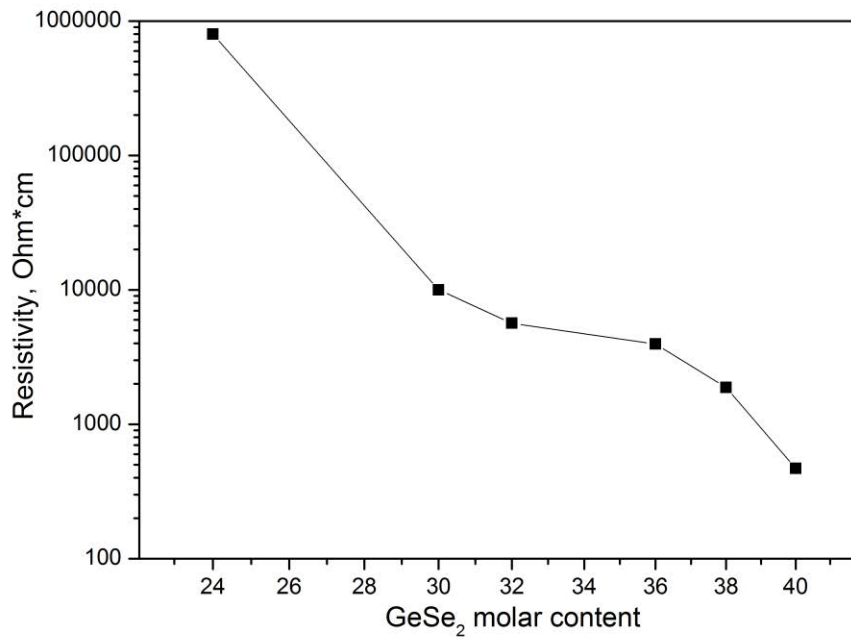


Figure 3-39 Dependence of electrical resistivity on GeSe₂ molar content

PEC curves of corresponding glass-ceramics are presented in fig. 3-40. Compositions with 38 mol. % and 36 mol. % of GeSe₂ shows similar to 40GeSe₂ - 40Sb₂Se₃ - 20CuI photocurrent under positive and negative bias. Further, current density slightly decreases, probably, because of the overall conductivity reduction. In case of 24GeSe₂-56Sb₂Se₃-20CuI sample we can notice weakening of photocurrent under negative bias down to 1 μ A/cm². It is possible to explain this reduction with several suggestions:

- Current density reduces due to overall reduction of glass-ceramics bulk conductivity, which is shown in fig. 3-39.
- Dramatic decrease of photocurrent under negative electric bias stays for quantitative reduction of p-type Cu₂GeSe₃ phase, as discussed before.
- The microstructure of obtained glass-ceramics does not favor contribution of p-type non-stoichiometric Sb₂Se₃ phase.

The resulting photocurrent densities under +0.6V and -0.6V bias are presented in fig. 3-43. We can conclude that it is possible to slightly reduce the amount of GeSe₂ without severe change of electric properties. However the reduction is possible only to the certain extent (i.e. 36 mol. % of GeSe₂ component), which allows maintaining relatively low bulk resistivity ($< 5 \times 10^3 \Omega \times \text{cm}$).

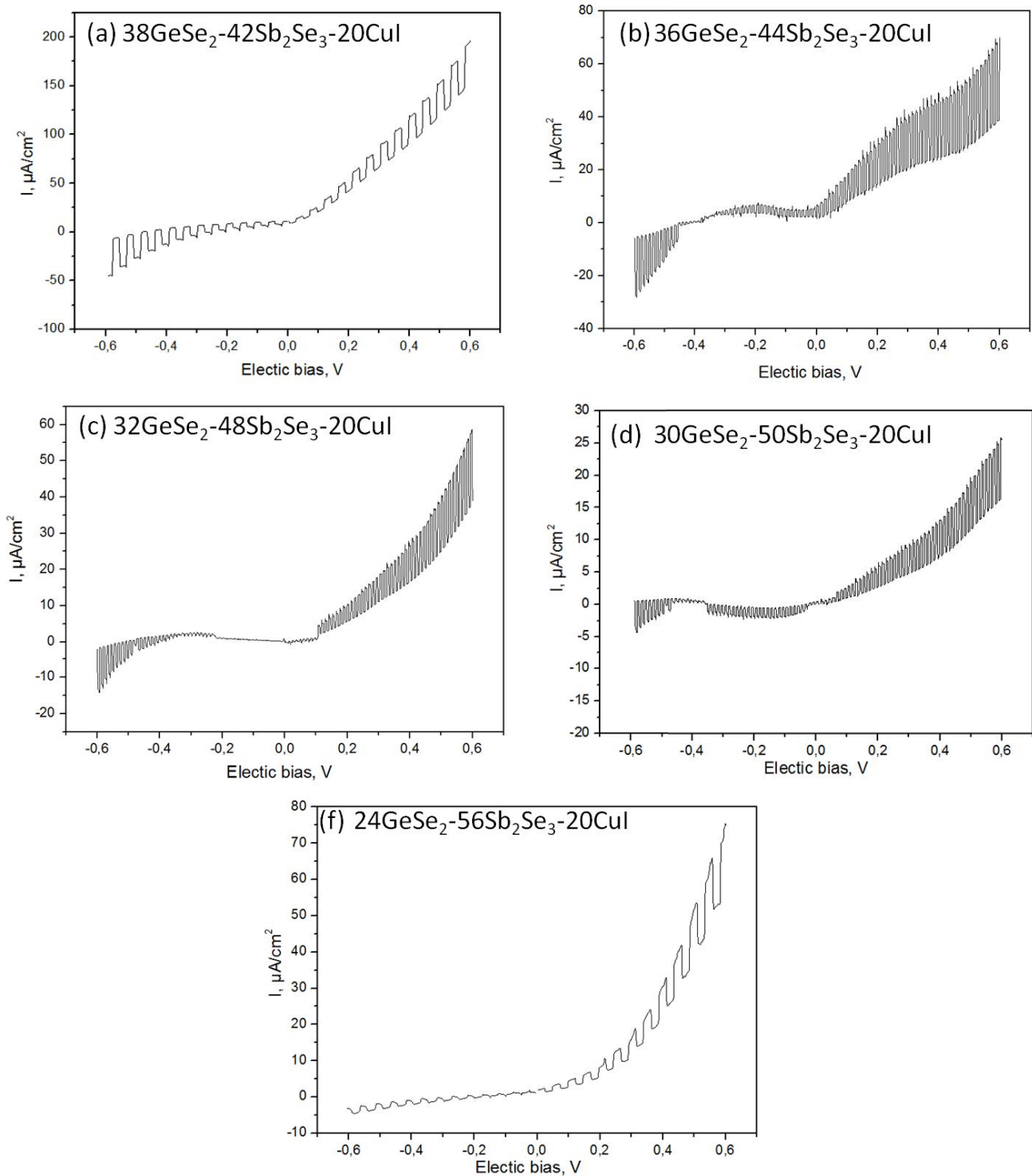


Figure 3- 40 PEC curves of glass-ceramics with reduced GeSe₂ content

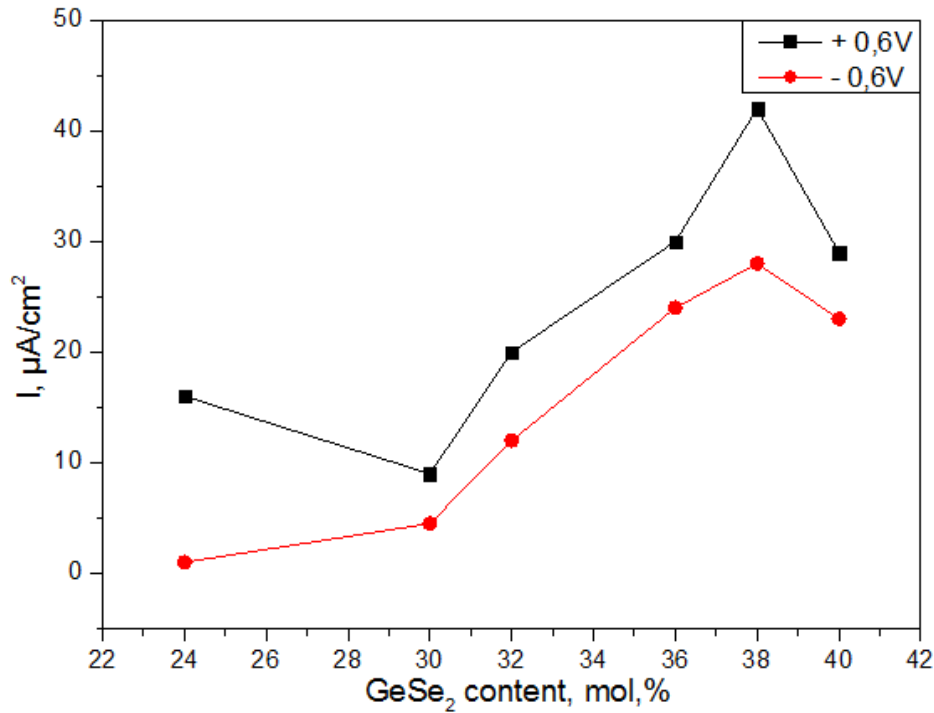


Figure 3- 41 Maximal photocurrent density obtained under +0.6V and -0.6V electric bias as a function of GeSe₂ molar content in prepared glass-ceramics.

4. Study of $x\text{GeSe}_2 - y\text{Sb}_2\text{Se}_3 - (1-x-y)\text{Cu}(\text{Br},\text{Cl})$ system

4.1 On the utilization of CuBr and CuCl.

So far, copper halides are known for their non-linear properties. For instance CuBr doped silica glass shows strong non-linear absorption due to quantum confinement of small CuBr crystals in glassy matrix, which leads to radical change in glass energy spectra⁴². CuBr attracted attention mostly because of its high exciton binding energy (107 meV) which leads to broad absorption band at different temperatures including room temperature. This property could be used for glass optical properties tuning, since the absorption coefficient of small microcrystals determines absolutely the absorption coefficient of composite according to Maxwell-Garnet theory⁴³.

CuBr is also known for being utilized in thermoelectric materials where it is used as intrinsic scattering center, which allows tuning of charge carrier mobility, it leads to the increase of maximal Seebeck coefficient temperature and shifts a Figure 3- of merit towards higher temperature due to the increase in electron concentration^{44,45}

CuCl is also used for the design of non-linear optics. Tokizaki et. al report high third order nonlinear susceptibility for CuCl microcrystallites embedded in glass matrix⁴⁶, as long as non-linear refractive index n_2 for CuCl borosilicate glass, where the non-linearity can be tuned by simple variation of particle size⁴⁷. It has also been utilized as semiconductor quantum dots with increased dephasing time and homogeneous broadening⁴⁸

As we have shown previously iodine doping significantly changes Sb_2Se_3 electric properties and plays a key role in appearance of photoconductivity of Sb_2Se_3 crystals and $40\text{GeSe}_2\text{-}40\text{Sb}_2\text{Se}_3\text{-}20\text{CuI}$ glass-ceramics. However iodine doping it is not capable of severe modification of Fermi level energy compared to bare Sb_2Se_3 . This lead us to assume that it is possible to dope Sb_2Se_3 with Cl and Br in the same manner, which therefore would drastically influence Sb_2Se_3 electronic properties. Since “light” halides are the elements of highest electronegativity in the periodic table, according to Vegard’s law of approximation²¹, even weak doping of Sb_2Se_3 crystals with Cl or Br could significantly change its electronic properties, especially E_f regarding their high electronegativity.

4.2 Glass precursor preparation

In fig. 3-42, Gibbs triangles of studied systems are presented. We should underline that in this case, we use term “glass” to describe the IR transparent materials that show no Rayleigh scattering, and present a well pronounced glass-transition peak in DSC curve. Term “glass-ceramics” is applied to the samples with pronounced glass-transition peak but with clearly expressed Rayleigh scattering associated to the presence of crystallized phase or opaque materials due to quantitatively more significant crystallization. “Crystallized” is attributed to materials without glass-transition peak.

Thus, one could mention that compare to pseudo-ternary system $\text{GeSe}_2 - \text{Sb}_2\text{Se}_3 - \text{CuI}$ obtained via the same synthesis technique (see Calvez L.⁴⁹) glass forming region shrinks to an “edge” of 10 mol. % of CuCl or CuBr content.

At the same time some technological problems raised during sample preparations in these systems. We will describe the most important ones:

- 1) Explosions. Using synthesis profile of $40\text{GeSe}_2 - 40\text{Sb}_2\text{Se}_3 - 20\text{CuI}$ (described in Chapter II, paragraph 1.2.1, fig. 3- 3) in 9 mm tube, all the samples with the content of CuBr or CuCl above 10 mol. % underwent an explosion during the melting process. Looking at fig. 3-43 we can notice that vapor pressure increases exponentially as a reverse function of the halide atomic weight. We already faced a problem of excessive vapor pressure in sulphur containing compounds (paragraph 2.2). However, application of thermal procedure proposed for sulphur-containing glasses did not resolve the problem. Concerning high hygroscopicity of CuBr and CuCl powders we suspected an important amount of molecular water in commercial products. Molecular water is capable of creating excessive pressure during the heating, which results in tube explosion. Thus, before the glass synthesis powders of CuBr or CuCl were purified. Powder was put in the silica tube and heated to 300 °C for 2 hours under vacuum pumping. This could allow releasing excessive moisture and molecular water. Combining purification step with temperature profile depicted in fig. 3-44 we succeeded to extend synthesis region up to 35-40 mol. % of CuBr (CuCl). Beyond this concentration, explosions were inevitable and therefore melting-quenching process cannot be recommended for these purposes.
- 2) Adhesion of the matter to the internal part of the tube. This problem was discussed previously in context of GeSe_2 reduction. In fig. 3-45, one can see that the compound is strongly adhesive and therefore its extraction from the tube is very complicated. In some cases we had to use a tube of 15 mm diameter to be able to extract some intact pieces of material. However, a tube with larger diameter leads to the reduction of the melt cooling rate during quenching. This results in obtaining of partially crystallized precursors.

3) Porosity of CuCl containing samples caused by excessive partial pressure over the melt. Porosity can be slightly reduced by adding of a pre-quenching step (in fig. 3-44), when the temperature reduces slowly without rocking the furnace. It allows reduction of partial pressure and the amount of bubbles in a bulk sample.

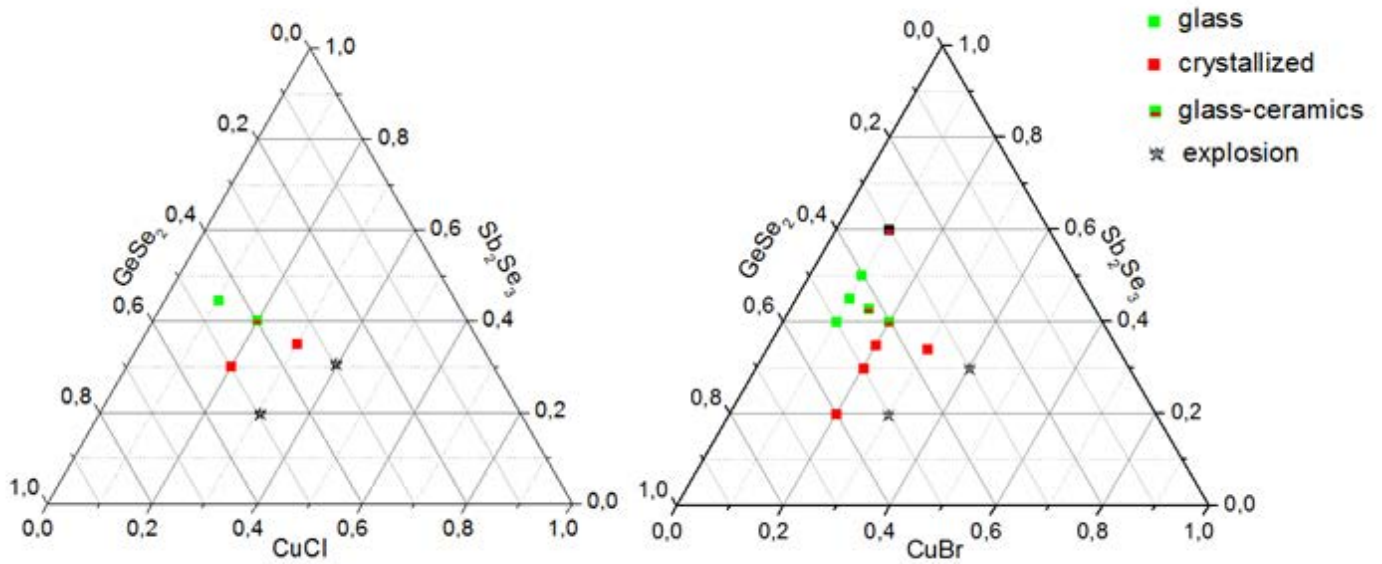


Figure 3-42 Gibbs triangles of pseudo-ternary systems (a) - $\text{GeSe}_2\text{-Sb}_2\text{Se}_3\text{-CuCl}$, (b) - $\text{GeSe}_2\text{-Sb}_2\text{Se}_3\text{-CuBr}$

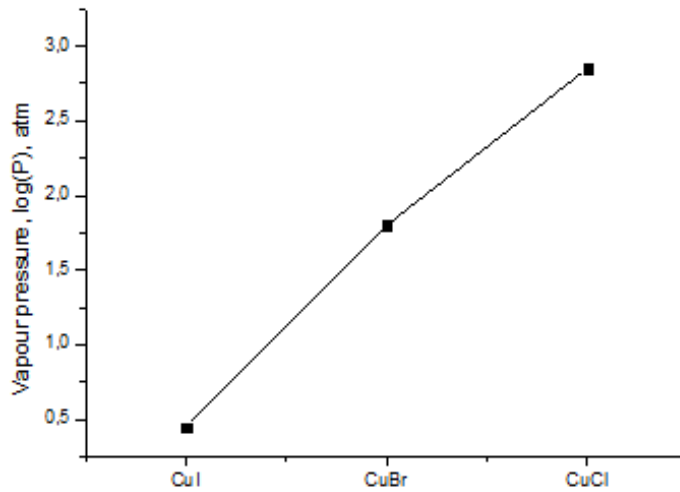


Figure 3-43 Vapor pressure of some copper halides⁵⁰

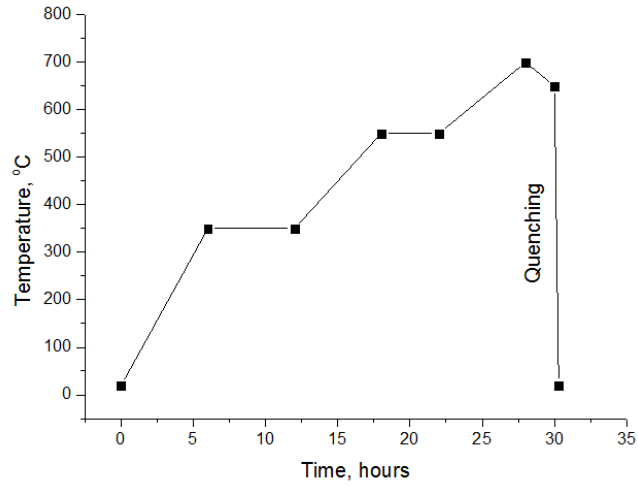


Figure 3-44 Synthesis profile of glass-precursor

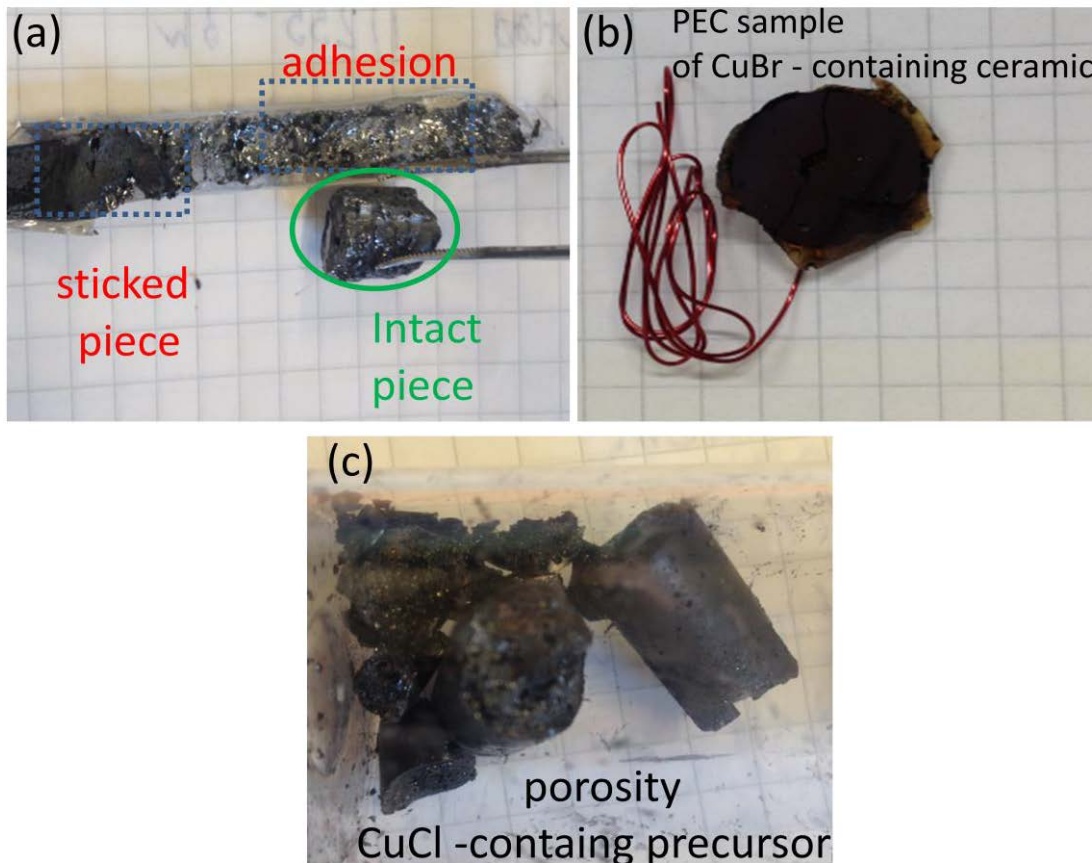


Figure 3-45 Photograph of obtained precursors and ceramics: CuBr containing precursor demonstrates visible adhesion of glassy matter to the tube and extracted piece (a), PEC sample prepared from intact pieces of CuBr-containing precursor (b), visible strong porosity of CuCl-containing precursor rod (c).

4.3 Glass precursor analysis. Controllable crystallization. Electric properties

As we can see in fig. 3-46 (a), glass-transition and crystallization temperatures reduce upon the increase of CuBr (or CuCl) content. Precursor with 10 mol. % of CuCl shows decent stability with T_g

= 229 °C and $T_x = 355$ °C, however stability region shrinks fast with additional introduction of copper halide. In the case of CuCl, T_g and T_x shift to 214 °C and 265 °C, respectively, for 20 mol. % sample. At the same time its transparency rate (fig. 3-49 (a)) decreases below 20% signing strong Mie scattering. Thus even in the absence of Rayleigh scattering tail we could suppose certain crystallization of initial glass. CuBr-containing compound shows less stability for 10 mol. % glass with $T_g = 230$ °C and $T_x = 314$ °C, and comparable stability for 20 mol. % composition. In fig. 3-47 (b), one can mention obvious signs of precursor crystallization (Rayleigh scattering). Similar thermal behavior of 20 mol. % CuBr (CuCl) compounds could be explained by the fact that the residual phase of stable glass is similar for both precursors, while less stable phase has already undergone a crystallization. On fig. 3-46 (b) typical DSC curve of completely crystallized precursor 35GeSe₂-35Sb₂Se₃-30CuBr is shown. Crystallized precursors do not show any transparency and in all cases demonstrate high porosity, being extremely fragile.

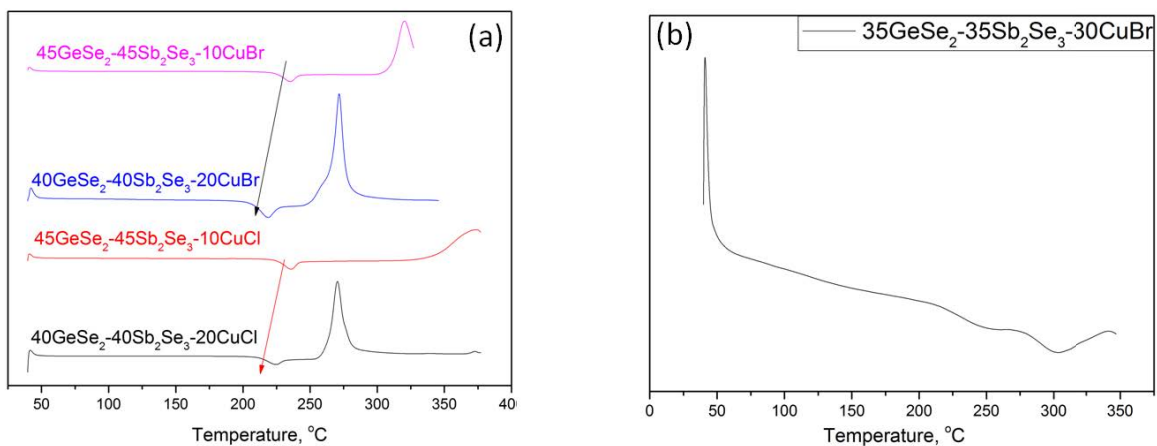


Figure 3-46 DSC spectra of glassy precursors (left) and as-prepared crystallized precursor (right)

Transmission spectra of IR transparent precursors are shown in fig. 3-47. In fig. 3-47 (a, b) we observe that increase of CuBr or CuCl content leads to decrease of transparency. For CuCl-containing precursor Mie scattering is the major scattering mechanism, while for CuBr-containing precursors it is rather Rayleigh scattering, strongly pronounced for 40GeSe₂-40Sb₂Se₃-20CuBr sample. Comparing fig. 3-47 (b) and fig. 3-47 (d), we conclude that only precursor with 10 mol. % of CuBr shows no scattering due to crystallized fraction and can be considered as a “glass”. Comparing fig. 3-47 (a, red line and black line) and fig. 3-47 (c), it can be concluded that both increase of halide content and decrease of GeSe₂ ration lead to reduced glass stability and partial crystallization of glassy precursor.

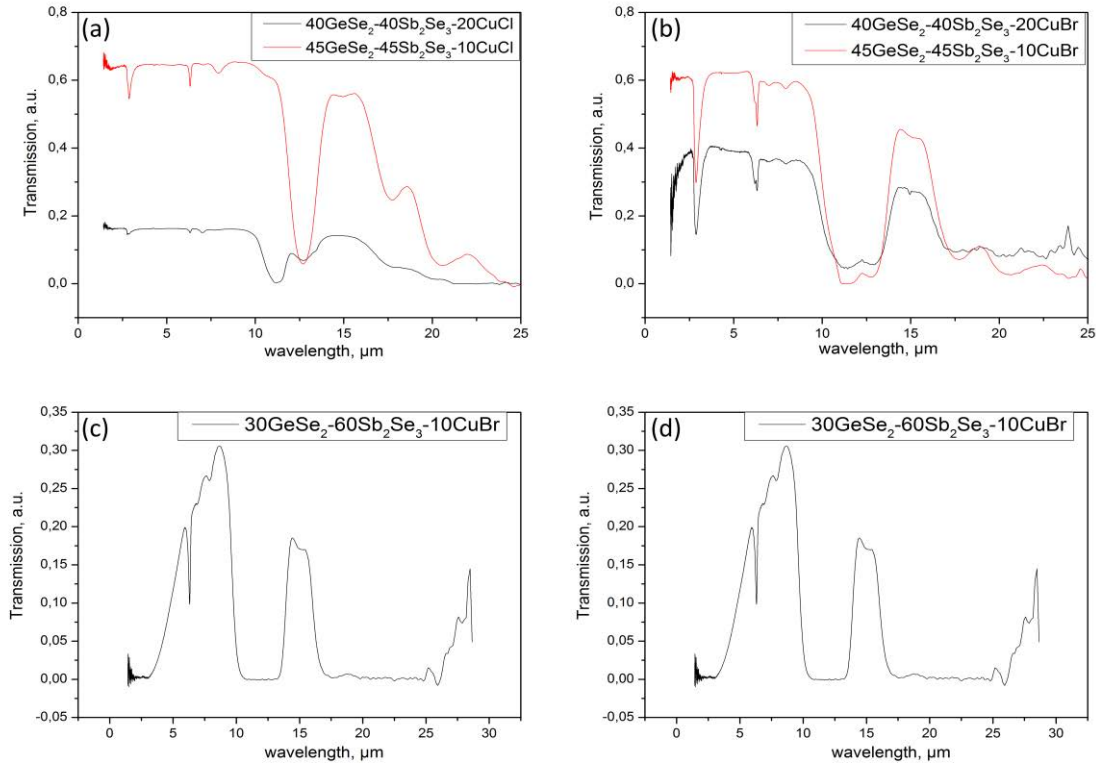


Figure 3-47 IR transmission spectra of copper bromide (copper chloride) glassy precursors

Looking at SEM images of glass precursors presented in fig. 3-48 one can clearly see the difference between their morphologies caused by the increase of copper halide content. Glass precursor $45\text{GeSe}_2\text{-}45\text{Sb}_2\text{Se}_3\text{-}10\text{CuBr}$ shows smooth surface without any signs of crystallization (fig. 3-48 (a)). Precursor $40\text{GeSe}_2\text{-}40\text{Sb}_2\text{Se}_3\text{-}20\text{CuBr}$ demonstrates white traces and dots on the gray glass surface, which stays for certain crystallization occurred in precursor immediately after preparation (fig. 3-48 (b)). Glass $45\text{GeSe}_2\text{-}45\text{Sb}_2\text{Se}_3\text{-}10\text{CuCl}$ also demonstrates a decent quality without pronounced crystallized areas (fig. 3-48 (c)). In case of $40\text{GeSe}_2\text{-}40\text{Sb}_2\text{Se}_3\text{-}20\text{CuCl}$ one can observe a smooth glassy surface with a “hole” in the center (fig. 3-48 (d)). We observe several “fiber” – like crystals of Sb_2Se_3 morphology inside the “hole”. It means that certain amount of unstable phase is significantly crystallized forming geometrically arranged crystalline clusters, which stay for strong Rayleigh scattering found for this sample (fig. 3-47 (b), black curve).

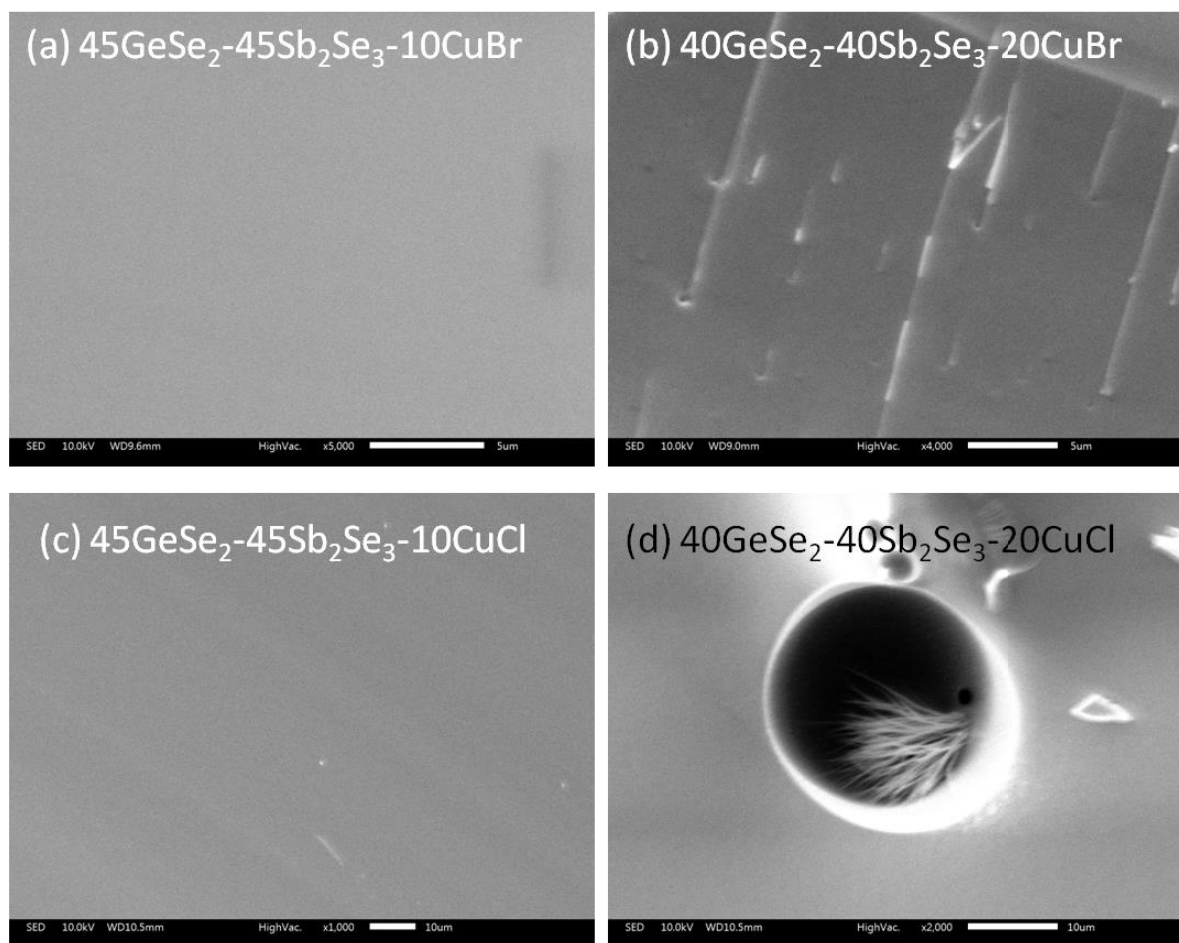


Figure 3-48 SEM images of as-prepared (no annealing) precursors with different content of CuBr (a,b) and CuCl (c,d)

XRD patterns of prepared glass-ceramics are shown in fig. 3-49. We can notice that precursor with 10 mol. % of copper halide, and especially the one with CuCl, shows decent stability and do not incur severe crystallization below T_x , as shown in fig. 3-49 (a,b - black curves). On the other hand, compounds with 20 mol. % of CuBr (CuCl) are pre-crystallized to the extent which allow crystallization at (T_x-30) temperature (fig 49(c, d – black curves). We found out that the same phases with the same orientations are crystallized under both T_x and (T_x-30) temperatures. They are similar to those observed for $40\text{GeSe}_2-40\text{Sb}_2\text{Se}_3-20\text{CuI}$ glass-ceramics. It is possible to conclude that low stability and initial (even slight) ceramization of precursor could seriously affect the crystallization process making it much less controllable. We also noticed that $45\text{GeSe}_2 - 45\text{Sb}_2\text{Se}_3 - 10\text{CuCl}$ (fig. 3-49 (b) – red curve), which requires higher temperature to be crystallized, shows some deviations compare to other samples, i.e. unexpected growth of Cu_2GeSe_3 with (0 2 0) preferential orientation instead of conventional (0 0 1) and observed for the other the compounds orientation.

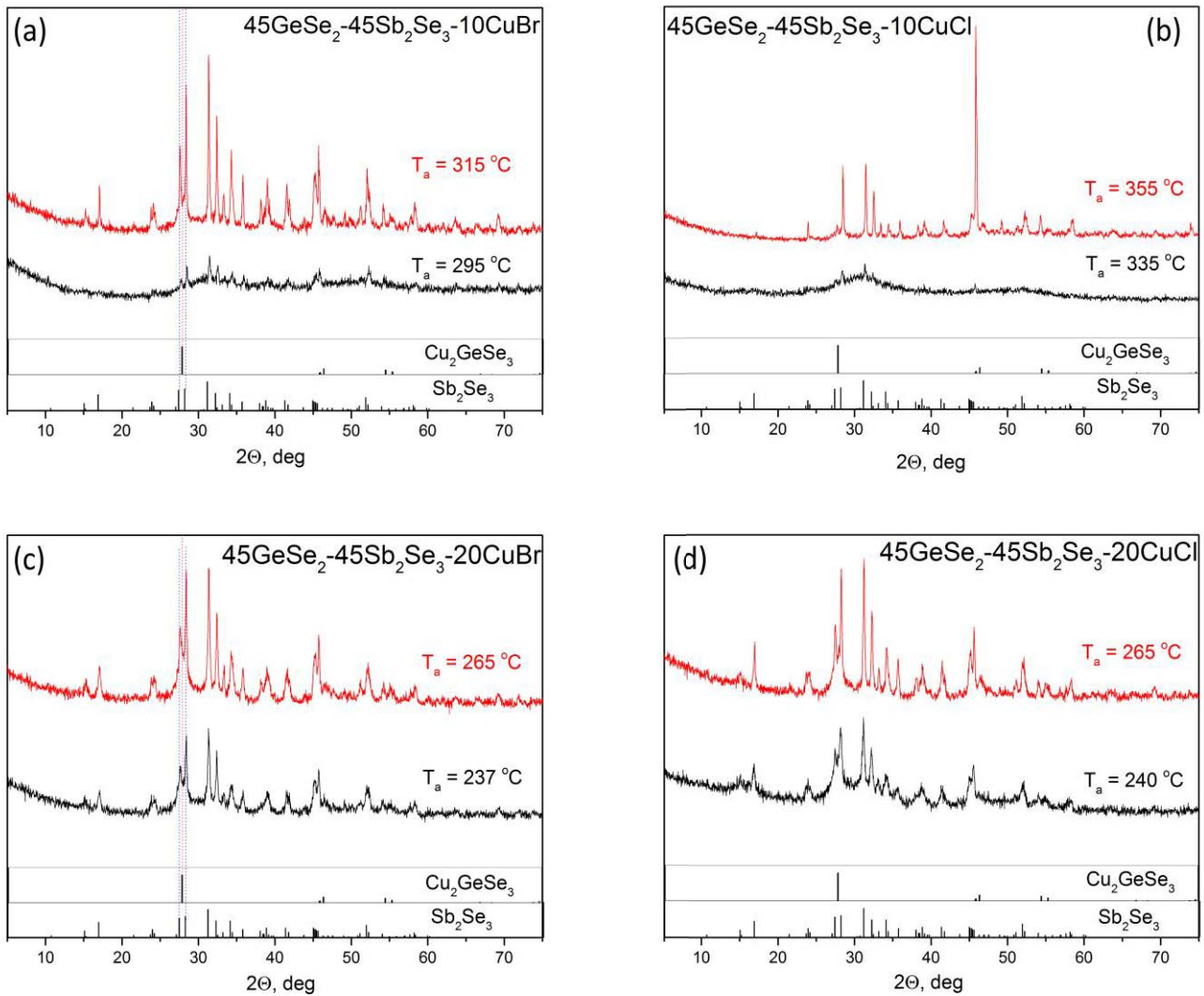


Figure 3-49 XRD diffractogram of obtained glass-ceramics

Comparing XRD diffractogram of glass-ceramics with different concentrations of copper halides (CuI, CuBr, CuCl), summarized in fig. 3-50, we could barely underline any difference in crystallized phases content with exception of the glass-ceramic with 10 mol. % of CuCl, which was annealed at higher temperature and demonstrates some exceptional difference in Cu_2GeSe_3 preferential orientation.

That was not surprising since, according to our previous conclusions, an XRD pattern of crystallized phase is not determined by halide nature or its presence or absence.

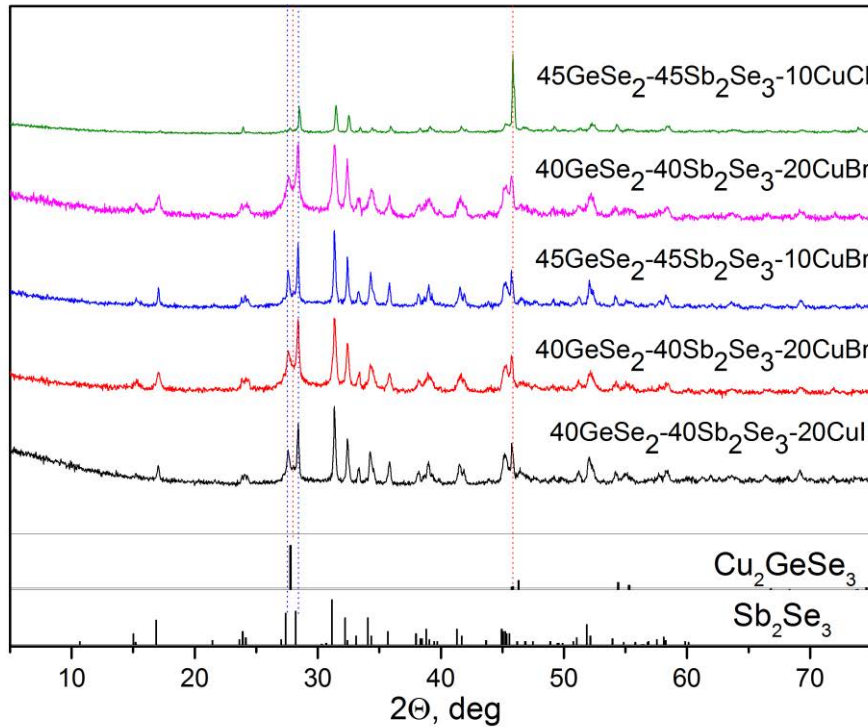


Figure 3-50 Comparison of XRD diffractograms for glass-ceramics containing CuI, CuBr and CuCl.

However, further investigation of electrical resistivity showed that glass-ceramics with CuBr and CuCl possess much higher resistivity compared to CuI samples (see table 3-3).

Only sample with 10 mol. % of CuBr showed distinctive, but weak photoresponse. Photocurrent density in PEC measurement reaches $8\mu\text{A}/\text{cm}^2$ (+0.6V) and $4\mu\text{A}$ (-0.6V) respectively, as shown in fig. 3-51(a). Other samples possess conductivity comparable to bulk Sb_2Se_3 (which is $\rho = 10^9 \Omega \times \text{cm}$) and demonstrate diode behavior with current density below $1 \mu\text{A}/\text{cm}^2$ and no photoconductive response fig. 3-51 (b - d).

Table 3-3 Resistivity and conductivity type for different copper halides nature

Composition	Resistivity, $\Omega \times \text{cm}$	Conductivity type
40GeSe ₂ -40Sb ₂ Se ₃ -20CuI	2.17×10^2	n
40GeSe ₂ -40Sb ₂ Se ₃ -10CuBr	6.59×10^6	n
40GeSe ₂ -40Sb ₂ Se ₃ -20CuBr	2.8×10^8	n
40GeSe ₂ -40Sb ₂ Se ₃ -10CuCl	3×10^8	n
40GeSe ₂ -40Sb ₂ Se ₃ -10CuCl	1.55×10^8	N

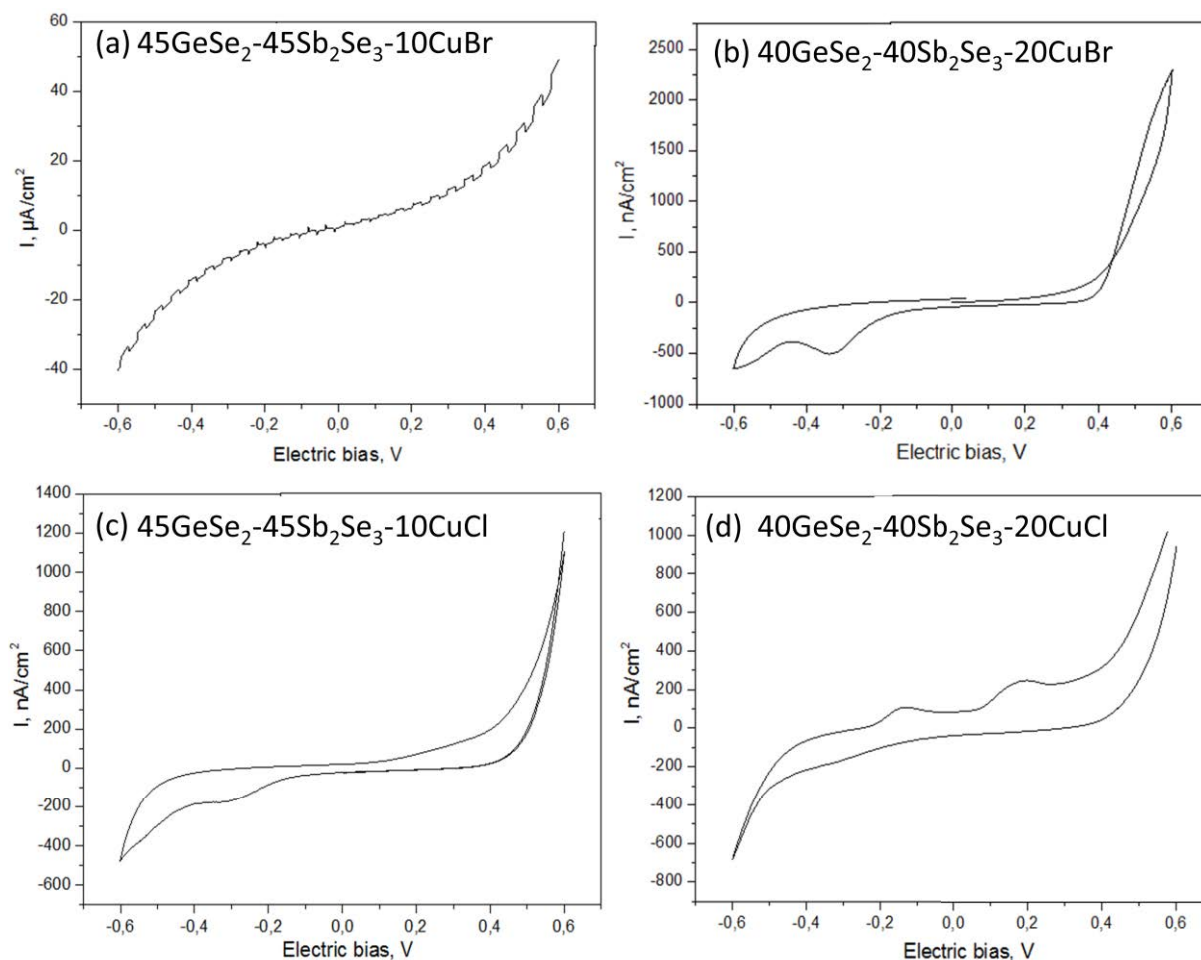


Figure 3-51 PEC curves for glass-ceramics

To conclude, we found out that bromine and chlorine doping does not contribute to Sb_2Se_3 bulk conductivity similarly to iodine. These highly electronegative elements are capable of severe stretching of E_g and E_F tuning. At the same time, it was shown that only iodine contributes positively to bulk conductivity of Sb_2Se_3 crystals and $\text{GeSe}_2\text{-Sb}_2\text{Se}_3\text{-CuI}$ glass-ceramics. Doping mechanism proposed in Chapter II, paragraph 2.1, fig. 3-21 supposes that iodine substitutes Se, which leads to the appearance of free charge carriers. Apparently, neither bromine nor chlorine is not capable of such substitution.

5. Conclusion

We investigated the influence of anion and cation substitutions on electric properties of glass-ceramics in pseudo-ternary system $\text{GeSe}_2\text{-Sb}_2\text{Se}_3\text{-CuI}$. It was shown that introduction of small amount of sulphur (1 mol. % and more) leads to dramatic loss of conductivity and photo response.

Bismuth doping favors formation of n-type phase, while p-type is not pronounced in the presence of Bi. When more than 10 mol. % of antimony is substituted by bismuth we observe fast change of morphology accompanied with reduction of conductivity and photocurrent density.

Introduction of tin in glassy matrix in small quantities (0.1 mol. %, 1 mol. %) promotes Sn doped Sb_2Se_3 phase formation, which is known to be a p-type semiconductor. Glass-ceramics with 1 mol. % of Sn shows photocurrent density of $81 \mu\text{A}/\text{cm}^2$, which is 4 times higher compared to non-doped

40GeSe₂-40Sb₂Se₃-20CuI glass-ceramics (21 $\mu\text{A}/\text{cm}^2$). However, further doping leads to formation of SnSe₂ and promotes unfavorable microstructure formation, which results in increase of resistivity and diminution of photocurrent density.

We showed that it is possible to reduce GeSe₂ component content without affecting electric properties of glass-ceramics. On the other hand, reduction of GeSe₂ below 36 mol. % leads to slight loss in conductivity and photocurrent density. With important deficiency of GeSe₂ component we observe attenuation of p-type phase photo response down to 4 $\mu\text{A}/\text{cm}^2$ (under -0.6V bias).

We carried out the study on glass-ceramics, where CuI was substituted by CuCl and CuBr halides. It was demonstrated that chlorine and bromine do not play the same role as iodine. Apparently, these atoms are not capable of incorporating in Sb₂Se₃ crystalline structure and do not contribute to its electronic properties.

6. References

- ¹ Yang Xu, Bo Fan, Xianghua Zhang, Qianhong Shen, Minjia Wang, Hongli Ma, *Crystallization optimization of the 40GeSe₂-40Sb₂Se₃-20CuI glass for improvement of photoelectric properties*. Journal of Non-Crystalline Solids, 2016, Volume **431**: pp. 61-67.
- ² Xianghua Zhang, et al., *Correction: Enhancement of charge photo-generation and transport via an internal network of Sb₂Se₃/Cu₂GeSe₃ heterojunctions*. J. Mater. Chem. A, 2014, **2**: pp. 17099-17106.
- ³ Hezhu Shao, Xiaojian Tan, Tianqi Hu, Guo-Qiang Liu, Jun Jiang and Haochuan Jiang, *First-principles study on the lattice dynamics and thermodynamic properties of Cu₂GeSe₃*. EPL (Europhysics Letters), 2015, **109**(4): p. 47004.
- ⁴ Alan Fahrenbruch, Richard Bube, *Fundamentals Of Solar Cells: Photovoltaic Solar Energy Conversion*. Elsevier Inc, 1983, p. 13-14
- ⁵ Yang Xu, *Les propriétés photoélectriques de vitracéramiques de chalcogénures*. Thesis, 2014.
- ⁶ Wilhelm Melitz, et al., *Kelvin probe force microscopy and its application*. Surface Science Reports, 2011, **66**: pp. 1-27
- ⁷ Nelson, Jenny, *The Physics of Solar Cells*. Imperial College Press, 2003.
- ⁸ Pablo P. Boix, et al., *Open-Circuit Voltage Limitation in Low-Bandgap Diketopyrrolopyrrole-Based Polymer Solar Cells Processes from Different Solvents*. J. Phys. Chem. C, 2011, **115**(30):pp. 15075-15080.
- ⁹ Garcia-Belmonte, G., Bisquert, J., *Open-Circuit Voltage Limit Caused by Recombination through Tail States in Bulk Heterojunction Polymer-Fullerene Solar Cells*. Appl. Phys. Lett., 2010, **96**: p. 113301.
- ¹⁰ Arora, Narain D., *MOSFET Models for VLSI Circuit Simulation Theory and Practice N*. Springer, 1993, p.39-43.
- ¹¹ C.B. Roy, D.K. Nandi, P.K. Mahapatra, *Photoelectrochemical cells with n-type ZnSe and n-type Sb₂Se₃ thin film semiconductor electrodes*. Electrochimica Acta, 1986, 31: pp.1227-1229.
- ¹² Zhou Y, Leng M, Xia Z, Zhong J, Song H, Liu X, Yang B, Zhang J, Chen J, Zhou K, Han J, Cheng Y, Tang J. *Solution-processed antimony selenide heterojunction solar cells*. Advanced Energy Materials, 2014, **4**(8): 1301846
- ¹³ Chao Chen, et al., *Characterization of basic physical properties of Sb₂Se₃ and its relevance for photovoltaics*. Frontiers of Optoelectronics, 2017, **10**(1): pp 18-30.

- ¹⁴ G. Marcano, D. Bracho, C. Rincón, G.S. Pérez, L. Nieves, *On the temperature dependence of the electrical and optical properties of Cu₂GeSe₃*. Journal of Applied Physics, 2000, **88**: pp. 822-828.
- ¹⁵ M.R. Filip, C.E. Patrick, F. Giustino, GW *Quasiparticle band structures of stibnite, antimonselite, bismuthinite, and guanajuatite*. Physical Review B, 2013, **87**: p.205125.
- ¹⁶ M.A. Villarreal, B.J. Fernández, M. Pirela, A. Velásquez-Velásquez, *Electrical properties of the ternary compound Cu₂GeSe₃*. Revista Mexicana de Fisica, 2007, **53**; pp.303-306.
- ¹⁷ Wang, C. Song, X. Fu, X. Li, *Growth of one-dimensional Sb₂S₃ and Sb₂Se₃ crystals with straw-tied-like architectures*. Journal of Crystal Growth, 2005, **281**: pp.611-615.
- ¹⁸ A. M. Moustafa and E. A. El-Sayad, *Synthesis and Crystal Structure Refinement of Sb₂Se₃-xSx Solid Solutions by Rietveld Analysis of X-Ray Powder Diffraction Data*. Egypt. J. Solids, 2009, **32**(1): p.71.
- ¹⁹ Rencheng Jin, et al., *Facile synthesis of sulfur doped Sb₂Se₃ nanosheets with enhanced electrochemical performance*. Journal of Alloys and Compounds. 2013, **579**: pp. 209–217.
- ²⁰ Bo Yang, et al., *Hydrazine solution processed Sb₂S₃, Sb₂Se₃ and Sb₂(S_{1-x}Se_x)₃ film: molecular precursor identification, film fabrication and band gap tuning*. Sci Rep., 2015, **5**: p.10978.
- ²¹ Vegard L., Schjelderup H., *Constitution of mixed crystals*. Phys. Z., 1917, **18**: p. 93–96.
- ²² A.H. Nethercot Jr., *Prediction of Fermi energies and photoelectric thresholds based on electronegativity concepts*. Phys. Rev. Lett., 1974, **33**(18): p.1088
- ²³ Alexander V. Kolobov, Junji Tominaga, *Chalcogenides: Metastability and Phase Change Phenomena*. Springer Series in Materials Science, 2012, p.15.
- ²⁴ G. Campet, et al. *Electronegativity versus Fermi energy in oxides: the role of formal oxidation state*. Materials Letters, 2004, **58**: pp. 437 – 438.
- ²⁵ E. Huheey, E.A. Keiter, R.L. Keiter, *Inorganic Chemistry: Principles and Reactivity*. Harper Collins College Publishers, 1993.
- ²⁶ E. H. Baker, *The Vapour Pressure and Resistivity of Selenium at High Temperatures*. J. Chem. SOC. (A), 1968, p.1089.
- ²⁷ H. Rau, T. R. N. Kutty. and J. R. F. Guedes de Carvalho, *High temperature saturated vapour pressure of sulphur and the estimation of its critical quantities*. J. Chem. Thermodyn., 1973, **5**(833): pp. 201-203.
- ²⁸ Daniel W Hewak, *Chalcogenide Glasses for Photonics Device Applications*. Retrieved from: <http://chalcogenides.com/ChalcogenideGlassesforPhotonicsDeviceApplications.pdf>
- ²⁹ Yi Zhang, et al., *Crossover of Three-Dimensional Topological Insulator of Bi₂Se₃ to the Two-Dimensional Limit*. Nature Physics, 2010, **6**: pp.584–588.
- ³⁰ Haijun Zhang, et al., *Topological insulators in Bi₂Se₃, Bi₂Te₃ and Sb₂Te₃ with a single Dirac cone on the surface*. Nature Physics, 2009, **5**: pp. 438 – 442.
- ³¹ Dohun Kim, et al., *Surface conduction of topological Dirac electrons in bulk insulating Bi₂Se₃*. Nature Physics, 2012, **8**: pp. 459–463.
- ³² Fu, L., Kane, C. L., Mele, E. J., *Topological Insulators in Three Dimensions*. Phys. Rev. Lett., 2007, **98**: p. 106803.
- ³³ Qianfan Zhang, et al., *Exotic Topological Insulator States and Topological Phase Transitions in Sb₂Se₃ - Bi₂Se₃ Heterostructures*. ASC Nano, 2012, **6** (3): pp. 2345–2352.
- ³⁴ J.C. Bailar Jr., J. Urbanan, H.J. Emeleus, T.F. Trotman-Dickenson, *Comprehensive Inorganic Chemistry*. Pergamon Press, Oxford, 1973, Vol.2: p. 616
- ³⁵ B.R. Sankapal, C.D. Lokhande, *Studies on photoelectrochemical (PEC) cell formed with SILAR deposited BiSe – SbSe multilayer thin film*. Solar Energy Materials & Solar Cells, 2001, **69**: pp. 43-52.

- ³⁶ C. Julien, M. Eddrief, I. Samaras and M. Balkanski, *Optical and electrical characterizations of SnSe, SnS₂ and SnSe₂ single crystals*. Materials Science and Engineering: B, 1992, **15**(1): pp. 70-72.
- ³⁷ Keun Lee, et al., *Characteristics of SnSbSe (SSS) Thin Films Grown by Atomic Layer Deposition for High Performance Phase Change Random Access Memory (PCRAM)*. ECS Transactions, 2013, **53**(6):pp. 45-51.
- ³⁸ K Kadel, et al., *Synthesis and Thermoelectric Properties of Bi₂Se₃ Nanostructures*. Nanoscale Res. Lett., 2010, **6**:p. 57.
- ³⁹ Long Ren, et al., *Large-scale production of ultrathin topological insulator bismuth telluride nanosheets by a hydrothermal intercalation and exfoliation route*. :J. Mater. Chem., 2012, **22**: p. 4921.
- ⁴⁰ P. Kumar, R. Thangaraj, *Effect of Sn addition on the photoconductivity of narrow-gap Sb₂Se₃ films*. Philosophical Magazine Letters, **89**(4): pp. 241-249.
- ⁴¹ P. Kumar , T.S. Sathiaraj and R. Thangaraj, *Optical properties of amorphous Sb₂Se₃:Sn films*. Philosophical Magazine Letters, 2010, **90**(3): pp. 183-192.
- ⁴² G.Tamulaitis, R.Baltramiejūnas, S.Pakalnis, A.I.Ekimov, *Dynamics of nonlinear optical response of CuBr-doped glasses*. Superlattices and Microstructures, 1993, **13**(2): p. 199.
- ⁴³ K.C.Rustagi, C.Flyzanis, *Optical nonlinearities in semiconductor-doped glasses*. Optics Letters, 1984, **9**: pp. 344-346.
- ⁴⁴ D. B. Hyun, et al., *Thermoelectric properties of the n-type 85% Bi₂Te₃-15% Bi₂Se₃ alloys doped with SbI₃ and CuBr*. Journal of Materials Science, 1998, **33**(23), pp. 5595–5600.
- ⁴⁵ O. Ceyda Yelgel and G. P. Srivastava, *Thermoelectric properties of n-type Bi₂(Te_{0.85}Se_{0.15})₃ single crystals doped with CuBr and SbI₃*. PHYSICAL REVIEW B, 2012, **85**: p.125207.
- ⁴⁶ Takashi Tokizaki, et al., *Large Enhancement of Third-Order Optical Susceptibility in CuCl Quantum Dots Embedded in Glass*. Jpn. J. Appl. Phys., 1993, **32**: L782.
- ⁴⁷ B. L. Justus, et al., *Excitonic optical nonlinearity in quantum confined CuCl doped borosilicate glass*. Appl. Phys. Lett., 1990, **57**: p. 1381.
- ⁴⁸ Michio Ikezawa, Yasuaki Masumoto, *Observation of homogeneous broadening of confined excitons in CuCl quantum dots*. Journal of Luminescence, 2000, **87-89**: pp. 482-484.
- ⁴⁹ L. Calvez, *Nouveaux verres et vitrocéramiques transparents dans l'infrarouge pour l'imagerie thermique*. Thesis, 2006, Rennes 1, p. 88.
- ⁵⁰ R. A. J. Shelton, *Vapour pressures of the solid copper (I) halides*. Transactions of the Faraday Society, 1961, **57**: p. 2113.

Chapter IV

Preparation of thin film solar cells via magnetron sputtering

Table of contents

1.Introduction.....	147
2.Preparation of targets for magnetron sputtering	149
2.1.Preparation of chalcogenide targets by melting-quenching process.....	149
2.1.1.Targets synthesis.....	149
2.1.2.Targets characterization	151
2.2.Preparation of targets by hot pressing.....	154
2.2.1.Targets preparation and characterization	154
3.Thin films preparation and characterization	156
3.1.Some fundamentals of magnetron sputtering	156
3.2.Preparation of bulk heterojunction within thin films based on 40GeSe ₂ -40Sb ₂ Se ₃ -20CuI composition.....	159
3.3.Preparation of thin films based on Cu ₃ SbSe ₄ composition.....	172
3.4.Fabrication of planar heterojunction with thin films of p-type [40GeSe ₂ -40Sb ₂ Se ₃ -20CuI].....	176
4.Conclusion	182
5.References.....	183

1. Introduction

Our initial considerations about the structure of 40GeSe₂-40Sb₂Se₃-20CuI glass-ceramics gave us an idea to prepare a similar structure within a thin film, deposited on a conductive layer of indium-tin-oxide (ITO), and use it for light harvesting.

We supposed to deposit an amorphous layer of 40GeSe₂-40Sb₂Se₃-20CuI via magnetron sputtering, which would be an analogue of glass-precursor. And further anneal it at certain temperature (controllably crystallize) to obtain a network of bulk heterojunctions p-Cu₂GeSe₃/n-Sb₂Se₃ as we did for bulk glass-ceramics, discussed in chapter I, paragraph 3.3.2.

Fig. 4-1 gives a primitive comprehension of different mixing scenarios in thin film device. Fig. 4-1 (a) shows a very fine dispersion and intimate intermixing of donor and acceptor materials, which in our case is an infinite amorphous matrix of precursor. The ideal charge separation could be provided by planar heterojunction depicted in fig. 4-1 (b), however it limits charge generation area by the vicinity of the interface, which is not favorable considering the poor conductivity of Sb₂Se₃ absorber ($\sim 10^{-6}$ - $10^{-2} \Omega^{-1} \times m^{-1}$)^{1,2,3,4}. Logically, structure of periodic p-n junctions with adjusted thickness (depend on absorption coefficient) and distance ($>2L$, where L is the charge carrier diffusion length), shown in fig. 4-1 (c), should provide highest efficiency. On one hand, charge generation occurs at larger surface (one can compare the length of junction interface in case of fig. 4-1 (b) and fig. 4-1 (c)), and on the other hand, strict orientation and periodicity allows efficient charge transfer towards electrodes⁵. However this highly oriented structure is difficult to prepare and cannot be obtained via facile synthesis method as we proposed before. Upon the crystallization of thin film amorphous precursor by direct heating we rather expected to obtain morphology depicted in fig. 4-1 (d). Random distribution of donor and acceptor domains of several hundreds of nanometers along with their intimate intermixing leads to limited absorption area and far from optimal charge transfer properties⁶.

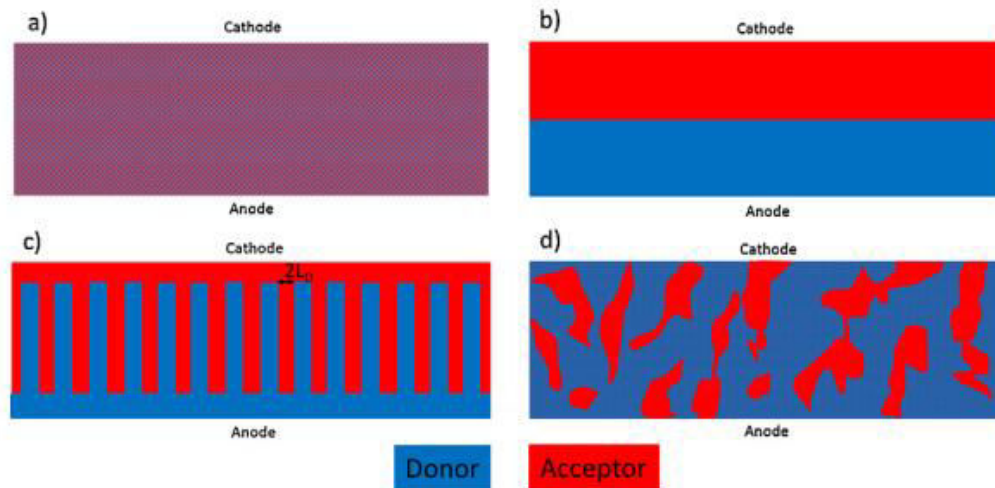


Figure 4-1 Different morphologies of two-phase mixture: homogeneous mixture (a), ideal planar junction (b), ideal periodical morphology of the bulk junction (c), typical real bulk junction morphology (c)⁶

Trying to obtain bulk heterojunctions of p-Cu₂GeSe₃/n-Sb₂Se₃ by simple crystallization of amorphous 40GeSe₂-40Sb₂Se₃-20CuI thin film, we had also considering different mixing scenarios on the

interface of interacting phases. To give an idea how two phases can interplay, it is useful to make an analogy with organic molecular thin films for photovoltaics.

Assume that upon the crystallization, we obtain two spatial spherical-symmetrical phases without any interaction. These two phases will be mixed according to scenarios depicted in fig. 4-2, the probability of each scenario governed by binominal distribution, since each spatial scenario is independent and has no relations with other scenarios⁷:

$$P = \sum_{k=0}^n \binom{n}{k} x^k a^{n-k} = \binom{4}{n} \frac{1^k}{2} \frac{1^n}{2}, \quad (4.1)$$

the probability P to find k spheres A and n spheres B at 4 different sites around sphere A

Thus, by simple calculation one can obtain the highest probability of equal distribution of spheres A and B around sphere A in a mixture.

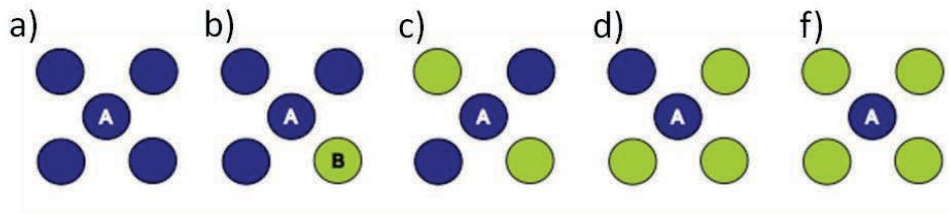


Figure 4-2 Possible mixing scenarios of two non-interacting ideal spheres. The highest probability is for the mixture where sphere A is surrounded by equal quantity of spheres A and B : a) p =6.25%, b) p = 25%, c) p = 37.5%, d) p = 25%, e) p = 6.25%⁸

However in real mixture of phases interaction cannot be neglected at least nearest-neighbor interactions should be taken into account. This interaction is described by interaction parameter χ , which depends on interaction energies between phase A and phase B. Thus different mixing scenarios occur due to different interaction energies of two phases. It can be either strong intermixing with clear long – range order (fig. 4-3 (a)) if the interaction energy between spheres of different phases (A-B, B-A) is higher than within the phase (A-A, B-B), or phase separation in case when interaction energy of spheres of the same kind (A-A, B-B) is stronger than between each other (A-B, B-A) (fig. 4-3 (b)), or random distribution when interacting energies are equal (fig. 4-3 (c))^{9,10}.

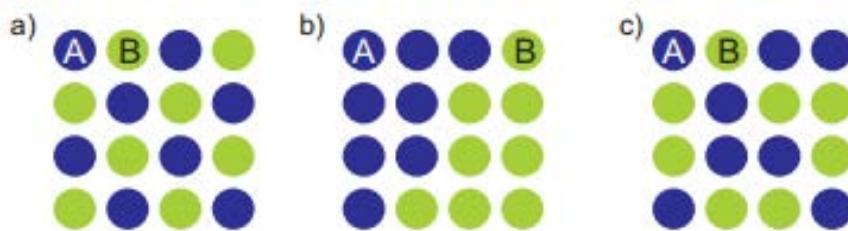


Figure 4-3 Mixing scenarios of interacting spheres, as a function of interaction parameter χ : a) $\chi < 0.5$, A-B pairing and long range order, b) $\chi > 2$, phase separation, c) $\chi = 0$. Statistical mixing⁸

These preliminary considerations brought us to the conclusion that the finite composition of the phases, their size and spatial interaction will significantly influence the overall performance of photovoltaic cell.

Trying to obtain optimal configuration, we carried out a variety of investigations with different target compositions, deposit and annealing conditions.

2. Preparation of targets for magnetron sputtering

2.1. Preparation of chalcogenide targets by melting-quenching process

2.1.1. Targets synthesis

To prepare sputtering targets ($d = 4.9$ cm), the same process as for the bulk glasses and glass-ceramics material can be used (described in details chapter II). Targets were made by melting of raw materials, which were previously purified, weighted inside the glove-box and pumped to obtain the pressure 10^{-5} mbar (fig. 4-4).

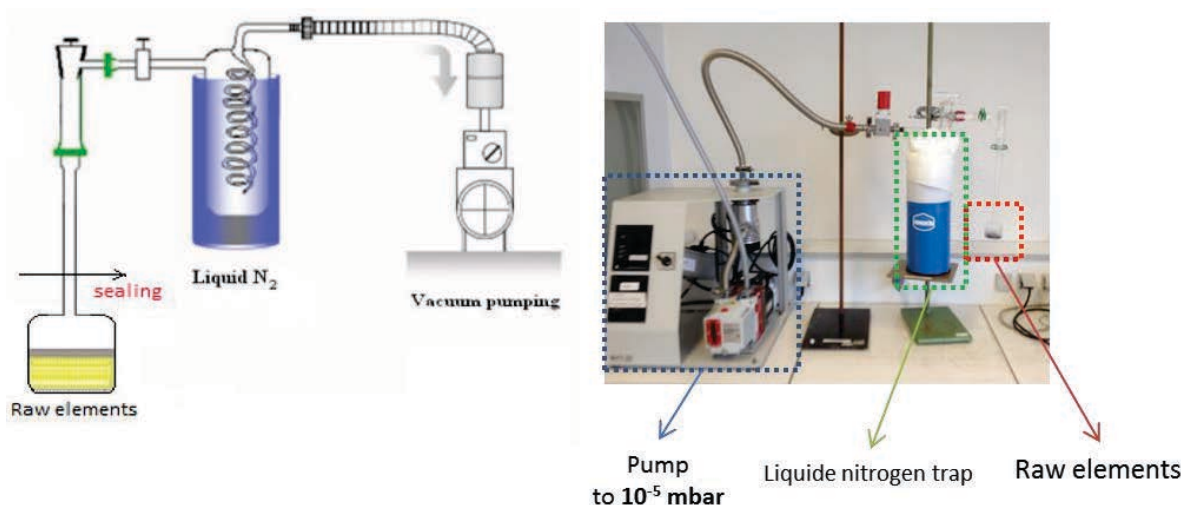


Figure 4-4 Setup for vacuum pumping of the ampoule with raw materials. Schema (left), laboratory realization (right).

Since these targets were used for preparation of electronic devices, their high purity was a prerequisite, in table 4-1 raw elements utilized for target synthesis are summarized.

Table 4-1 Table of raw elements for melting-quenching synthesis

Element	Supplier	Purity	Additional Purification
Se	UMICORE	5N	Heated at 220°C under vacuum and distillation at 330°C , to eliminate oxygen and carbon impurities
Sb	Alfa Aesar	99.999%	Not required
Ge	UMICORE	5N	Not required
CuI	Sigma Aldrich	99.999%	Not required
Cu	Alfa Aesar	99.999%	Not required
Iodine	Alfa Aesar	99.99%	Not required / Stored in glove-box refrigerator

It is worth mentioning that the melting-quenching process was different depend on the composition of a target. Glass-ceramics targets of $40\text{GeSe}_2\text{-}40\text{Sb}_2\text{Se}_3\text{-}20\text{CuI}$ composition (and its variations) were synthesized similarly to bulk rods with the thermal process shown in fig. 4-5 (a).The

ampoule was quenched in water for a few seconds and the following annealing at 200°C for 3 hours was made for all the targets in order to reduce the stress.

Crystalline targets of Sb_2Se_3 (and modifications) and Cu_3SbSe_4 were also synthesized at slightly lower temperatures and were cooled down in a furnace with a speed 5 deg/min (fig. 4-5 (b)). It was empirically found out, that it is not possible to obtain these materials in glassy or glass-ceramics forms, since the quenching lead to mechanical collapse of the target despite different synthesis and quenching regimes. During this slow cooling the complete crystallization of the target occurs, no additional annealing is needed.

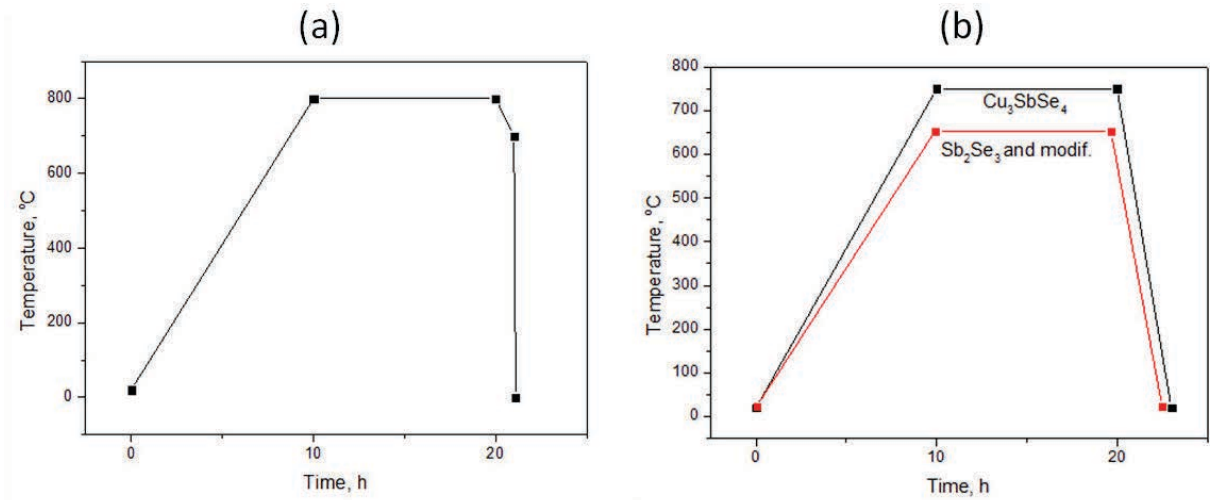


Figure 4-5 Synthesis profiles of 40GeSe₂-40Sb₂Se₃-20CuI (and modifications) glass-ceramics targets (a) and crystalline targets Sb₂Se₃ and Cu₃SbSe₄ (b)

Obtained targets are depicted in fig. 4-6. One can see the difference between glass-ceramics target (fig. 4-6 (a)) and crystalline targets (fig. 4-6 (b,c)) with bear eye. Surface of glass-ceramics target is much more brilliant, smoother and homogeneous, usually covered with multiple cracks. We mentioned its higher (compared to crystalline targets) fragility during polishing and utilization in sputtering machine. Target of Sb_2Se_3 is fully crystallized, one can see that rod-like structure described previously in chapter II and chapter III on microscopic level reaches its macroscopic scale here (fig. 4-6 (b)). Being doped with iodine we are facing higher porosity of $\text{Sb}_2\text{Se}_3\text{:I}$ target surface, probably due to increased vapor pressure over the melt. Porous surface can be removed by mechanical elimination of 1-2 mm of subsurface matter (fig. 4-6 (c)).

Then, in order to proceed for the sputtering, all targets undergo mechanical polishing to obtain thickness of 3-4 mm with mirror-like surface.

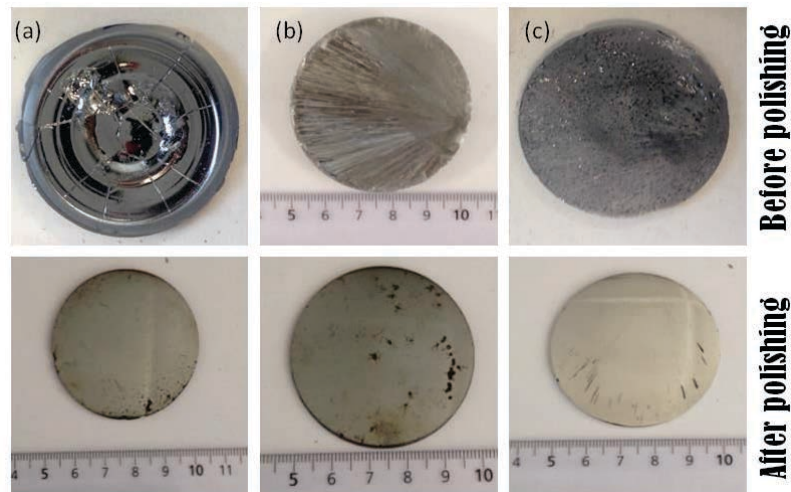


Figure 4-6 Photograph of targets obtained by melting-quenching process: 40GeSe₂-40Sb₂Se₃-20CuI glass-ceramics (a), Sb₂Se₃ (b), Sb₂Se₃:I (c)

2.1.2. Targets characterization

We have found that despite fast cooling, 40GeSe₂-40Sb₂Se₃-20CuI glass-ceramic target is severely crystallized, which can be seen from both SEM image (fig. 4-7) and XRD graphic (fig. 4-8). From SEM image in fig. 4-7 we can conclude that multiple phases are crystallized within the target: we found several different topological zones, characterized by different morphology and composition. Dark spots, apparently, stay for Cu₂GeSe₃ phase with the presence of negligible quantity of Sb and I (specter 1 - red), long bright strips are rod-like Sb₂Se₃ (specter 2 - green). Another spatial zone, which surrounds Sb₂Se₃ strips, may stay for amorphous GeSe₂-Sb₂Se₃-CuI mixture or for superposition of several different crystalline phases (specter 3 - violet). The most important point here is the presence of iodine in this phase since its quantity in other spatial zones is very limited.

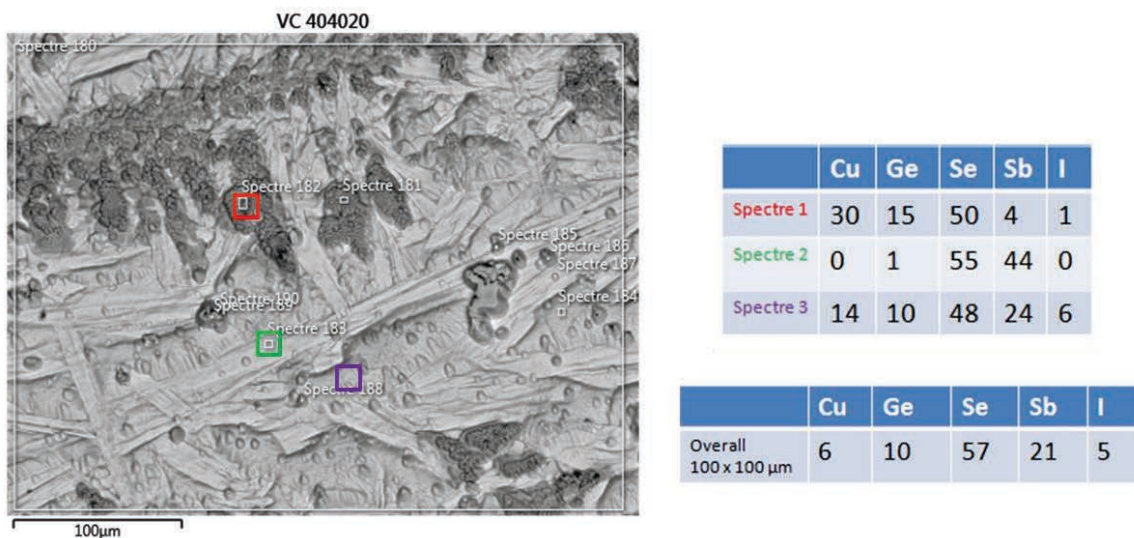


Figure 4-7 SEM image of 40GeSe₂-40Sb₂Se₃-20CuI glass-ceramics target shows severe multi-phase crystallization with 3 different phases pronounced.

Obvious inhomogeneity of the target could raise the question, if it corresponds to the stoichiometry of 40GeSe₂-40Sb₂Se₃-20CuI glass-ceramics. However if one would analyze a more vast spatial area (superior than 100x100µm), quite fare fit to the atomic composition of glass-ceramics could be found.

Fig. 4-8 depicts XRD patterns of different glass-ceramics targets. We have prepared a number of targets with increased amount of iodine. As it can be seen the overall spectra does not change significantly and we observe a strong peak of the Cu_2GeSe_3 phase at 27.796° that stays for (0 0 1) orientation. The intensity of this peak depends on the point of scanning and can vary from board to center, which is understandable if one considers significant spatial inhomogeneity of crystallization within the target, induced by different cooling rate. But the position of all major peaks does not change. We observe no signs of SbSeI phase in iodine poor samples. The only target that shows clear evidence of SbSeI phase formation is 40GeSe_2 - $40\text{Sb}_2\text{Se}_3$ - 40CuI (doubled quantity of CuI) with the peak at 29.495° which corresponds to SbSeI phase (1 1 2) orientation.

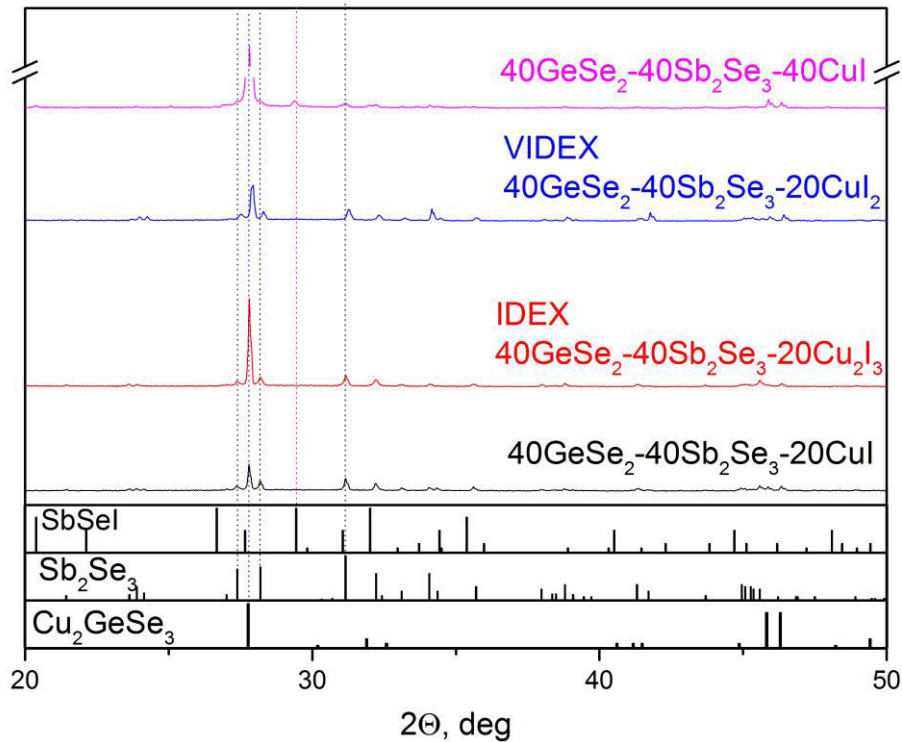


Figure 4-8 X-ray diffraction spectra of different 40GeSe_2 - $40\text{Sb}_2\text{Se}_3$ - 20CuI target modification. 40GeSe_2 - $40\text{Sb}_2\text{Se}_3$ - 20CuI (black), iodine enriched 40GeSe_2 - $40\text{Sb}_2\text{Se}_3$ - $20\text{CuI}_{1.5}$ (red), iodine enriched 40GeSe_2 - $40\text{Sb}_2\text{Se}_3$ - 20CuI_2 (blue), CuI rich 40GeSe_2 - $40\text{Sb}_2\text{Se}_3$ - 40CuI (pink)

We observe some peculiarities for Sb_2Se_3 based targets also. As it can be seen from fig. 4-9 (a), the major peaks intensity does not correspond to the PDF card, while the peak position fits perfectly. The dominant orientation (1 3 0) at 23.901° for Sb_2Se_3 (black line) vanishes upon the introduction of iodine. For the target with 10 mol. % of iodine, this intensity becomes less important, however some unconventional orientations become pronounced as (1 2 0) at 16.874° or (0 6 1) at 51.878° . This discrepancy can be explained by different occupation rate compared to stoichiometric Sb_2Se_3 compound. As we mentioned in Chapter II, Sb_2Se_3 prepared via melting-quenching are highly inhomogeneous and show different Sb/Se ratio at different spatial zones, which can entail various occupation rate of crystal lattice sites and result in the peak relative intensity change. However peak positions do not undergo any significant shift which signifies no change in cell parameters. At the same time we can observe appearance of SbSeI phase peak for 10 mol. % doped target (red line) at 29.445° and 32.018° , which is minor for this composition but undergoes fast growth upon the introduction of 20% of iodine (blue line).

And apparently, the SbSeI phase even becomes the major phase within the bulk (compare SbSeI peak at 29.445° between red and blue lines).

XRD pattern of Cu₃SbSe₄ is presented in fig. 4-9, as it can be seen this target is crystallized in a conventional way with good correspondence to PDF card.

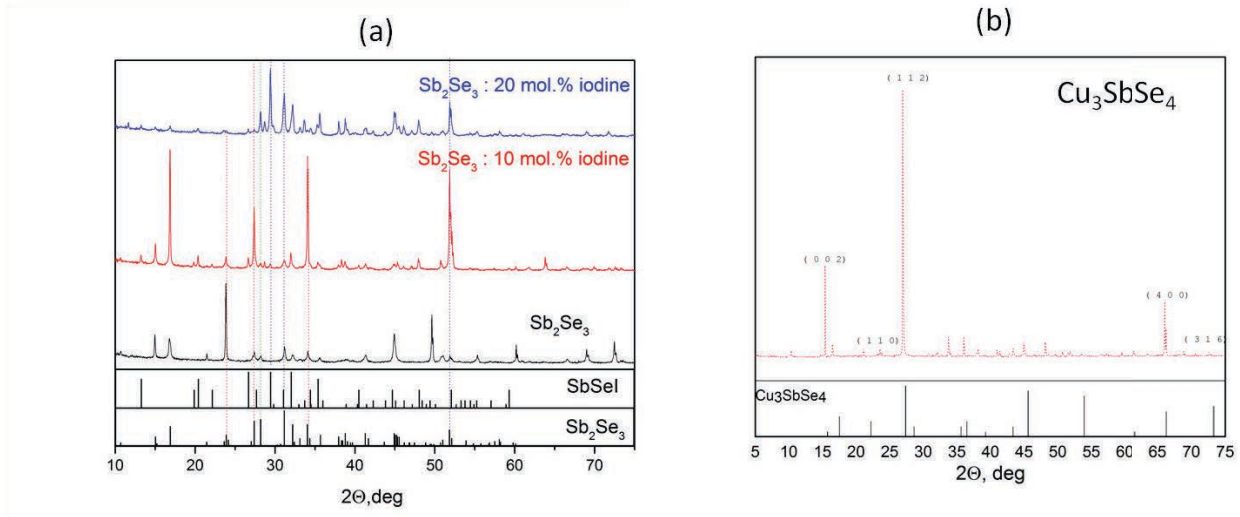


Figure 4-9 XRD patterns of (a) - Sb₂Se (black), Sb₂Se₃ doped with 10 mol. % of iodine (red), Sb₂Se₃ doped with 20% of iodine (blue), and (b) – Cu₃SbSe₄

One of the major properties for the target is the conductivity. Since during the magnetron sputtering, target is bombarded by ionized gas atoms, it is important to prevent charging of the target surface. In order to avoid this, targets should be either sufficiently conductive or the sputtering should be realized by using alternative current. As we mentioned before, the obtained targets are very inhomogeneous, thus its conductivity was measured by four-probe method in seven different sites. The mean value was taken into account. However for the 40GeSe₂-40Sb₂Se₃-40CuI target, some zones (probably Cu-rich) show metallic conductivity, while the majority of sites have conductivity comparable with 40GeSe₂-40Sb₂Se₃-20CuI target. We can also mention the difference between the conductivity of iodine doped targets (diameter of 50 mm) and that of bulk samples (diameter of 9 mm) of the same composition described in Chapter II. It can be explained by different thermal history. Apparently, during the slow cooling, iodine has enough energy to form SbSeI phase, which is clear from XRD and which explain for the low conductivity of the target. While during the fast cooling of smaller bulk samples, iodine is rather inserted into Sb₂Se₃ lattice than forms SbSeI phase and provides electronic conductivity. Summary on prepared targets and their conductivity is given in table 4-2.

Table 4-2 List of targets (diameter of 50 mm) prepared via melting-quenching process, their synthesis profile and resistivity

Target composition	Synthesis profile (fig. 4-5)	Resistivity, Ω×cm
40GeSe ₂ -40Sb ₂ Se ₃ -20CuI (“40-40-20”)	A	2.6 × 10 ²
40GeSe ₂ -40Sb ₂ Se ₃ -40CuI (“40-40-40”)	A	3×10 ² - 0.02
40GeSe ₂ -40Sb ₂ Se ₃ -20CuI _{1.5} (“IDEX”)	A	1.8 × 10 ⁻²
40GeSe ₂ -40Sb ₂ Se ₃ -20CuI ₂ (“VIDEX”)	A	5.4 × 10 ⁻¹

Cu_3SbSe_4 (“CSS”)	B	0.57
Sb_2Se_3 (“SS23”)	B	3.25×10^8
Sb_2Se_3 doped 10% iodine (“SS231”)	B	1.76×10^2
Sb_2Se_3 doped 20% iodine (“SS232”)	B	3.76×10^6

2.2. Preparation of targets by hot pressing

To prepare a photovoltaic device some additional material were needed. First of all, we had to prepare CuI target. This material is known as a hole-conductor, which is efficient to collect holes from active layer in planar type devices¹¹. It is particularly used in perovskite structures, where it is used for charge separation¹²; and in planar architectures with copper doped NiO_2 in quality of a p-type layer with favorably matched energy levels¹³, and in p-i-n structure with metal-halcogenide based i-layer¹⁴. In our case, CuI could be used as p-type semiconducting layer for collection of the charge generated within the “40-40-20” active layer, as well as for compensation of copper and iodine loss during the deposition of the $\text{GeSe}_2\text{-Sb}_2\text{Se}_3\text{-CuI}$ system.

Another target to be prepared was ZnO that belongs to the transparent conductive oxides widely used in photovoltaics as a window material¹⁵. It is an n-type material which is mostly used as an active layer when paired with metal-oxides such as Cu_2O ¹⁶ and as a transparent conductive layer for efficient charge separation due to favorable band energy match with a number of promising photovoltaic materials such as CdS^{17,18}, lead-perovskites¹⁹, PbSe quantum dots²⁰.

2.2.1. Targets preparation and characterization

To fabricate these targets we choose hot pressing technique from highly pure commercial powders: CuI 99.999% (STEM) and ZnO 99.999% (STEM).

Hot pressing allows obtaining of simple geometries such as cylinders or plates. Pressing molds are usually made of graphite and the applied pressure is typically in the range 20-150 MPa with temperature up to 2100 °C, which makes it suitable for a variety of materials. The hot pressing chamber is schematically depicted in fig. 4-10. To avoid porosity, sintering occurs at temperatures close to melting temperature of material (usually 0.7-0.8T_m), which promotes the grain growth. Details on hot pressing technique can be found elsewhere^{21,22,23}.

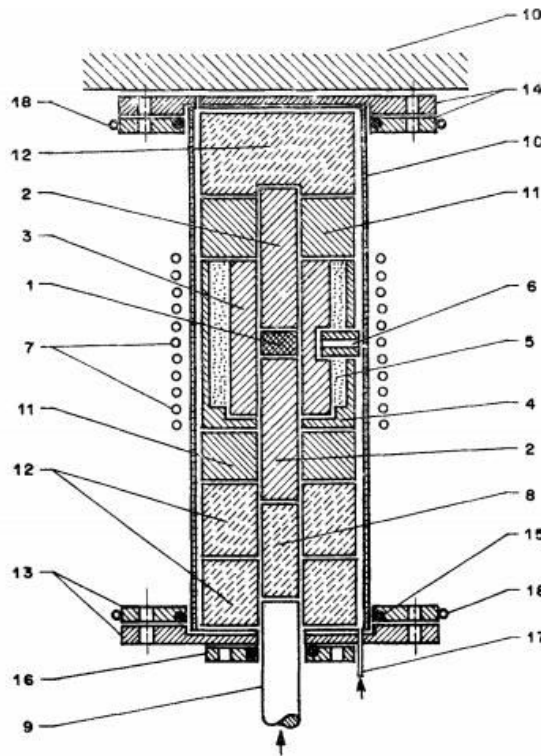


Figure 4-10 Uniaxial hot pressing assembly (schematic). (1) Sample, (2) graphite punches, (3) graphite die, (4) BN housing, (5) graphite powder insulation, (6) BN tube for viewing, (7) RF coil, (8) pyrophyllite punch, (9) SS plunger of hydraulic press, (10) transparent quartz tube, (11) BN spacers, (12) pyrophyllite spacers, (13) lower SS flange, (14) upper SS flange, (15) 'O' ring seals, (16) sealed flange of SS plunger, (17) gas/vacuum connection, (18) copper tubing for water circulation, and (19) MS stand as stopper.²⁴

There are a number of studies devoted to ZnO fabrication via hot pressing. Wang et al. showed the increase in density from 78% to 96%, when synthesis temperature increased from 800 °C to 1100 °C at 35 MPa. It shows a quite stable behavior of relative density upon the reduction of pressure, which decreases to 91%, when the pressure decreased from 35 to 20 MPa²⁵. Slightly lower temperature of 900°C and higher pressure of 50 MPa, with increased to 6 hours synthesis time, allow obtaining 99% of final density²⁶ with grain size of about 2µm. Confirmed after by Mazaheri et al., who showed close to 100% relative density and 1.4µm grain size for the same conditions²⁷, these synthesis conditions were chosen

for ZnO target preparation in our case. Prepared ZnO target was analyzed by XRD (fig. 4-13 (b)). It shows perfect fit to PDF reference in several different points confirming the homogeneity of the target.

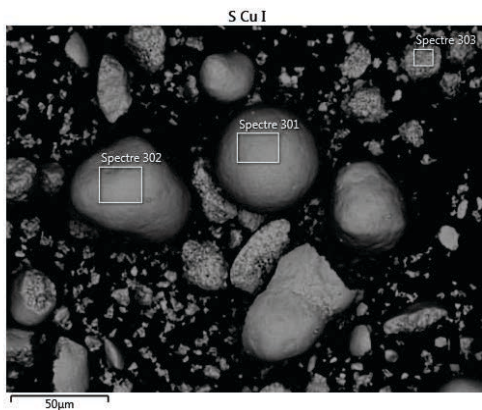


Figure 4-11 SEM image of CuI commercial powder.

For CuI, we firstly analyzed commercial powder, which showed large dispersion of grain size, varying from several microns to hundreds of microns as it can be seen on SEM image in fig. 4-11

Target was synthesized under increased pressure up to 98 MPa at 570 °C, which is about 0.9 of CuI melting temperature. The synthesis process and the obtained target of 3.5mm thickness are shown in fig. 4-12. Visible roughness of the surface was eliminated by mechanical polishing.

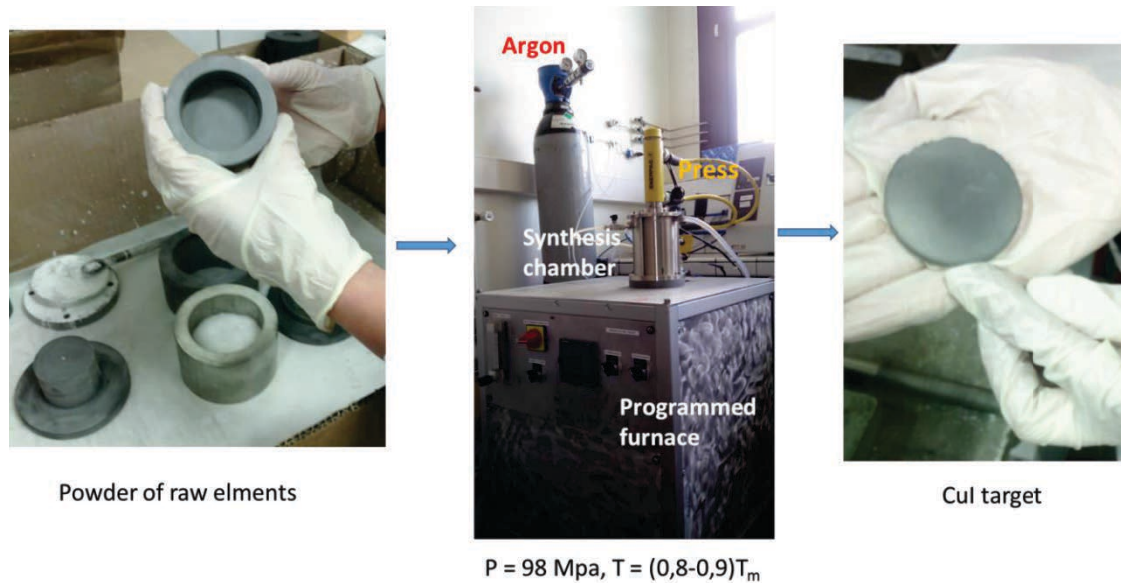


Figure 4-12 Preparation of CuI target by hot pressing

After, CuI target was analyzed by means of XRD (fig. 4-13 (a)), showing precise fit to PDF reference in several different spots.

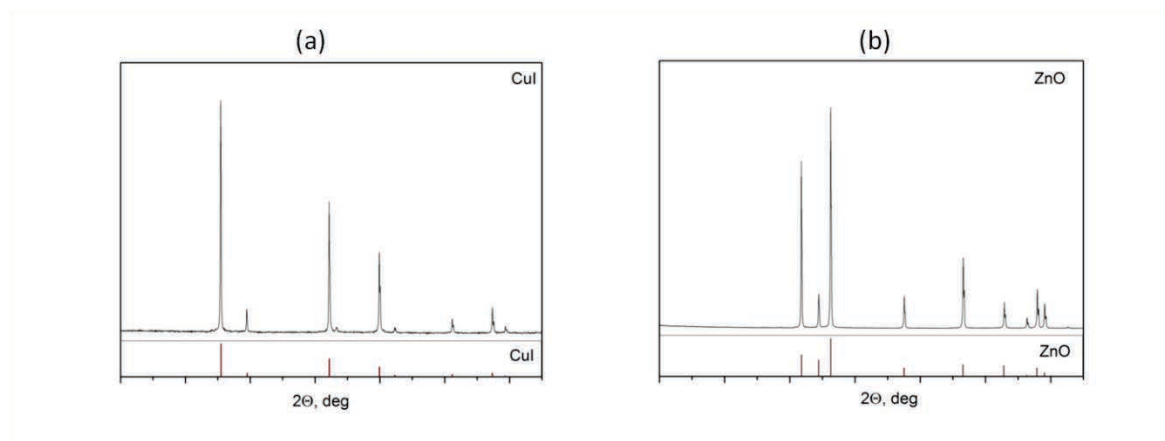


Figure 4-13 XRD patterns of CuI (a) and ZnO (b) targets

3. Thin films preparation and characterization

3.1. Some fundamentals of magnetron sputtering

Sputtering is a physical vapor deposition process (PVD)²⁸, when the surface of a target is bombarded by high energy ions of plasma such as Ar⁺ which leads to the ejection of matter from a target towards a substrate²⁹. Thus, one should provide high vacuum in order to guarantee unhindered movement of ejected

atoms towards substrate and argon plasma, which maintenance is crucial for deposition process. The most primitive deposition chamber with DC voltage acceleration is depicted in fig. 4-14. It begins when electrically neutral Ar⁰ atoms are introduced to the sputtering chamber at a pressure of 1 – 10 mTorr. A DC voltage between anode and cathode ionizes Ar⁺ and creates a plasma (or glow discharge) which consist of ionized atoms of argon and electrons. Ar⁺ is accelerated by negative potential of cathode where target is installed. High energy collisions between Ar⁺ and target surface occurs with ejection of atoms and electrons from the surface of a target. The ejected electrons play an important role in maintain of plasma. To provide sputtering regime high current density is required (usually more than 1mA×cm⁻²). However this regime can easily create an arc due to chaotic movement of ions and electrons and cause drop of resistance and incontrollable grow of current²⁸. Also DC diode sputtering is limited by deposition rates, low ionization efficiency of plasma and substrate heating effect³⁰, which is particularly undesirable if we speak about amorphous films deposition and their controllable crystallization.

To improve deposition rate and to increase efficiency of plasma, a permanent magnet can be installed under the cathode. This method is called magnetron sputtering. While in DC system electric field is perpendicular to the target, specifically arranged magnets³⁰ will create the lines of magnetic flux parallel to the target. Thus the lines of electro-magnetic field will bend towards the cathode. Created electro-magnetic field confines plasma in a vicinity of target and traps ejected electrons near the target surface. This enhances bombardment of the target and facilitates the maintaining of plasma. Plasma efficiency can be illustrated by fig. 4-14 (b) and (c), where non-confined DC sputtering plasma distribution is compared with confined plasma state³¹. In addition, increased intensity of collision allows reducing of operational pressure of argon down to 10⁻³ mbar³¹.

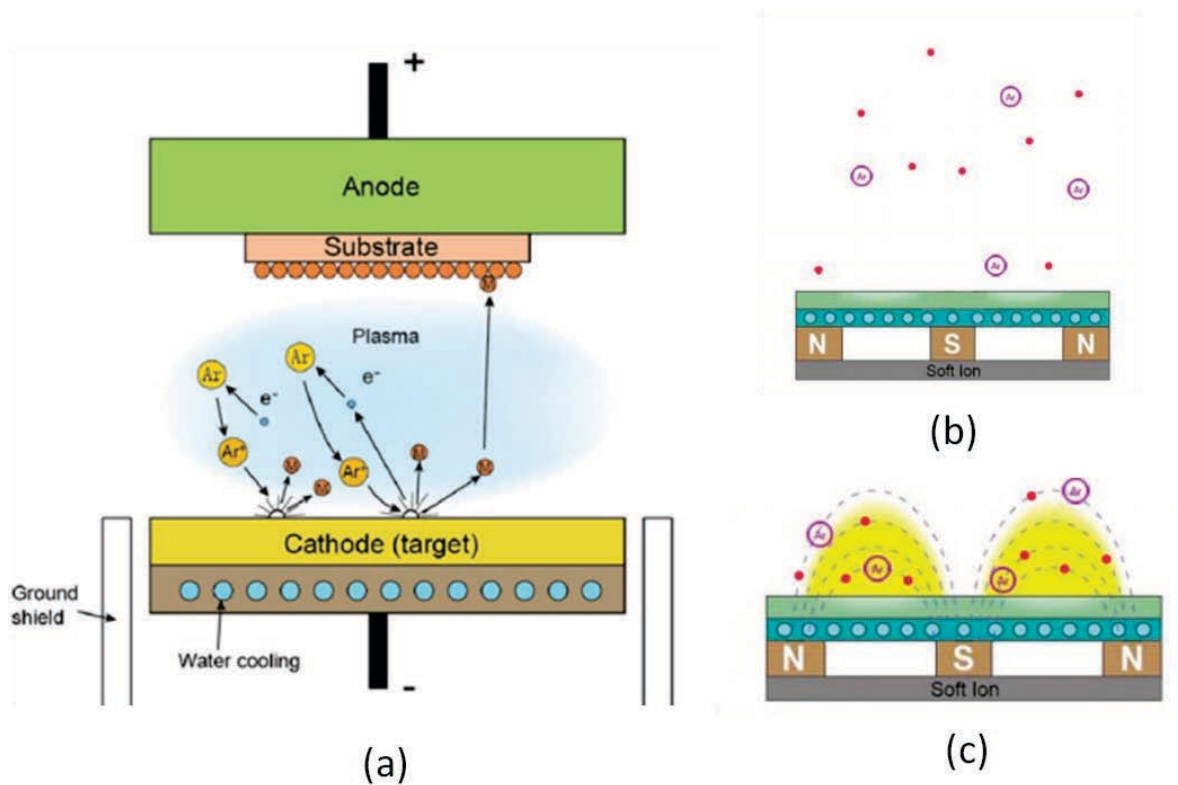


Figure 4-14 DC diode sputtering chamber, PVD process (a), Plasma distribution in non-magnetron sputtering chamber (b), plasma confinement by strong magnetic field in magnetron sputtering chamber³²

The microstructure of thin films obtained by magnetron sputtering is governed by the atom mobility during growth. This mobility is related to the thermal effect, chemical reactions at the substrate and ionic bombardment. First theory which related microstructure and deposit parameters was brought by Movchan and Demchishin. This theory has connected topology of thin films with target melting temperature to substrate temperature ratio. They established 3 different scenarios for thin film microstructure, depicted in fig. 4-15. $T_s/T_m < 0.3$ – zone I is formed by small elongated grains which form columnar structure with porous morphology and weakly bonded grains. $0.3 < T_s/T_m < 0.45$ – zone II with higher diffusion rate of the atoms, which leads to more dense structure without porosity, borders between grains and columns are sintered, grain size increase in 3 dimensions and can extend from the substrate to thin film surface. $0.45 < T_s/T_m$ – zone III of volumetric diffusion, diffusion occurs into the grains, which entails its growth and re-crystallization^{33,34}.

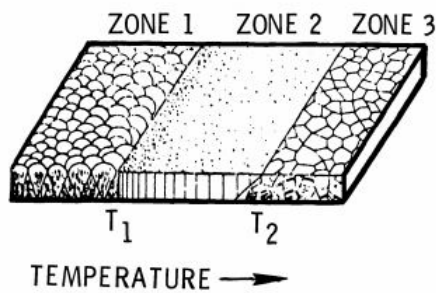


Figure 4-15 Thin film morphology as a function of T_s/T_m ratio according to Movchan and Demchishin³⁴

However, as we could see before, plasma behavior has a great influence on deposition rate. Different gas pressure and voltage, magnetic field can influence significantly the kinetic energy of ions as well as on mean free path of ejected particles. Thornton considered this and refined the concept of Movchan and Demchishin by adding the argon pressure parameter³⁷. Microstructural morphology of thin film as a function of argon pressure and T_s/T_m ratio is depicted in fig. 4-16. In Thornton's model, transition zone T between zone I and zone II described by Movchan and Demchishin consists of grains defined by the limits of the low porosity. The surface of zone-T is denser and less rough compared to zone I and zone II³⁵. It is interesting to mention that with increase of gas pressure, zone I severely extends due to higher mobility of adatoms caused by ionic bombardment.

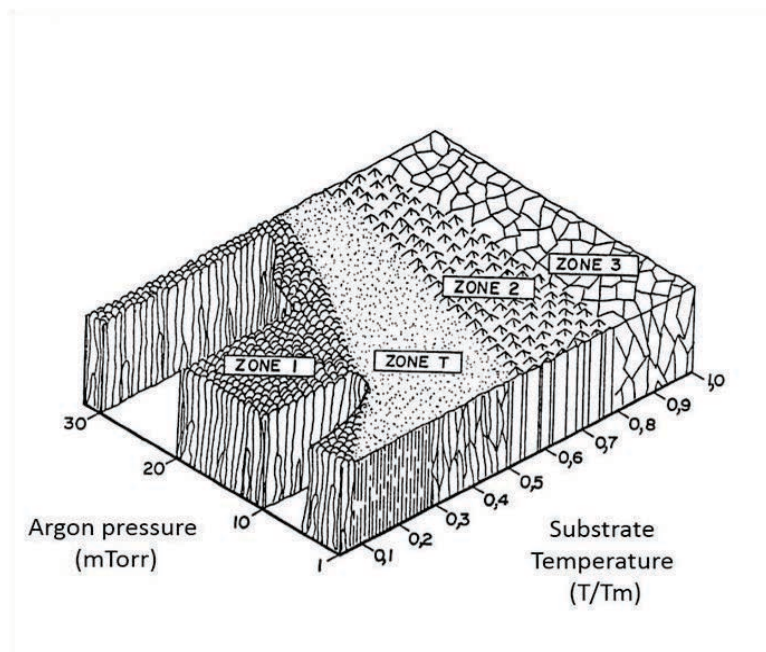


Figure 4-16 Thornton Structure-zone diagram for metal films deposited by magnetron sputtering³⁶

Indeed, we could see this effect for the “40-40-20” film deposition. Considering that the melting temperature of the 40GeSe₂-40Sb₂Se₃-20CuI glass-ceramics is 624 °C and the substrate temperature is 30 °C, one can obtain $T_s/T_m = 0.34$. Thus the pressure of 5×10^{-3} mbar or 3.75 mTorr was chosen for the deposition. As it can be seen in fig. 4-17 (b), this regime allows obtaining zone T morphology, grains are well sintered, we cannot see any separation, and the surface is very smooth. Upon the increase of pressure to 6 mTorr, evident transition to zone I occurs (fig. 4-17 (a)): on a lateral SEM image we can distinguish separate columns and roughness increase.

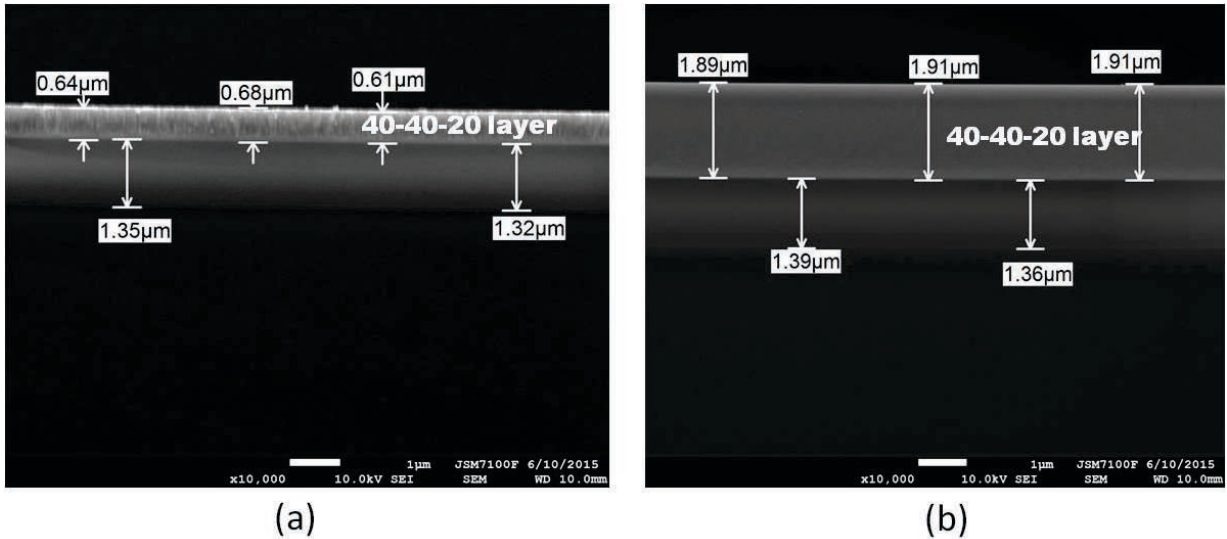


Figure 4-17 Lateral SEM image of "40-40-20" thin film deposited on SiO₂ substrate. Deposit at ambient temperature with argon pressure 6 mTorr, zone I morphology (a), deposition with argon pressure 3.75 mTorr, zone T morphology (b)

3.2. Preparation of bulk heterojunction within thin films based on 40GeSe₂-40Sb₂Se₃-20CuI composition.

Following our initial concept, we prepared first thin films of “40-40-20” composition on a BK7 glass substrate. Sputtering was performed with the substrate at ambient temperature and pressure of 3.75 mTorr to guarantee flat surface with continuous non-column structure (fig. 4-17(b)). Since “40-40-20” possess high absorption coefficient, we sputtered relatively thin amorphous film of 200 nm thickness as sketched on fig. 4-18. The annealing was made directly inside the sputtering chamber under argon atmosphere to prevent possible oxidation and thin film mechanical degradation which could occur in case of annealing

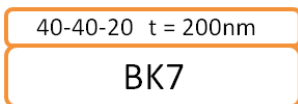


Figure 4-18 Configuration of thin film based on "40-40-20" ceramics

in external furnace exposed to atmosphere. Annealing was made at 300°C temperature, which is compatible with crystallization temperature of these glass-ceramics.

Obtained thin films were analyzed structurally and optically. As it can be seen in fig. 4-19, annealed thin film is not homogeneous and substantially consists of two spatial zones: dense spherical islands of diameter of about 100 μm (blue zone) and separately distributed species of several tens of microns in length (red zone). On magnified images, it can be seen that the blue zone is characterized by tight packing of thin and relatively short needles with diameter below 100nm, which fuse into randomly oriented aggregates with diameter of

about 1 μ m. While red zone is rather characterized by longer (>10 μ m) and thicker needles with more pronounced preferential orientation. As we mentioned before, needle-like structure is usual for Sb₂Se₃ and its modifications. We cannot see clear presence of Cu₂GeSe₃ phase on SEM image since Ge could be diluted in non-crystallized phase (dark spaces on SEM image, which surround crystallized species in zone of lower density) or crystallize in small particles shadowed by larger Sb₂Se₃ aggregates.

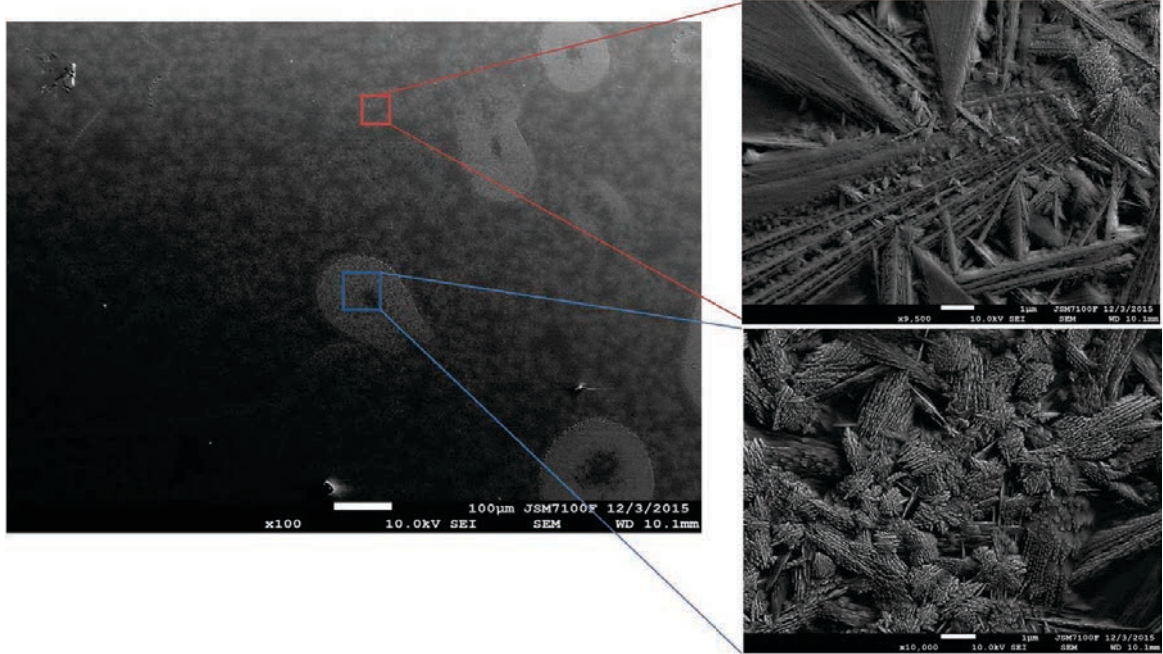


Figure 4- 19 SEM image of "40-40-20" thin film annealed at 300 °C

However when we analyzed the composition of this thin film in multiple zones, we found the absence of iodine and extremely low quantity of copper, which is reflected in table 4-3. As we showed in previous chapters, there are two possible mechanisms of conductivity in "40-40-20" composite. Conductivity can be provided by spatially interconnected rods of iodine doped Sb₂Se₃ or by Cu₂GeSe₃ phase. It is clear that in the absence of Iodine in sufficient quantity, conductive iodine doped Sb₂Se₃ phase is not formed enough to provide conductivity. At the same time, the amount of copper is so negligible that formation of continual coating of Cu₂GeSe₃ on top of Sb₂Se₃ rods according to the mechanism described by Zhang et al.³⁷ is also very unlikely. Thus, non-surprisingly we found that "40-40-20" thin film is not conductive, since apparently its major phase is Sb₂Se₃.

Table 4-3 Conductivity and elemental analysis of "40-40-20" annealed thin film

Configuration	R, Ohm*cm	n, cm-3	Type	Cu	Ge	Se	Sb	I
				% atomic				
« 40-40-20»	>10 ⁸	NA	NA	1-2	10	50-55	35-40	0

At the same time, one can find only weak shift of transparency region and reflectance intensity for the annealed thin film. The shift towards longer wavelengths can be explained by additional scattering losses induced by presence of crystals in the annealing film³⁸.

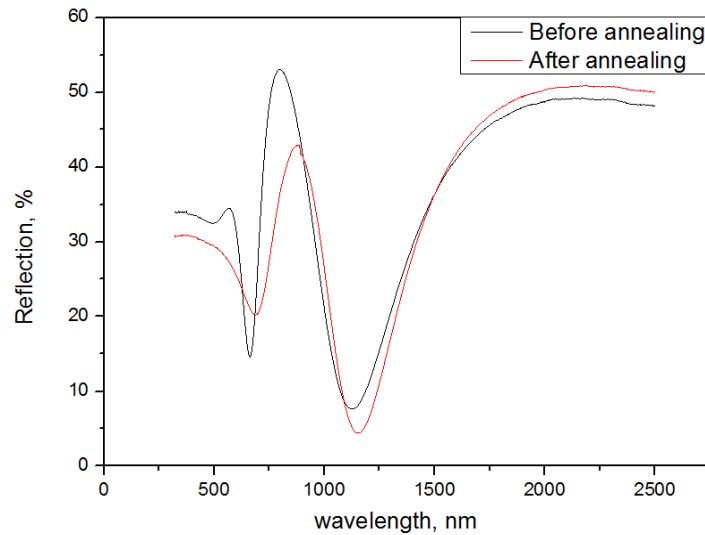


Figure 4-20 Reflectance spectra of "40-40-20" thin films before (black) and after annealing (red)

We supposed that this problem can be connected with weak atomic adhesion to BK7 surface as well as with slow crystallization, when intensive atomic movement is not supported by fast nucleation and growth of crystalline phase, which lead to elemental loss. To overcome the excessive loss of copper and iodine, we decided to sputter a very thin film of CuI prior to the deposition of the principal film of "40-40-20" as it is sketched in fig. 4-21. It is necessary to underline that thin film of 3nm thickness deposited via magnetron sputtering cannot be a continuous film in any case and will be presented as multiple islands of

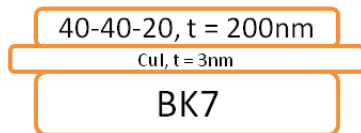


Figure 4-21 Configuration of conductive thin film based on "40-40-20" ceramics with 3 nm layer of CuI

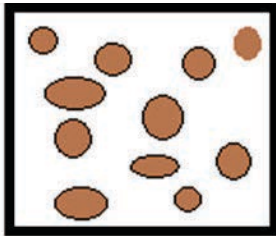


Figure 4-22 Schematic repartition of CuI within a thin film of 3nm thickness

matter which are not interconnected with each other as shown in fig. 4-22. Such repartition was already observed for instance in MgB₂ ultra-thin films³⁹. After deposition, we have measured the conductivity of the surface covered with 3nm layer of CuI. We found no conductivity for this film and therefore made a conclusion that grains are not connected with each other.

When we had made sure that CuI underlying film does not provide conductivity itself, we deposited a 200nm film of "40-40-20" and performed annealing at 300 °C. The morphology of obtained film is shown in fig. 4-23. In this case we also can distinguish two different zones. Red zone consist of needles with diameter of several tens of nanometers and about 500 nm in length. One can made an analogy with red zone in "40-40-20" film depicted in fig. 4-19, however there is a substantial dimensional difference. With underlying layer of CuI, those needles are much smaller and much denser at the same time. In blue zone we find copper rich spherical particles of 2-5 μm in diameter immersed in medium defined by red zone. Apparently crystallization of these spherical particles is induced by underlying spots of CuI. The present island-like morphology is correlated with our suggestion of CuI repartition in island-like way shown in fig. 4-22.

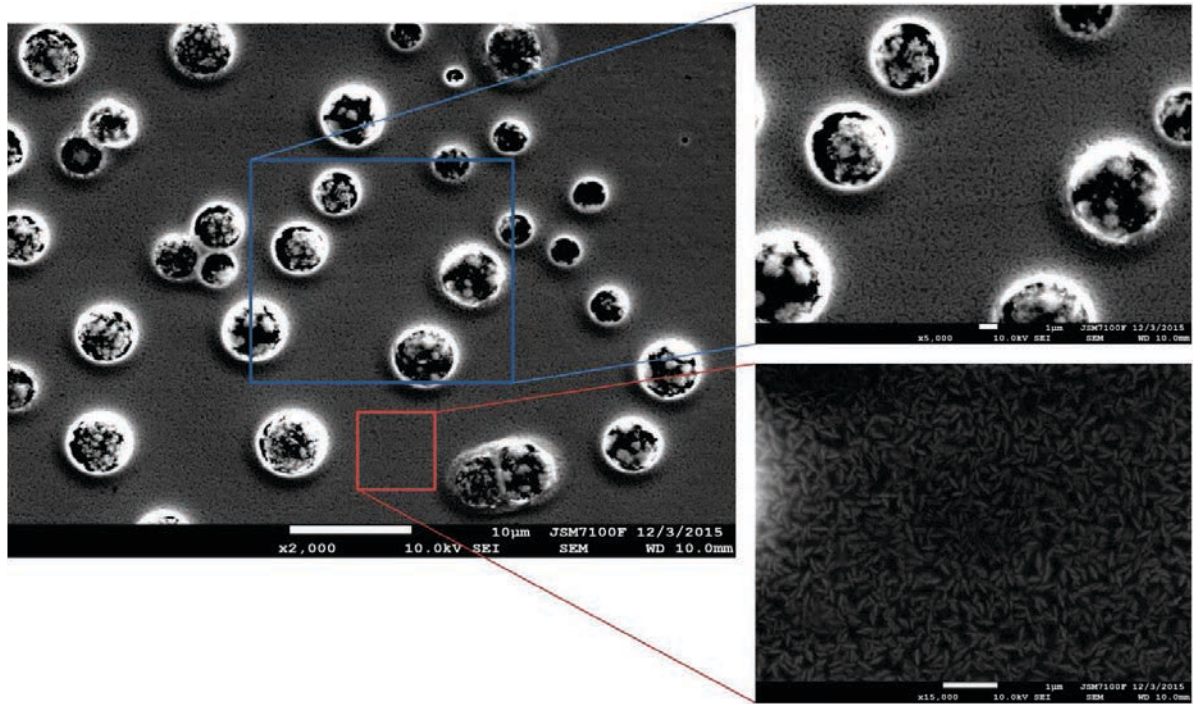


Figure 4-23 SEM image of conductive configuration bi-layer film CuI | "40-40-20"

We turned to electric measurements summarized in table 4-4 and found that this thin film is conductive with $R = 8 \times 10^2 \Omega \times \text{cm}$. By means of Hall Effect measurement, we found that we prepared a p-type semiconductor with free charge carrier concentration of $3 \times 10^{21} \text{ m}^{-3}$. Elemental mapping shows severe inhomogeneity mostly connected with spherical particles where one can find up to 7% of Cu and 30% of Sb, while in red zone we found 2% of copper and 1-2% of iodine. Evidently, this amount of copper and iodine could not be provided by negligible quantity of pre-deposited CuI. The obtained film is rather connected with increased atomic adhesion and crystallization behavior thanks to this bi-layer structure, where CuI spots played the role of crystallization center, protecting major thin film from loss of elements upon the crystallization.

Table 4-4 Comparison of atomic content and conductivity for solely deposited "40-40-20" and for bi-layer configuration CuI/"40-40-20"

Configuration	R, Ohm*cm	n, m-3	Type	Cu	Ge	Se	Sb	I
				% atomic				
« 40-40-20»	$>10^8$	NA	NA	1-2	10	50-55	35-40	0
CuI « 40-40-20»	$8 \cdot 10^2$	$3 \cdot 10^{21}$	P	2-7	10	45-50	30-35	1-2

One can find a severe difference in reflectance spectra for two different above-described configurations. Bi-layered configuration has low reflectance in non-transparent region; however, its short-wavelength cutoff edge is significantly shifted towards longer wavelengths. If "40-40-20" film has a cut-off at 500 nm, which corresponds to the energy 20000 cm^{-1} (optical gap 2.5eV), configuration with CuI layer gives rise to a red shift towards 800nm, i.e. 12500 cm^{-1} (1.6eV). In fact such loss in transparency is favorable for solar harvesting since all the visible light can be effectively absorbed in the second case.

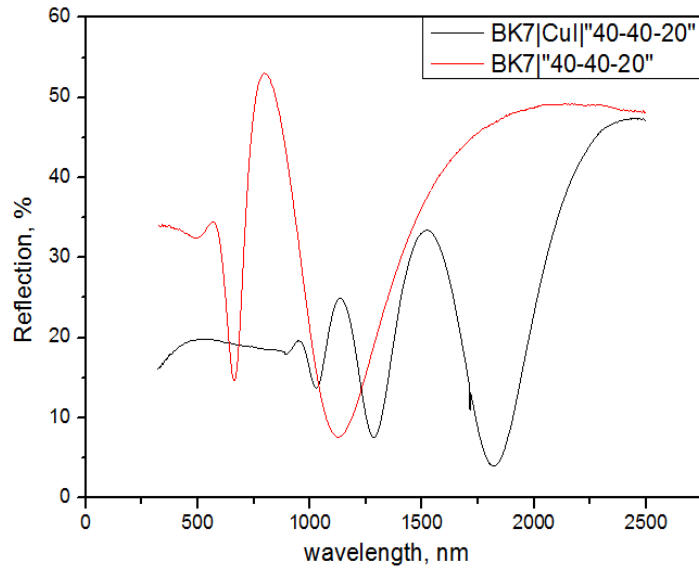


Figure 4-24 Reflectance spectra of "40-40-20" thin film with underlying layer of CuI (black) and without it (red)

In fig. 4-25 X-ray diffractogram of the two configurations are presented. It is difficult to judge about Cu_2GeSe_3 phase, since some significant shift of Sb_2Se_3 related peaks can be supposed due to deviations from stoichiometry. However significant increase of peak at 27.769° associated with Cu_2GeSe_3 (0 1 1) orientation can be noticed. At the same time, we observe promotion of Sb_2Se_3 related peak at 28.199° (2 1 1) and appearance of (2 2 1) orientation related peak at 31.159° . Thus we can suppose that both Sb_2Se_3 and Cu_2GeSe_3 phases are contributing to the major peak intensity in close vicinity of $2\Theta = 28^\circ$. X-ray diffractogram confirms that introduction of CuI layer promotes much more expressed crystallization of major thin film according to the expected crystalline phases.

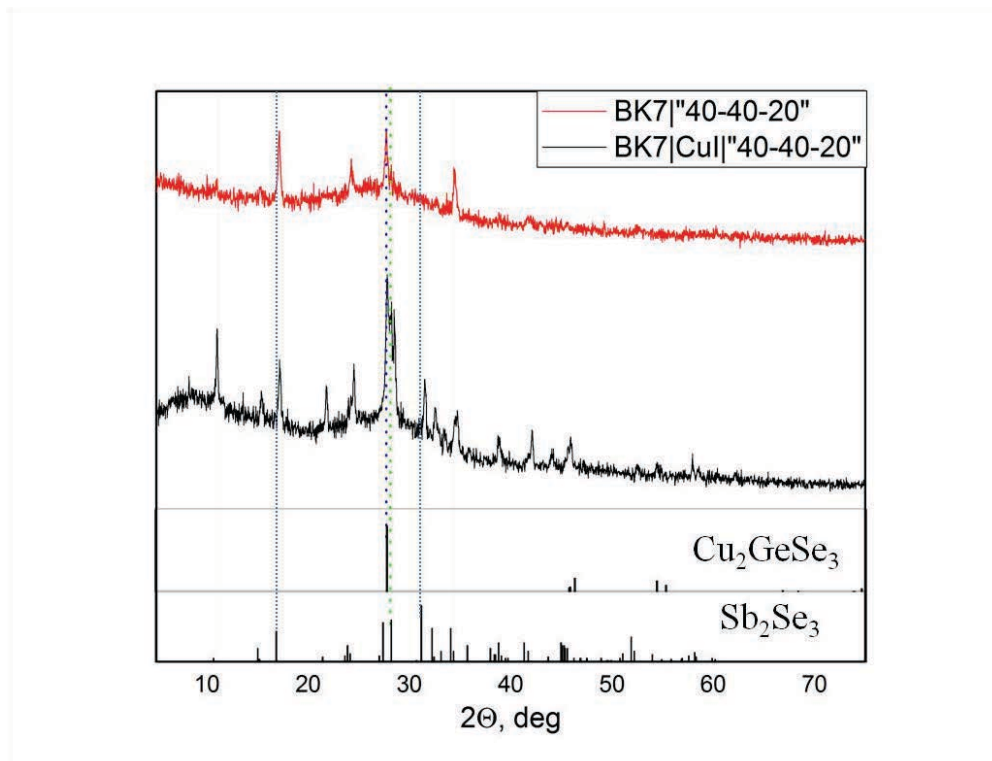


Figure 4- 25 X-ray diffractograms of annealed thin films: "40-40-20" (red) and CuI "40-40-20" (black)

Another difference between these two configurations can be demonstrated by in-situ recorded reflectance spectra depicted in fig. 4-26. Upon the growth and heat treatment, the thickness of thin film is controlled optically at $\lambda = 780$ nm. Major oscillations in left part of the spectra are associated with change of positive interference condition due to change of film thickness. At point A we start a heat treatment. As one can see, thin film with CuI layer does not undergo severe dilatation (fig. 4-26 (a)) which can be seen on A-B interval for thin film without pre-deposited CuI layer (fig. 4-26 (b)). This can be explained by lower thermal coefficient of thin film with CuI layer resulting in its higher stability. At point B thin film undergoes phase transition which is irreversible if the heating is turned off. It is interesting to mention that configuration with CuI layer shows more expressed B-C step upon phase transition compare to solely deposited film.

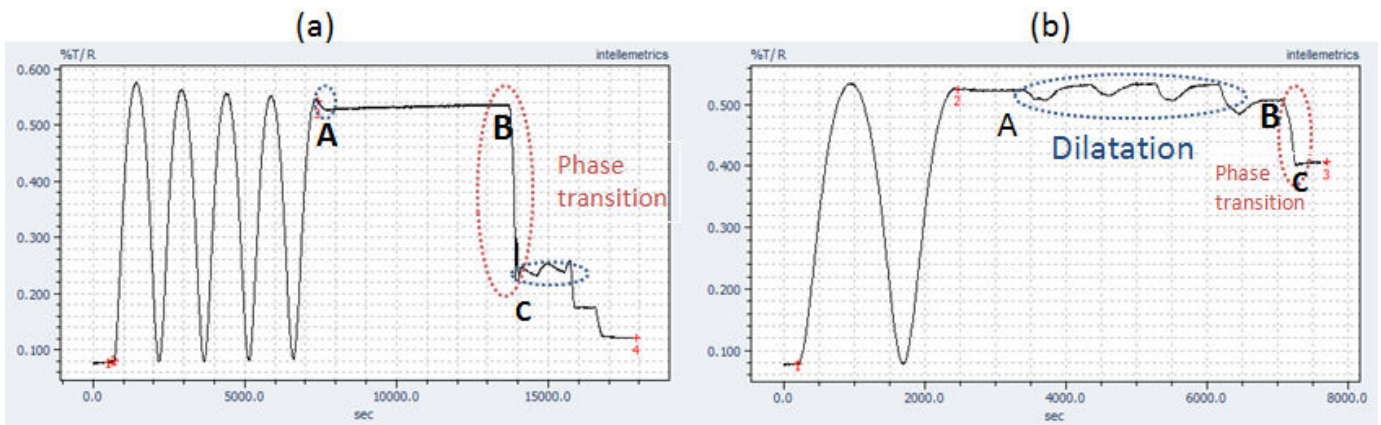


Figure 4-26 In-situ reflectance measurement at the wavelength 780 nm. Conductive configuration CuI| "40-40-20" (a), non conductive thin film "40-40-20" (b)

For electric measurements, we prepared two sets of samples. One for PEC measurement which consists of CuI| "40-40-20" assembly on ITO film with Ag paste for a working electrode connection as shown in fig. 4-27 (left). And a sample for photovoltaic measurement made similarly with Au electrodes on top, shown in fig. 4-27 (right)



Figure 4-27 Samples for PEC (left) and PV (right) measurements

Results are presented in fig. 4-28. In PEC measurement (fig. 4-28 (a)), the thin film showed strong p-type photoconduction behavior obtaining photocurrent of $700 \mu\text{A}/\text{cm}^2$ under -0.6V bias, without any pronounced n-type photoconducting phase expression under positive bias. This behavior is very different compare to bulk $40\text{GeSe}_2-40\text{Sb}_2\text{Se}_3-20\text{CuI}$ glass-ceramics behavior or PEC performance for crystals of iodine-doped Sb_2Se_3 or Sb_2Se_3 with excess of Sb. As we established for bulk glass-ceramics, it is Sb_2Se_3 phase which contributes to photoconductivity mostly due to donor doping and stoichiometry deviations.

Apparently, for thin films, we do not have sufficient quantity of iodine to assure needed level of Sb_2Se_3 doping at the same time no Sb rich sites are formed within the thin film. We showed that for the bulk, $Sb_2Se_{3-x}I_x$ and $Sb_{2+x}Se_{3-x}$ contribute to both n-type photocurrent (positive bias) and p-type photocurrent (negative bias) due to severe inhomogeneity. It is probably not the case for thin films where only possible candidate for p-type photoconductivity is Cu_2GeSe_3 phase. For PV measurement (fig. 4-28 (b)), we obtain simple Ohmic resistivity with weak photoconductive effect received from sub-electrode area and absence of photovoltaic effect.

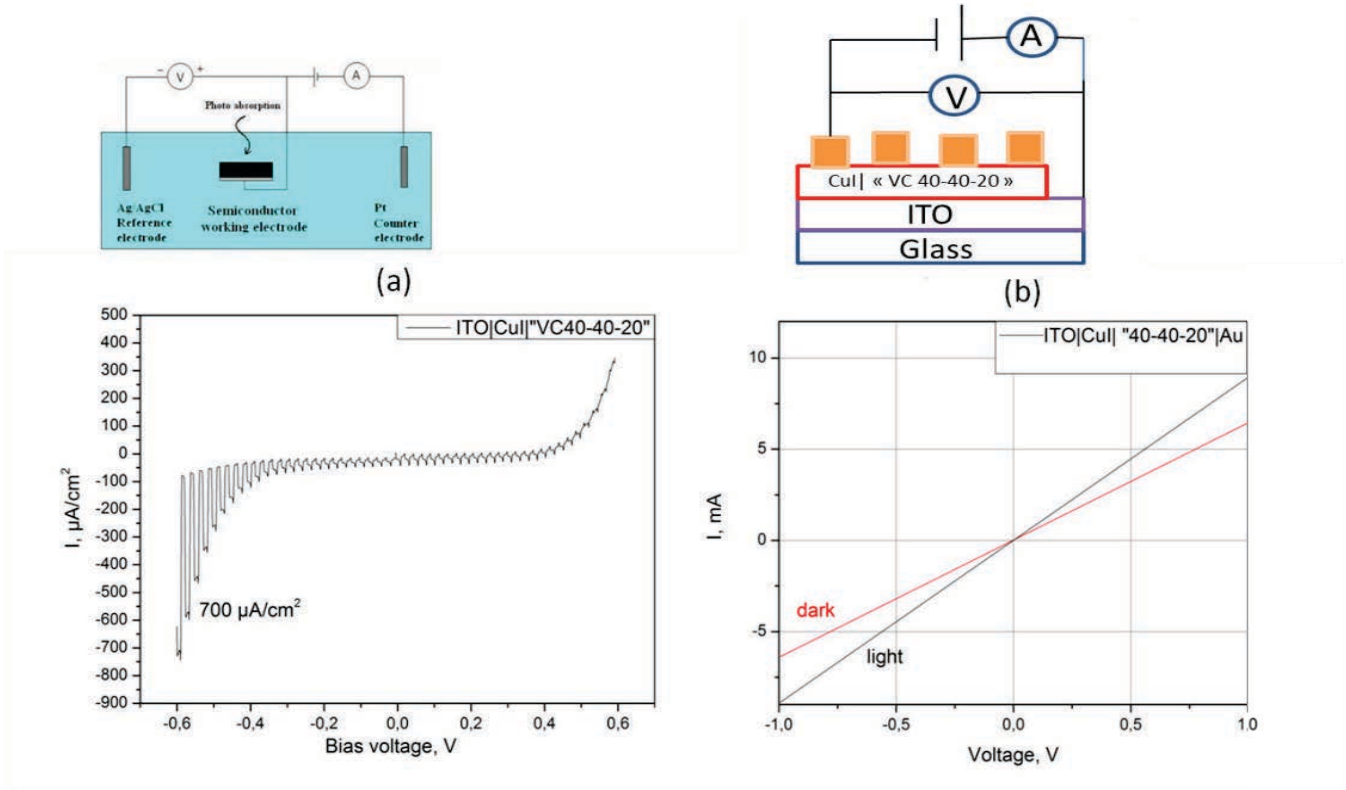


Figure 4- 28 Electric measurements of CuI| "40-40-20" configuration: PEC under chopped illumination(a) and IV curve under continuous illumination (b)

We can conclude that bulk heterojunction is not formed inside this thin film due to absence of sufficiently conductive n-type phase. There could be also an issue with the spatial distribution of p- and n-type phases resulting in non-favorable configuration for light absorption or/and charge separation between them. However the major problem is probably simple absence of n-type semiconductor which could take part in p/n junction formation. Otherwise we expected to see a PEC response at positive bias.

We tried to overcome this issue by varying deposition parameters in order to influence the structure of thin film. Several depositions in pre-heated chamber instead of post-deposition heat treatment were carried out. We prepared two thin films of "40-40-20" composition on top of pre-deposited CuI layer under two different deposition temperatures $T_1 = 320\text{ }^\circ\text{C}$ and $T_2 = 350\text{ }^\circ\text{C}$.

For thin film deposited at T_1 we are still in the zone T according to Thornton, however we observe substantially different morphology compared to thin films deposited at ambient temperature (fig. 4- 29). Surface is much denser and the thin film consists of leaf like structures with domains of several hundreds of nanometers in length, which are tightly sealed with each other. We do not observe any major voids

(less than 200nm) or amorphous zones. Compared to thin films deposited at room temperature, we cannot distinguish different morphological zones on thin films deposited on heated substrates. Black spots are probably due to certain compositional and morphological inhomogeneity. However their size $\sim 1\mu\text{m}$ does not allow precise analysis of their composition via EDS without touching surrounding zone.

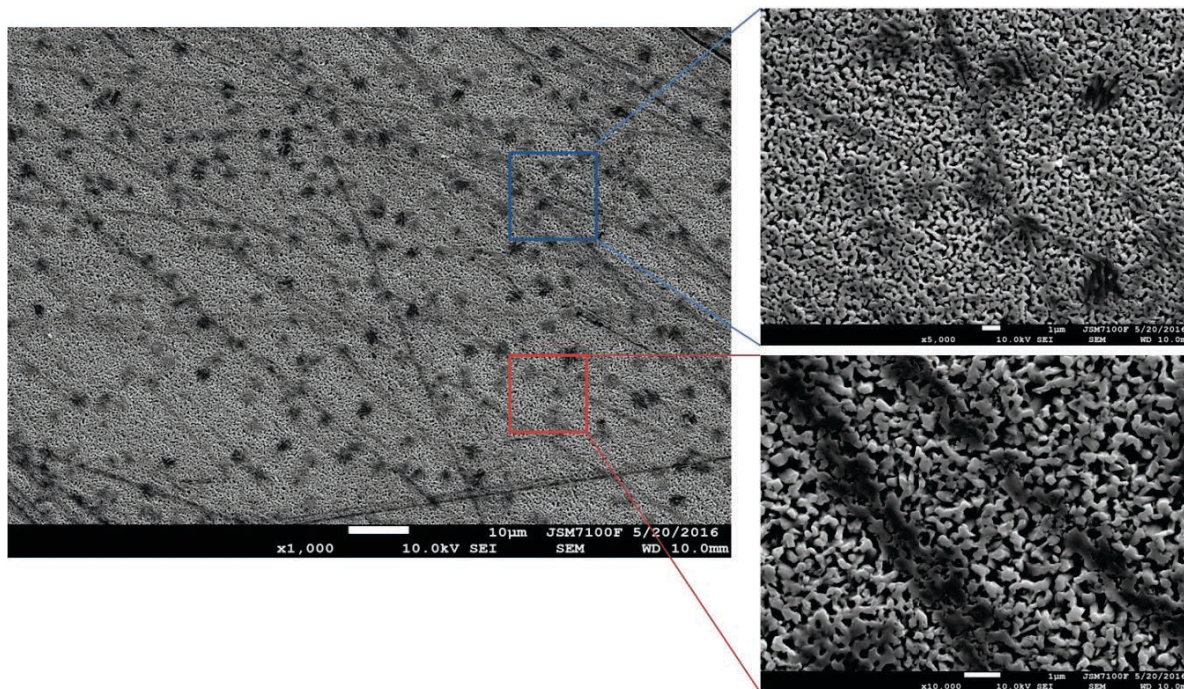


Figure 4-29 SEM image of CuI "40-40-20" thin film, growth under $T_1 = 320\text{ }^\circ\text{C}$ temperature

For thin film sputtered at $T_2 = 350\text{ }^\circ\text{C}$, we observe morphological transition to zone II. Size of particles is very small and the grains are sintered to very dense columnar structures, with voids less than 50 nm, which extend through the whole thickness of thin film. Some signs of re-crystallization appear as well as separation of coating by true grain boundaries³⁷. Various of spatial orientations of columnar structures can be seen as well.

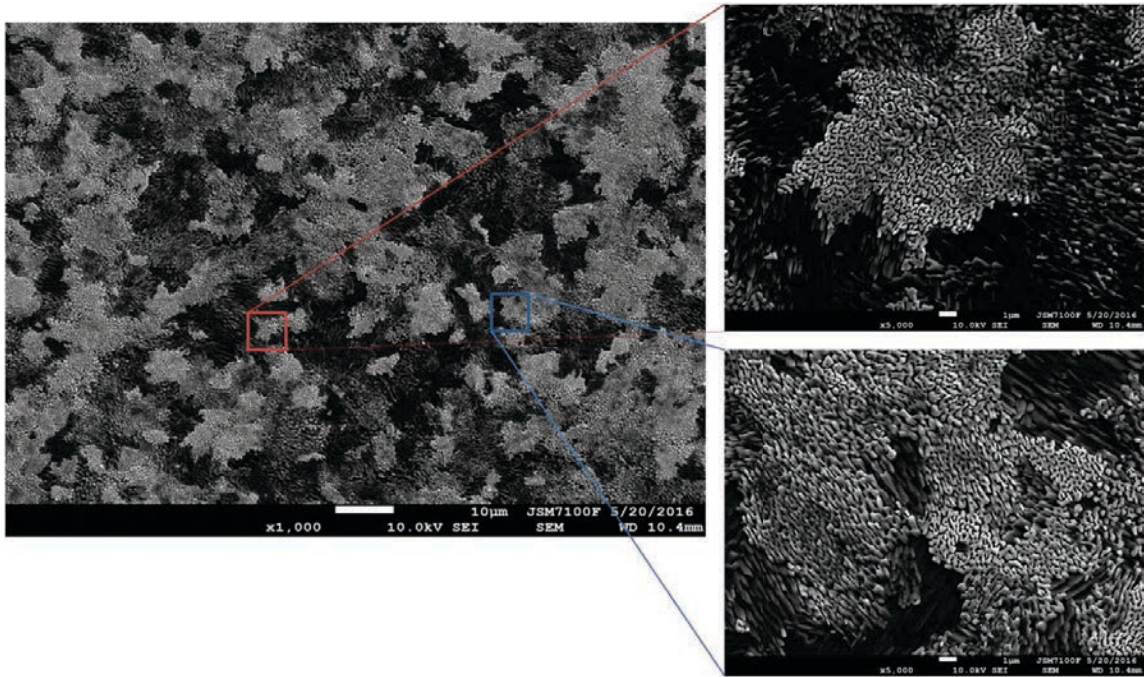


Figure 4-30 SEM image of CuI "40-40-20" thin film, growth under $T_2 = 350^\circ\text{C}$ temperature

If one would compare X-ray spectra of thin films (fig. 4-31 (a,b)) deposited at 320°C and at 350°C (black curves), it became evident that higher temperature leads to more expressed and full crystallization especially for Sb_2Se_3 related peaks at 28.199° (2 1 1) and 31.159° (2 2 1). Overall intensity of XRD peaks shows signifies increase of the size of crystals, which was described by Thornton as aggregation of columns via sintering to columnar dimensionally larger aggregates.

It is also interesting to notice that ITO modifies XRD pattern (red curves) of "40-40-20" thin film in terms of relative intensities (especially Sb_2Se_3 related peak at $2\theta = 32.220^\circ$ (3 0 1)), which can stay for change in occupation rate within Sb_2Se_3 cell due to modified substrate nature. However no phase change or substantial shift in peak positions can be found.

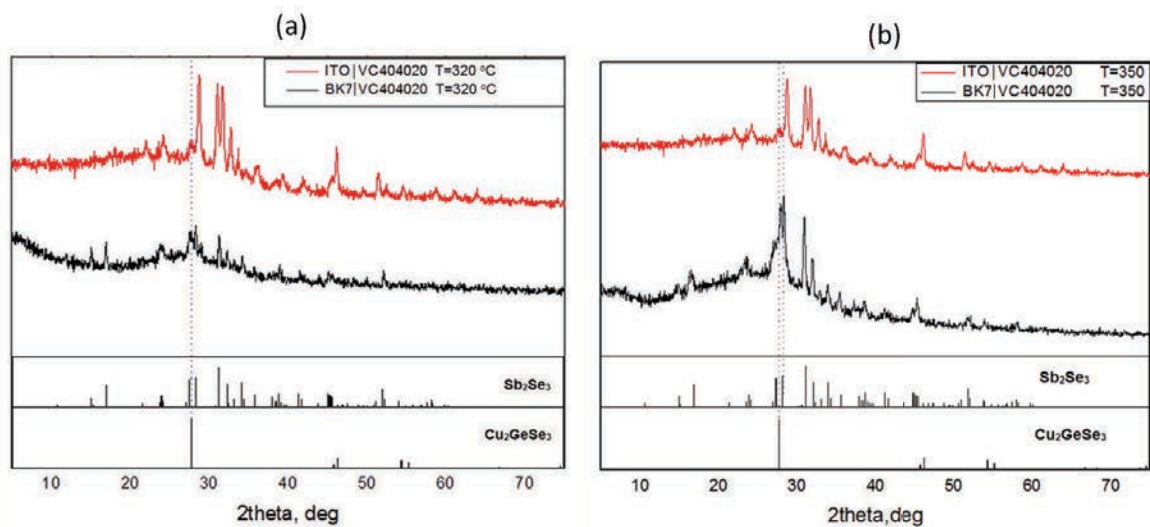


Figure 4-31 XRD patterns of CuI "40-40-20" thin film, grown at $T_1 = 320^\circ\text{C}$ (a) and $T_2 = 350^\circ\text{C}$ (b). On BK7 substrate (black lines) and ITO (red lines)

Comparing to “cold” deposition with post-thermal treatment, we can conclude that no improvement for PEC response was made (fig. 4-32). Thin film deposited at 320 °C shows 370 $\mu\text{A}/\text{cm}^2$ maximum at -0.6V bias, while film deposited at higher temperature gives higher current density up to 530 $\mu\text{A}/\text{cm}^2$. However this value is still lower than one obtained for “cold” grown film, which was then post-annealed after deposition.

This can be explained by different morphology of light absorbing phase. As it is known, various mixing scenarios lead to different absorption spectra. We can distinguish several cases represented in fig. 4-33. In fig. 4-33 (a) planar mixing is depicted with strict ideally smooth interface which property is a linear combination of red material and blue material. Fig. 4-33 (b) represents rough interface described by Bruggeman model⁴⁰ and fig. 4-33 (c) Maxwell-Garnett model⁴¹. As we can conclude, planar junction would be optimal for charge separation however limits light absorption due to minimal length of interface. Rough interface can be favorable for light absorption due to extended interfacial surface but with unfavorable charge separation. Maxwell-Garnett case seems less favorable for charge separation but not for light absorption since spherical particles possess maximal length of surface.

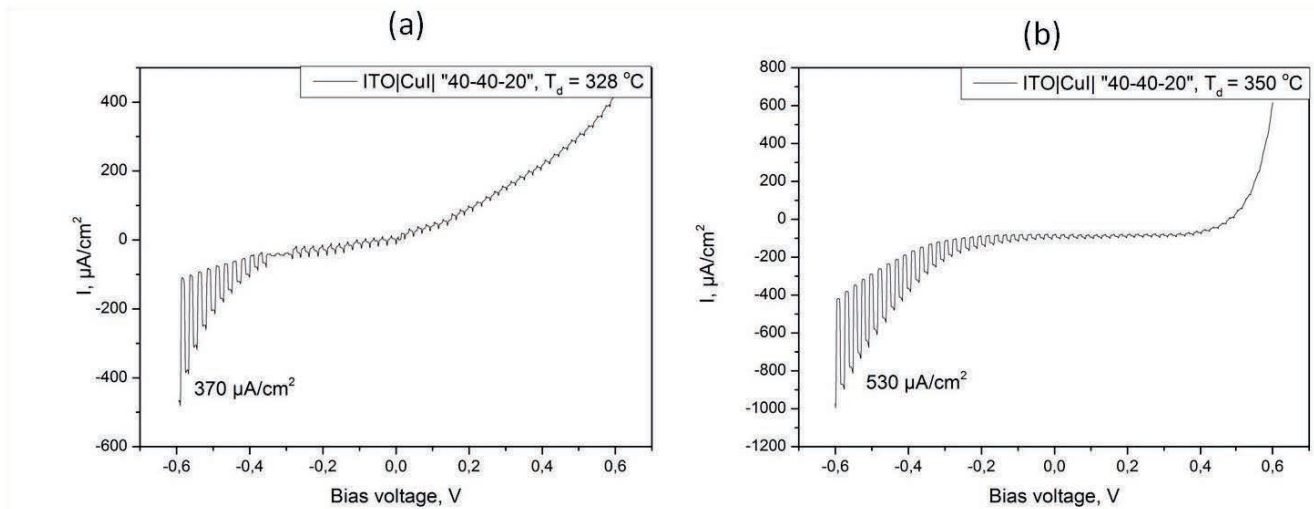


Figure 4-32 PEC curves of CuI "40-40-20" grown at $T_1 = 320\text{ }^\circ\text{C}$ (a) and $T_2 = 350\text{ }^\circ\text{C}$

It is possible that for CuI "40-40-20" with post-growth treatment, we are dealing with the case of copper-rich spherical inclusions which could be responsible for light absorption and contribute to photoconductivity. While in case of thin films grown in pre-heated chamber, we are more likely dealing with rough interface, since these films are much better arranged and do not show severe morphological inclusions. Therefore light absorption of absorbing phase in these structures is lower resulting in poor PEC response.

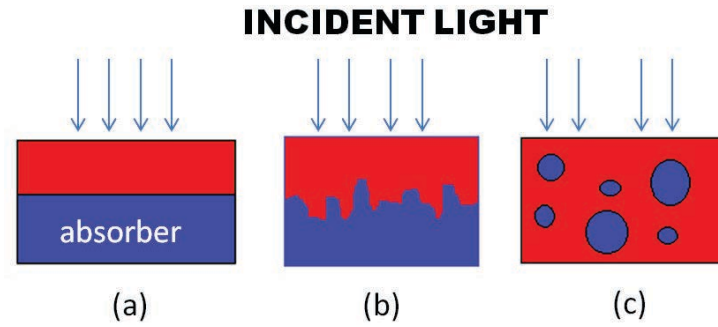


Figure 4-33 Different scenarios of phase mixing resulting in variety of morphologies: planar (a), rough boundary (b), spherical inclusion (c)

However the most important result of PEC test is the absence of n-type phase response. Thus, it was not surprising that photovoltaic effect is not detected for the devices based on these thin films (fig. 4-34 (a,b)). The absence of conductive n-type phase, probably due to extremely low quantity of iodine, still seems the major problem for the preparation of internal heterojunction $p\text{-Cu}_2\text{GeSe}_3/n\text{-Sb}_2\text{Se}_3\text{:I}$. Also we observe a lack of iodine compare to bulk glass-ceramics (5.5%) for thin film based on the same composition (1-2%).

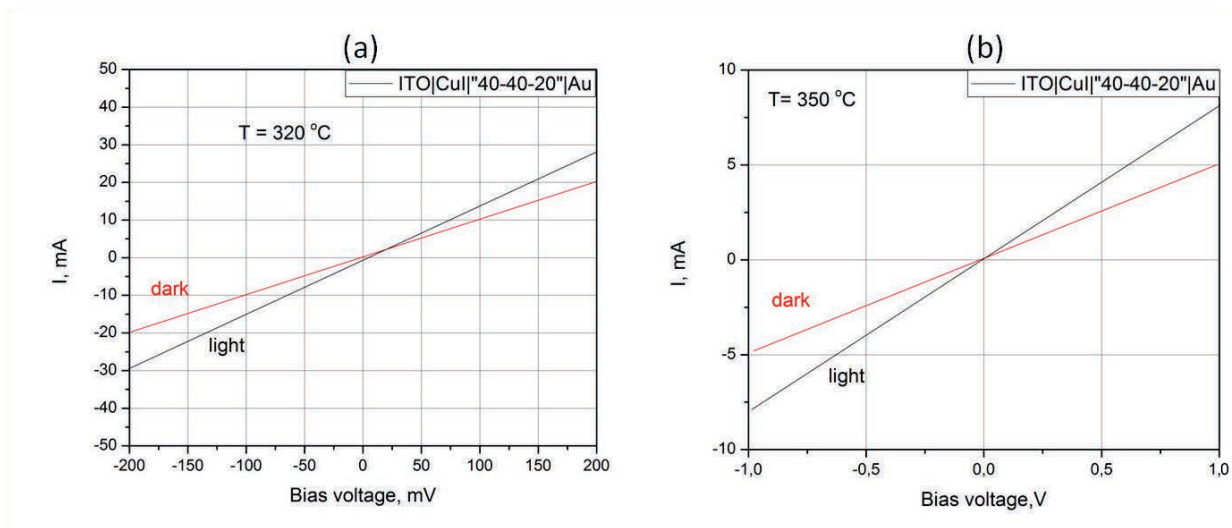


Figure 4-34 IV curves of solar devices based on $\text{CuI}'40-40-20'$ grown at $T_1 = 320 \text{ oC}$ (a) and $T_2 = 350 \text{ oC}$

Trying to solve this problem, we decided to increase physically the amount of copper and iodine by doubling the content of CuI in the sputtering target of $40\text{GeSe}_2\text{-}40\text{Sb}_2\text{Se}_3\text{-}40\text{CuI}$ composition.

After first attempts to prepare thin films with this target we found out that even if succeeded to maintain relatively high atomic percentage of iodine and cooper, thin film is not conductive without pre-deposited thin film of CuI. This fact confirmed our previous consideration that pre-deposited layer plays a role of crystallization center and influences rather structure and crystallization kinetics than composition. Comparative composition analyzes of “40-40-40” thin film with pre-deposited CuI layer is summarized in table 4-5.

Table 4-5 Atomic composition of “40-40-40” thin films before and after annealing comparison with bulk glass-ceramics

	Composition of bulk glass ceramics, 40GeSe ₂ -40Sb ₂ Se ₃ -20CuI	Thin film « 40-40-40» before annealing	Thin film « 40-40-40» after annealing
Ge	11	10	10
Se	55	53	54
Sb	22	21	23
Cu	5.5	10	8-9.5
I	5.5	5	2-3.5

We tried several different substrates to compare morphology and optical properties of “40-40-40” film. We tried to use sputtered aluminum as bottom electrode, with consecutive deposition of CuI and “40-40-40” films on it at ambient temperature and at the pressure of 3.7 mTorr. We also used ZnO as a transparent oxide and BK7 glass as a reference. In fig. 4-35 a set of SEM images of “40-40-40” thin film is presented. We maintained the same conditions for all the films deposited. However as it can be seen, their morphologies are significantly different. Thin film deposited on Al (fig. 4-35 (a)) demonstrates relatively high porosity which is however lower than the one shown on BK7 glass (fig. 4-35 (b)). It is worth mentioning that compared to “40-40-20” film, the “40-40-40” film does not show any columnar-like structure but rather low dispersion leafs weakly sealed with voids of about 1 μm in diameter. Probably this morphology still belongs to type T, where need-like Sb₂Se₃ are already sintered to form micron-size domains. However larger grains are not formed and major voids still present. Thin film grown on ZnO shows the lowest porosity with low surface roughness , relatively good homogeneity of matter distribution and surface consisting of small but well sintered crystals of submicron size (fig. 4-35 (c)).

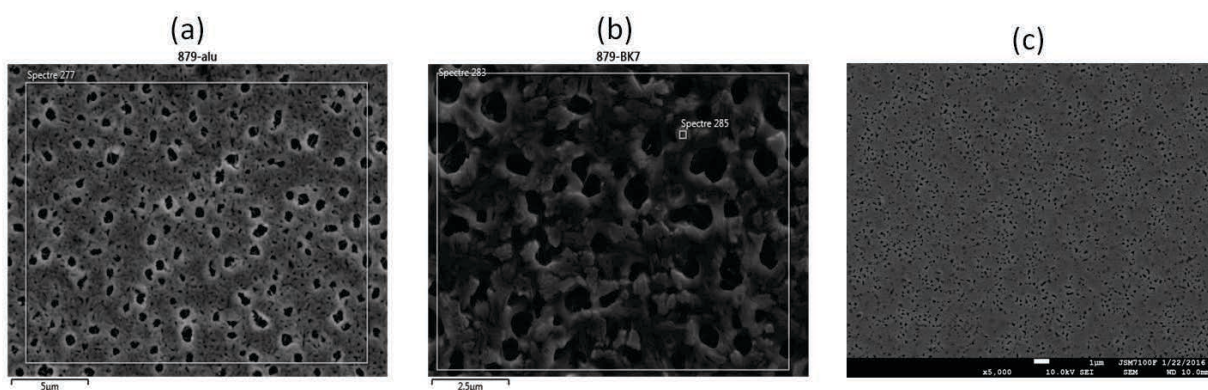


Figure 4-35 SEM images of CuI/“40-40-40” thin films deposited on aluminum (a), BK7(b), and ZnO (c)

Reflectance spectra of those thin films are shown in fig. 4-36. Thin films with aluminum layer/electrode shows the narrowest transparency region with a cut off at 1150 nm (black), which is much higher compared to thin film sputtered on BK7 reference glass with a cutoff around 880nm (red). ZnO

provides the largest transparency region with a shifted reflectance cut off to 680 nm (blue). Thus, for further preparation of solar device, we decided to use transparent oxide ZnO as a bottom electrode since it provides wider range of wavelengths for absorption with “40-40-40” layer. One can notice that only a few differences can be distinguished on XRD of “40-40-40” (red) and “40-40-20” (green) thin films presented in fig. 4-37. The weaker pronouncement of Sb_2Se_3 related peak at 23.901° is related to the (1 3 0) orientation and the appearance of a peak at 32.220° peak corresponds to the (3 0 1) orientation. We can also underline overall weaker intensity of all the major peaks for “40-40-40” thin film despite the fact that it is rich in copper compared to the “40-40-20” composition. Slightly weaker crystallization can be explained by larger amount of iodine which is a heavy atom with large poling radius. It requires more energy to be installed in crystalline lattice with probably slightly higher disorder in the crystalline structure of Sb_2Se_3

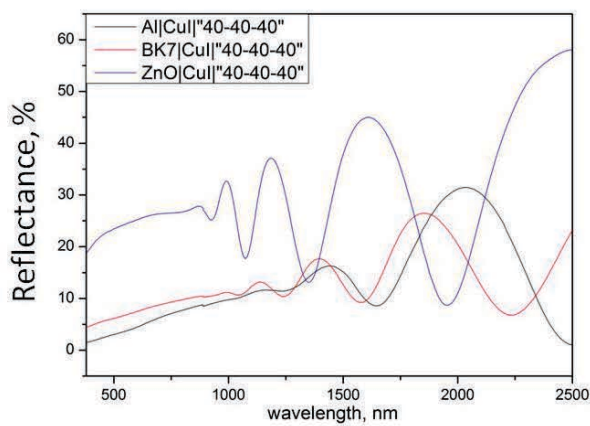


Figure 4-36 Reflectance spectra of CuI|'40-40-40' thin films deposited on aluminum (black), BK7 (red), and ZnO (blue)

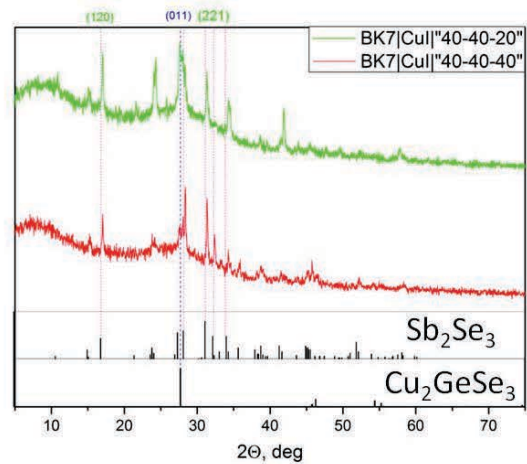


Figure 4-37 XRD spectra of “40-40-40” thin film (red) in comparison with “40-40-20” composition (green)

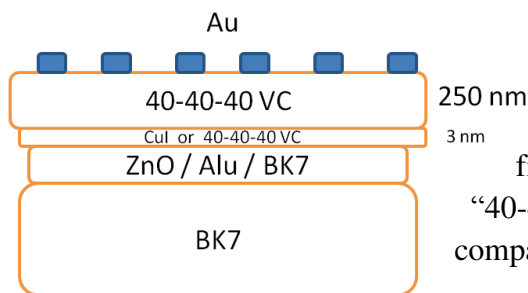


Figure 4-38 Schematic representation of solar cell based on "40-40-40" thin film

For solar cell test, we fabricated a multi-film structure, which is presented in fig. 4-38. We verified several configurations. In the absence of difference in principal film behavior upon variation of pre-deposited layer (CuI or “40-40-40”), we have chosen CuI for the preparation of sample to compare it with “40-40-20” more precisely. IV curves of the

fabricated devices are shown in fig. 4-39. The “40-40-40” thin film deposited on ZnO, with Au electrode (fig. 4-39 (a)) is characterized by rectifying type of curve compared to Ohmic for “40-40-20”. In the dark, we observe a large depletion region with internal barrier voltage of junction comparable to silicone $\sim 0.6V$ and we observe also exponential growth of current density beyond this value. Basically we observe a behavior of simple diode under positive bias.

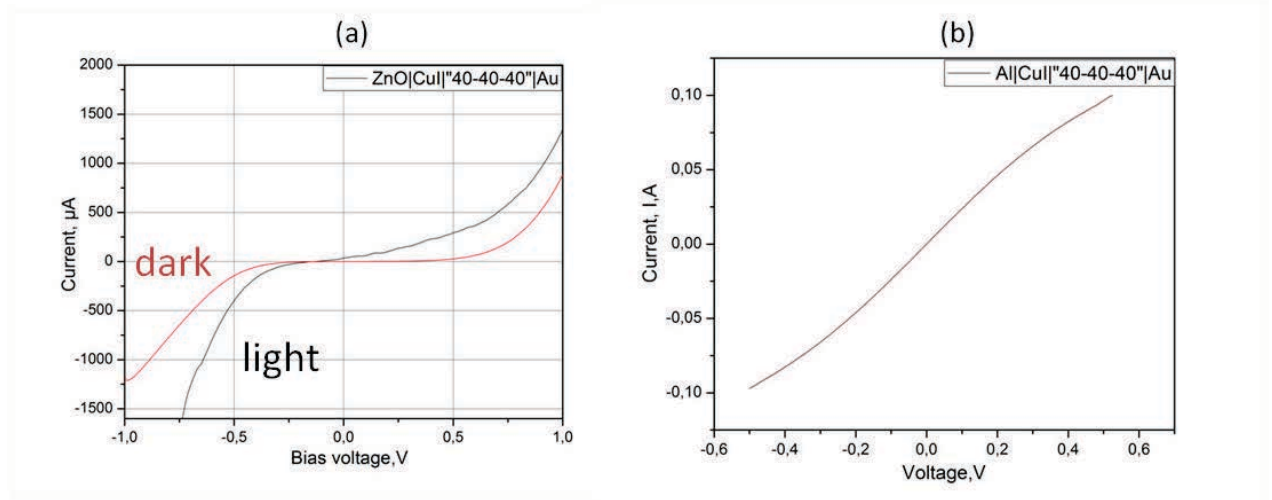


Figure 4-39 IV curves $\text{CuI}^{40-40-40}$ thin films deposited on aluminum (a), BK7(b), and ZnO (c)

Under illumination, we observe a photoconductive effect and even very weak photovoltaic effect with $I_{sc} = 70\mu\text{A}$ and $V_{oc} = -100\text{ mV}$. However this effect appears rather due to the Schottky rectifying contact occurred on the interface between photoconductive phase and Au electrode. The device with Al electrode (fig. 4-39 (b)) demonstrates low resistive behavior with slight non-linearity. In any case, its conductivity is close to that metallic contact probably due to the diffusion of Al through the thin film during heat treatment and this creates high conductive paths and eliminates semiconducting phases from the electric chain.

3.3. Preparation of thin films based on Cu_3SbSe_4 composition

Along with investigations of thin films based on $40\text{GeSe}_2-40\text{Sb}_2\text{Se}_3-20\text{CuI}$, we have carried out a research on Cu_3SbSe_4 behavior upon the annealing. Cu_3SbSe_4 is a p-type semiconductor mostly known for thermoelectric applications^{42,43,44}. Typical morphology of Cu_3SbSe_4 annealed at $300\text{ }^\circ\text{C}$ is depicted in fig. 4-40. One can find here several different morphological species: extended to $1\mu\text{m}$ rods with diameter of 100-200 nm, spherical dots of 10-50 nm diameter and thin needles of 10-20 nm in diameter. Wu et al. showed that nanoparticles of Cu_3SbSe_4 possess similar morphology. Extended rods are similar to Sb_2Se_3 expressed in "40-40-20" thin film (fig. 4-23).

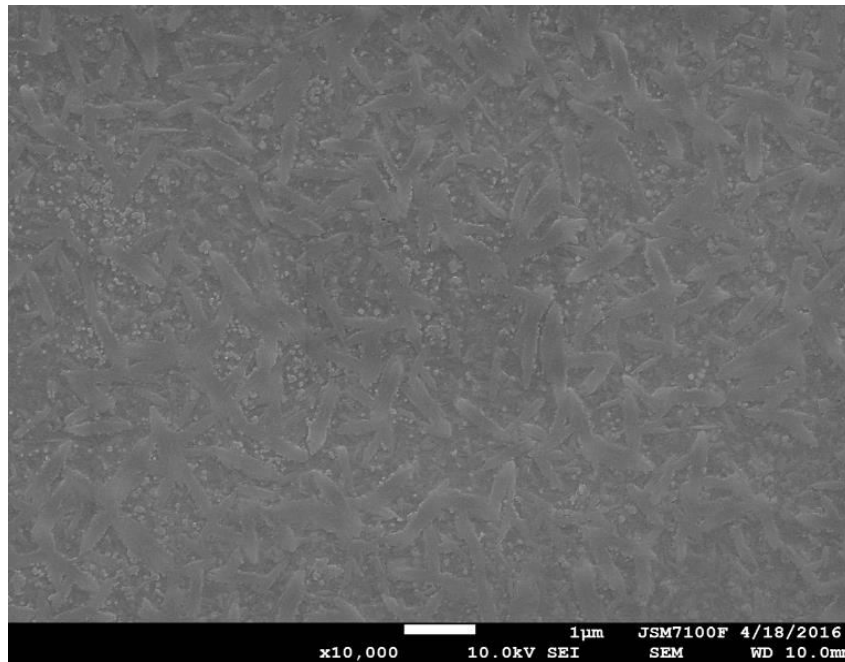


Figure 4-40 SEM image of thin film Cu_3SbSe_4 annealed at 300 °C

Annealing does not significant influence on reflectance cut off, which is 760 nm for all prepared thin films with or without additional heat treatment (fig. 4-41). Unlike to the “40-40-20” based thin films, Cu_3SbSe_4 does not undergo severe loss of chemical elements. However on XRD spectra shown in fig. 4-42, we noticed certain structural evolution. Thin film annealed at 150 °C (violet curve) is not sufficiently crystallized, however 180 °C (red line) is already enough to generate Cu_3SbSe_4 crystalline phase expressed in pronounced peak at 27.420 which stays for (1 1 2) orientation and peak at 45.642° for (2 0 4) orientation of permingeatite with tetragonal symmetry and cell parameters $a=b=5.63 \text{ \AA}$, $c = 11.23 \text{ \AA}$. With increase of temperature, these peaks gradually grow up to 250 °C (pink curve). When growth of crystals with these orientations stops and some other peaks appear, in particular at 27° and 49°, this peaks reach their maximal at annealing temperature of 300 °C and can be associated with some orientation of Sb_2Se_3 , i.e (0 2 1) at 27.022° and (2 1 2) at 48.907°. Presence of this phase could explain the needle-like structures visible on SEM of thin film annealed at 300 °C.

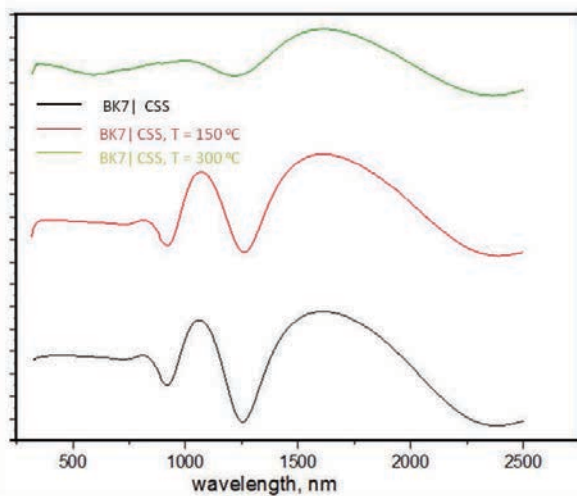


Figure 4-41 Reflectance spectra of Cu_3SbSe_4 annealed at different temperatures: not annealed (black), 150 °C (red), 300 °C (green)

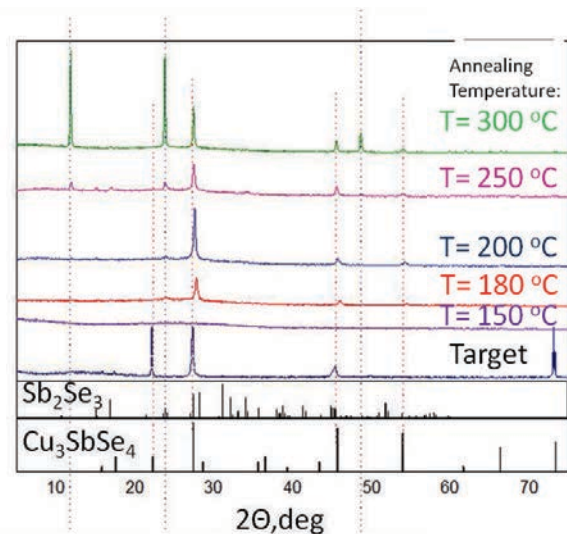


Figure 4-42 XRD spectra of Cu_3SbSe_4 annealed at different temperatures: 150 °C (violet), 180 °C (red), 200 °C (blue), 250 °C (pink), 300 °C (green) and target spectrum (black)

Hall Effect measurement and EDS measurement are summarized in table 4-6. As it can be seen, no significant change in atomic composition occurs after annealing and the composition stays almost perfectly stoichiometric. We observe an interesting transition from N to P type semiconductor at 180 °C, which correlates with announced crystallization of Cu_3SbSe_4 phase seen on XRD spectra. Without annealing or after treatment at 150 °C, which does not lead to crystallization, Cu_3SbSe_4 thin film is a weak n-type semiconductor with relatively low charge concentration and mobility. With appearance of pronounced crystalline phase, mobility and concentration of charge carriers rapidly increase, in consequence resistivity decreases. It is interesting to mention that the highest charge carrier concentration of 10^{21} m^{-3} is found for thin film annealed at 180°C. Further annealing decreases charge carrier concentration by 10^3 times with slight increase of mobility. It results in overall loss of conductivity by approximately 10 times. This effect can be connected with the appearance of significant amount of Sb_2Se_3 phase, which reduces overall conductivity and charge carrier concentration. However it does not correlate with increase of mobility, which, according to Matthiessen's law, should be decreased since Sb_2Se_3 phase would serve as a scattering center. Since the composition does not change substantially, we can conclude that only the structural features such as presence of secondary phase, composition and grain size, play the key role in electric properties of thin films.

Table 4-6 Summary of Hall measurement and EDS measurement of Cu_3SbSe_4 thin films annealed at different temperatures

Annealing Temperature	Charge carriers concentration	Mobility, $\text{cm}^2/(\text{V}\cdot\text{s})$	Resistivity Ohm-cm	Type of conductivity	Cu(%)	Se(%)	Sb(%)
NR	$7 \cdot 10^{18}$	$7.9 \cdot 10^{-2}$	10	N	38	50	12
150	$9 \cdot 10^{18}$	$9.45 \cdot 10^{-2}$	7.14	N	38	50	12
180	$1 \cdot 10^{21}$	2.58	$1.8 \cdot 10^{-3}$	P	35	49	16
200	$9 \cdot 10^{20}$	3.07	$2.1 \cdot 10^{-3}$	P	38	47	15
250	$9 \cdot 10^{18}$	29	$2.24 \cdot 10^{-2}$	P	38	49	13
300	$4 \cdot 10^{18}$	45	$3 \cdot 10^{-2}$	P	37	47	16

Further we proceeded to PEC test of all prepared thin films. Despite severe difference in conductivity and charge carrier concentration, all films showed similar performance in the interaction with LiClO_4 solution used as the electrolyte. Thin films showed weak p-type semiconducting behavior far behind the results obtained with “40-40-20” thin films. Photocurrent of $9\text{-}20 \mu\text{A}/\text{cm}^2$ under -0.6V was obtained. There is no correlation between Hall parameters and photocurrent intensity. Even the thin film annealed at 150 °C, which possess n-type conductivity according to Hall Effect measurement shows similar results, compared to other samples with p-type photoconductivity.

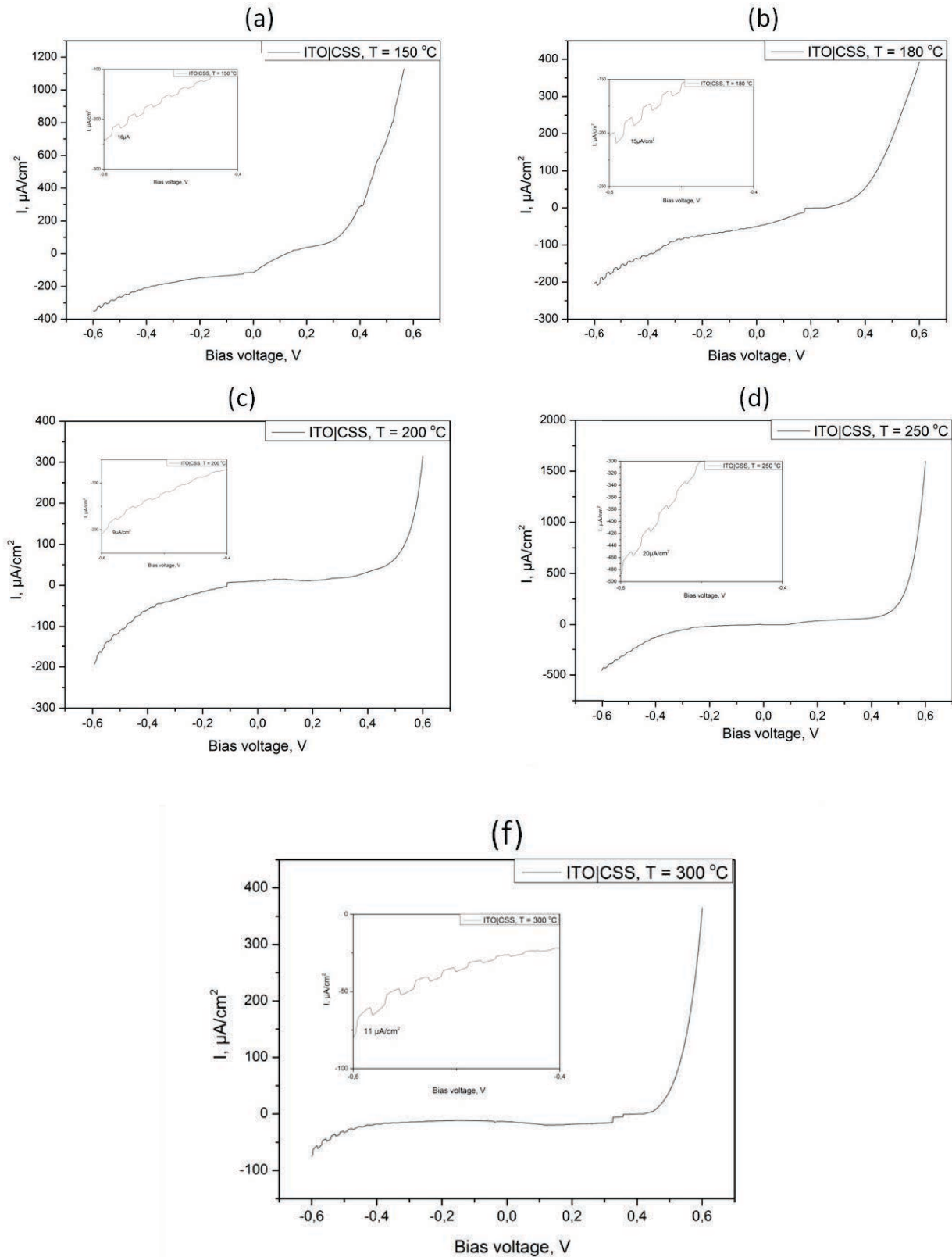


Figure 4-43 PEC curves of Cu_3SbSe_4 thin films annealed at different temperatures; 150 °C (a), 180 °C (b), 200 °C (c), 250 °C(d), 300 °C(f).

Despite the opposite result of PEC measurement and Hall effect measurement for certain thin films, we tried to prepare a planar p-n junction of n- Cu_3SbSe_4 annealed at 150 °C (100 nm) and p- Cu_3SbSe_4 annealed at 300 °C (300nm). This junction was sandwiched between thin layers of transparent conductors:

p-type conductor CuI (50nm) on the bottom and n-type ZnO (50 nm) on the top with Au contacts for electrodes as shown on fig. 4-44.

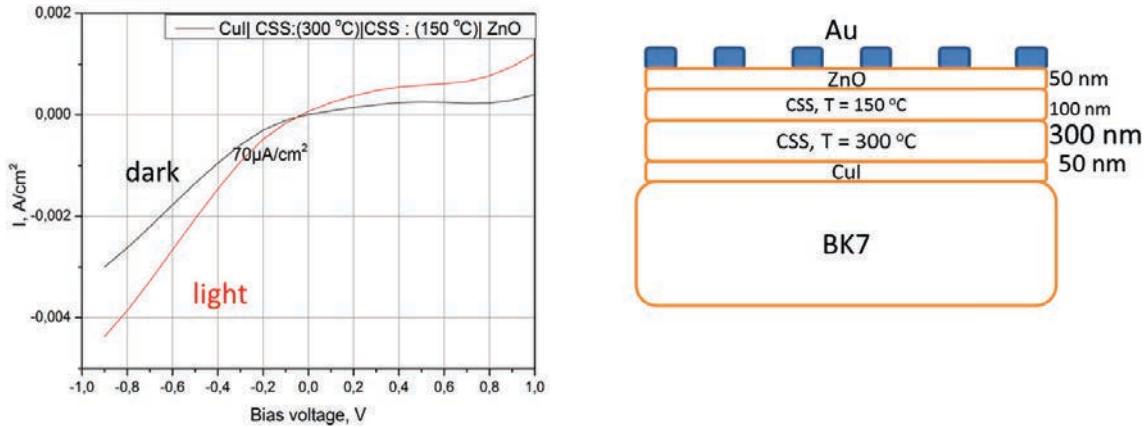


Figure 4-44 Schema of planar p-n junction made of n-Cu₃SbSe₄/p-Cu₃SbSe₄ and its IV curve

As a result, we obtained rectifying junction similar to “40-40-40” thin film with weak photovoltaic effect, which can be accounted to transitional processes in CSS|ZnO|Au junction and photo-charge generation at metal/semiconductor interface. However it is evident that we did not succeed in fabricating planar p-n junction with only Cu₃SbSe₄. It is also dubious to use this material as a p-type layer since its performance is inferior to that of thin films based on the “40-40-20” composition.

3.4. Fabrication of planar heterojunction with thin films of p-type [40GeSe₂-40Sb₂Se₃-20CuI]

Since Cu₃SbSe₄ did not show any interesting performance for photovoltaic application we turned back to thin films based on 40GeSe₂-40Sb₂Se₃-20CuI. We succeeded in compensating possible loss of elements during deposition and annealing with CuI enriched target composition, the “40-40-40” modification. However we found certain excess of copper in these films, which is undesirable since copper can be responsible for appearance of metallic conductivity. Thus we tried to protect our films from loss of iodine but by keeping the amount of copper below 5.5%. We also took into account the fact that it is less likely that we can obtain bulk heterojunction within solely deposited “40-40-20” thin film (or its modification). However, these films had some potentials to be used as p-type layers in planar heterojunction. We also made an attempt to prepare thin films based on Sb₂Se₃ doped iodine, since bulk samples of this composition showed n-type conductivity with some interesting photoconductive effects.

Therefore, for the purpose of iodine conservation, we prepared iodine-rich versions of the 40GeSe₂-40Sb₂Se₃-20CuI target, i.e 40GeSe₂-40Sb₂Se₃-20CuI_{1.5} (“IDEX”) and 40GeSe₂-40Sb₂Se₃-20CuI₂ (“VIDEX”). To prepare iodine doped Sb₂Se₃, we fabricated two targets with 10 mol. % and 20 mol. % of iodine.

Firstly, we present two PEC curves (fig. 4-45) of IDEX deposited on ITO (a) and of a planar junction between Sb₂Se₃:I and IDEX sputtered also on ITO (b). IDEX was deposited with 250nm thickness, Sb₂Se₃:I of about 200 nm. Both films were annealed at 272 °C. As one can see, both p-type photocurrent under negative bias and n-type photocurrent under positive bias are present. For IDEX, p-type photocurrent is much stronger obtaining 490 μA/cm² at -0.6V comparable with the “40-40-20” film.

However, the presence of n-type semiconducting phase is quite evident with $50 \mu\text{A}/\text{cm}^2$ at $+0.6\text{V}$. For the planar junction we observe a reduction of photocurrent under negative bias with slightly better enhancement of the one at positive bias. Obviously, IDEX itself contains enough $\text{Sb}_2\text{Se}_3:\text{I}$ phase to produce strong photocurrent under positive bias (case of fig. 4- 45(a)). It is possible that the additional thin film of $\text{Sb}_2\text{Se}_3:\text{I}$, in the case of fig. 4-45(b), also contributes to photo-charge generation, explaining the enhancement of higher photocurrent intensity at positive bias.

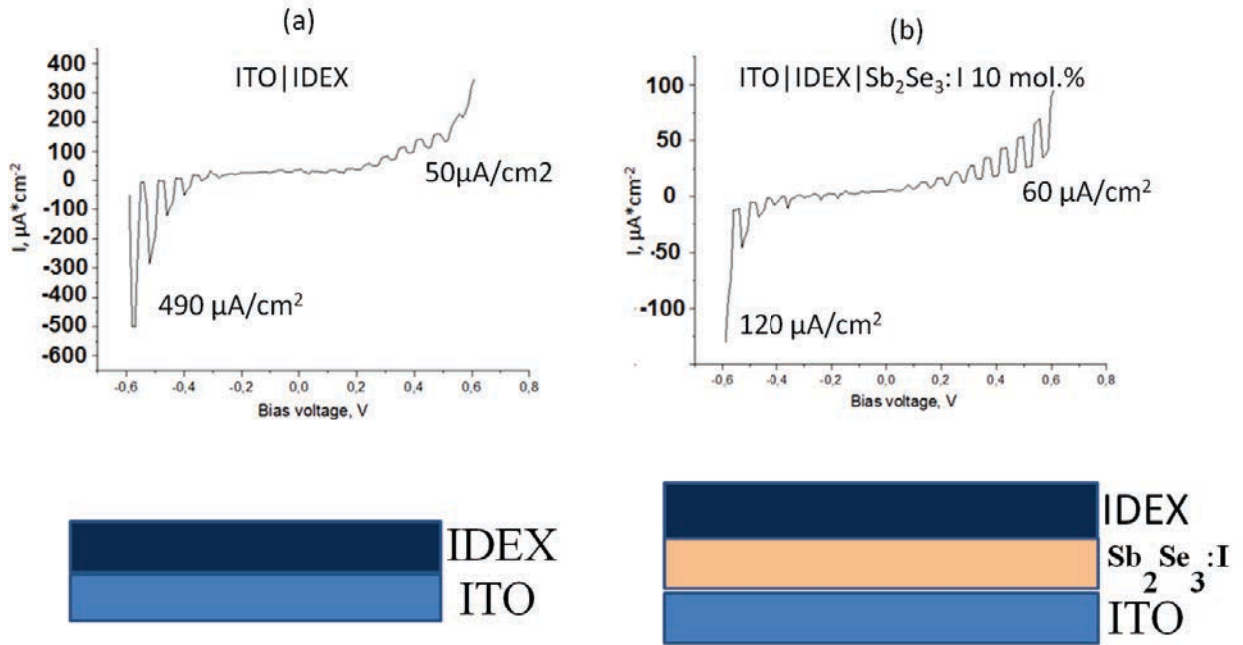


Figure 4- 45 PEC curves of IDEX (a) and planar junction $\text{Sb}_2\text{Se}_3:\text{I}$ (10 mol. %)|IDEX (b)

To understand possible loss in photocurrent produced by IDEX phase in planar configuration, it is interesting to have a look on the reflectance spectra of IDEX and of $\text{Sb}_2\text{Se}_3:\text{I}$ shown in fig. 4-46. As one could see, there is now shift in reflectance cut off for IDEX before and after annealing (compare blue line and grey line). But we easily could find this shift for $\text{Sb}_2\text{Se}_3:\text{I}$ (compare orange and red lines). Upon the annealing, transparency region of $\text{Sb}_2\text{Se}_3:\text{I}$ shifts towards longer wavelengths from 630 nm to 730 nm with substantial increase in reflectance up to 50-55% which is crucial for light harvesting in IDEX. Losing a significant part of absorption spectra and incident light intensity, charge generation inevitably becomes less intense which results in overall decrease of IDEX phase contribution to the observed photoconductive effect.

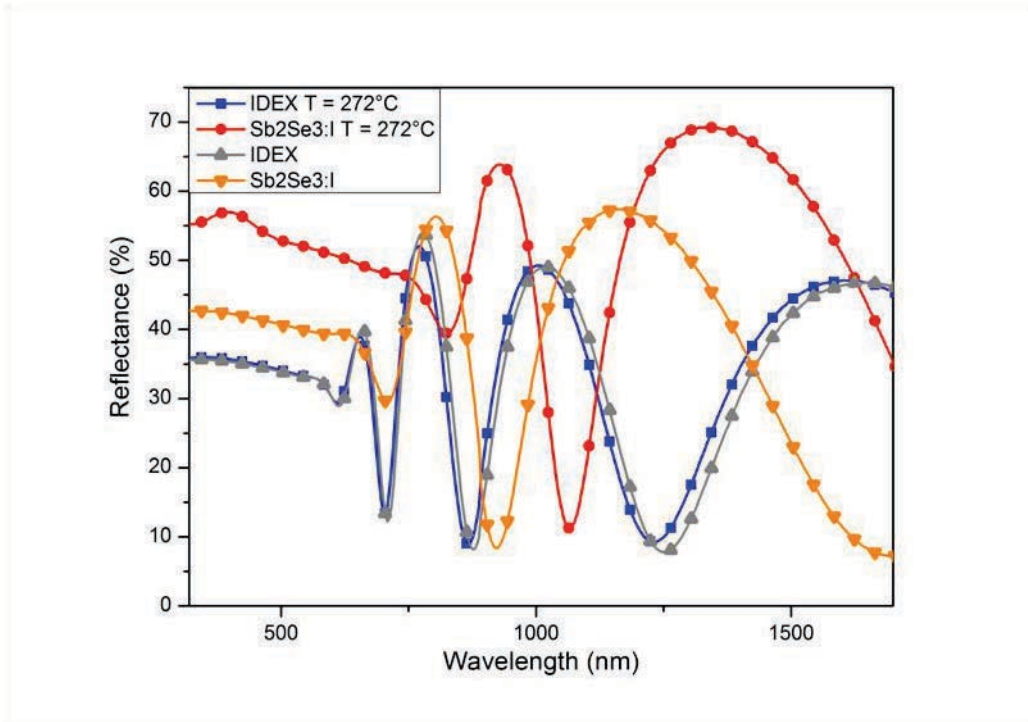


Figure 4-46 Reflectance spectra of IDEX before (grey) and after (blue) annealing and Sb₂Se₃:I before (orange) and after (red) annealing

Having promising PEC results, we prepared planar junction between IDEX and Sb₂Se₃:I in two different configuration. IV curves of these cells are shown in fig. 4-47. As it can be seen, configuration (b) is much more favorable with $J_{sc} = 10 \text{ mA/cm}^2$ and $V_{oc} = 255 \text{ mV}$, when in reverse configuration (a) photocurrent drops to $J_{sc} = 0.5 \text{ mA/cm}^2$ and $V_{oc} = 170 \text{ mV}$.

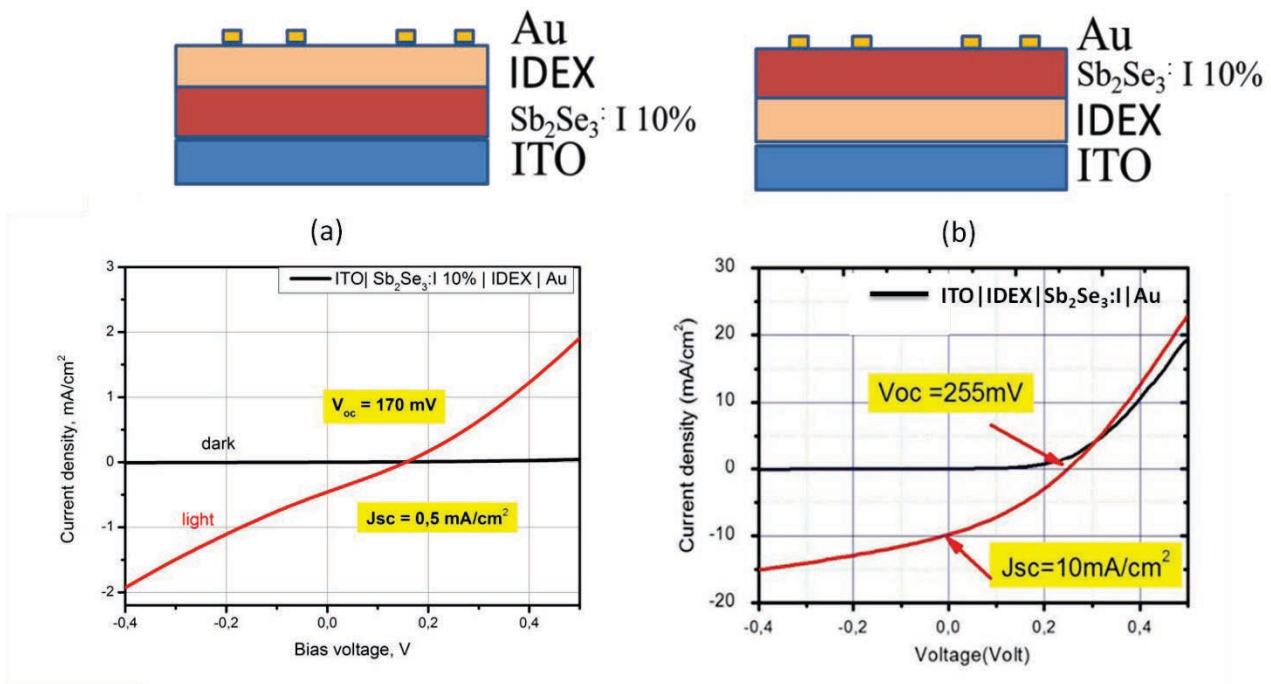
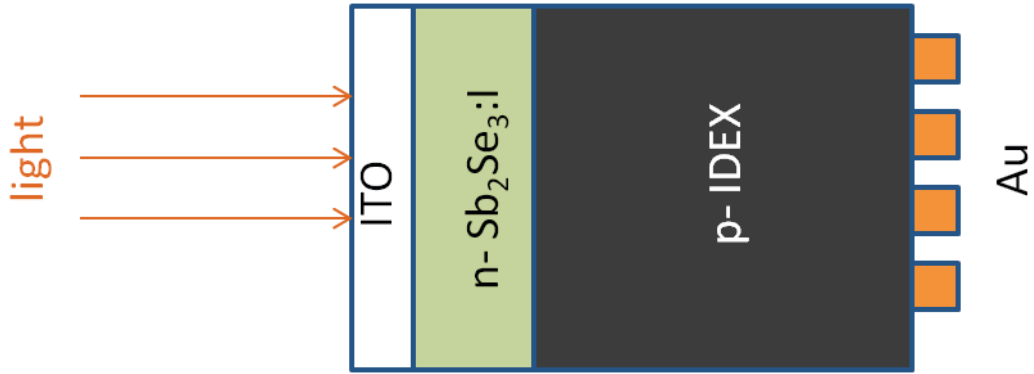


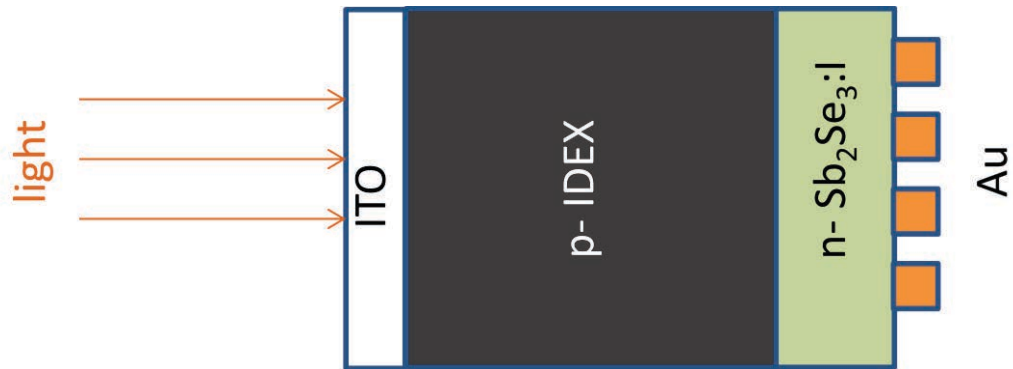
Figure 4-47 IV curve of two different configuration ITO| Sb₂Se₃ : I | IDEX | Au (a), ITO|IDEX|Sb₂Se₃:I| Au (b)

What is the most important here is to answer the question: are we dealing with planar p-n junction or a Schottky barrier in this case? We suppose that IDEX is a p-type semiconductor and Sb₂Se₃:I is an n-

type. If one will go back to the introduction and have a look on fig. 4-18, he will find out that usually incident light falls on n-type semiconductor, which is relatively thin, and then absorbed by p-type semiconductor. It is explained by the effective mass of electrons and holes and their mobility. Electrons are “lighter” and have higher mobility, thus p-layer can be thicker and photogenerated electrons still will be able to reach p-n junction interface. We use ITO as a transparent conductor, which makes it even more evident to use the n-type layer in front of p-type on the path of incidence. Thus an optimal structure would be the following:



Here electron hole pair generated in IDEX can be driven by p-n junction electric field: electrons can be brought to n-type $\text{Sb}_2\text{Se}_3:\text{I}$, holes can be collected by Au electrode. Electrons can be brought from $\text{Sb}_2\text{Se}_3:\text{I}$ to ITO. This is what we have prepared and measure in fig. 4-47 (b). However this configuration does not work! We face the same problem we had with “40-40-20” film, i.e weak rectification, near Ohmic contact between active layer and electrode. At the same time, we obtain stronger photocurrent and open circuit voltage for the configuration that does not have logical sense from above described point of view. We paired n-ITO with p- IDEX, which is strongly absorbing, and separate it from Au electrode by n- Sb_2Se_3 :



The most of the light is absorbed in thick layer of p-IDEX and the electron-hole pairs are almost impossible to be separated, since hole needs to pass n- $\text{Sb}_2\text{Se}_3:\text{I}$ to get the Au electrode and contribute to the current. n- $\text{Sb}_2\text{Se}_3:\text{I}$ is polycrystalline material with a lot of grain boundaries and defects besides its n-type semiconducting characteristic with high concentration of free charge carriers. Considering this, one can conclude that n- $\text{Sb}_2\text{Se}_3:\text{I}$ is impermeable barrier for the holes and solar cell will not be functioning in this configuration, at least, not via the p-n junction interface.

The reason why we observe an effect is probably similar to what described in n-CdS|Al junction⁴⁵ with comparable J_{sc} and V_{oc} , attributed to the Schottky barrier photodiode. In our case, an incident light absorbed by n- $\text{Sb}_2\text{Se}_3:\text{I}$ can cause generation of e-h pairs, h is collected by Au electrode⁴⁶ while electron

is brought to IDEX, which contains significant quantity of Sb_2Se_3 :I either. This phase can share its iodine doped Sb_2Se_3 conductive paths to bring electrons at ITO gate. This relatively resistive path causes fall of electric tension and appearance of V_{oc} . This assumption was partially confirmed when we observed a decrease of V_{oc} upon the decrease of IDEX thickness.

Another interesting sample is IDEX on ZnO. Transparent semiconductor allows high-grade absorption by IDEX and one can observe photovoltaic effect with J_{sc} IDEX = 2 mA/cm² and V_{oc} = 60 mV. As it was observed in several previous cases, we found near-Ohmic contact between Au and IDEX with sub-contact charge carrier generation. The reason why we are observing this effect in IDEX and did not obtain it for “40-40-20” film is a sufficient quantity of Sb_2Se_3 :I phase, which apparently contributes to the most to the photo-charge carrier generation.

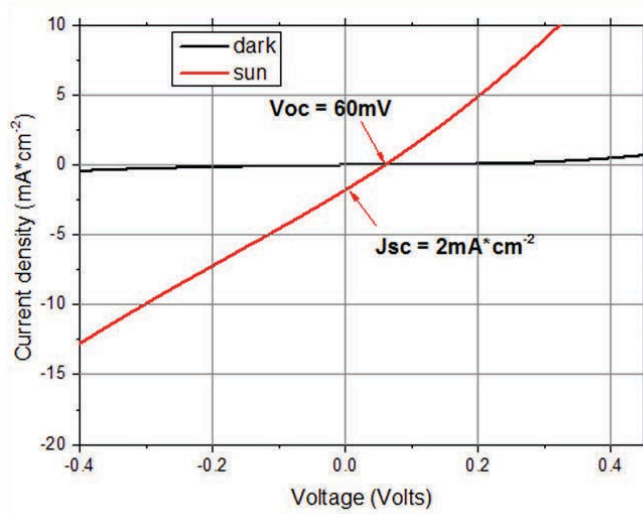
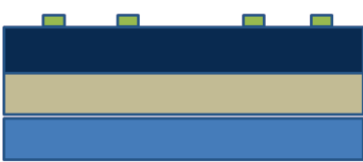


Figure 4-48 IV curve of ITO|ZnO|IDEX|Au device

It is also interesting to consider several structures with iodine rich thin films, i.e. VIDEX and Sb_2Se_3 : I 20 mol. %. On fig. 4-49 one can see SEM image of VIDEX annealed at 272 °C. Generally it is fairly similar to the “40-40-20” thin film with pre-deposited layer of CuI. We can see spherical inclusions of 5-10 μm in diameter as well as well-sintered rods of Sb_2Se_3 with diameter of several hundreds of nanometers. SEM image of Sb_2Se_3 : I 20 mol. % thin film presented on fig. 4-50 is also similar to Sb_2Se_3 related compound widely studied in this dissertation. One can distinguish several types of rods here: thicker rods of 500 nm in diameter and randomly mixed thin, relatively short rods with diameter below 100 nm. It is interesting that most of the thin film surface is smooth without any voids or defects. A crack which is observed on SEM image probably appeared due to inhomogeneous heat distribution during the annealing process when different zones expanded with different speed, which resulted in local exfoliation of the layer. By analyzing the composition, we found however not more than 10% of iodine. The reason of severe loss of iodine for the target with 20 mol. % of I is that for plasma launching it requires higher electric power (20 W compare to 12-15 W usually), which probably leads to reduced adsorption of iodine atoms on the substrate. Therefore increased amount of iodine is compensated by increased loss due to some technical peculiarities of magnetron sputtering. For the moment, it is difficult to point out any difference between thin film obtained from targets with 10 and 20 mol. % of iodine.

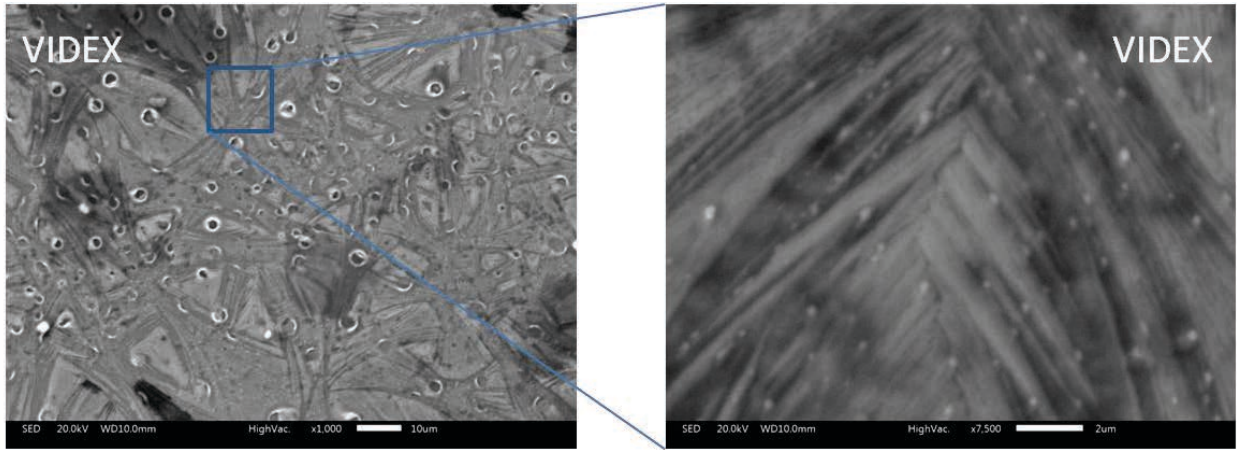


Figure 4-49 SEM image of VIDX thin film annealed at 272 °C

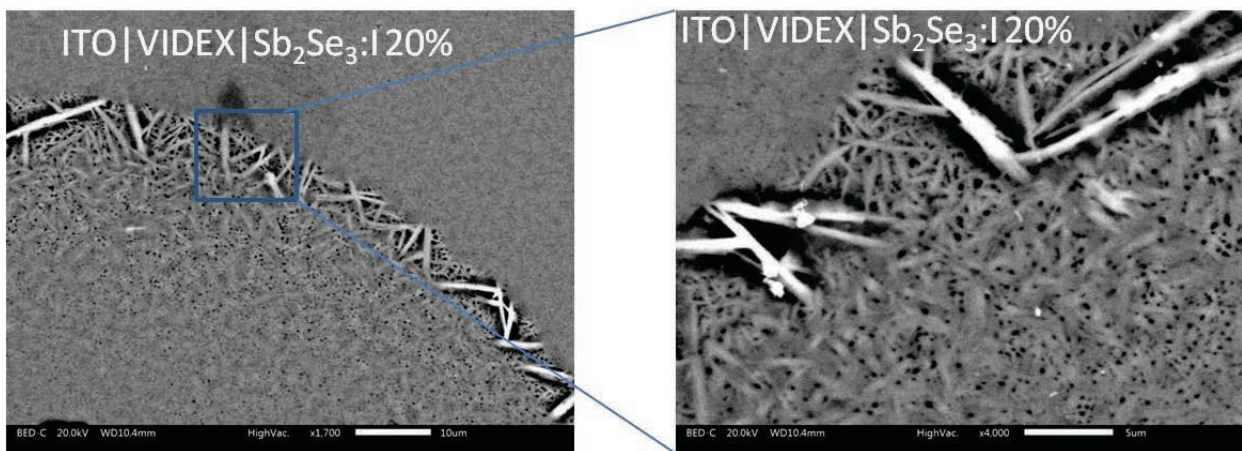


Figure 4-50 SEM image of ITO|VIDEX|Sb₂Se₃ :I thin film annealed at 272 °C

As it can be seen from fig. 4-51 (a), the IV curve of VIDX|Sb₂Se₃: I (10 mol. %) underwent some change compared to IDEX|Sb₂Se₃: I (10 mol. %) fig. 4- 47 (b). J_{sc} is comparable and equals to 8 mA/cm² and V_{oc} has a quite interesting value of 298 mV. Sb₂Se₃ doped with 20% of iodine shows the same J_{sc} when paired with VIDX fig. 4-51(b) as Sb₂Se₃ with 10% iodine with IDEX, which signifies probably that the amount of iodine reaches its optimum for IDEX

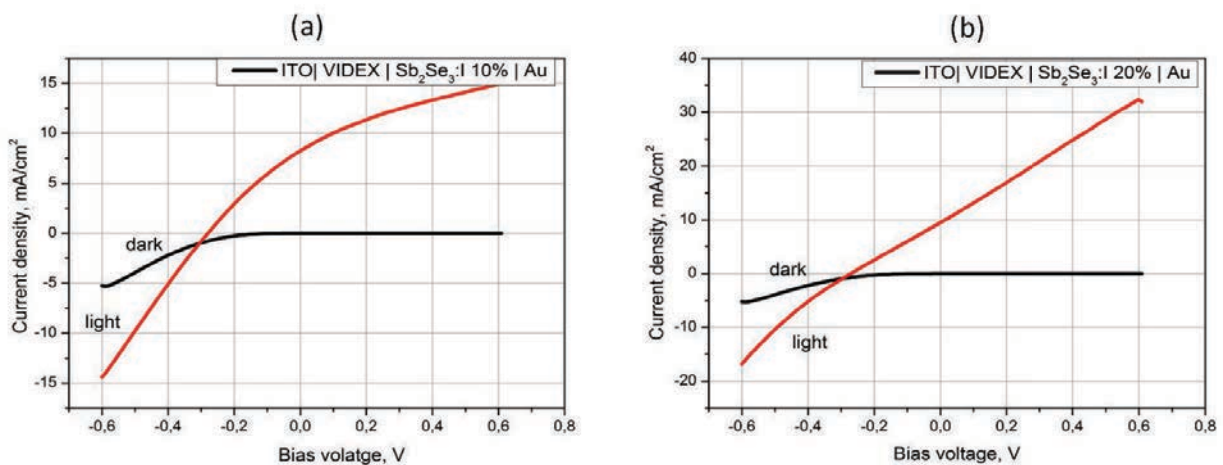


Figure 4-51 I-V curves of VIDX|Sb₂Se₃: I (10 mol. %) (a) and VIDX|Sb₂Se₃: I (20 mol. %) (b)

We also made an attempt to pair p-Sb₂Se₃ and n-Sb₂Se₃:I, obtaining V_{oc} = 200 mV and I_{sc} = 5 mA/cm² (fig. 4-52). That is comparable to the IDEX|Sb₂Se₃:I configuration and indirectly confirms the hypothesis that the major contribution to photocurrent is brought by Schottky junction between Sb₂Se₃:I and Au electrode, while underlying thin film, IDEX, VIDEX or simple Sb₂Se₃ play a role of spacer, which contributes to electric tension fall on the chain of electric circuit between Sb₂Se₃:I and ITO electrode.

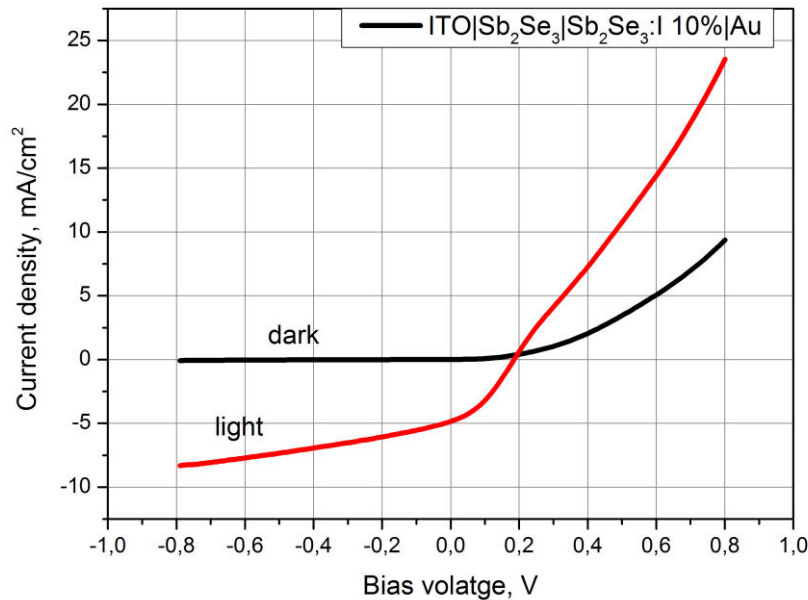


Figure 4-52 I-V curve of solar cell ITO|Sb₂Se₃|Sb₂Se₃:I 10%|Au

4. Conclusion

In conclusion we have prepared and characterized a various thin films based on 40GeSe₂-40Sb₂Se₃-20CuI glass-ceramics composition and crystalline chalcogenides as various iodine-doped Sb₂Se₃ and Cu₃SbSe₄.

It was shown that deposit conditions have severe influence on microstructure and photoconductivity of “40-40-20” based thin films. The most intense photocurrent (700μA/cm² at -0.6V under 250 W×cm²) was obtained for the thin film with pre-deposited CuI layer and post-growth heating treatment. This film demonstrates pronounced p-type behavior.

Various attempts to overcome loss of iodine were made. Thin film based on CuI rich target “40-40-20” shows weak photovoltaic effect. Thin films based on iodine-rich “40-40-20” compositions: VIDEX and IDEX were prepared and characterized. They demonstrate both n-type and p-type behavior signifying co-existence of two phases with different type of conductivity.

The most remarkable photovoltaic effect with J_{sc} = 10 mA/cm² and V_{oc} = 255 mV was found for ITO|p-IDEX|n-Sb₂Se₃:I|Au planar thin film design. This effect takes place, probably, due to Shottky-barrier photosensitive contact between n-Sb₂Se₃:I and Au-electrode.

5. References

- ¹Iovu, M. S., Colomeico, E. P. & Vasiliev, I. A., *Photoconductivity of Amorphous Sb₂Se₃ and Sb₂Se₃:Sn Thin Films*. CHALCOGENIDE LETT., 2007, **4**: pp. 109–113.
- ²Mehta, R. J., et al., *High Electrical Conductivity Antimony Selenide Nanocrystals and Assemblies*. Nano Lett., 2010, **10**: pp. 4417–4422.
- ³Zhai, T. et al., *Single-Crystalline Sb₂Se₃ Nanowires for High-Performance Field Emitters and Photodetectors*. Adv. Mater., 2010, **22**: pp. 4530–4533
- ⁴Vadapoo, R., Krishnan, S., Yilmaz, H. & Marin, C., *Electronic structure of antimony selenide(Sb₂Se₃) from GW calculations*. Phys. status solidi B, 2011, **248**: pp. 700–705.
- ⁵Watkins PK, Walker AB, Verschoor GB, *Dynamical Monte Carlo modelling of organic solar cells: the dependence of internal quantum efficiency on morphology*. Nano Letters ,2005, **5**: p.1814–8.
- ⁶M.C. Scharber, N.S. Sariciftci, *Efficiency of bulk-heterojunction organic solar cells*. Progress in Polymer Science, 2013, **38** (12): pp. 1929-1940.
- ⁷J. H. Hildebrand, *Solubility. XII. Regular solutions*. J. Am. Chem. Soc., 1929, **51**: 66.
- ⁸K.Broch, *Interplay of Ordering Behavior and Optical Properties in Organic Semiconductor Blends*. Thesis, Tübingen, 2013.
- ⁹A. Kitaigorodsky, *Molecular crystals and molecules*. Edited by E. M. Loebl, Academic Press, London, New York, 1973.
- ¹⁰A. Kitaigorodsky, *Mixed crystals*. Edited by M. Cordona, Springer Verlag, Heidelberg, 1984.
- ¹¹Gaveshana A. Sepalag, et al., *Copper(I) Iodide as Hole-Conductor in Planar Perovskite Solar Cells: Probing the Origin of J – V Hysteresis*. Adv. Funct. Mater., 2015, **25**: pp. 5650–5661
- ¹²Jeffrey A. Christians, et al., *An Inorganic Hole Conductor for Organo-Lead Halide Perovskite Solar Cells. Improved Hole Conductivity with Copper Iodide*. J. Am. Chem. Soc., 2014, **136** (2): pp. 758–764.
- ¹³Spencer Williams, et al., *High-Performance and Environmentally Stable Planar Heterojunction Perovskite Solar Cells Based on a Solution-Processed Copper-Doped Nickel Oxide Hole-Transporting Layer*. Adv. Mater. 2014, online.
- ¹⁴Zhi Yang, et al., *Developing Seedless Growth of ZnO Micro/Nanowire Arrays towards ZnO/FeS₂/CuI P-I-N Photodiode Application*. Scientific Reports **5**, Article number: 11377.
- ¹⁵Lars Stolt, et al., *ZnO/CdS/CuInSe₂ thinfilm solar cells with improved performance*. Appl. Phys. Lett., 1993, **62**: pp. 597-599.
- ¹⁶J. Katayama, *Performance of Cu₂O/ZnO Solar Cell Prepared By Two-Step Electrodeposition*. Journal of Applied Electrochemistry, 2004, **34**(7): pp. 687–692.
- ¹⁷Dieter Schmid, Martin Ruckh, Hans Werner Schock, *A comprehensive characterization of the interfaces in Mo/CIS/CdS/ZnO solar cell structures*. Solar Energy Materials and Solar Cells, 1996, **41-42**: pp. 281-294.
- ¹⁸Miguel A. Contreras, et al., *19.9%-efficient ZnO/CdS/CuInGaSe₂ solar cell with 81.2% fill factor*. Prog. Photovolt: Res. Appl. 2008, **16**: pp. 235–239.
- ¹⁹Zong-Liang Tseng, Chien-Hung Chiang & Chun-Guey Wu, *Surface Engineering of ZnO Thin Film for High Efficiency Planar Perovskite Solar Cells*. Scientific Reports **5**, Article number: 13211
- ²⁰Hoye RL, et al., *Improved Open- Circuit Voltage in ZnO-PbSe Quantum Dot Solar Cells by Understanding and Reducing Losses Arising from the ZnO Conduction Band Tail*. Adv Energy Mater. 2014, **4**(8):pp. 1301544.
- ²¹Wolfgang Kaysser, *Powder Metallurgy and Sintered Materials*, Wiley-VCH Verlag GmbH, 2012.

- ²² Olivier Guillon, et al., *Field-Assisted Sintering Technology Spark Plasma Sintering: Mechanisms, Materials, and Technology Developments*. ADVANCED ENGINEERING MATERIALS, 2014, **16**(7): pp. 830-849.
- ²³ R. Pantou et al., *Hot pressing sintered $Cu_xMo_8S_6$ targets for laser ablation thin films deposition*. Solid State Sciences, 1999, **t. 1**: pp. 647-656.
- ²⁴ D.S. Mungekar, et al., *A laboratory design for uniaxial hot pressing*. Bull. Mater. Sci., 1990, **13**(5): pp. 365-369.
- ²⁵ Qing-Ming Wang, et al., *Preparation of Al-doped ZnO sputter target by hot pressing*. Transactions of Nonferrous Metals Society of China, **21**: pp.1550-1556.
- ²⁶ K.F. Cai, X.R. He, L.C. Zhang, *Fabrication, properties and sintering of ZnO nanopowder*. Mater. Lett., 2008, **62**: pp. 1223–1225.
- ²⁷ Mehdi Mazaheri, et al., *Hot pressing of nanocrystalline zinc oxide compacts: Densification and grain growth during sintering*. Ceramics International, 2009, **35**: pp. 991–995.
- ²⁸ S. Swann, *Magnetron sputtering*, Phys. Technol., 1988, **19**: pp. 67-75.
- ²⁹ John A. Thornton, *Magnetron sputtering: basic physics and application to cylindrical magnetrons*. Journal of Vacuum Science and Technology, 1978, **15**: p. 171.
- ³⁰ P.J. Kelly, et al., *Magnetron sputtering: a review of recent developments and applications*. Vacuum, 2000, **56**: pp. 159-172.
- ³¹ D.L. Smith, *Thin-Film Deposition: Principles Practice*. McGrawHill, 1995.
- ³² *Magnetron Sputtering Technology*, Micro Magnetics, Inc, retrieved from : http://www.directvacuum.com/pdf/what_is_sputtering.pdf
- ³³ B.A. Movchan, A.V. Demchishin, *Fizika Metallov i Metallovedenie (Physics of Metals and Metallography)*. 1969, **28**: p. 653.
- ³⁴ Marcello Rubens, Barsi Andreetta, *Crystallization – Science and Technology*. InTech, 2012, p.397.
- ³⁵ John A. Thornton, *Structure-Zone Models of Thin Films*. SPIE, 1987, Vol. **821 Modeling of Optical Thin Films**: p. 95.
- ³⁶ J.A. Thornton, *Influence of apparatus geometry and deposition conditions on the structure and topography of thick sputtered coatings*. J. Vac. Sci. Technol., 1974, **11**: p. 666.
- ³⁷ Xianghua Zhang, et al., *Enhancement of charge photo-generation and transport via an internal network of Sb_2Se_3/Cu_2GeSe_3 heterojunctions*. J. Mater. Chem. A, 2014, **2** : pp. 17099-17106.
- ³⁸ V. Weidenhof, et al., *Atomic force microscopy study of laser induced phase transitions in $Ge_2Sb_2Te_5$* . Journal of Applied Physics, 1999, **86** : p. 5879.
- ³⁹ Yuhao Zhang, et al., *Ultrathin MgB_2 films fabricated on Al_2O_3 substrate by hybrid physical-chemical vapor deposition with high T_c and J_c* . Supercond. Sci. Technol., 2011, **24**: p.015013.
- ⁴⁰ D. A. G. Bruggeman, *Berechnung verschiedener physikalischer Konstanten von heterogenen Substanzen. I. Dielektrizitätskonstanten und Leitfähigkeiten der Mischkörper aus isotropen Substanzen*. Ann. Phys., 1935, **416**: p. 636.
- ⁴¹ J. C. M. Garnett, *Colours in metal glasses and in metallic films*. Phil. Trans. R. Soc. Lond. A **203**: p. 385.
- ⁴² Chongyin Yang, et al., *New stannite-like p-type thermoelectric material Cu_3SbSe_4* . J. Phys. D: Appl. Phys., 2011, **44**: p. 295404.
- ⁴³ Eric J. Skouga, Jeffrey D. Cain, and Donald T. Morelli, *High thermoelectric Figure 4- of merit in the $Cu_3SbSe_4-Cu_3SbS_4$ solid solution*. Appl. Phys. Lett., 2011, **98**: p. 261911.
- ⁴⁴ Skoug, Eric J., et al., *Doping Effects on the Thermoelectric Properties of Cu_3SbSe_4* . Science of Advanced Materials, 2011, **3**(4): pp. 602-606(5).
- ⁴⁵ A.A.M. Farag, et al., *Electrical and photovoltaic characteristics of Al/n-CdS Schottky diode*. International journal of hydrogen energy, 2009, **34**: pp. 4906–4913.
- ⁴⁶ J. K. Sheu, et al. *High-transparency Ni/Au ohmic contact to p-type GaN*. Appl. Phys. Lett., 1999, **74**(16): pp. 2340-2342.

General conclusions and perspectives

In this work we demonstrated a complete production cycle from elaboration of new compositions and bulk characterization to preparation of thin films and fully functional solar devices based on these compositions.

The photoelectric properties of the 40GeSe₂-40Sb₂Se₃-20CuI glass-ceramics found by chance were studied in details. We showed that iodine plays a key role on appearance of conductivity within the bulk glass-ceramics, which is associated with iodine doped Sb₂Se₃ phase. To prove it we synthesized Sb₂Se₃ crystals with different amount of iodine separately. We demonstrated that iodine improves conductivity of Sb₂Se₃ by several orders in magnitude even being added in small quantities (3 – 5 mol. %). Iodine doped Sb₂Se₃ showed a decent photoconductive performance reaching current density equal to 650 μA/cm² at positive electric bias +0.6V under illumination of 250 W/m² intensity, which is more than 8 times higher than a current density obtained for optimized 40GeSe₂-40Sb₂Se₃-20CuI glass-ceramics (74 μA/cm² in the same conditions).

We also investigated stoichiometric deviation influence on glass-ceramics and Sb₂Se₃ electric behavior. It was found out that the excess of selenium in glassy precursor is capable of improving its conductivity and photoelectric performance. At the same time we observed high flexibility of composition for Sb₂Se₃ which showed increase of conductivity and appearance of photoconductive properties with deficiency of selenium without severe change of crystal structure. It is interesting to mention that in the excess of selenium Sb₂Se₃ behaves as a p-type semiconductor, while in the case of selenium deficiency it is n-type semiconductor with strongly pronounced n-type features.

We showed the influence of small cation and anion substitutions of electric properties of 40GeSe₂-40Sb₂Se₃-20CuI glass-ceramic. It was found that even small additives of sulphur (< 1 mol. %) lead to photoconductive effect vanishing. It also affects negatively glass-forming capabilities of 40GeSe₂-40Sb₂Se₃-20CuI precursor.

We also elucidated the role of bismuth and tin additives on photoelectric properties of 40GeSe₂-40Sb₂Se₃-20CuI glass-ceramic. We showed that bismuth introduction leads to the expression of n-type phase within the bulk glass-ceramic, while tin doping leads to pronounced p-type behavior. It is clear that these doping influence strongly its resistivity and conduction type.

It was found out that neither chlorine nor bromine is capable of doping Sb₂Se₃ crystals and do not contribute to its electric properties. Despite the attractive possibility of Sb₂Se₃ Fermi level tuning by adding highly electronegative elements, both chlorine and bromine showed themselves as useless for improvement of photoelectric properties of glass-ceramics.

Carrying out investigation on thin films we found out that samples based on glass-ceramic composition of 40GeSe₂-40Sb₂Se₃-20CuI show themselves as strong p-type photoconductors and do not demonstrate any n-type behavior. We established that excessive iodine doping in 40GeSe₂-40Sb₂Se₃-20CuI sputtering target leads to appearance of both p-type and n-type phases, which was proven via PEC experiment. However, no photovoltaic effect was

found for this thin film. Fabrication of planar p-n junction between p-type 40GeSe₂-40Sb₂Se₃-20CuI based thin film and n-type iodine doped Sb₂Se₃ was made. This device demonstrates photovoltaic effect with $J_{sc} = 10 \text{ mA / cm}^2$ and $V_{oc} = 255 \text{ mV}$.

Since no additional improvement of annealing conditions was made, it is possible that this result can be improved by optimizing annealing time and temperature.

Sb₂Se₃ showed itself as extremely flexible material with a variety of promising electric properties as resistivity tuning in a wide range and conductivity type transition. It is interesting to investigate the possibility to fabricate planar p-n junction between n-type iodine doped Sb₂Se₃ and p-type tin doped Sb₂Se₃. It could also be interesting to make attempt to fabricate planar and bulk p-n junctions using Sb₂Se₃ solely by varying only the quantity of selenium.

Regarding our experience Sb₂Se₃ can serve as substrate for obtaining new materials with tunable optical and electrical properties by simple doping of it with a variety of elements. Some promising studies on Sb₂Se₃ doping with small amounts of sulphur were published recently.

40GeSe₂-40Sb₂Se₃-20CuI glass-ceramic is a complex system containing both p-type and n-type phases. Its charge generation and charge transfer properties strongly rely on its microstructure and spatial orientation of crystals comprising p-n junctions. It could be interesting to investigate this material further in order to obtain appropriately organized micro domains of p-n junctions with enhanced charge collection capabilities.

40GeSe₂-40Sb₂Se₃-20CuI glass-ceramic is also a promising material for photocatalytic applications. Formation of nano and microscale p-n junctions and conductive domains can enhance separation of photogenerated carriers which is necessary for efficient photocatalytic performance. Therefore, further study is needed to improve glass-ceramic microstructure in order to develop its potential for efficient photocatalyst.

ABSTRACT

Energy crisis and global ecological problems are considered as important challenges of nearest future. Eco-friendly and renewable sources of energy are still severely undeveloped and contribute weakly to the energy production. One of the most attractive and promising domains of renewable energy is a solar light harvesting. However, existing solar panels still possess negative quality factor, i.e. their fabrication and maintenance require more energy that they are capable to produce during their life cycle. Despite exponential reduction of the price, solar cells are not efficient enough in terms of light-to-energy conversion. Recent breakthroughs in material science contributed a lot to the increase of efficiency, however further investigation of novel materials are needed. Here, chalcogenide glass-ceramics of $\text{GeSe}_2\text{-Sb}_2\text{Se}_3\text{-CuI}$ system were studied in details. Within this system various chemical compositions were prepared and analyzed for their structure and photoelectric properties. We found that Sb_2Se_3 phase, responsible for the appearance of photoelectric effect in glass-ceramics, have a great potential for light harvesting due to its suitable optical properties. In the present work we demonstrated the influence of various dopants on photoelectric properties of Sb_2Se_3 crystals. We showed a possibility of conductivity type and resistivity tuning of bulk Sb_2Se_3 crystals in a wide range of values. Thin film devices based on studied bulk compositions were prepared by RF sputtering and characterized structurally and electrically as well. We demonstrated a fully functional thin film solar device based on iodine doped Sb_2Se_3 and $40\text{GeSe}_2\text{-40Sb}_2\text{Se}_3\text{-20CuI}$ glass-ceramic.

RESUME

La crise de l'énergie ainsi que les problèmes écologiques sont considérés comme les défis les plus importants de demain. Cependant, les sources d'énergies renouvelables et respectueuses de l'environnement ne sont pas suffisamment développées, ce qui entraîne une contribution faible à la production d'énergie. Les cellules solaires font partie des sources d'énergies renouvelables les plus attractives et prometteuses. Cependant, les panneaux solaires existants ont toujours un facteur de qualité négatif, c'est-à-dire que leur production et leur entretien demandent plus d'énergie qu'ils ne sont capables de produire pendant leur cycle de fonctionnement. Malgré la réduction exponentielle du prix des panneaux solaires, leur efficacité de conversion n'est pas suffisante. Les succès récents dans la science des matériaux ont beaucoup contribué à son amélioration, néanmoins des études sur les nouveaux matériaux photovoltaïques sont nécessaires. Les travaux de recherche présentés dans ce manuscrit concernent les vitrocéramiques de chalcogénures dans le système $\text{GeSe}_2\text{-Sb}_2\text{Se}_3\text{-CuI}$. De nombreuses compositions chimiques différentes ont été préparées et analysées du point de vue structural et électrique dans le cadre de ce système. Il a été démontré que la phase Sb_2Se_3 , responsable des propriétés photoélectriques dans les vitrocéramiques, possède un grand potentiel pour les applications photovoltaïques grâce à ses propriétés optiques bien adaptées. L'influence des modifications de la composition des cristaux de Sb_2Se_3 sur la structure et les propriétés électriques a été étudiée. La flexibilité du type de conductivité et la résistivité des cristaux massifs de Sb_2Se_3 ont été montrées. Enfin, les couches minces à base de vitrocéramiques et cristaux massifs étudiés ont été préparées par la pulvérisation cathodique RF magnétron. Leur structure et les propriétés électriques sont également décrites dans cette thèse. Une cellule solaire complètement fonctionnelle, basée sur Sb_2Se_3 dopé iode et sur la vitrocéramique de $40\text{GeSe}_2\text{-40Sb}_2\text{Se}_3\text{-20CuI}$, a été préparée et caractérisée.